

Microscopic Theory of Semiconductor Laser Material Systems



Dissertation
zur
Erlangung des Doktorgrades
der Naturwissenschaften
(Dr. rer. nat.)

dem Fachbereich Physik
der Philipps-Universität Marburg
vorgelegt

von
Christian Berger

aus Kassel

Marburg (Lahn), 2016

Vom Fachbereich Physik der Philipps-Universität Marburg
als Dissertation angenommen am 23.06.2016

Hochschulkenziffer: 1180

Erstgutachter: Prof. Dr. Stephan W. Koch
Zweitgutachter: Dr. habil. Wolfgang Stolz

Tag der mündlichen Prüfung: 06.07.2016

Zusammenfassung

Ein Leben ohne Halbleitertechnologie ist heutzutage kaum noch vorstellbar, da viele Aspekte des Alltags eingeschränkt wären. Obwohl es vielen Menschen nicht bewusst ist, sind Halbleiter in den verschiedensten elektronischen und optoelektronischen Geräten verbaut. Die bekanntesten sind Computer, Flachbildfernseher, Autos und Smartphones. Im Gegensatz zu diesen Beispielen, gibt es auch viele Bereiche die von der Halbleitertechnik erobert werden, welche Jahrzehnte lang ohne sie auskamen. In Autos, Straßenlaternen und als LED-Leuchten übernehmen sie den Beleuchtungsmarkt im Privaten und im öffentlichen Raum. Darüber hinaus gibt es noch weitere Bereiche welche die Halbleitertechnologie verwenden, ohne das sie vom Endnutzer wahrgenommen wird. Beispiele dafür sind lasergestützte Operationen oder Telekommunikation und Datenübertragung über Glasfaser.

Seit der Erfindung des Photophons im Jahr 1880 durch Alexander Graham Bell und Charles Sumner Tainter [1], welches als erstes Gerät Sprache über Licht übertrug, haben sich Telekommunikation und optische Kommunikation weiterentwickelt. Heutzutage wird beinahe die gesamte Kommunikation nur noch digital durchgeführt. Daher werden alle zu übertragenden Daten in digitale Signale umgewandelt, was üblicherweise von halbleiterbasierten Geräten übernommen wird. Diese Signale werden dann als Lichtpuls in Lichtwellenleiter eingekoppelt und übertragen, dabei sind Halbleiterlaser für die Erzeugung der Lichtpulse zuständig. Solche Lasersysteme müssen Licht mit bestimmten Wellenlängen der sogenannten Telekombänder emittieren. Die Telekombänder ergeben sich aus den Minima der Materialdispersion in Lichtwellenleitern, welche zu einer Minimierung von Verlusten bei der Datenübertragung führen [2]. Daher sind Halbleiterlaser ein essentieller Bestandteil der globalen Kommunikation, unter anderem für die Telekommunikation und Computernetzwerke, wie das weltweite Internet. Lichtwellenleiter, gebündelt zu Glasfaserkabeln, werden in vielen Teilen des Internets genutzt. Dies geschieht bereits seit geraumer Zeit in interkontinentalen Seekabeln und mittlerweile auch vermehrt auf der letzten Meile, die den Endnutzer mit dem Internet verbindet. Neben der Erzeugung der optischen Signale werden Halbleiterlaser auch zur Verstärkung genutzt um Informationsverlust bei längeren Laufstrecken

vorzubeugen. Daher ist es nicht übertrieben zu behaupten, dass die gesamte heutige Kommunikation ohne Halbleitertechnologie nicht möglich wäre.

Durch die Vielzahl an Halbleitermaterialien und die Möglichkeiten durch Kombination Heterostrukturen herzustellen, existieren die verschiedensten Halbleiterlaser. Eine Unterscheidung erfolgt zwischen Kantenemittern, zum Beispiel mit SCH-Struktur (englisch: separate confinement heterostructure) [3], und Oberflächenemittern, wie einem VECSEL (englisch: vertical-external-cavity surface-emitting laser) [4–6]. Beide basieren auf einer aktiven Region bestehend aus Halbleiterquantenfilmen. Kantenemitter werden üblicherweise elektrisch betrieben, während VECSEL optisch und daher unter unterschiedlichen Bedingungen angeregt werden können. Zusätzlich haben VECSEL den Vorteil, dass im externen Teil ihres Resonators optische Elemente platziert werden können und so direkt im Strahlengang Manipulationen vorgenommen werden können [7–9]. Somit eignen sie sich als System für eine Fülle an verschiedenen Anwendungen und zum Testen von neuen Materialsystemen, sowie zur Grundlagenforschung.

Die Vielzahl an Anwendungen für Halbleiterlaser in der Telekommunikation und optischen Datenübertragung [10] führt zu hohen Ansprüchen an eben diese. Minima von Materialabsorption und -dispersion können für Lichtwellenleiter um 1300 nm und 1550 nm gefunden werden, jedoch ist das ein energetischer Bereich in dem Augerverluste anfangen die materialspezifischen Verlustprozesse in Halbleitern zu dominieren [11–13]. Laser für diese Anwendungen sind typischer Weise auf InP basiert und funktionieren am besten in einem konstanten Umgebungsklima [14, 15]. Daher wäre ein flexibleres Materialsystem wünschenswert, welches beispielsweise in einem größeren Bereich von Umgebungstemperaturen operieren kann.

Um diese Probleme zu überwinden wird in dieser Dissertation ein verbessertes Konzept im Vergleich zu den üblichen Halbleiterlasern basierend auf Typ-I Bandanordnungen diskutiert. Durch die Kombination von zwei Halbleitermaterialien, mit jeweils relativ großen Bandlücken verglichen mit dem Nahinfrarotbereich, wird eine effektive Übergangsenergie im gewünschten Bereich realisiert [16]. Dies ist möglich, da die Rekombination von Ladungsträger in einem solchen System durch die Grenzfläche zwischen den beiden Quantenfilmen von statten geht, siehe Abbildung 0.1. Eine Anordnung in der Elektronen und Löcher nicht im selben Quantenfilm lokalisiert sind, wird als Typ-II Bandanordnung bezeichnet. In diesem Fall sind die Quantenfilme so angeordnet, dass das Confinement-Potential der Elektronen ein namensgebendes „W“ bildet. Solch ein System hebt die Überlappung der Wellenfunktionen von Elektronen und Löchern in den Vordergrund, da sie betrachtet werden muss um eine Rekombinationsrate zu erhalten die groß genug ist, um einen Laserbetrieb zu ermöglichen. Bisherige Studien zeigen, dass die intrinsischen Verluste für solche Systeme kleiner als in Typ-I Systemen sind [17, 18]. Es bietet sich deshalb an, „W“-artige Typ-II Systeme weiterführend zu untersuchen.

Die sorgfältige theoretische Konzeption und experimentelle Realisierung eines Halbleiterlasers gehen Hand in Hand. Ausgehend von einem theoretischen Vorschlag, basierend auf den gewünschten optischen Eigenschaften, beginnt ein geschlossener Entwicklungskreislauf. Dieser wird durch Anwendung einer vollständig mikroskopischen Theo-

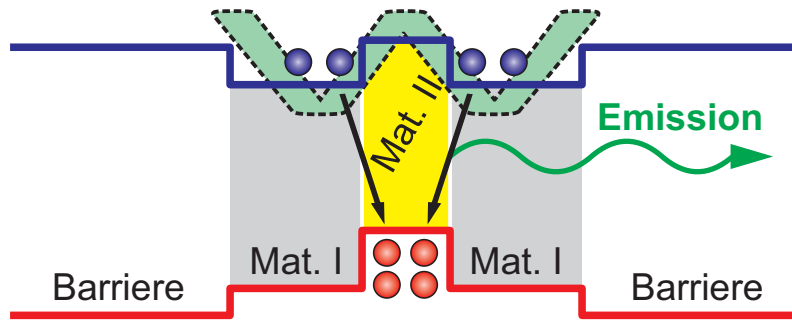


Abbildung 0.1: Skizze einer Typ-II “W”-Quantenfilmanordnung. Das Confinement-Potential (Linien) wird gezeigt für zwei Quantenfilmmaterialien (Flächen), die von einem Barrierenmaterial eingeschlossen sind. Die Emission von Licht durch die Rekombination von Ladungsträgern ist ebenfalls dargestellt (Pfeile).

rie erstellt, sprich durch lösen der Halbleiter-Bloch-Gleichungen [19, 20]. Im nächsten Schritt wird die vorgeschlagene Struktur epitaktisch als Halbleiterchip gewachsen. Danach wird eine ausführliche strukturelle Analyse und eine grundlegende Charakterisierung des Lasers durchgeführt. Durch diese Analyse werden die nominellen Parameter der Probe bestimmt. Zu ihnen gehören die Materialzusammensetzung, welche durch hochauflösende Röntgenbeugungsmessungen [21] ermittelt wird, und die optischen Eigenschaften, zum Beispiel die Photolumineszenz. Die experimentellen Photolumineszenzmessungen werden dann mit numerischen Ergebnissen, die durch die Anwendung der Halbleiter-Lumineszenz-Gleichungen [20, 22] erzielt werden, verglichen. So kann eine direkte Rückmeldung zu den nominellen Parametern und der inhomogenen Verbreiterung der Probe erfolgen. Photolumineszenzauswertungen sind im ersten Schritt dieses Entwicklungskreislaufs ein probates Mittel, da sie an Quantenfilmheterostrukturen durchgeführt werden können und die Proben nicht bis zum Niveau eines Halbleiterlasers prozessiert werden müssen. Daher können sie ohne größeren Aufwand zur Überprüfung des Wachstumsprozesses eingesetzt werden. Sobald ein vollständiger Laser prozessiert ist können weitere Untersuchungen durchgeführt werden, um ihn komplett zu charakterisieren.

Ein anderer Typ von Halbleiterlaser basiert auf Quantenpunkten: die Quantenpunktlaser [23]. Bedingt durch ihre Struktur haben sie ein stärkeres Ladungsträger-Confinement und daher beinahe atomare Eigenschaften. Idealerweise stammt ihre Laseremission nur von einem einzelnen Quantenpunkt in einem Mikroresonator, welcher verschiedene Formen haben kann [24]. Als Laser stechen sie durch ihre linearen und beinahe schwellenlose Eingangs-/Ausgangscharakteristik hervor, die sie unter nicht-resonanter Anregung zeigen [25]. Ihre Anwendungsfelder sind ähnlich zu denen von Halbleiterlasern, welche die Ladungsträger in höherdimensionalen Strukturen einfangen. Sie eignen sich hervorragend zur Grundlagenforschung in der Quantenelektrodynamik [20, 24, 26] und zu Quantenphänomenen wie Vakuum-Rabi Aufspaltung [27,

28] oder der Emission einzelner [29–31] und verschränkter [32] Photonen, sowie Experimenten zu besonders starker Licht–Materie Kopplung [28, 33, 34]. Folglich eignen sie sich hervorragend als Modellsystem in quantenoptischen Studien.

Diese Dissertation fasst die Ergebnisse mehrerer Publikationen zu grenzflächendominierten Laserstrukturen und Quantenpunktemissionscharakteristiken zusammen und erweitert sie an gegebener Stelle. Alle Untersuchungen erfolgen mit der Zielsetzung die makroskopischen Eigenschaften der Systeme durch mikroskopische Theorien zu beschreiben. Eine Einführung in die theoretischen Modelle kann in Kapitel 2 gefunden werden. Ausgehend vom Jaynes–Cummings Modell [35] wird eine Erweiterung dieses Modells eingeführt, analog zu Publikation [I]. Dies wird zur Untersuchung von Quantenpunkten die mehrere zwei-Niveausysteme beherbergen, und sich in einem Mikroresonator befinden, genutzt. Des weiteren werden die Halbleiter-Blochgleichungen beschrieben, beginnend beim Hamiltonoperator zur Beschreibung des physikalischen Systems bis hin zur Verknüpfung zu makroskopischen Größen wie Absorption und Brechungsindexänderung. Weiterhin werden die durch die Quantisierung des Lichtfeldes zu erhaltenden Halbleiter-Lumineszenz-Gleichungen vorgestellt. Zum Abschluss von Kapitel 2 wird in Analogie zu Veröffentlichung [III] die Berechnung von Photomodulationsspektren [36] unter Zuhilfenahme der Halbleiter-Blochgleichungen besprochen. Alle theoretischen Ansätze werden angewandt, um umfangreiche Experiment–Theorie Vergleiche durchzuführen, und damit das physikalische Verständnis von neuartigen Lasermaterialsystemen zu bessern.

Das Ziel von Kapitel 3 ist die systematische Untersuchung eines neuartigen Typ-II Lasermaterialsystems. Es gibt einen Überblick über die Untersuchungen die bisher zu Typ-II band-angeordneten „W“-Strukturen durchgeführt wurden, siehe Publikationen [II], [III], [IV], [V] und [VII], und erweitert sie. Alle Publikationen haben als Fundament das direkte Zusammenspiel von Experiment und Theorie. Neben dem Inhalt der Veröffentlichungen beginnt das Kapitel mit einer allgemeinen Einführung in Typ-II Systeme, insbesondere in die „W“-Anordnung. Sie werden, unter Anwendung der Halbleiter-Blochgleichungen, mit gewöhnlichen Typ-I Systemen verglichen. Als Resultat zeigt sich ein temperaturstabileres Verhalten und ein spektral breiterer Materialzugewinn. Des weiteren reagieren Typ-II Systeme anders auf eine Erhöhung der Ladungsträgerdichte, da durch die Ladungsträger das Confinement-Potential verändert wird, was zu einer Blauverschiebung der Emission führt. Dies resultiert aus der Ladungstrennung in die unterschiedlichen Quantenfilme. Nachfolgend wird, als wichtiger Bestandteil eine Entwicklungsprozesses, der Experiment–Theorie-Vergleich für Photolumineszenzspektren von epitaktisch gewachsenen „W“-Strukturen gezeigt. Basierend auf den nominellen Strukturparametern wird analog zur Publikation [II] der Materialzugewinn dieser Struktur berechnet. Weiterführend werden exzitonische Übergänge und ihre räumliche Komponente untersucht, um sie als Typ-II Übergang zu identifizieren, dies wurde erstmals in Publikation [III] präsentiert. Daher sind diese Strukturen vielversprechende Kandidaten für den Einsatz als aktives Medium in einer Laserstruktur.

Basierend auf den vorherigen Untersuchungen wurde ein „W“-VECSEL entworfen, realisiert und untersucht. Die zugehörige experimentelle Charakterisierung sind in den

Publikationen [IV] und [V] veröffentlicht. Zusätzlich wird eine ausführliche Analyse der Eigenschaften mit Hilfe der mikroskopischen Theorie durchgeführt. Unter anderen werden Reflektionsspektren in Abhängigkeit der Ladungsträgerdichte untersucht, um die experimentell bestimmte Laserwellenlänge zu bestätigen. Die Laserprobe weist in Übereinstimmung von Experiment und Theorie einen resonanten Aufbau mit einer Emissionswellenlänge von 1180 nm auf. In Anlehnung an Publikation [VII] werden die Verstimmung vom aktiven Material und dem Resonators, sowie die modale Zugewinn bestimmt. Daraus kann geschlossen werden, dass in der Probe eine niedrige Laserschwelle vorliegt. Type-I Systeme mit einer Emission bei 1180 nm [37] erreichen Ausgangsleistungen von 20 W. Hingegen wurde für den “W”-VECSEL bisher nur 4 W gemessen [IV]. Aus den theoretischen Analysen wird geschlossen, dass eine stärker negative initiale Verstimmung zur Erhöhung der Ausgangsleistung führen würde. Zusätzlich werden in Abschnitt 3.5 Optimierungen des Ladungsträger-Confinements durch Veränderung der Grenzflächen und Barrieren diskutiert. Die Untersuchungen zeigen, dass durch die Bearbeitung der Grenzflächen der Wellenfunktionsüberlapp erhöht und somit der Materialzugewinn um bis zu 10 % gesteigert werden kann. Auch durch eine Änderung im Aufbau der Barrieren kann eine vergleichbare Steigerung erreicht werden. Zuletzt werden drei mögliche Materialzusammensetzungen vorgestellt die eine Laseremission bei 1300 nm ermöglichen.

Eine direkte Weiterführung der hier vorgestellten Aktivitäten zur Untersuchung von Typ-II „W“-Strukturen kann durch die Anwendung eines Rastertransmissionselektronenmikroskop erfolgen. Damit können die Eigenschaften wie Rauigkeit oder Konzentrationsgefälle an der Grenzfläche in Abhängigkeit der Wachstumsbedingungen systematisch untersucht werden. Somit könnte eine Optimierung des Ladungsträger-Confinements erreicht werden. Wie in Publikation [VI] vorgestellt, wurden mittlerweile auch Kantenemitter basierend auf Typ-II „W“-Strukturen gewachsen und charakterisiert. Auch diese können im weiteren Optimierungsprozess eingebunden werden. Mit dem Ziel „W“-Laser für die Telekommunikation zu realisieren, sollten die Untersuchungen von Materialzusammensetzungen die eine Emission von 1300 nm ermöglichen intensiviert werden. Dazu wären Berechnungen des Einfangs der Ladungsträger, insbesondere der Löcher, in ihren Potentialtöpfen hilfreich. Mit dem Wissen über Einfangraten könnten Obergrenzen für Konzentrationen in bestimmten Quantenfilmen angegeben werden. Alternativ zu dem neuartigen Materialsystem welches in dieser Dissertation und den zugehörigen Publikationen diskutiert wird, gäbe es auch die Möglichkeit die Zusammenstellung eines Quantenfilms zu verändern, um eine Emissionswellenlänge von 1300 nm zu erreichen [38–41]. Auch die Wellenlänge von 1550 nm im anderen Telekomfrequenzband wurde bereits ausführlich untersucht [40, 42, 43], es ist aber unrealistisch diese Wellenlänge basierend auf dem vorliegenden Materialsystem zu erreichen. Nichtsdestotrotz leiden Typ-I Laser bei 1550 nm unter der internen Hitzeentwicklung [44], daher wäre es wünschenswert eine Alternative in Form eine Typ-II Systems zu haben.

Im zweiten Teil dieser Dissertation werden unerwartete Oszillationen in der Emission von optisch gepumpten Halbleiterquantenpunkten in Mikroresonatoren diskutiert und analysiert, wie in Publikation [I] vorgestellt. Dazu beginnt Kapitel 4 mit

der experimentell gemessenen Eingangs-/Ausgangsleistungscharakteristik welche diese Oszillationen unterhalb der Laserschwelle offenlegt. Eine Erweiterung des Jaynes-Cummings Modells ermöglicht die Reproduktion dieser Oszillationen und identifiziert sie als Quantengedächtniseffekt. Dieser wird durch vorhergehende Emissions- und Absorptionsereignisse aufgebaut. Es wurde herausgefunden, dass das Quantengedächtnis als Korrelation zwischen Resonator-Photonen und Besetzung der Quantenpunktzustände, aufgebaut durch verstimmte Rabioszillationen, beschrieben werden kann. Zusätzliche Untersuchungen konnten die Sensitivität der Systems auf quantenoptische Fluktuationen im anregenden Lichtfeld herausstellen. Sie kann benutzt werden um die Stärke der Oszillationen, zum Beispiel mit Hilfe von quantenoptischer Spektroskopie, zu verändern. Auch wenn heutzutage keine Lichtquellen mit beliebig einstellbaren Quantenfluktuationen verfügbar sind, so gibt es doch einen Eindruck von den Möglichkeiten die man hat, um diesen Effekt zu kontrollieren.

Zusammenfassend wurden zwei unterschiedliche Halbleiterlasermaterialsysteme mit Hilfe von mikroskopischen Quantentheorien untersucht. Die verschiedenen Theorien ergeben zusammen einen umfangreichen Werkzeugsatz, welcher seine Stärken bei der Anwendung in intensiven Experiment-Theorie Kollaborationen zeigt. So wird ermöglicht direkt Rückmeldungen zum strukturellen Aufbau von Proben zu geben und Vorhersagen über Materialeigenschaften zu treffen, welche durch strukturelle Veränderungen erreicht werden können.

Danksagung

Diese Dissertation wäre ohne Unterstützung nicht zustande gekommen. Daher möchte ich die Gelegenheit nutzen und mich bei den folgenden Personen bedanken. Bei ...

- ... Prof. Dr. Stephan W. Koch für die Betreuung in der Zeit als Doktorand in der Arbeitsgruppe Theoretische Halbleiterphysik (AG). Außerdem bei Prof. Dr. Mackillo Kira für die lehrreiche Zeit im „quantum memory“-Projekt und die Aufnahme in den CCC. Beiden gilt mein Dank für die freundliche Aufnahme in ihrer Arbeitsgruppe und die stets gute Zusammenarbeit in den letzten Jahren.
- ... Dr. habil. Wolfgang Stolz für die Übernahme des Zweitgutachtens und die gute Zusammenarbeit im „W“-Laser-Projekt. Sowie bei Prof. Dr. Peter Lenz für die Übernahme des Vorsitzes meiner Prüfungskommission.
- ... allen Kollaborateuren mit denen ich gemeinsam geforscht habe, insbesondere bei Christoph Möller und Christian Fuchs.
- ... der gesamten AG einschließlich aller Ehemaligen für die stets gute Gesellschaft, Diskussionen und Unternehmungen außerhalb der Mainzer Gasse. Ohne Anspruch auf Vollständigkeit möchte ich mich bei meinen Weggefährten Martin S., Lukas, Thomas, Christoph, Benni, Martin M., Dominik, Jakob, Phillip, Tineke und Osmo und meinen Bürokollegen Felix, Thorsten, Gunnar, Daniel, Alex, Uli, Johannes, Lars und Markus danken.
- ... Prof. Dr. Dr. hc. Peter Thomas für die unermüdliche Organisation der alljährlichen AG-Wanderung.
- ... Martin für viele gemeinsame Kilometer auf dem Fahrrad und in den Laufschuhen.
- ... meiner Familie, insbesondere meinen Eltern, ohne die das alles nicht möglich gewesen wäre. Danke!
- ... Melissa – Danke, dass du mir den Rücken freihältst und immer da bist.

Author's Contributions

This Thesis consists of an introductory review discussing the main ideas and results of my doctoral studies followed by seven research publications.

Publications in Peer-Review Journals

- [I] C. Berger, U. Huttner, M. Mootz, M. Kira, S. W. Koch, J.-S. Tempel, M. Aßmann, M. Bayer, A. M. Mintairov, and J. L. Merz, “Quantum-Memory Effects in the Emission of Quantum-Dot Microcavities”, *Physical Review Letters* **113**, 093902 (2014).
- [II] C. Berger, C. Möller, P. Hens, C. Fuchs, W. Stolz, S. W. Koch, A. Ruiz Perez, J. Hader, and J. V. Moloney, “Novel type-II material system for laser applications in the near-infrared regime”, *AIP Advances* **5**, 047105 (2015).
- [III] S. Gies, C. Kruska, C. Berger, P. Hens, C. Fuchs, A. Ruiz Perez, N. W. Rosemann, J. Veletas, S. Chatterjee, W. Stolz, S. W. Koch, J. Hader, J. V. Moloney, and W. Heimbrodt, “Excitonic transitions in highly efficient (GaIn)As/Ga(AsSb) type-II quantum-well structures”, *Applied Physics Letters* **107**, 182104 (2015).
- [IV] C. Möller, C. Fuchs, C. Berger, A. Ruiz Perez, M. Koch, J. Hader, J. V. Moloney, S. W. Koch, and W. Stolz, “Type-II vertical-external-cavity surface-emitting laser with Watt level output powers at 1.2 μm ”, *Applied Physics Letters* **108**, 071102 (2016).
- [V] C. Möller, C. Berger, C. Fuchs, A. Ruiz Perez, S. W. Koch, J. Hader, J. V. Moloney, and W. Stolz, “1.2 μm emitting VECSEL based on type-II aligned QWs”, in *SPIE LASE*, edited by K. G. Wilcox, (Mar. 2016), 97340H.

In Preparation

- [VI] C. Fuchs, C. Berger, C. Möller, M. Weseloh, S. Reinhard, J. Hader, J. V. Moloney, A. Beyer, K. Volz, S. W. Koch, and W. Stolz, “Electrical Injection Type-II (GaIn)As/Ga(AsSb)/(GaIn)As Single “W”-Quantum Well Laser at 1.2 μm ”, 2016.
- [VII] C. Lammers, M. Stein, C. Berger, C. Möller, C. Fuchs, A. Ruiz Perez, A. Rahimi-Iman, J. Hader, J. V. Moloney, W. Stolz, S. W. Koch, and M. Koch, “Gain spectroscopy of a type-II VECSEL chip”, 2016.

Posters and Talks

- C. Möller, C. Berger, C. Fuchs, A. Ruiz Perez, S. W. Koch, J. Hader, J. V. Moloney, and W. Stolz, “1.2 μm emitting VECSEL based on type-II aligned QWs”, Contributed Talk by C. Möller at SPIE Photonics West, San Francisco (2016).
- C. Berger and S. W. Koch, “Microscopic Theory of “W”-Laser Structures”, Talk at SFB 1083 Workshop: Type-II Semiconductor Interfaces, Fachbereich Physik und wissenschaftliches Zentrum für Materialwissenschaften, Philipps-Universität Marburg (2015).
- C. Berger, C. Möller, C. Fuchs, P. Hens, A. Ruiz Perez, W. Stolz, and S. W. Koch, ““W”-Laser Simulations”, Poster presented at Materialforschungstag Mittelhessen 2015, Philipps-Universität Marburg (2015).
- S. Gies, C. Kruska, N. Rosemann, C. Berger, P. Hens, W. Stolz, K. Volz, S. Chatterjee, S. W. Koch, and W. Heimbrodt, “Type-II Excitons in (Ga,In)As/Ga(N,As)-quantum wells & (Ga,In)As/Ga(Sb,As)-“W”-Lasers on GaAs”, Poster presented by S. Gies at Materialforschungstag Mittelhessen 2015, Philipps-Universität Marburg (2015).
- C. Berger and S. W. Koch, “Microscopic Theory of Semiconductor Lasers — An Introduction”, Talk and Poster presented at SFB 1083 Winter Student Seminar 2015, Hirschegg/Kleinwalsertal (2015).
- C. Berger, and S. W. Koch, “Microscopic treatment of W-Laser Quantum Wells”, Talk at SFB 1083 Workshop Theory, Fachbereich Physik und wissenschaftliches Zentrum für Materialwissenschaften, Philipps-Universität Marburg (2014).
- U. Huttner, C. Berger, M. Mootz, M. Kira, S. W. Koch, J. S. Tempel, M. Aßmann, M. Bayer, A. M. Mintairov, and J. L. Merz, “Controlling quantum-memory effects in quantum-dot micro cavity emission”, Poster presented by U. Huttner at Junior Researcher Conference - Nonlinear Spectroscopy meets Quantum Optics, Freiburg Institute for Advanced Studies (FRIAS), Albert-Ludwigs-Universität Freiburg (2014).

- C. Berger, U. Huttner, M. Mootz, M. Kira, S. W. Koch, J. S. Tempel, M. Aßmann, M. Bayer, A. M. Mintairov, and J. L. Merz, “Quantum-dot micro cavity emission with a quantum memory”, Poster presented at 12th International Conference on Nonlinear Optics and Excitation Kinetics in Semiconductors (NOEKS 12), Universität Bremen (2014).
- C. Berger, U. Huttner, M. Mootz, M. Kira, and S. W. Koch, “Microscopic Theory of Semiconductor Lasers”, Poster presented at International Summer School on Semiconductor Interfaces: Methods and Model Systems, Donostia International Physics Center, Universität Baskenland, San Sebastián (2014).
- C. Berger, U. Huttner, M. Mootz, M. Kira, S. W. Koch, J. S. Tempel, M. Aßmann, M. Bayer, A. M. Mintairov, and J. L. Merz, “Microscopic Theory of Semiconductor Lasers”, Poster presented at Materialforschungstag Mittelhessen 2014, Justus-Liebig-Universität Gießen (2014).

Original Contributions

All studies presented in this Thesis are the result of frequent group meetings where intermediate results have been discussed and new calculations have been planned.

In my first project, unexpected oscillations in the input/output characteristics of quantum-dot microcavities were identified as quantum-memory effect. This was done in collaboration with the group of M. Bayer at Technische Universität Dortmund which performed all experiments. The theoretical analysis was carried out at our group in Marburg by U. Huttner, M. Mootz, and myself under the supervision of M. Kira and S. W. Koch. My part was the development of a microscopic description of the experimental results. The Jaynes–Cummings model was extended to include multiple two-level systems and to be pumped externally. After the derivation of the equation of motion for the density matrix, I implemented a computer program to solve the equation numerically. Additionally, I performed analytical derivations to identify the source of the oscillations as quantum-memory effect. U. Huttner and M. Mootz studied the quantum-memory effect with quantum spectroscopy, and U. Huttner calculated the matter’s quantum response with this concept. The findings of this project are presented in Paper [I], to which I contributed by writing parts of the manuscript and the supplemental material. The results were presented as a Poster on national and international conferences by U. Huttner and myself. The results of this project are reviewed in Chapter 4, while the theoretical background is discussed in Chapter 2.

The second project during my doctoral studies was the investigation of interface-dominated laser structures in the near-infrared regime, i.e. the “W”-laser, under the supervision of S. W. Koch. All samples were grown and initially characterized in the group of W. Stolz at Philipps-Universität Marburg by P. Hens and C. Fuchs. In the first publication belonging to this project, experimental photoluminescence spectra of type-II aligned “W”-multiple quantum-well heterostructures, measured by C. Möller,

were compared to calculated spectra retrieved by applying the semiconductor luminescence equations. Additionally, the material gain properties of these samples were calculated to forecast the usability of the semiconductor heterostructure as active medium in a laser. The theoretical background to this microscopic theory is reviewed in Chapter 2, which I also presented on two occasions as introductory talks on microscopic modeling of semiconductor lasers. I performed the calculations with the help of the software package SimuLase [45]. These results are published in Paper [II] which was partially written by myself. To investigate the excitonic transitions in the same samples, photomodulated reflectance spectroscopy measurements were performed in the groups of W. Heimbrodt and S. Chatterjee at Philipps-Universität Marburg. Therefore, I calculated the photomodulated reflectance signal based on the results of the semiconductor Bloch equations to perform a qualitative experiment–theory comparison. The analysis, which I performed with the electron and hole wave functions, identified all transitions either as type-II or type-I. Moreover, I contributed to the writing of the manuscript which summarizes the results and is published as Paper [III]. All results on the photomodulated reflectance of type-II “W”-multiple quantum-well heterostructures were presented on several occasions as Posters by S. Gies and me.

The subsequent work addressed the optimization of type-II “W”-structures through C. Möller, C. Fuchs, and myself. It carried out the realization of a vertical-external cavity surface-emitting laser. To make this possible, I contributed systematic investigations of the optical properties of the active region with “W”-band alignment. Especially the charge-carrier dependent shifts have been quantified with the help of my calculations. Different quantum-well compositions and thicknesses were discussed and thus, the optical gain was balanced against the difficulty of experimental realization. The initial characterization of the VECSEL sample is presented in Papers [IV] and [V]. The latter one was presented as a Contributed Talk at SPIE Photonics West by C. Möller. Additional experiments to characterize the gain in this sample were performed in the group of M. Koch at Philipps-Universität Marburg by C. Lammers and M. Stein. To this work I contributed by calculations of the material gain, the modal gain, and the reflection for different charge carrier densities. Thus, an agreement between experiment and theory could be found and a laser mode was identified. These results are summarized in Paper [VII] to which I contributed by writing parts of the text and which is currently in preparation.

As last part of this project so far, edge-emitting laser devices were created and characterized by C. Fuchs. Their successful characterization could be supported by luminescence and material absorption spectra which I calculated. I contributed to the writing of the manuscript of Paper [VI] which is currently in preparation.

Contents

1	Introduction	1
2	Theoretical Background	5
2.1	External driven multiple-Level Jaynes–Cummings Model	6
2.1.1	Hamiltonian	6
2.1.2	Density Matrix Approach	7
2.2	Semiconductor Bloch Equations	8
2.2.1	Hamiltonian	8
2.2.2	Equations of Motion	9
2.2.3	Optical Response	12
2.3	Semiconductor Luminescence Equations	13
2.3.1	Hamiltonian	13
2.3.2	Equations of Motion	14
2.3.3	Photoluminescence	15
2.4	Photomodulated Reflection Spectroscopy	15
3	Interface-Dominated Laser Structures	17
3.1	“W”-Quantum-Well Heterostructure Approach	19
3.2	Theoretical Predictions for “W”-aligned multiple Quantum Wells	20
3.2.1	Comparison to Type-I Setups	21
3.3	Analysis of Epitaxially Grown “W”-multiple Quantum-Well Heterostructures	26
3.3.1	Photoluminescence	27
3.3.2	Prediction of Gain Properties	28
3.3.3	Excitonic Transitions	29
3.4	Investigation of a Type-II VECSEL	32
3.4.1	Longitudinal Light Mode and Reflectivity	32
3.4.2	Detuning and Modal Gain	34

Contents

3.5	Optimization Capabilities of Type-II Lasers	37
3.5.1	Graded Interfaces	37
3.5.2	Barrier Height	38
3.5.3	1300 nm Emission Wavelength	40
4	Nonlinearities in Quantum-Dot Emission	43
4.1	Extraction of Nonlinear Behavior	44
4.2	Modeling and Identification of Sources to Quantum-Dot Emission . . .	45
4.3	Quantum-Optical Sensitivity	48
5	Conclusion	51
	Bibliography	53
	Papers	65
	Paper I	69
	Supplemental Material	77
	Paper II	87
	Paper III	97
	Paper IV	105
	Paper V	113
	Paper VI	121
	Paper VII	129

Introduction

Life without semiconductor technology is no longer imaginable today as it would constrain many areas of our daily life. Even though many people are unaware of their use, semiconductors are implemented in various electronic and optoelectronic devices. The most common ones are personal computers, flat panel TVs, cars, and smartphones. In contrast to this prominent examples, the technology is often invisible to the user as semiconductors conquer applications which were carried out without them for decades. Found in cars, streetlights, and as LED lamps, semiconductors take over the market of illumination at home and in public areas. In addition, other fields make heavy use of semiconductor technology which may not be visible to the end user. Examples are medical applications, e.g. laser surgery or telecommunication and data transfer via optical fibres.

Since the invention of the photophone in 1880 by Alexander Graham Bell and Charles Sumner Tainter [1], which was one of the first communication device that transmitted speech via a beam of light, telecommunication and optical communication has advanced. Nowadays, most kinds of communication are carried out in a digital manner. Therefore, all data transmitted has to be translated into digital signals, which is usually done by semiconductor-based devices. These signals are then send through optical fibres in form of a light pulse. The creation of such light pulses is carried out by semiconductor lasers. These lasers are required to operate at a specific wavelength in one of the so-called telecom wavelength bands. This arises from a material dispersion minimum in optical fibres which allows for a reduction of the losses during data transmission [2]. Thus, semiconductor laser devices are an essential part of the global communication, e.g. for telecommunication and computer networks like the internet. Optical fibres are used in all parts of the internet from long distance communication in submarine communications cables right up to the last mile, which connects the end user with the network. Besides the generation of the light pulses, semiconductor lasers are also used to amplify the signal after a certain distance to its original strength to not lose any information. Hence, it is not exaggerated to say that the whole present-day communication is based on semiconductor technology.

Due to the variety of semiconductor materials available and the several possibilities

to combine them into heterostructures, a lot of different semiconductor lasers exist. A distinction is made between edge-emitting devices like separate confinement heterostructure lasers [3] and surface-emitters like vertical-external-cavity surface-emitting lasers (VECSELs) [4–6], both of them are based on semiconductor quantum wells. Edge-emitting devices are usually electrically pumped while VECSELs are optically pumped and can therefore be excited by a wide range of different excitation conditions. Additionally, VECSELs have the advantage that they allow for optical elements in the cavity beam path as they are build with an external cavity on one side [7–9]. Therefore, they are an ideal system for a wide range of applications and first-order principle testing of new material systems and fundamental research.

The wide range of applications for semiconductor lasers in telecommunication and optical data transfer [10] leads to a high requirement on the quality of such devices. Unfortunately, the material absorption and dispersion minima of optical fibres at 1300 nm and 1550 nm are in an energetic range where Auger losses start to dominate the intrinsic loss processes in semiconductors [11–13]. Laser devices used for this application are typically based on InP as material system and perform best under stable ambient conditions [14, 15]. A more flexible material system would be desirable, e.g. such that the devices could be used under a wide range of temperatures.

To overcome this problem, an improved concept compared to ordinary semiconductor laser devices based on type-I band alignment is discussed in this Thesis. By combining two semiconductor materials with rather large band gap compared to the near-infrared regime, an effective transition energy at the desired wavelength is achieved [16]. This is possible due to a new recombination path for the charge carriers in the system, which goes spatially through the interface between the two quantum wells. An arrangement where electrons and holes are not spatially located in the same quantum well is called type-II band aligned. Figure 1.1 presents a scheme where an array of quantum wells is aligned in a manner that it is symmetric and the electrons' confinement potential forms an eponymous “W”. Here, aspects like wave function overlap have to be considered to have a recombination rate, which is strong enough for laser operation in type-II systems. Previous studies suggest that the intrinsic losses are small compared to type-I quantum-well setups [17, 18] and thus commend a thorough investigation.

A careful theoretical design and experimental realization of semiconductor laser devices go hand in hand. A closed-loop design process starts with a suggestion from the theory side, which is based on the optical properties that the new device has to achieve. They are calculated by applying a fully microscopic theory which yields the well-known semiconductor Bloch equations (SBEs) [19, 20]. In a next step, expertise in epitaxial growth is required in order to implement the design into a semiconductor chip. After the growth, a detailed structural analysis and a fundamental laser characterization are carried out by different experimental methods to extract its nominal material composition and optical properties, i.e. high resolution X-ray diffraction (HR-XRD) [21], photoluminescence (PL), and more complex measurements. The experimental PL measurements are compared to numerical results obtained by solving the semiconductor luminescence equations (SLEs) [20, 22] to give immediate feedback

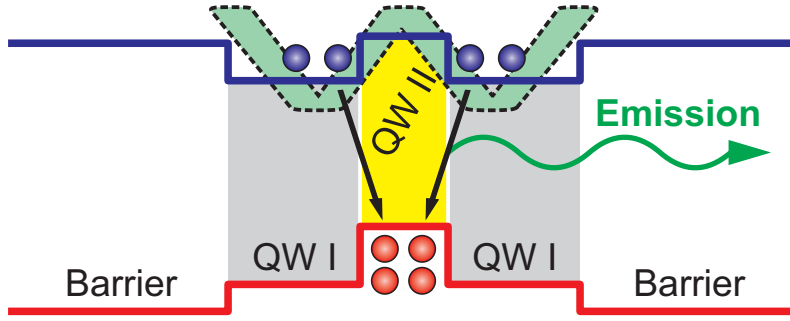


Figure 1.1: Sketch of a type-II “W”-quantum well alignment. The confinement potential (solid lines) of two different quantum-well (QW) materials (shaded areas) enclosed by a barrier material is shown. Light emission through recombination of charge carriers is depicted by arrows.

on the nominal parameters and define the inhomogeneous broadening of the sample. As first analyzing step of a closed-loop design process, the PL analysis is very convenient as the experiment can be performed on a multiple quantum-well heterostructure (MQWH) without further sample preparation. Thus, it can be used as zeroth-order check, to evaluate whether the growth of a semiconductor heterostructure was successful and a laser shall be processed. Once a full laser device is processed, e.g. a VECSEL consisting of the resonant periodic gain (RPG) region and a distributed Bragg reflector (DBR), additional investigations are performed to characterize it entirely.

Another type of semiconductor lasers are quantum-dot lasers [23]. Their charge carrier confinement stemming from their structural configuration is stronger and thus they have atom-like electronic properties. Ideally their laser emission originates from only one quantum dot inside a microcavity, which can be of different forms [24]. As lasers they stand out by their linear and nearly thresholdless input/output (I/O) characteristics under off-resonant excitation conditions [25]. They are used in the same fields of application as higher dimensional laser structures nowadays. In fundamental research they are a versatile system to investigate quantum electrodynamics [20, 24, 26] and several quantum phenomena, such as vacuum Rabi splitting [27, 28], single-photon [29–31] and entangled photon-pair emission [32], and strong coupling experiments [28, 33, 34]. Thus, they are very a promising model system for quantum-optical studies.

This Thesis provides an overview on microscopic theories for the description of semiconductor laser material systems. Therefore, Chapter 2 gives an overview about three theoretical models used for the description of different properties of semiconductors. First, an extension to the original Jaynes–Cummings model (JCM) [35] is introduced, as discussed in Paper [I]. It is later used for the investigation of quantum dots hosting multiple electronic levels placed inside a microcavity. Advancing to a different approach, second, the SBEs are discussed together with the system Hamiltonian and the resulting measurable macroscopic quantities, i.e. absorption and refractive index change. As third model, the SLEs are presented to calculate PL spectra where the

1 Introduction

quantized properties of the light are taken into account. Last, in correspondence to Paper [III], the evaluation of photomodulated reflectance (PR) spectroscopy [36] based on the SBEs is presented.

Chapter 3 reviews and extends all investigations made in the context of type-II band-aligned “W”-systems in Papers [II], [III], [IV], [V], and [VII]. Besides the content presented in these publications, the chapter starts with a general introduction of type-II and especially “W”-aligned MQWHs. They are compared to traditional type-I systems in terms of temperature and charge carrier density dependence. The differences are studied based on the SBEs. Subsequently, as part of the closed-loop process, an experiment–theory comparison for PL measurements of epitaxially grown “W”-MQWHs is presented. Based on the nominal parameters, i.e. quantum-well thickness and concentration, the material gain of this structure is computed, as first done in Paper [II]. Excitonic transitions and their spatial recombination path are investigated, in correspondence to Paper [III], to identify their type-II character. Subsequently, a systematic analysis of the “W”-VECSEL sample as reported in Papers [IV] and [V] is carried out. Here, charge carrier dependent reflection spectra are presented to confirm the experimentally determined lasing wavelength, cf. Paper [VII]. The investigation of the VECSEL concludes with the determination of detuning and modal gain of the sample. In addition, in Sec. 3.5 optimization capabilities are discussed by the means of the carrier confinement due to graded interfaces and different barrier materials. As a last point in this chapter, material compositions suitable to increase the emission wavelength to 1300 nm are suggested based on calculations.

Unexpected oscillations in the emission of optically pumped semiconductor quantum-dot microcavities are discussed and analyzed in Chapter 4. The usual linear slope of the I/O characteristics of this setup is modified. To figure out the origin of the nonlinearities, a systematic theoretical investigation is applied which identifies them as genuine quantum-memory effect. They are found to be directly addressable by utilizing the quantum-optical fluctuations of the exciting light field.

Theoretical Background

Semiconductor heterostructures confine charge carriers in within quasi-two, quasi-one, or quasi-zero dimensional space. Namely, these are quantum wells, quantum wires, and quantum dots, which only allow for two-dimensional, one-dimensional, or zero-dimensional movement of the charge carriers, respectively [20, 46, 47]. In this Thesis, theoretical models for quantum dots as well as quantum wells are presented. Ideal quantum dots are zero dimensional as they consist of only one atom and the movement of involved charge carriers is restricted in all three dimensions of space. In contrast, quantum wells only confine charge carriers in one dimension and therefore create a quasi-two dimensional space. As a consequence, both structural configurations have different electronic dispersion relations. For quantum dots it is a reasonable approximation to treat them as two-level systems, with the optical band gap as level spacing [48]. In turn, quantum wells have a more complex electronic structure which has to be considered. Besides the electronic properties of the semiconductor itself, there are two possibilities for the treatment of the interacting light field. It can be either treated classically or fully quantized where the light source's quantum statistics is taken into account [49, 50]. Both methods have their individual applications and are legitimate descriptions of certain phenomena.

In this chapter, the light-matter interaction of quantum dots with a quantized light field will be described by the JCM [35, 50] which will be extended to handle multiple detuned quantum dots and an external optical pump field as introduced in Paper [I]. Additionally, the SBEs, which contain the Coulomb interaction among charge carriers and a semi-classical treatment of the light-matter interaction, are presented as a description of more complex geometries including semiconductor quantum wells and their optical properties [19, 20, 51]. In turn, treating the light field fully quantized yields the SLEs [20, 22]. They can be applied to calculate fully quantum-optical problems like PL and other situations which are not accessible by a semi-classical theory. At last, PR spectroscopy is modeled based on the absorption and refractive index changes resulting from the SBEs [36, 52].

2.1 External driven multiple-Level Jaynes–Cummings Model

The JCM, originally developed to describe atoms interacting with a quantized single-mode light field [35, 50], has already experienced several different extensions. As a fully quantum-optical model, it provides insights into non-classical effects such as intensity dependent JCM ladder splitting or collapse and revival behavior in time [20, 50]. It was extended to describe multiple two-level systems under the name Tavis–Cummings model [53], multiple light modes [54], and dephasing mechanisms via couplings to one or more reservoirs [55–57]. Thus several quantum-optical effects like reversible spontaneous emission [58, 59], quantum-Rabi flopping [60], and entanglement effects [61–66] could be described.

In order to calculate the quantum-optical interaction between quantum dots and light inside a cavity, the JCM can be applied [35]. Due to the dimensional restrictions of quantum dots, it is reasonable to approximate their electronic structure as N two-level system [48, 67]. To properly depict quantum dots, the system Hamiltonian of the JCM is extended to include multiple electronic levels which are slightly detuned with respect to the cavity. Additionally, coupling to an external field is added to model experiments utilizing an optical pump.

2.1.1 Hamiltonian

The starting point for the objective to obtain a system’s dynamics is its Hamiltonian [20, 68]. Considering the JCM, it includes three parts, the light energy $H_{\text{light mode}}$, the two-level system $H_{\text{two-level system}}$, and the quantum-optical light–matter interaction $H_{\text{interaction}}$ [20, 35, 50, 69]. The Hamiltonian addressed in this Thesis is extended to include multiple two-level systems as well as an external optical pump field H_{pump} such that it reads

$$H_{\text{extended JCM}} = H_{\text{light mode}} + H_{\text{two-level system}} + H_{\text{interaction}} + H_{\text{pump}}. \quad (2.1)$$

Overall, this model contains the non-interacting energy of both the single light mode and the two-level systems, the fully quantum-optical light–matter interaction, and the semi-classical pump term.

The energy of the cavity mode is characterized by a harmonic oscillator,

$$H_{\text{light mode}} = \hbar\omega_{\mathbf{q}} \left(B_{\mathbf{q}}^{\dagger} B_{\mathbf{q}} + \frac{1}{2} \right), \quad (2.2)$$

where $\hbar\omega_{\mathbf{q}}$ is the energy of a single photon of light mode \mathbf{q} , while $B_{\mathbf{q}}^{\dagger}$ and $B_{\mathbf{q}}$ are bosonic creation and annihilation operators. The energy of N two-level systems originating from quantized states in a quantum dot is described by

$$H_{\text{two-level systems}} = \sum_{n=1}^N \hbar\omega_{21,n} P_{z,n}, \quad (2.3)$$

with the level-specific energy spacing $\hbar\omega_{21,n}$ and the population-inversion operator $P_{z,n}$ for state n . In general, the states are not in resonance with the cavity mode, and therefore their energies are detuned by $\hbar\delta_n = \hbar(\omega_{21,n} - \omega_{\mathbf{q}})$. All interactions between the two-level systems and the single-mode light field are taken into account by the interaction Hamiltonian,

$$H_{\text{interaction}} = -\hbar g \sum_{n=1}^N (B_{\mathbf{q}}^\dagger P_n + B_{\mathbf{q}} P_n^\dagger) , \quad (2.4)$$

within the rotating-wave approximation [20]. Here, g is the effective coupling strength between cavity mode and two-level systems, and P_n is the polarization operator for state n . The polarization operator and its complex conjugate are the lowering and rising Pauli operators for the corresponding state n , known from the original JCM [68]. Optical pumping of the two-level systems is described by a semi-classical model via

$$H_{\text{pump}} = - \sum_{n=1}^N (\alpha_{\text{L}}^*(t) P_n + \alpha_{\text{L}}(t) P_n^\dagger) , \quad (2.5)$$

using either continuous wave (cw) excitation $\alpha_{\text{L}}^{\text{cw}}(t) = \alpha_0 e^{-i\omega_{\text{L}}t}$, where the light fields amplitude is given by α_0 and $\hbar\omega_{\text{L}}$ is the photon energy of the pump laser, or a classical pump pulse $\alpha_{\text{L}}^{\text{pulse}}(t) = \alpha_{\text{L}}^{\text{cw}}(t) e^{-\frac{t^2}{\tau^2}}$, with the pulse duration τ .

2.1.2 Density Matrix Approach

The dynamics of the system can be derived, e.g., with a density matrix approach, which is advantageous in the way that it describes the full dynamics without any approximation. Thus, any expectation value can be calculated from the density matrix at any point in time. A more realistic treatment is reached by taking dephasing mechanisms of the polarization, the population, and the photons in the cavity into account. These dephasing channels couple the system to baths and enable the corresponding dissipation processes.

For the definition of the density matrix, it is important to decide what states shall be included in the model system. The single light mode can be described by the Fock states $|n\rangle$. For N two-level systems, 2^N different basis states $|S\rangle$ have to be used, as all two-level systems can independently be either excited or unexcited. Using these states, the density matrix ρ writes as

$$\rho = \sum_{n_1, n_2}^{\infty} \sum_{S_1, S_2} |S_1\rangle |n_1\rangle C_{n_2, S_2}^{n_1, S_1} \langle n_2| \langle S_2| . \quad (2.6)$$

Applying the Liouville–von Neumann equation [70], the time evolution of ρ including dissipation processes is obtained via

$$i\hbar \frac{\partial}{\partial t} \rho = [H, \rho]_- + i\hbar \left(\gamma_z \sum_{n=1}^N \text{L}[P_{z,n}] + \gamma_a \sum_{n=1}^N \text{L}[P_n] + \kappa \text{L}[B_{\mathbf{q}}] \right) . \quad (2.7)$$

Here, all dephasing mechanisms are implemented via a Lindbladian [55],

$$L[O] = 2O\rho O^\dagger - O^\dagger O\rho - \rho O^\dagger O. \quad (2.8)$$

Thus, polarization dephasing is taken into account by the constant $\gamma = \gamma_z + \gamma_a$, population dephasing by $2\gamma_a$, and cavity photon dephasing by κ . This time evolution can be solved by numerical methods like a Runge–Kutta algorithm of 4th order [71]. The only approximation necessary is to choose an upper limit for the Fock states included. From the dynamics of the density matrix the expectation values of any quantity O can be obtained via

$$\langle O \rangle = \text{Tr} [O\rho]. \quad (2.9)$$

2.2 Semiconductor Bloch Equations

To describe the electronic states and interaction process in semiconductors, a different approach has to be chosen, due to the large dimensionality of the corresponding density matrix. The SBEs constitute such an approach while simultaneously being adaptable to semiconductor structures of arbitrary dimensionality [19, 20, 51, 72]. They can be applied to obtain changes to the semiconductor’s optical properties induced by charge carriers and are an established tool to describe the dynamics in semiconductors induced by optical excitation [73, 74]. Especially, the absorption features and the induced refractive index change is of great interest for theoretical investigations and experiment–theory comparisons. This section covers the SBEs, starting from the Hamiltonian and the electronic properties of the semiconducting material to the equations of motion and the resulting optical response.

2.2.1 Hamiltonian

Including interaction processes inside semiconductor heterostructures requires a microscopic description of their electronic and phononic properties. Both Coulomb and electron–phonon interaction are essential to have an appropriate description of a semiconductor. Therefore, they are included in the SBEs to enable a realistic modeling of all microscopic processes involved.

The system Hamiltonian,

$$H_{\text{system}} = H_0 + H_{e-e} + H_{l-m} + H_{e-p}, \quad (2.10)$$

includes the single-particle energies of electrons and phonons H_0 , the Coulomb interaction between electrons H_{e-e} , the light–matter interaction H_{l-m} , and the interaction between electrons and phonons H_{e-p} . Equation (2.10) can be used to compute the dynamics of any quantum-mechanical operator within this system via the Heisenberg equation of motion [19, 20].

In detail, the single-particle Hamiltonian of electrons and phonons is

$$H_0 = \sum_{\lambda} \sum_{\mathbf{k}} \varepsilon_{\mathbf{k}}^{\lambda} a_{\lambda, \mathbf{k}}^\dagger a_{\lambda, \mathbf{k}} + \sum_{\mathbf{p}} \hbar F_{\mathbf{p}} \left[D_{\mathbf{p}}^\dagger D_{\mathbf{p}} + \frac{1}{2} \right]. \quad (2.11)$$

with the single-particle energies $\varepsilon_{\mathbf{k}}^{\lambda}$ of an electron having momentum \mathbf{k} in band λ [19]. The fermionic operators $a_{\lambda,\mathbf{k}}^{\dagger}$ and $a_{\lambda,\mathbf{k}}$ create and annihilate an electron in a certain state λ, \mathbf{k} [19, 20]. The phonon energy dispersion $\hbar F_{\mathbf{p}}$ describes the energetic alignment of the phonons with momentum \mathbf{p} [75]. While $D_{\mathbf{p}}^{\dagger}$ and $D_{\mathbf{p}}$ are the bosonic creation and annihilation operators, counting the total amount of phonons in state \mathbf{p} . Equivalently to photons, they obey the bosonic commutation relations.

The single-particle energies can be obtained by evaluating an 8×8 Luttinger $\mathbf{k} \cdot \mathbf{p}$ model [72, 76]. At the same time, the single-particle wave functions of charge carriers are obtained for the desired semiconductor heterostructure. Induced strain effects in between the different layers of the semiconductor heterostructure arrangement can be included as described in, e.g., Ref. [77]. To be able to handle systems with local charge inhomogeneities, the Schrödinger–Poisson equation has to be solved [78]. This is necessary for spatially asymmetric charge distributions or high carrier densities.

The second term, H_{e-e} depicts the Coulomb interaction between the electrons,

$$H_{e-e} = \frac{1}{2} \sum_{\lambda, \lambda'} \sum_{\mathbf{k}, \mathbf{k}', \mathbf{q} \neq 0} V_{|\mathbf{q}|}^{\lambda, \lambda', \lambda', \lambda} a_{\lambda, \mathbf{k}+\mathbf{q}}^{\dagger} a_{\lambda', \mathbf{k}'-\mathbf{q}}^{\dagger} a_{\lambda', \mathbf{k}'} a_{\lambda, \mathbf{k}}, \quad (2.12)$$

with the Coulomb matrix element $V_{|\mathbf{q}|}^{\lambda, \lambda', \lambda', \lambda}$, which is the Fourier transform of the Coulomb potential in real space. All possible interactions are taken into account by a summation over all bands λ and λ' . The matrix elements $V_{|\mathbf{q}|}^{\lambda, \lambda', \lambda', \lambda}$ are computed using single-particle wave functions [79]. Furthermore, it includes restrictions due to the confinement of the carriers [80].

The light–matter interaction is defined by

$$H_{l-m} = - \sum_{\lambda, \lambda'} \sum_{\mathbf{k}} E(t) \left(d_{\mathbf{k}}^{\lambda, \lambda'} a_{\lambda, \mathbf{k}}^{\dagger} a_{\lambda', \mathbf{k}} + \text{h.c.} \right). \quad (2.13)$$

It describes a dipole transition between two bands, λ and λ' , with the classical electric field $E(t)$ and the dipole-transition matrix element $d_{\mathbf{k}}^{\lambda, \lambda'}$ [72]. The dipole matrix elements are computed from the single-particle wave functions and energies obtained from the band-structure calculation [72].

The last part of the Hamiltonian describes the interaction between electrons and phonons via

$$H_{e-p} = \sum_{\lambda} \sum_{\mathbf{k}, \mathbf{p}} G_{\mathbf{k}, \mathbf{p}}^{\lambda} \left[D_{\mathbf{p}} + D_{-\mathbf{p}}^{\dagger} \right] a_{\lambda, \mathbf{k}}^{\dagger} a_{\lambda, \mathbf{k}-\mathbf{p}}. \quad (2.14)$$

where $G_{\mathbf{k}, \mathbf{p}}^{\lambda}$ is the so-called Fröhlich matrix element [22].

2.2.2 Equations of Motion

Starting from the Hamiltonian, it is possible to compute the many-particle dynamics of any microscopic quantity in the system. The most relevant quantities regarding optics are the microscopic polarization and carrier distributions. Their dynamics is

2 Theoretical Background

described by the so-called semiconductor Bloch equations (SBEs). Macroscopic features, such as optical properties, are directly connected to this microscopic properties [19, 20]. Thus, this fully microscopic theory determines the macroscopic properties of a semiconductor.

The microscopic polarization between two arbitrary electronic bands λ and ν can be expressed in terms of fermionic operators, $p_{\mathbf{k}}^{\lambda,\nu} = \langle a_{\nu,\mathbf{k}}^\dagger a_{\lambda,\mathbf{k}} \rangle$. This expectation value is the transition probability of an electron between the bands ν and λ . Speaking of semiconductors, a widely used concept is to describe missing electrons in the valence band as quasiparticle holes [81]. Thus, the excitation of a semiconductor is illustrated in terms of electrons and holes in the conduction and valence band, respectively. Hence, other interesting quantities are the carrier distributions of electrons and holes in their respective bands. They are defined by $f_{\mathbf{k}}^{\lambda,e} = \langle a_{\lambda,\mathbf{k}}^\dagger a_{\lambda,\mathbf{k}} \rangle$ for electrons in the conduction band λ and by $f_{\mathbf{k}}^{\nu,h} = 1 - \langle a_{\nu,\mathbf{k}}^\dagger a_{\nu,\mathbf{k}} \rangle$ for the holes in the valence band ν . Both quantities are depicted in Fig. 2.1, which shows a schematic band structure with only one valence (ν) and conduction (λ) band in momentum space. Each band is filled up to a certain level with charge carriers, holes (red circles) in the valence band and electrons (blue circles) in the conduction band. The polarization between conduction and valence band is depicted by arrows.

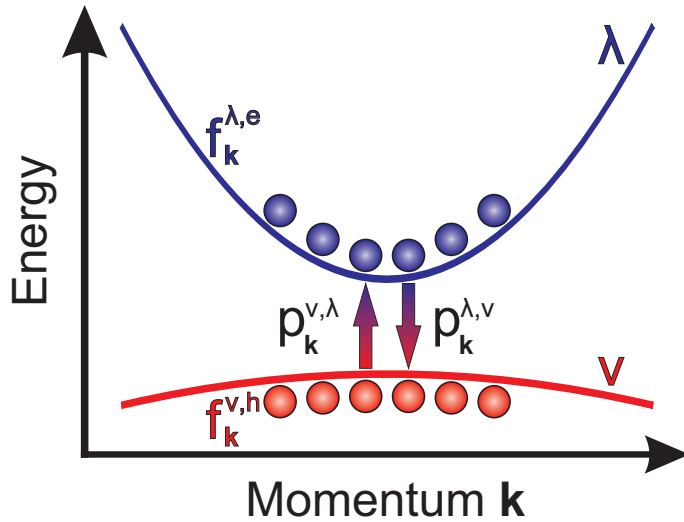


Figure 2.1: Schematic plot of microscopic polarizations (arrows) in \mathbf{k} -space, with electrons (blue circles) and holes (red circles) distributions in their respective bands λ and ν .

The temporal dynamics of any quantum-mechanical operator O for a system can be obtained using the Heisenberg equation of motion [19, 20],

$$i\hbar \frac{\partial}{\partial t} O = [H, O]_- . \quad (2.15)$$

This leads to a hierarchy of coupled differential equations, which has to be truncated to obtain a closed set of equations, e.g. by the cluster-expansion approach [20, 22].

Evaluating the Heisenberg equation of motion for the polarization and the charge carrier distributions leads to three coupled differential equations. The dynamics of the microscopic polarizations are

$$\begin{aligned} \frac{\partial}{\partial t} p_{\mathbf{k}}^{\lambda,\nu}(t) = & -\frac{i}{\hbar} \sum_{\lambda',\nu'} \left[\mathcal{E}_{\mathbf{k}}^{\lambda,\lambda',e} \delta_{\nu,\nu'} + \mathcal{E}_{\mathbf{k}}^{\nu,\nu',h} \delta_{\lambda,\lambda'} \right] p_{\mathbf{k}}^{\lambda',\nu'}(t) \\ & - \frac{i}{\hbar} \left[1 - f_{\mathbf{k}}^{\lambda,e}(t) - f_{\mathbf{k}}^{\nu,h}(t) \right] \Omega_{\mathbf{k}}^{\lambda,\nu}(t) + \frac{\partial}{\partial t} p_{\mathbf{k}}^{\lambda,\nu}(t) \Big|_{\text{scatt}}. \end{aligned} \quad (2.16)$$

Here the discrimination between the electron and hole bands is made by the indices λ and ν for electron and hole bands, respectively. Compared to the optical Bloch equations, the single-particle energies ε and the Rabi frequency $\Omega = dE$ are replaced by the Coulomb renormalized energies and the Coulomb renormalized Rabi frequency,

$$\mathcal{E}_{\mathbf{k}}^{\lambda,\lambda',e} = \varepsilon_{\mathbf{k}}^{\lambda} \delta_{\lambda,\lambda'} - \sum_{\lambda''} \sum_{\mathbf{q}} V_{|\mathbf{k}-\mathbf{q}|}^{\lambda,\lambda'',\lambda',\lambda''} f_{\mathbf{q}}^{\lambda'',e}(t), \quad (2.17)$$

$$\mathcal{E}_{\mathbf{k}}^{\nu,\nu',h} = \varepsilon_{\mathbf{k}}^{\nu} \delta_{\nu,\nu'} - \sum_{\nu''} \sum_{\mathbf{q}} V_{|\mathbf{k}-\mathbf{q}|}^{\nu,\nu'',\nu,\nu''} f_{\mathbf{q}}^{\nu'',h}(t), \quad (2.18)$$

$$\Omega_{\mathbf{k}}^{\lambda,\nu}(t) = -d_{\mathbf{k}}^{\lambda,\nu} E(t) - \sum_{\lambda',\nu'} \sum_{\mathbf{q}} V_{|\mathbf{k}-\mathbf{q}|}^{\lambda,\nu',\lambda',\nu'} p_{\mathbf{q}}^{\lambda',\nu'}(t). \quad (2.19)$$

They represent the many-particle character of the system as changes induced by the Coulomb interaction are taken into account. Here, Eq. (2.16) is explicitly written up to the Hartree–Fock level [68], which is equivalent to a singlet approximation in the cluster-expansion approach [20, 22]. The higher-order correlations are denoted by $\frac{\partial}{\partial t} p_{\mathbf{k}}^{\lambda,\nu}(t) \Big|_{\text{scatt}}$. They include electron–electron and electron–phonon scattering and are treated on the level of the second Born approximation and using the Markov approximation, the detailed form of the scattering terms can be found in Refs. [72, 79, 82]. It is necessary to treat all equations of motion up to this level to accurately describe the intrinsic dephasing mechanisms. Only then, the line shapes, the density dependence, and the position of the peak values in the spectra coincide with experiments [83]. This fully microscopic treatment gives correct homogeneously broadened spectra in comparison to a phenomenological ansatz with dephasing times extracted from experiments [84].

Electron and hole carrier distributions follow from

$$\frac{\partial}{\partial t} f_{\mathbf{k}}^{\lambda,e}(t) = \frac{2}{\hbar} \text{Im} \left[\sum_{\nu} \Omega_{\mathbf{k}}^{\lambda,\nu}(t) \left(p_{\mathbf{k}}^{\lambda,\nu}(t) \right)^* \right] + \frac{\partial}{\partial t} f_{\mathbf{k}}^{\lambda,e}(t) \Big|_{\text{scatt}}, \quad (2.20)$$

$$\frac{\partial}{\partial t} f_{\mathbf{k}}^{\nu,h}(t) = \frac{2}{\hbar} \text{Im} \left[\sum_{\lambda} \Omega_{\mathbf{k}}^{\lambda,\nu}(t) \left(p_{\mathbf{k}}^{\lambda,\nu}(t) \right)^* \right] + \frac{\partial}{\partial t} f_{\mathbf{k}}^{\nu,h}(t) \Big|_{\text{scatt}}. \quad (2.21)$$

The higher order terms for the charge carrier densities are treated on the same level as the scattering terms of the polarization. This set of coupled differential equations,

2 Theoretical Background

Eqs. (2.16), (2.20), and (2.21), can be solved numerically, e.g. using a Runge–Kutta algorithm of fourth order [71].

An alternative to the calculation of the dynamics (2.20) and (2.21) is to assume a quasi equilibrium. This ansatz is appropriate for situations like laser operation where no major changes to the amount and distribution of charge carriers in the system are expected. Therefore, carrier densities are prepared to be Fermi–Dirac distributed and are kept constant [85–87],

$$f_{\mathbf{k}}^{\lambda/\nu, e/h} = \frac{1}{\exp \left[\beta (\varepsilon_{\mathbf{k}}^{\lambda/\nu} - \mu_{\lambda/\nu}) + 1 \right]}, \quad (2.22)$$

where the distribution is specified by a temperature in the thermodynamic beta $\beta = \frac{1}{k_{\text{B}}T}$ and the chemical potential $\mu_{\lambda/\nu}$ of the system. This way, the carrier density equations are uncoupled from the polarization equation, which reduces the numerical effort.

2.2.3 Optical Response

With the microscopic polarization, the dynamics of the most interesting microscopic quantity is known by solving the SBEs. It can be used to derive the macroscopic polarization $P(t)$. The optical properties of a semiconductor are connected to macroscopic quantities via the optical susceptibility χ [19, 88]. It is proportional to the macroscopic polarization and antiproportional to the applied electric field [89],

$$\chi(\omega) \propto \frac{P(\omega)}{E(\omega)}. \quad (2.23)$$

The macroscopic polarization can be calculated directly from the microscopic polarizations via [19]

$$P(t) = \frac{1}{S} \sum_{\lambda, \nu} \sum_{\mathbf{k}} \left(d_{\mathbf{k}}^{\lambda, \nu} \right)^* p_{\mathbf{k}}^{\lambda, \nu}(t) + \text{c.c.}, \quad (2.24)$$

with S being the quantization area of the semiconductor quantum well.

Knowing the optical susceptibility, the optical properties of the excited semiconductor are directly accessible via the following proportionalities. The real part of the optical susceptibility is proportional to the carrier-induced refractive index change [90],

$$\delta n(\omega) = \frac{\omega}{100 n_{\text{bg}} c} \text{Re} [\chi(\omega)], \quad (2.25)$$

measured in 1/cm, containing the background refractive index n_{bg} . It defines how the presence of carriers in the system, described by its carrier distributions, alters the refractive index of the semiconductor material.

Additionally, the connection between optical susceptibility and material absorption is made through its imaginary part [91],

$$\alpha(\omega) = \frac{\omega}{100 n_{\text{bg}} c} \text{Im} [\chi(\omega)], \quad (2.26)$$

also given in units of $1/\text{cm}$. It describes the amount of light which is absorbed while a light pulse is propagating through the material. For an unexcited system, it shows sharp excitonic resonances [19]. They broaden with an increasing carrier density and can even become negative once the system reaches population inversion. A system's inversion is indicated by a vanishing or even negative phase space filling factor, $\left[1 - f_{\mathbf{k}}^{\lambda,e}(t) - f_{\mathbf{k}}^{\nu,h}(t)\right]$, c.f. Eq. (2.16). In this situation, the system is in the regime of optical gain, which is equivalent to negative absorption. Light frequencies within the gain region get amplified while propagating through the semiconductor.

The SBEs within the second Born–Markov approximation intrinsically incorporate homogeneous broadening of the material system due to their scattering terms. In contrast to that, inhomogeneous broadening, due to statistical fluctuations of the band gap which are the result of imperfections in the crystal structure, is not implemented directly. They originate from small variations during the growth process and impurities in a sample. To handle these unavoidable fluctuations properly, a convolution of the resulting spectra with a Gaussian is applied [84].

The material absorption and the carrier-induced refractive index change calculated with the SBEs can be used to analyze experiments. As the composition of the semiconductor material is the only required input, the SBEs are a versatile tool to compare experimentally grown samples and their spectra to the compositions intended to be grown. The computation of the SBEs in the limit of the second Born–Markov approximation and quasi-equilibrium, together with a database of material parameters, is implemented in the software package SimuLase [45], which has been used for the calculation of all spectra within this Thesis.

2.3 Semiconductor Luminescence Equations

The SBEs use a semiclassical description of the light–matter interaction $H_{\text{l-m}}$, with the electronic part being quantized and expressed through the fermionic operators of electrons and holes, while the electric field is described classically. Such a semiclassical description does not allow to model quantum-optical effects such as spontaneous emission [22, 92]. To include such effects into the theoretical model, the light field has to be quantized. In the following, this quantum-optical description of the light field will be combined with the many-body Hamiltonian (2.10) used to derive the SBEs.

2.3.1 Hamiltonian

For a fully quantized description of the light field, the energy of the light field has to be added to the Hamiltonian H_{system} , Eq. (2.10), which reads

$$H_{\text{light}} = \sum_{\mathbf{q}} \hbar\omega_{\mathbf{q}} \left[B_{\mathbf{q}}^{\dagger} B_{\mathbf{q}} + \frac{1}{2} \right], \quad (2.27)$$

with the sum over all light modes \mathbf{q} , their respective energy $\hbar\omega_{\mathbf{q}}$, and the photon number operator $B_{\mathbf{q}}^{\dagger} B_{\mathbf{q}}$, compare Eq. (2.2).

2 Theoretical Background

The semiclassical Hamiltonian H_{1-m} is replaced by the fully quantized light-matter interaction Hamiltonian,

$$H_{\text{quantized } 1-m} = - \sum_{\lambda, \nu} \sum_{\mathbf{k}, \mathbf{q}} \mathcal{F}_{\mathbf{k}, \mathbf{q}}^{\lambda, \nu} \left[B_{\mathbf{q}} - B_{-\mathbf{q}}^{\dagger} \right] a_{\lambda, \mathbf{k}}^{\dagger} a_{\nu, \mathbf{k}-\mathbf{q}} + \text{h.c.}, \quad (2.28)$$

with the dipole matrix element $\mathcal{F}_{\mathbf{k}, \mathbf{q}}^{\lambda, \nu}$ describing the coupling between a certain light mode and an electronic transition.

2.3.2 Equations of Motion

After extending the Hamiltonian with the quantized light-matter interaction, the dynamics of any operator can be solved again using the Heisenberg equation of motion (2.15). To obtain the spontaneous emission, the equation of motion for the photon number correlation $\Delta \langle B_{\mathbf{q}}^{\dagger} B_{\mathbf{q}} \rangle$ of a certain light mode \mathbf{q} has to be solved. It provides information on the change of the amount of photons in a certain light mode at any time, and therefore the semiconductors luminescence activity. The temporal evolution of the general operator $\Delta \langle B_{\mathbf{q}}^{\dagger} B_{\mathbf{q}'} \rangle$ is [20, 22]

$$\frac{\partial}{\partial t} \Delta \langle B_{\mathbf{q}}^{\dagger} B_{\mathbf{q}'} \rangle = i(\omega_{\mathbf{q}} - \omega_{\mathbf{q}'}) \Delta \langle B_{\mathbf{q}}^{\dagger} B_{\mathbf{q}'} \rangle + \sum_{\lambda, \nu} \sum_{\mathbf{k}} \left(\mathcal{F}_{\mathbf{k}, \mathbf{q}}^{\lambda, \nu} \left(\Pi_{\mathbf{k}, \mathbf{q}'}^{\lambda, \nu} \right)^* + \left(\mathcal{F}_{\mathbf{k}, \mathbf{q}'}^{\lambda, \nu} \right)^* \Pi_{\mathbf{k}, \mathbf{q}}^{\lambda, \nu} \right). \quad (2.29)$$

It is directly coupled to the photon-assisted polarization $\Pi_{\mathbf{k}, \mathbf{q}}^{\lambda, \nu} = \Delta \langle B_{\mathbf{q}}^{\dagger} a_{\nu, \mathbf{k}-\mathbf{q}}^{\dagger} a_{\lambda, \mathbf{k}} \rangle$. To calculate the dynamics of the photon number operator, the dynamics of the photon-assisted polarizations have to be solved as well, which is

$$i\hbar \frac{\partial}{\partial t} \Pi_{\mathbf{k}, \mathbf{q}}^{\lambda, \nu} = (\varepsilon_{\mathbf{k}}^{\lambda} - \varepsilon_{\mathbf{k}-\mathbf{q}}^{\nu} - \hbar\omega_{\mathbf{q}}) \Pi_{\mathbf{k}, \mathbf{q}}^{\lambda, \nu} + \mathcal{S}_{\mathbf{k}, \mathbf{q}}^{\lambda, \nu, \text{SE}} - (1 - f_{\mathbf{k}}^{\lambda, \text{e}} - f_{\mathbf{k}}^{\nu, \text{h}}) \mathcal{S}_{\mathbf{k}, \mathbf{q}}^{\lambda, \nu, \text{ST}}. \quad (2.30)$$

The photon-assisted polarization has two source terms. First, a part associated with the spontaneous emission $\mathcal{S}_{\mathbf{k}, \mathbf{q}}^{\lambda, \nu, \text{SE}}$ and second, a part describing the stimulated emission $\mathcal{S}_{\mathbf{k}, \mathbf{q}}^{\lambda, \nu, \text{ST}}$. The detailed form of the source terms for the photon-assisted polarization can be found in Refs. [22, 93, 94]. To derive this set of source terms, the hierarchy is truncated at the same level as for the SBEs using the cluster-expansion approach [20, 22].

Together, Eqs. (2.29) and (2.30) build a set of coupled differential equations. The system is assumed to be in a quasi-equilibrium state as done for the SBEs, see Sec. 2.2.2. Hence, the carrier densities are modeled by Fermi-Dirac distributions and kept constant. These equations, which are called semiconductor luminescence equations (SLEs) [22, 89], are formally equal to the SBEs and thus can be solved numerically.

2.3.3 Photoluminescence

Being able to calculate the amount of photons in a certain light mode at any time can be used to derive the PL which is emitted by a semiconductor. It is defined as

$$\text{PL}(\omega_{\mathbf{q}}) = \frac{\partial}{\partial t} \Delta \langle B_{\mathbf{q}}^\dagger B_{\mathbf{q}} \rangle = 2\text{Re} \left[\sum_{\lambda, \nu} \sum_{\mathbf{k}} \mathcal{F}_{\mathbf{k}, \mathbf{q}}^{\lambda, \nu} \left(\Pi_{\mathbf{k}, \mathbf{q}}^{\lambda, \nu} \right)^* \right], \quad (2.31)$$

which is the change of the amount of photons in a mode at a given time. To achieve a reasonable agreement in experiment–theory comparisons, an inhomogeneous broadening is applied to the PL spectra as well, cf. Sec. 2.2.2. The SLEs are implemented in the software package SimuLase [45] in the same limits as the SBEs. In this Thesis, all presented PL spectra were calculated using this software package.

2.4 Photomodulated Reflection Spectroscopy

Investigation techniques beyond ordinary PL measurements are needed to analyze the optical and electronic properties of a semiconductor heterostructure in detail. The electronic structure of samples can be investigated using PR spectroscopy. This method utilizes two reflection measurements of a light pulse on a sample to compare them by their normalized difference. In the first measurement, the sample is completely unexcited, in the second, it gets excited before the reflection is measured, which induces a modulation of the band gap [95]. Due to the changes induced to the band gap, this spectroscopy technique allows for investigations of the oscillator strength of all possible transitions in a semiconductor heterostructure.

To model the experimental conditions, an expression for the monitored quantity $\Delta R/R$ has to be derived. The reflection R of an optical pulse on the sample is measured under an angle of about 45° . Before the measurements, the sample is prepared in either an unexcited or an excited state. To distinguish between both cases the reflectivity is named R_0 and R_x , respectively, while their difference is $\Delta R = R_0 - R_x$.

Even if the light pulse propagates under an angle of 45° with respect to the sample, the light propagation is assumed to be perpendicular to the internal interfaces. This is a reasonable assumption due to the high refractive index of semiconductor material in comparison to air. Therefore, it is legit to use the Fresnel equation to calculate the reflection between barrier and quantum wells. For an angle of 0° it reads [96]

$$R = 1 - \frac{4 n_{\text{barrier}} n_{\text{well}}}{(n_{\text{barrier}} + n_{\text{well}})^2}. \quad (2.32)$$

Here, n_{barrier} is the background refractive index of the barrier material. To calculate n_{well} for the excited case, the SBEs are applied because the optical properties of the sample are changed by an optical excitation. Thus, n_{well} consists of two parts, its background refractive index n_{bg} and contributions from the change of the refractive index due to the optical excitation δn_x . Solving the SBEs yields real and imaginary

2 Theoretical Background

part of the optical susceptibility. The dielectric function $\epsilon(\omega) = n_{\text{bg}}^2 + \chi(\omega)$ is directly connected to the optical susceptibility [19, 90],

$$\text{Im}[\epsilon(\omega)] = \text{Im}[\chi(\omega)], \quad (2.33)$$

$$\text{Re}[\epsilon(\omega)] = n_{\text{bg}}^2 + \text{Re}[\chi(\omega)]. \quad (2.34)$$

To express the absorption and the full refractive index of the excited material via the dielectric function, the relations [90]

$$\alpha(\omega) = \frac{\omega}{n_{\text{bg}}(\omega)c} \text{Im}[\epsilon(\omega)], \quad (2.35)$$

$$n(\omega) = \sqrt{\frac{1}{2} \left[\text{Re}[\epsilon(\omega)] + \sqrt{\text{Re}[\epsilon(\omega)]^2 + \text{Im}[\epsilon(\omega)]^2} \right]}, \quad (2.36)$$

are utilized. While the absorption has only contributions from the imaginary part of $\epsilon(\omega)$, the full refractive index is build up with contributions from both real and imaginary parts. Using $n(\omega)$, a value for the reflectivity R for excited and unexcited conditions is obtained from Eq. (2.32). Hence, $\Delta R/R$ is calculated and all the induced differences by the PR spectroscopy technique can be visualized.

The modulation of the band gap, as it is done in an experiment, is simulated by a change of the temperature, and thus a linear reduction of the band gap [97]. Additionally, the inhomogeneous broadening is varied to take excitation induced dephasing into account, c.f. Paper [III]. Overall, the PR signal is defined as

$$\text{PR} = \frac{R_0(T, \gamma_0) - R_x(T + \Delta T, \gamma_x)}{R_0(T, \gamma_0)}. \quad (2.37)$$

The resulting spectrum reveals the position and the oscillator strength of excitonic transitions in semiconductor heterostructures, as discussed in Sec. 3.3.3.

Interface-Dominated Laser Structures

Semiconductor heterostructures are of great interest for fundamental research as well as for commercially sold devices. A whole of different applications can be realized by optimizing their material composition, growth conditions, and spatial alignment and in this way their properties. Their flexibility, especially in terms of their optical band gap and other optical properties, is of great interest. Usually, optical transitions in semiconductors are designed to take place spatially within one layer of a heterostructure. Growing a heterostructure with transitions possible between spatially separated layers enables an additional degree of freedom in the design process. To differentiate between direct and indirect transitions in real space, the indirect ones are called type-II. They are discussed already for several years [16, 98–100] and up to today investigations on their properties are performed [41, 101].

One common application for semiconductor lasers is the optical data transfer in the near-infrared regime since dispersion and losses of optical fibres are minimized in this spectral region, especially at 1300 nm and 1550 nm [2, 10, 102]. Traditional type-I semiconductor lasers are not performing very well for this application. They suffer from internal losses due to the small optical band gap of heterostructures emitting in this regime [103, 104]. Therefore, a different approach is investigated by introducing a setup with an optical transition across an internal interface. Here, the combination of two materials with their intrinsic emission wavelength gives hope not to pay any Auger penalty and to reduce characteristic losses. This allows for the combination of two semiconductors with rather large band gaps compared to the near infrared [16].

In this chapter, general properties of interface-dominated systems are investigated and compared to traditional double heterostructures. Analogously to Paper [II], the experimental realization of a “W”-MQWH is analyzed theoretically and its use as gain medium in a laser setup is investigated. Thorough experiment–theory comparisons for PL and PR spectra highlight their type-II character, cf. Paper [III]. Furthermore, an investigation of a VECSEL based on carrier recombinations across interfaces and emission in the near-infrared regime is presented according to the Papers [IV], [V], and [VII]. All experimental work, epitaxial growth and sample characterization, was done by the groups of W. Stolz, W. Heimbrodt, S. Chatterjee, and M. Koch at Philipps-

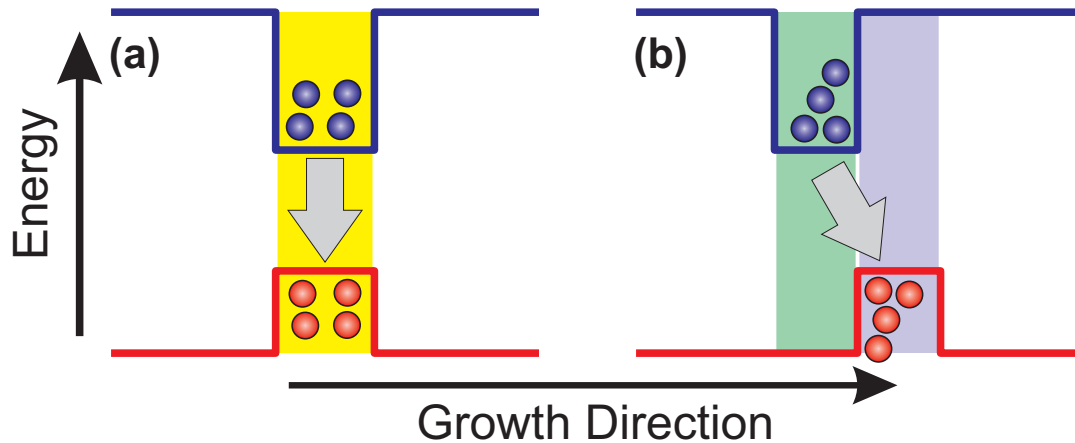


Figure 3.1: Illustration of (a) type-I (direct) and (b) type-II (indirect) quantum-well alignments. Schematic confinement potentials (solid lines) for electrons (blue circles) and holes (red circles) with an illustration of a recombination pathway (arrows).

Universität Marburg. Last, possible optimizations for VECSEL systems with this emission wavelength are discussed.

Traditional type-I systems are defined by the criterion of electrons and holes being confined in the same spatial position, as depicted in Fig. 3.1 (a). In contrast to type-I systems, a type-II alignment is defined by the separation of electrons and holes in two different and spatially separated quantum wells [16]. Accordingly, type-II configurations include an internal interface where recombinations of electrons and holes occur across, see Fig. 3.1 (b). The electronic levels of electrons and holes are determined individually by their confinement and the materials used. In principle, both quantum-well materials can be chosen independently, which allows tuning the properties of the type-II structure. In comparison to type-I systems this is a new degree of freedom enabled due to the recombination through the interface. It doubles the amount of parameters, like quantum-well arrangement, material, width, and concentrations. For a type-II setup, modifications on the electron well can be made independently from the hole well, and therefore specific emission properties can be tailored. Not to conceal that there is a multitude of combinations to achieve a specific type-II transition energy. To be able to use a type-II setup as laser gain structure, a sufficient overlap between electron and hole wave functions is needed. An increase in wave function overlap raises the transition and recombination probability between charge carriers in the different quantum wells.

In the beginning, type-II diode lasers were based on superlattice configurations and had an emission wavelength in the mid-infrared range using a (GaIn)Sb/InAs type-II transition [98, 105, 106]. Also, type-II quantum-cascade lasers were proposed [107] and realized showing emission wavelength of $2\ \mu\text{m}$ [108] and $3.8\ \mu\text{m}$ [109]. Type-II quantum-well luminescence was shown for the near-infrared region based on the

(GaIn)As/Ga(AsSb)/GaAs material system [16, 110]. Based on type-II quantum wells, optically pumped lasers were fabricated emitting in the mid-infrared using InAs/(GaIn)Sb/InAs/AlSb as material system [99]. This chapter focuses on the analysis in the near-infrared regime around 1200 nm using an improved type-II approach, the so-called “W”-configuration, which is introduced and discussed next.

3.1 “W”-Quantum-Well Heterostructure Approach

A specific type-II heterostructure is created by adding a third quantum well. They are arranged starting with an electron well followed by a hole well and a second electron well. This way, the setup has two internal interfaces between electron and hole wells. The symmetry increases the overlap between electron and hole wave functions in comparison to a two-quantum-well configuration. A scheme of the confinement potentials and the first electron and hole wave functions is shown in Fig. 3.2. Due to the alignment of the conduction band confinement potential, this arrangement is referred to as “W”-structure. Electrons are confined in two places, while the holes have only one place to relax into. Both sides of the hole well have an electron containing counterpart where recombinations across the interface takes place.

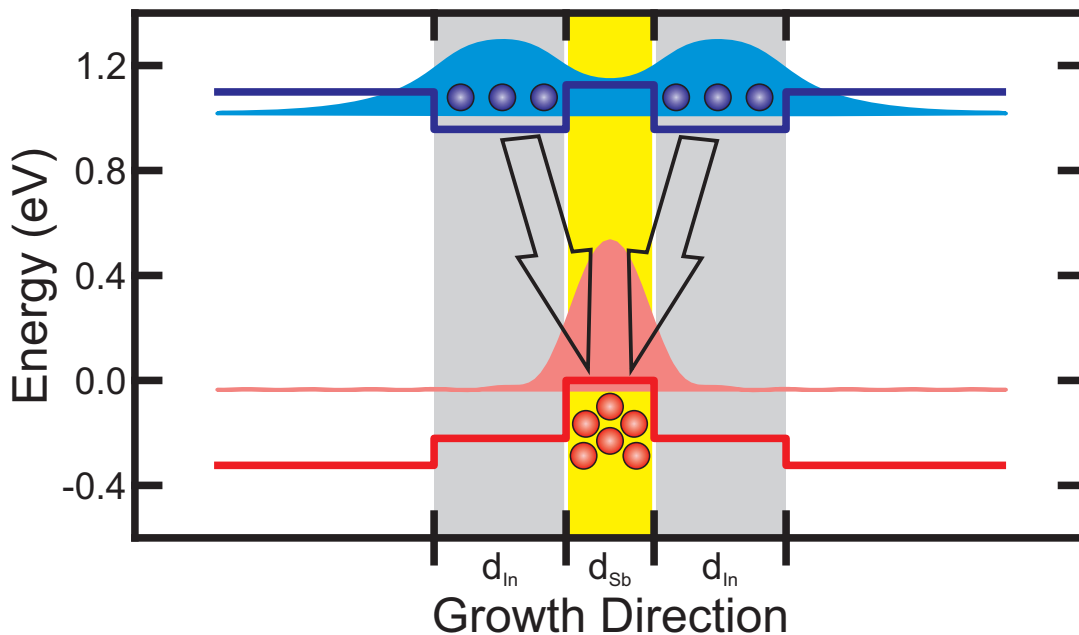


Figure 3.2: “W”-confinement potentials (solid lines) of electrons (blue) and holes (red). Wave functions (shaded areas) and charge carriers (circles) are plotted with an indication of their recombination process across the interface (arrows). This illustration is based on a (GaIn)As/Ga(AsSb)/(GaIn)As/GaAs material system.

Historically, the “W”-setup was first introduced by Meyer et al. in 1995 [111]. It

enables new material systems for emission wavelengths in the same way as ordinary type-II setups do, especially at low energies in the infrared where type-I systems suffer from intrinsic losses [104]. Hence, type-II “W”-alignments are most advantageous in wavelength regimes which are hard to achieve for traditional type-I configurations. Additionally, they improve the wave function overlap compared to ordinary type-II alignments, as explained above. The tailoring of laser emission properties leads to novel material systems for lasing in the near-infrared regime. One challenge for the concrete realization is the required interface quality, which is needed to achieve a sufficient overlap and minimize intrinsic losses.

First experimental studies on promising material systems for near-infrared emission were done by Peter et al. in 1995 [16] for type-II systems and by Dowd et al. in 1999 [112] for a “W”-setup. This first reported successful “W”-approach was accomplished with a (GaIn)As/Ga(AsSbP)/(GaIn)As/GaAs material system and showed PL between 1300 nm and 1550 nm. Another group of researchers confirmed this behavior one year later using the same material system [113]. Johnson et al. introduced a more complex strain compensated material setup of Ga(AsP)/GaAs/Ga(AsSb)/Ga(AsP)/GaAs and observed PL at 1300 nm. A wide range of PL emission wavelengths between 1200 nm and 1550 nm were covered in Refs. [43, 114, 115] by using (GaIn)(NAs)/Ga(AsSb)/(GaIn)(NAs)/GaAs as originally suggested by Tansu et al. [40]. Khandedkar et al. showed a 1400 nm PL removing In from the electron layers [116]. A 1300 nm composition using (GaIn)As/Ga(AsSb)/(GaIn)As/GaAs as setup was proposed [117] and later proven by experiments [118, 119]. Lowering the Sb content to roughly 20%, a PL at 1200 nm was measured in Papers [II] and [III]. Nevertheless, the first type-II “W”-VECSEL was presented just recently in Paper [IV].

This development shows promising results in the near-infrared spectral range with the “W”-setup. A first laser with rather low output powers up to 140 mW was presented [110], the following analysis and recent Papers [IV] and [V] underline that a “W”-structure on GaAs substrate can have an improved laser performance. Even if this Thesis focuses on near-infrared emission, which is usually done on a GaAs substrate, there is also a lot of interest in mid-infrared “W”-lasers based on GaSb and InP substrates as reviewed in Ref. [120] and seen in latest publications [121–127].

3.2 Theoretical Predictions for “W”-aligned multiple Quantum Wells

An actual scheme for a “W”-MQWH has already been proposed and presented in Ref. [119]. It consists of a sequence of 6 nm (GaIn)As with 20% In, 4 nm Ga(AsSb) with 20% Sb, and again 6 nm (GaIn)As with 20% In, grown on a GaAs as substrate. Emission properties for this material system are in the near-infrared regime. It is a promising candidate for the use as active medium in a VECSEL, because its emission is close to the telecom wavelengths. In addition, the (AlGa)As/AlAs DBR technique and established know-how can be used. Figure 3.2 presents the confinement potential

and the first electron and hole states as well as wave functions for this setup. This plot visualizes the overlap of electron and hole wave functions in the confined region very well, as it is the most crucial quantity for the strength of the transitions as explained above.

As active medium in a laser, the material must amplify a light mode through stimulated emission. A direct measure for this is a negative material absorption, the so-called gain. To proof the potential as active medium, the SBEs presented in Sec. 2.2.2 are utilized for the calculation of the absorption properties. The outcome is shown in Fig. 3.3. For carrier densities ranging from $0.1 \cdot 10^{12}/\text{cm}^2$ (bright) up to $3.0 \cdot 10^{12}/\text{cm}^2$ (dark), changes in the material absorption are observed. The result for the lowest charge carrier density still has an excitonic absorption peak, while starting from $1.5 \cdot 10^{12}/\text{cm}^2$ negative values for the material absorption are present. Thus, a material gain can be observed and the use as amplification medium in a laser becomes possible. Material gain up to half of the initial absorption is predicted here at a temperature of 300 K with carrier densities in the same order of magnitude as in type-I systems [72, 83]. This confirms that (GaIn)As/Ga(AsSb)/(GaIn)As/GaAs is a promising model system which is worth further investigations.

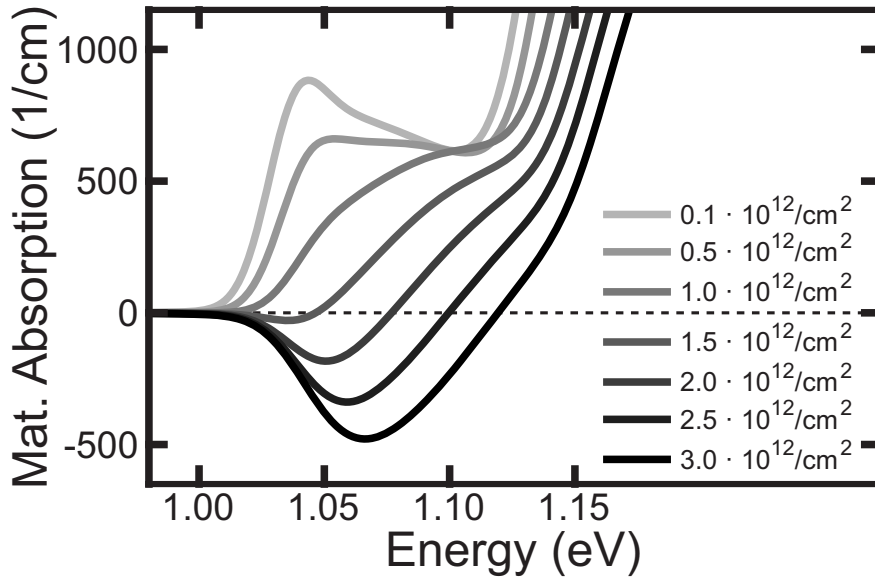


Figure 3.3: Material absorption of the (GaIn)As/Ga(AsSb)/(GaIn)As/GaAs system with thicknesses of 6/4/6 nm in the “W”-quantum well and concentrations of 20% for In and Sb. Carrier densities between $0.1 \cdot 10^{12}/\text{cm}^2$ (bright) and $3.0 \cdot 10^{12}/\text{cm}^2$ (dark) are plotted at a temperature of 300 K.

3.2.1 Comparison to Type-I Setups

This section presents a direct comparison between the properties of type-I and type-II systems, especially in “W”-configuration. Differences in the temperature dependence

of bulk band edges and type-II transition energies are investigated as well as differences arising from local charge separation of charge carriers in type-II systems.

Figure 3.4 presents a comparison between type-I and type-II systems' confinement potentials and wave functions while temperature and charge carrier densities are altered. As type-I system, a (GaIn)As quantum well of 6 nm thickness and with an In concentration of 40% surrounded by GaAs barriers is used in this section which is comparable to actual realizations in Refs. [128–130]. This type-I system is chosen to have the same low-density PL peak position as the type-II setup introduced in Sec. 3.2. An initial situation at 300 K with a vanishing charge carrier density is plotted in Fig. 3.4 for type-II (a) and type-I (d). Increasing the temperature to 350 K for type-II (b) and type-I (e) lowers their electron confinement potential, which is the characteristic red-shift of bulk band edges described by the Varshni formula [97]. Thus, a decrease in transition energy between the first electron level and the first hole level is observed for both types. Additionally to the temperature dependence, the valence (VBO) and conduction (CBO) band offsets and all other material parameters are chosen in correspondence to literature [45, 97]. However, different absolute shifts are observed for each quantum-well material in the “W”-structure, as these are intrinsic properties of each layer. Additionally, the type-II transition underlies another shift rate which originates from changes to the depth of the potential wells. The confinement changes as the barrier material GaAs and the second quantum-well material Ga(AsSb) have a different temperature dependence in comparison to (GaIn)As. As explained in Ref. [97], the VBO is a bulk parameter and is therefore independent of temperature. Having this in mind, it is not unexpected that the type-II transition shifts closely with the (GaIn)As band edge since the electron bands are influenced by an increasing temperature while the hole levels remain unchanged. The band edge has the main influence on the level of the electrons, while there is only a minor change due to the new depth of the potential well. Thus, the type-II transition shift is close to the one of the (GaIn)As band edge and there is no major difference between type-I and type-II in this aspect.

Besides the increase of temperature, changes to the charge carrier density have an effect on the transition energies in type-II systems, too. Due to a spatial carrier distribution in type-II setups, a difference between type-I and type-II systems is introduced. It is visualized by looking at the confinement potential for unexcited (b) and gain (c) conditions at an increased temperature of 350 K in Fig 3.4. The confinement potential is changed due to the attraction between spatially separated electrons and holes which does not appear in type-I alignments. The induced changes in the bands by charge carrier densities are treated by solving the Schrödinger–Poisson equation. Hence, the type-I system band gap is reduced with increasing temperature and no additional change is induced from an increased charge carrier density, cf. (e) and (f). In contrast to that, type-II systems exhibit a deformation of their confinement potential with increasing carrier density which leads to an overall increase of the transition energy in Fig. 3.4 (c). Altogether, it is a competition between temperature and carrier density dependent shift which anyway can lead to an overall shift of the type-II transitions to higher energies with increasing density.

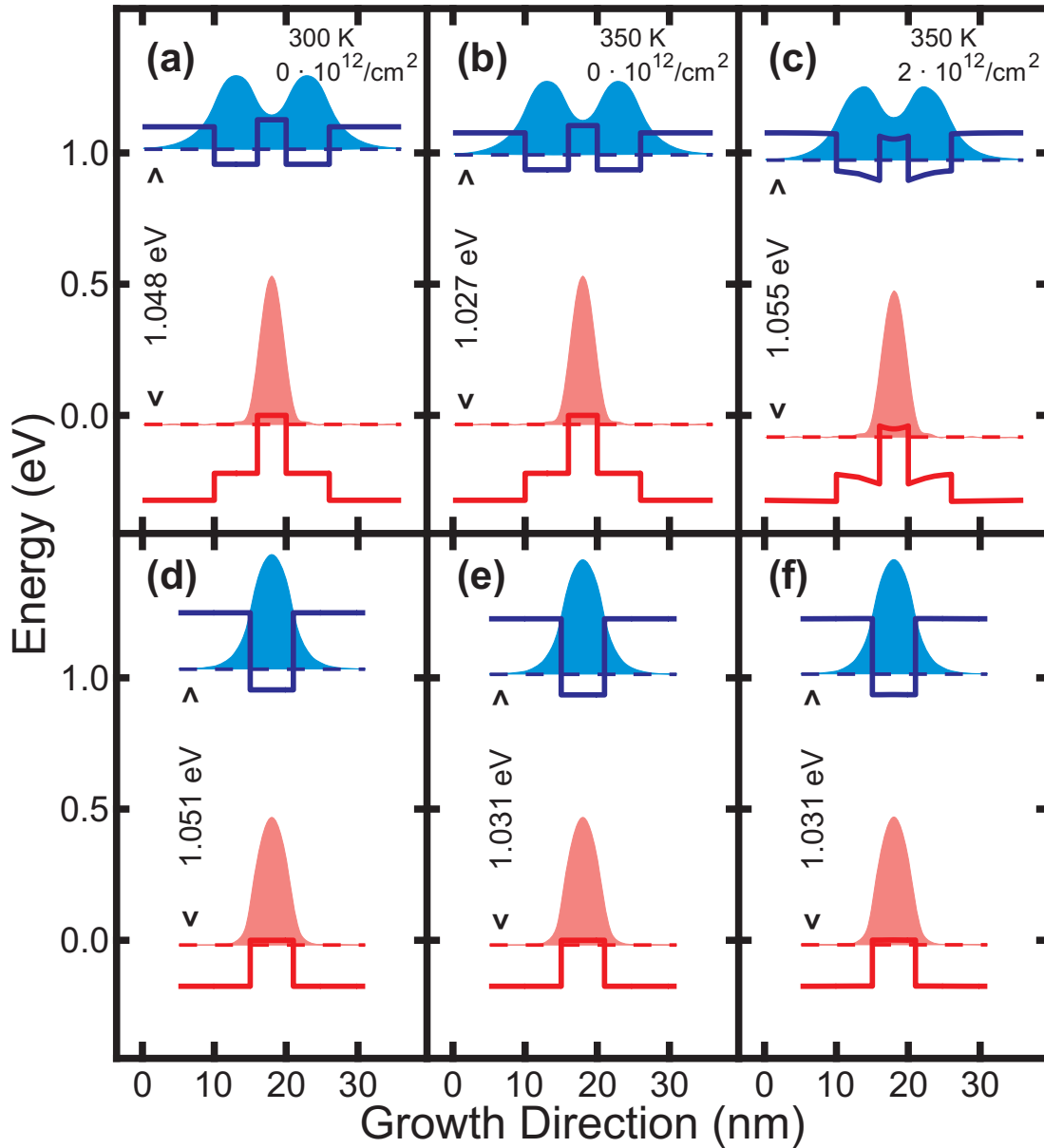


Figure 3.4: Confinement potentials (solid lines), wave functions (shaded areas), and energetic levels (dashed lines) for varied temperatures and charge carrier densities in type-I and type-II “W”-structures. Initial situation with vanishing charge carrier density at a temperature of 300 K for (a) type-II and (d) type-I. Temperature increase to 350 K for (b) type-II and (e) type-I. Charge carrier density of $2 \cdot 10^{12}/\text{cm}^2$ at 350 K for (c) type-II and (f) type-I. The transition energy between the first electron and the first hole band is explicitly denoted.

Next, the shift between the peak positions of a PL signal obtained at a low carrier density and the gain maximum at a fixed level is investigated. This examination provides insight in how many meV the gain maximum shifts in comparison to the spontaneous emission signal, both in the type-I and the type-II setup. It is useful to quantify this feature when implementing such semiconductor heterostructures inside a VECSEL as active material. PL measurements are used oftentimes to monitor the growth success of MQWHs. In general, they are easier to perform in comparison to the determination of gain spectra. As a VECSEL is optically pumped into its barriers, it heats up during operation. Therefore, one case with no temperature increase between the PL and gain measurement and another with an increase of 50 K is investigated to provide most realistic insights [131]. Hence, 350 K is a typical gain temperature at the threshold of such lasers systems under room temperature conditions [132].

Figure 3.5 presents the shift for type-I and type-II systems with roughly the same PL peak position. The PL signal at room temperature for type-I (solid line) and type-II (dotted line) is plotted in Fig. 3.5 (a). In Fig. 3.5 (b), the material gain spectra are presented for both systems and the two temperatures, namely 300 K and 350 K. The gain value is kept constant around 300/cm and the shift between PL and gain peak is denoted in the legend. From these calculations, the information that type-II systems do not have a red shift as large as for type-I systems with an comparable amount of gain is retrieved.

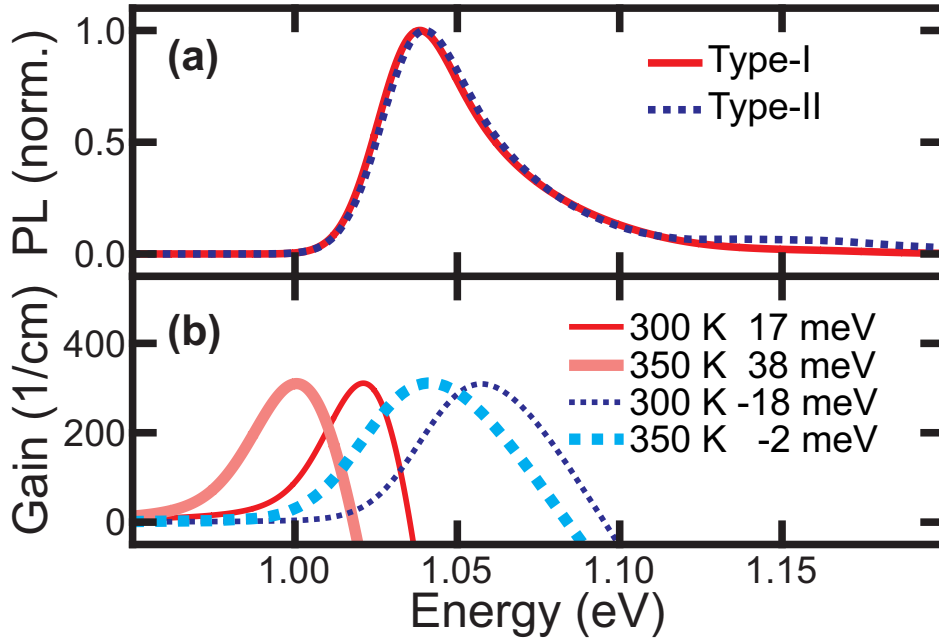


Figure 3.5: Detuning between PL and gain maximum for type-I and type-II systems. (a) Normalized PL spectra for type-I (solid line) and type-II (dotted line) at 300 K. (b) Material gain curves with peak of 310/cm for type-I (red) and type-II (blue) setup at 300 K (thin) and at 350 K (thick).

In general, for type-I gain behavior is observed energetically below the absorption due to a many-body effect, i.e. Coulomb renormalization in Eqs. (2.17) and (2.18). The compensation of this red shift in type-II setups is explained by the deformation of the confinement potential due to the carriers in the bands, as presented in Fig. 3.4. In this case it is even overcompensated and inverts the direction of the shift for 300 K. From the variation of the temperature it is found that increasing the temperature leads to a red shift in both cases, as expected. Even the size of this shift is nearly the same for both systems with 21 meV for the type-I and 16 meV for the type-II system. Thus, a vanishing overall shift between PL and gain maximum is found for the realistic consideration of type-II systems with room temperature PL and an increased sample temperature during laser operation. Additionally, the direct comparison between the gain curves in Fig. 3.5 (b) highlight a broader gain for the type-II system compared to type-I.

Furthermore, the temperature stability of the material gain shall be investigated by comparing the type-I and the type-II model systems. Figure 3.6 presents two temperature dependence studies. First, frames (a) and (c) show an analysis which keeps the gain maximum constant while changing the temperature from 260 K (bright) to 360 K (dark) by adjusting the charge carrier density from $1.649 \cdot 10^{12}/\text{cm}^2$ (bright) to $2.599 \cdot 10^{12}/\text{cm}^2$ (dark) for type-II and from $0.798 \cdot 10^{12}/\text{cm}^2$ (bright) to $1.334 \cdot 10^{12}/\text{cm}^2$ (dark) for type-I, respectively. This is done to investigate the temperature dependence at a fixed gain value. At this point it is important to note that there is a mismatch in the material gain position between type-I and type-II as both model systems were chosen to match in the low-density PL. Having the same PL peak position directly leads to a higher energetic material gain for the type-II structure due to the deformation of the confinement potential under gain conditions. Anyway, the results show a smaller relative carrier density increase by a factor of 1.58 for the type-II system in comparison to a factor of 1.67 for type-I. In addition, less absolute shift in peak position for the temperature variation is observed.

Second, the charge carrier density is kept constant at $2 \cdot 10^{12}/\text{cm}^2$ for type-II in Fig. 3.6 (b) and at $1 \cdot 10^{12}/\text{cm}^2$ for type-I in Fig. 3.6 (d). A smaller absolute and relative change in peak height is visible for type-II in comparison to type-I. Additionally a smaller absolute shift in peak position between 260 K and 360 K is observed. Overall, the type-II model system’s material gain is less temperature dependent which can be an advantage when using it as active medium in a laser with steady changes in the environment.

In general, the transition energy between the first conduction and the first valence band state is directly influenced by changes in the carrier density and the temperature. The first effect is the temperature dependent shift of the conduction band and the second the deformation of the confinement potential due to the charge carriers in the valence and conduction band which scales with the charge carrier density in the system. In comparison, a type-I system shows only a significant change due to the temperature dependent shift of its bands, but no deformation happens as the carriers are not spatially separated. This is the main difference between type-II and type-I systems at this level because the wave function overlap is negligible as long as it is

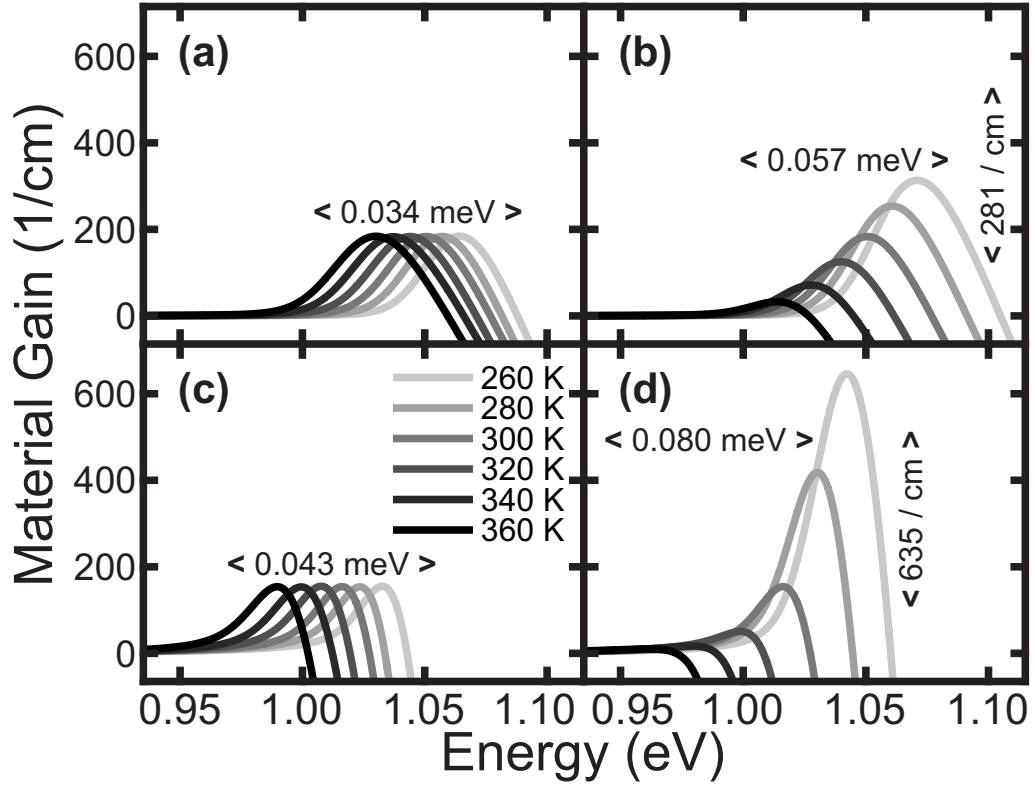


Figure 3.6: Temperature dependence of material gain for type-II and type-I setups. (a) Type-II and (c) type-I material gain spectra with a fixed maximum. (b) Type-II and (d) type-I material gain spectra with constant charge carrier density of $2 \cdot 10^{12} / \text{cm}^2$ and $1 \cdot 10^{12} / \text{cm}^2$ for type-II and type-I, respectively. All spectra show temperatures between 260 K (bright) to 360 K (dark). Absolute peak shifts are denoted.

large enough to see gain and emission for this investigation.

3.3 Analysis of Epitaxially Grown “W”-multiple Quantum-Well Heterostructures

In this section, a thorough analysis of two experimentally realized MQWHs is presented. All observations are based on an experiment–theory collaboration as reported in Papers [II] and [III].

Two epitaxially grown semiconductor heterostructures are investigated subsequently. Both consist of the same material system which was introduced in Sec. 3.2, but exhibit slightly different material compositions and layer thicknesses. Their concrete material composition was extracted from HR-XRD measurements and are presented in Tab. 3.1. Additionally, GaAs barriers of 10 nm width were added to both samples,

“W”-MQWH sample	(GaIn)As (nm)	In (%)	Ga(AsSb) (nm)	Sb (%)
#25987	5.6	21.7	4.2	17.3
#25989	5.7	21.6	4.0	21.3

Table 3.1: Nominal material composition of “W”-MQWHs obtained via HR-XRD measurements.

and roughly 140 nm of strain compensating Ga(AsP) barriers. The whole arrangement of “W”-quantum well and barriers was repeated 10 times for both samples. They differ mostly due to their Sb content, while the rest of the nominal parameters is approximately the same.

3.3.1 Photoluminescence

PL measurements were performed to characterize the sample properties of #25987 and #25989. An experiment–theory comparison of the PL results was performed in Paper [II] and will be reviewed in the following. The fully microscopic theory presented in Sec. 2.3 provides a checkup for deviations from the nominal parameters by a comparison between experimental and theoretical spectra. A selection of experimental and theoretical PL spectra are depicted in Fig. 3.7. Near-infrared emission can be observed for both samples in the experimental spectra (top row). Sample #25987 has two signatures, one major peak around 1.06 eV and a smaller one around 1.2 eV. In contrast, sample #25989 shows only one peak around 1.02 eV and the energetically higher one is only visible as a shoulder of the main peak. The main peak position of both samples differs due to the variation in their Sb content.

By comparing the theoretical spectra (bottom row), a very good agreement in general shape and peak position for main and side peak is found. The energetic analysis of the peaks identifies the transitions between the first electron and the first hole band as the main peak and between the second states as the side peak. This makes both of them a type-II signature, as it will be discussed later in Sec. 3.3.3. It can be observed that not only the peak position but also the strength of the side peak is related to the Sb content of the structures, as it differs between both samples. An analysis in Paper [II] finds adaptations for the material parameters needed to match peak position perfectly. It brings up that the theoretical spectra for #25987 match the experiment by changing the Sb content by 1.7% or increasing the (GaIn)As well width by 1 nm and the In content by 0.3%, with respect to the interpretation scope of the HR-XRD analysis. Sample #25989 matches already very well and an adjustment yields only a minor improvement. Overall, the PL emission is found to be in the near-infrared regime and the theory reproduces the experimental results very well, helping to understand the differences between both samples.

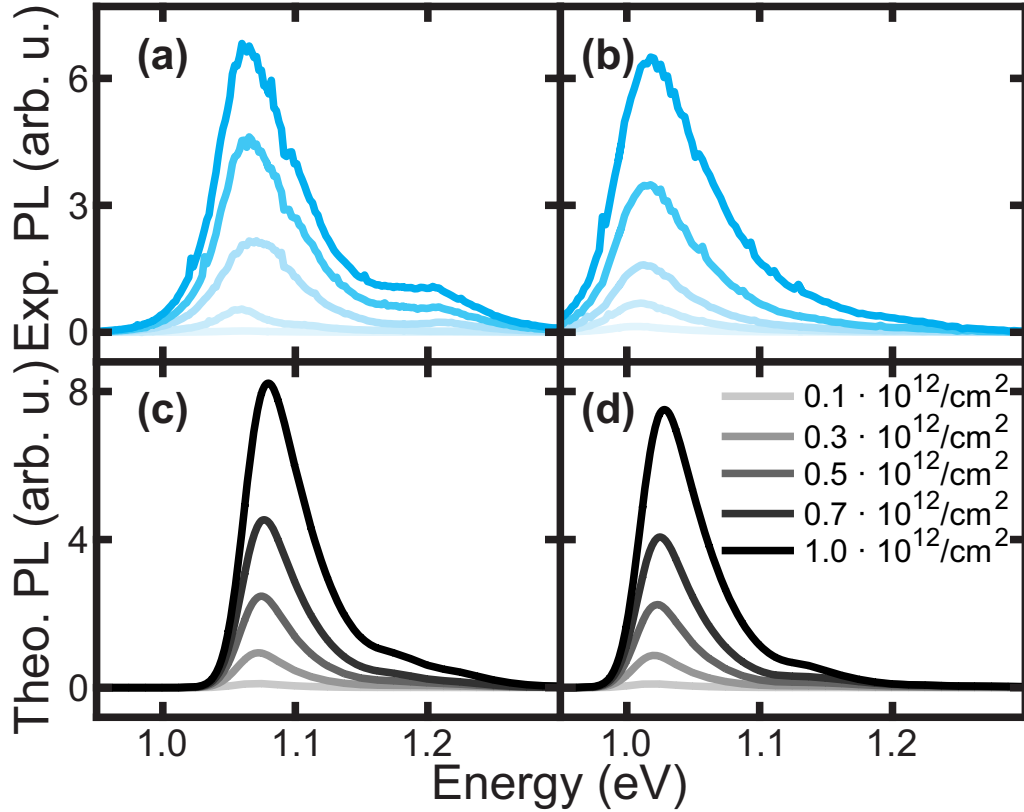


Figure 3.7: Experimental and theoretical PL spectra for samples #25987 (left column) and #25989 (right column). Experimental spectra (top row) were measured for increasing excitation powers (bright to dark) at room temperature. All theoretical spectra (bottom row) are calculated for charge carrier densities between $0.1 \cdot 10^{12}/\text{cm}^2$ (bright) and $1.0 \cdot 10^{12}/\text{cm}^2$ (dark) at 300 K and with an inhomogeneous broadening of 25 meV.

3.3.2 Prediction of Gain Properties

To intensify the analysis of the MQWHs, a calculation is performed to predict the material gain of both samples. This is a forecast on how well both material compositions perform as active medium in a VECSEL and which one is more preferable for the goal of near-infrared emission. Figure 3.8 presents the calculated material gain spectra of both samples. As presented earlier in Sec. 3.2 for the model system, increasing the charge carrier density leads to an increasing material gain. Sample #25989 shows a slightly higher gain at the same excitation strength compared to #25987. As for the PL peak positions, the increased Sb content shifts the gain peak position to lower energies for sample #25989 by 1.04 eV in comparison to 1.09 eV for sample #25987. The gain values reached for this excitation densities are as high as for the model system and thus also comparable to typical gain values for type-I systems [72, 83]. Therefore, the realized type-II “W”-MQWHs do not stand back from any point of view so far.

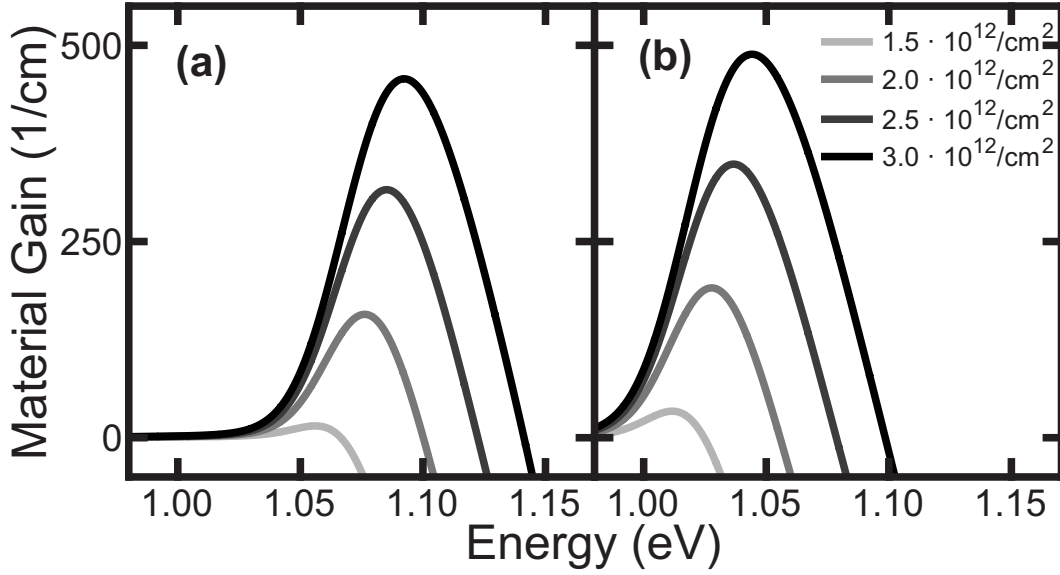


Figure 3.8: Calculated material gain spectra for (a) sample #25987 and (b) sample #25989. Charge carrier densities between $1.5 \cdot 10^{12}/\text{cm}^2$ (bright) and $3.0 \cdot 10^{12}/\text{cm}^2$ (dark) are plotted for a temperature of 300 K and an inhomogeneous broadening of 25 meV.

3.3.3 Excitonic Transitions

To further investigate the states involved in the emission of type-II “W”-structures, the theoretical results are compared to experimental measurements from PR spectroscopy [36] as presented in Paper [III]. A photomodulation of the band edges enables the measurement of a differential spectrum to visualize the oscillator strength of each transition. Hence, one is able to distinguish between type-II and type-I transitions and can analyze the origin of all emission, absorption, and gain signatures.

Figure 3.9 presents the PR measurements (solid lines) in direct comparison to the theoretical results (dotted lines) for both samples of Tab. 3.1. Information on the experiment can be found in Paper [III]. The calculations were done for room temperature conditions at 300 K and at a low charge carrier density of $1 \cdot 10^9/\text{cm}^2$. To take care of the excitation which induces the signatures to the differential spectrum, the band edges were varied by a minor increase of the temperature to 301 K. The inhomogeneous broadening was varied from 4 meV for the unexcited case up to 12 meV for the excited one to take care of excitation-induced dephasing. In addition to the PR spectra, the material absorption spectra are plotted to visualize the corresponding excitonic transitions.

All excitonic absorption features correspond very well to experimental PR signatures, which are reproduced in the calculated PR spectra. The vertical lines depict the single particle transition energies weighted by the dipole transition strength. They indicate which states are involved in a certain transition and how strong the transition

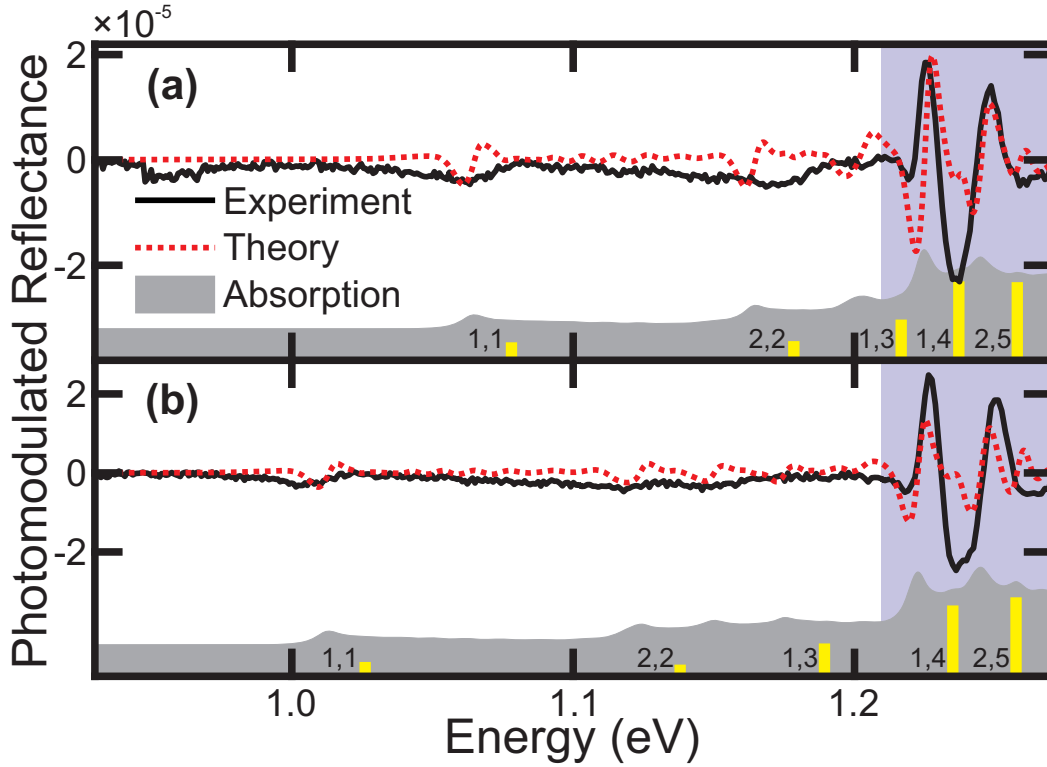


Figure 3.9: Experimental and theoretical PR spectra for samples (a) #25987 and (b) #25989. The experimental PR spectra (solid lines) are plotted together with the theoretical results (dotted lines). Vertical bars mark all single particle transitions between bound states weighted by their dipole transition strength. The labels contain the quantum numbers of the electron and hole state in between which the transition appears. Absorption spectra (shaded areas) are plotted for both samples.

is. This enables us to see that the first transitions, which are positioned below 1.2 eV, have smaller signatures in all spectra and are created by both the electron states e1 and e2 as well as the hole states h1 to h3.

To identify the type of the transitions, all signatures in the PR spectra with their energetic position are compared to the corresponding transition and their origin in the electronic structure of the system as presented in Fig. 3.10 for sample #25989. All bound states involved in type-II and type-I transitions within the spectral range of Fig. 3.9 are presented. From the spatial distribution, the transitions e1-h1, e2-h2, and e1-h3 are identified to be of type-II character, see Fig. 3.10 (a). Their electron states are confined within the (GaIn)As quantum wells while their hole states are confined in the Ga(AsSb) well. A transition between these states has to occur across the interface in between both materials. Contrary, Figure 3.10 (b) shows all wave functions involved in spatially direct transitions. All of them have their highest probability in the (GaIn)As well and a higher energy difference between their corresponding states.

Thus, all small signatures in the PR spectra, which are below 1.2 eV, originate from type-II transitions, while all type-I transitions are positioned energetically higher. Therefore, the spectra can be divided into two ranges, one having indirect transition and the other having direct transitions with the border at roughly 1.2 eV, emphasized by the background color in Fig. 3.9. Experimental and theoretical PR spectra present these ranges with the strong signature arising shortly after this border. Both samples show three type-II transitions, which have a different distance to the type-I range of the spectra. Type-II and type-I signatures of sample #25987 are really close to each other, whereas the type-II peak of #25989 is energetically lower and therefore separated from the direct range. All type-I transitions are quite similar for both samples as the (GaIn)As quantum-well configuration is nearly the same. Differences are primarily in the Sb content which induces changes especially to the energetic position of the type-II signatures. As the energetic positions are directly connected to the VBO of the Ga(AsSb) hole well and thus to the strength of the confinement of the holes, it is a direct measure of the Sb content.

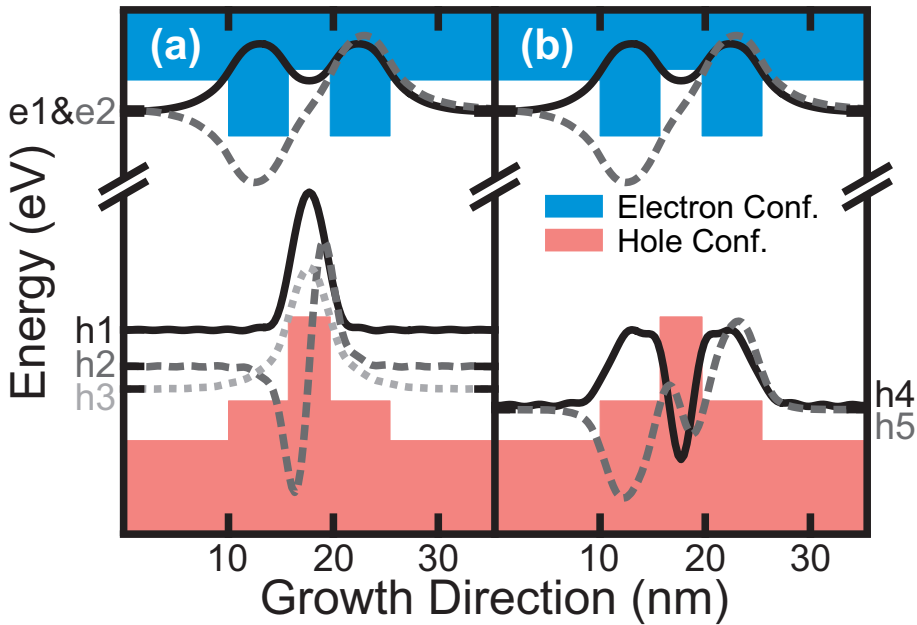


Figure 3.10: Confinement potential with electronic states for (a) type-II and (b) type-I transitions of sample #25989. The confinement potential (shaded areas) is plotted together with the electron and hole wave functions (lines) involved in the transitions of Fig. 3.9.

Overall, the comparison of experiment and theory shows a good reproduction of the peaks in the indirect range, while the direct range peaks are slightly off, especially in size. The reason is that in the experiment not all carriers are thermally distributed yet. All calculations are done using Fermi–Dirac distributions such that all carriers are already in thermal equilibrium. The correspondence between PR, absorption sig-

natures, and dipole transition strengths enables the identification of the transitions and label them as type-II and type-I. Hence, the electron- to hole-state transitions in the excitonic spectra are allocated and the Sb content is proven to be a valuable tool to alter the emission, i.e. an increase of the emission wavelength requires more Sb.

3.4 Investigation of a Type-II VECSEL

In the following, the investigated “W”-MQWH with its promising properties and predicted gain behavior is integrated as active region in a full VECSEL design. The growth of a working laser structure and its characteristics are presented in Papers [IV] and [V]. Here, the findings are summarized and some additional information is given about the analysis and optimization process of the VECSEL devices.

The active region was analyzed by a HR-XRD measurement and their nominal parameters are written in Tab. 3.2. In between each of the active regions, GaAs and Ga(AsP) barriers were implemented, as for the MQWHs presented in Sec. 3.3. Additionally, a (GaIn)P capping layer was added on one side of the chip, while on the other side an (AlGa)As/AlAs DBR was attached. A bond completes the VECSEL chip, further details can be found in Paper [IV].

VECSEL sample	(GaIn)As (nm)	In (%)	Ga(AsSb) (nm)	Sb (%)
#26371-2	5.5	20.3	4.0	19.8

Table 3.2: Composition of the active region in a grown VECSEL obtained by a HR-XRD measurement.

A good agreement is found comparing the VECSEL’s experimental edge PL with the calculations. The PL of sample #26371-2 is well reproduced with its emission slightly above 1200 nm and the gain prediction matches the peak power laser emission at 1182 nm, cf. Paper [IV]. Both properties are reproduced best by increasing the temperature above 300 K to take care for the higher pump intensity when measuring edge PL or laser emission.

3.4.1 Longitudinal Light Mode and Reflectivity

The complete investigation of a VECSEL goes further than only looking at the material properties of the RPG structure. For example, the resonance of the grown VECSELS is investigated by analyzing the longitudinal light modes propagating through the sample. Thereby, the light’s intensity at the position of the active regions is calculated. Additionally, the decay of the intensity and with this the reflection of the light at the DBR is verified. Here, the microscopic calculations for the change in material absorption and refractive index are used to calculate the light modes reflection via the transfer matrix method [20, 133]. In this manner, the wavelength of the VECSEL’s laser mode is distinguished in dependence on the charge carrier density.

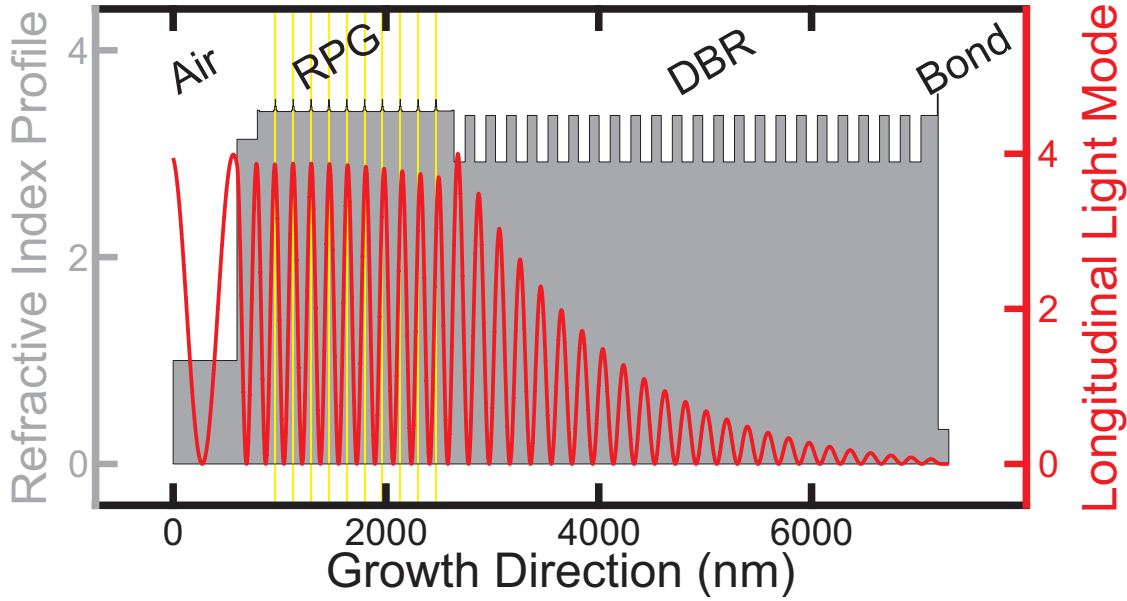


Figure 3.11: Longitudinal light mode intensity for 1171 nm (solid line) and the refractive index profile for the VECSEL sample #26371-2 (shaded area) are plotted at 300 K. The positions of the active regions in the RPG are highlighted by vertical lines.

The refractive index profile of VECSEL sample #26371-2 and the 1171 nm longitudinal light mode inside are plotted in Fig. 3.11. It is directly observable that the sample is resonant for the 1171 nm light mode because the standing wave has its maxima close to the positions of the active regions. Therefore, absorption and stimulated emission processes can happen with a high probability and efficiency. This structure is called a resonant setup, as no mismatch in detuning between the resonator and material gain is present. Laser emission from this sample was measured and presented in Papers [IV] and [V].

Spectrally resolved for all wavelengths, a filter function is defined to quantify the resonance properties of the cavity [134]. The definition of the filter function includes the intensity of the longitudinal light mode at the positions of the active regions in the RPG. A peak value of 4 is the maximum the filter function can reach as it is calculated for the in- and outward propagating light intensity.

Another quantity of interest is the total reflectivity of VECSEL chips. Experimental data in the form of a reflectivity spectrum was obtained for the unexcited sample #26371-2. Figure 3.12 compares the experimental reflectivity (shaded area) with the theoretically calculated spectra (solid lines) for no excitation up to gain conditions. Both unexcited spectra show a broad stop band, where ideally the laser mode should be placed centrally. The filter function peak and the absorption dip of both spectra show a good agreement in the position with the resonance around 1170 nm. In the computed curves, no peak arises right in the middle of the stop band as the excitation

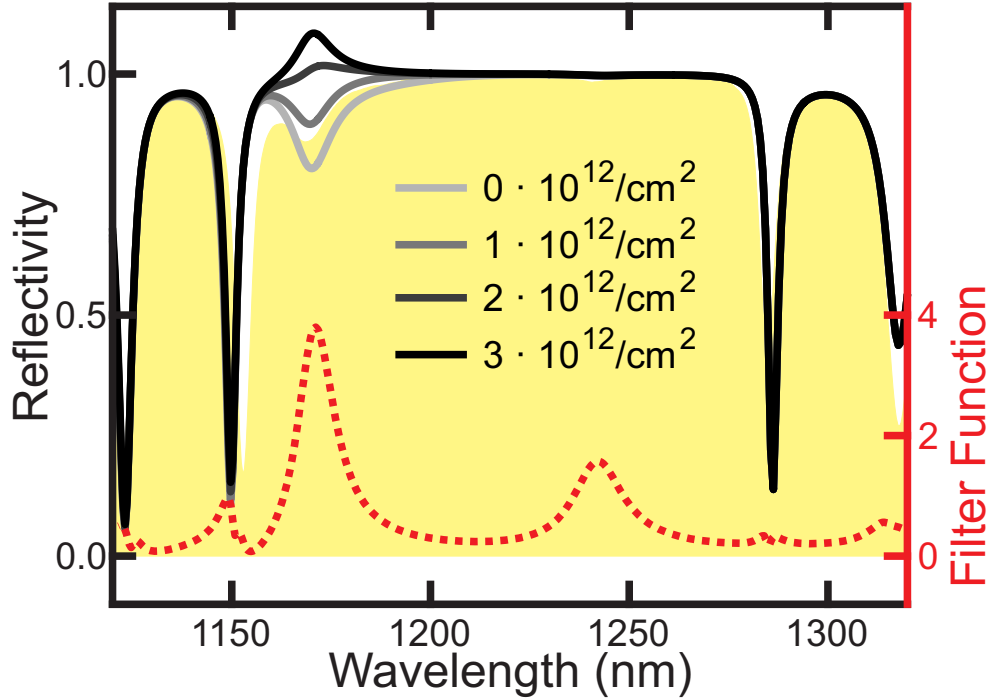


Figure 3.12: Experimental (shaded area) and theoretical (solid lines) reflectivity spectra and corresponding filter function (dotted line) at 300 K. The charge carrier density is varied between $0 \cdot 10^{12}/\text{cm}^2$ (bright) and $3 \cdot 10^{12}/\text{cm}^2$ (dark) and an inhomogeneous broadening of 20 meV is applied.

density is increased. Nevertheless, a laser mode around 1170 nm is predicted with the reflectivity rising to values higher than 1 at this position. This is in very good agreement with the experimentally found values ranging from 1173 nm up to 1183 nm in Paper [IV].

To further support this analysis, intensity dependent reflectivity measurements were performed in Ref. [VII]. It was confirmed that the laser mode is just at the edge of the stop band. The analysis in this Paper shows how the mode grows with excitation power.

3.4.2 Detuning and Modal Gain

Suggestions resulting from a theoretical analysis can be used to optimize the VECSEL structure. Therefore, it is very helpful to define quantities like the detuning between cavity resonance and the RPG's material gain maximum. The linkage of both brings up the modal gain of the system which highlights the amplification of material gain by the whole cavity. While the cavity resonance is presented in Paper [IV], the modal gain of sample #26371-2 is displayed in Ref. [VII] and presented in the following.

In comparison to the material gain of a semiconductor heterostructure, the modal gain also covers the influence of the cavity. It is a multiplication of material gain

and filter function and is influenced by the dependencies of both quantities. Therefore, it is reasonable to have a closer look at the temperature dependent shifts of both components of the modal gain. Both quantities have different shift rates as presented in Fig. 3.13 (a). The material gain (solid lines) and the filter function (dashed lines) are plotted having a charge carrier density of $2.0 \cdot 10^{12}/\text{cm}^2$ at 300 K (thin) and $2.5 \cdot 10^{12}/\text{cm}^2$ at 350 K (thick). It becomes clear that the material gain shifts faster with an increasing temperature even if the charge carrier density is increased. This suggests that with an increasing temperature, the gain outruns the cavity resonance and therefore no sufficient modal gain is present in sample #26371-2. Figure 3.13 (b) depicts the resulting modal gain for both cases. In direct comparison, for 300 K (thin) a more pronounced peak is present which is close to the peak position of the filter function. Meanwhile for 350 K (thick) the modal gain is smaller and decreases to zero as the sample's temperature is further increased.

From Fig. 3.13 it becomes clear that the peaks of the filter function and the material gain are not necessarily at the same position. Additionally, a different temperature dependence for both quantities is exposed. Thus, it is useful to specify a detuning between active material and cavity. To make this definition most general and practicable, the detuning is defined between the low-density PL of the semiconductor heterostructure and the resonance of the cavity. According to Ref. [131], a negative detuning,

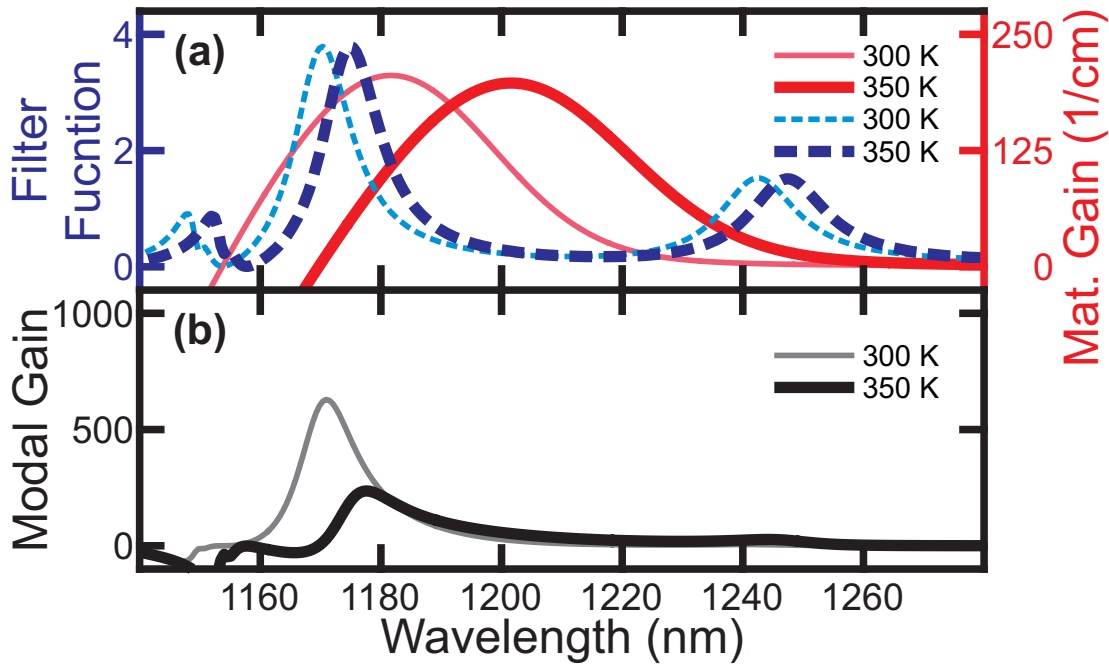


Figure 3.13: Modal gain properties of sample #26371-2. (a) Material gain (solid lines) and filter function (dashed lines) for 300 K (thin) and 350 K (thick), with carrier densities of $2.0 \cdot 10^{12}/\text{cm}^2$ and $2.5 \cdot 10^{12}/\text{cm}^2$ for 300 K and 350 K, respectively. (b) Resulting modal gain is plotted for both temperatures.

i.e. PL blue shifted to cavity, is needed for efficient laser operation in type-I systems. For a type-II setup instead, a positive detuning is preferable, as the material gain blue shifts when increasing the pump power, as explained in Sec. 3.2.1 and outlined in Papers [IV] and [V]. Nevertheless, even an increasing pump power together with a blue shift in the material gain can lead to an overall red shift of the modal gain. This case appears when keeping the temperature constant while the material gain amplitude increases faster than the overlap of cavity resonance and shifting material gain edge.

Corresponding to the previous result, the initial detuning between the low-density PL of the “W”-structure and the cavity resonance is an important quantity for VECSELs. This analysis suggests that for high power operation a situation is favorable where the gain is initially blue shifted in comparison to the cavity resonance. The overlap between both increases with increasing temperature and pump power, and therefore enables high power operation. For VECSEL #26371-2 a low threshold configuration is achieved as the experimental investigations in Paper [IV] confirm.

To demonstrate the low threshold behavior, a calculation of the modal gain in

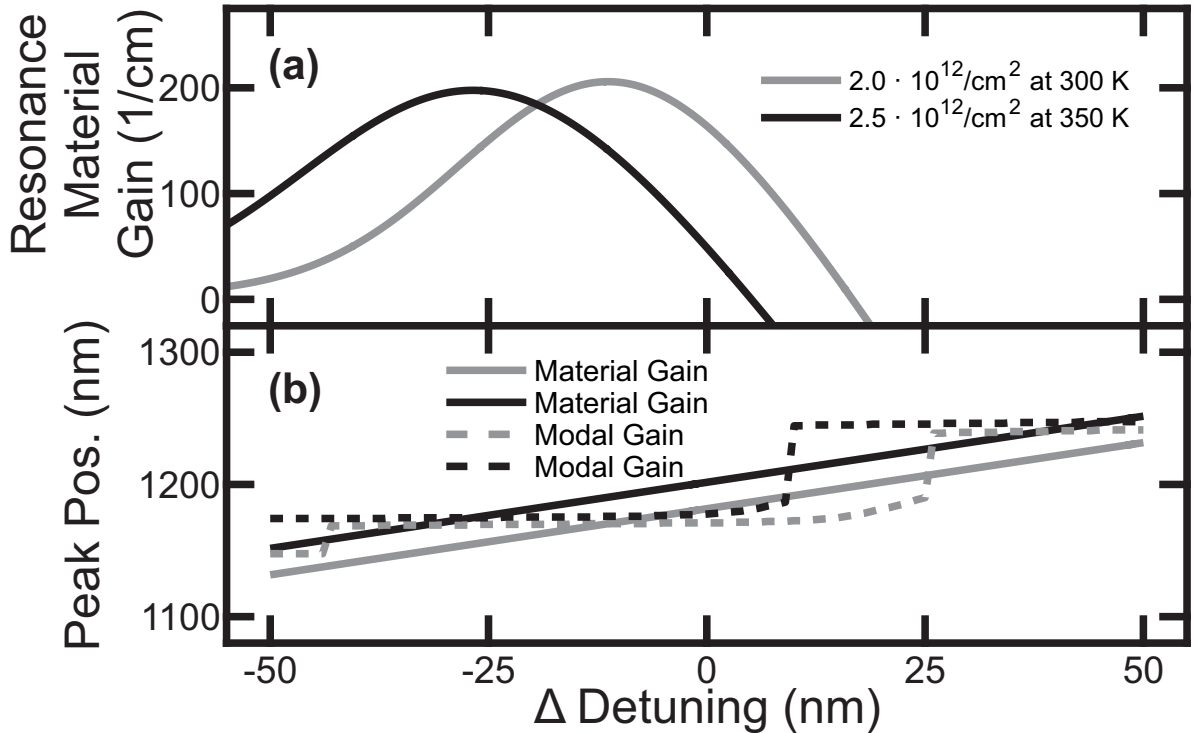


Figure 3.14: Effect of detuning change on modal gain. (a) Material gain value at the cavity resonance (peak position of the filter function) against an artificial change of the detuning. Carrier densities of $2.0 \cdot 10^{12}/\text{cm}^2$ (bright) and $2.5 \cdot 10^{12}/\text{cm}^2$ (dark) were assumed for 300 K and 350 K, respectively. (b) Corresponding material (solid lines) and modal (dashed lines) gain peak positions.

dependence of the detuning is performed. For this, the filter function is fixed, cf. Fig. 3.13 (a), but the spectral position of the material gain is shifted and thus the detuning altered. Figure 3.14 (a) shows the material gain value at the position of the cavity resonance in dependence of the detuning variation. A lowering of the detuning by 12 nm would be enough to maximize the overlap for 300 K (bright). At 350 K (dark) a decrease of the detuning by 27 nm is needed to increase the modal gain. Such a change would provide a higher threshold and high power operation would be possible. This observation underlines that a type-II laser with a low threshold is realized in sample #26371-2. In Fig. 3.14 (b) the material and modal gain peak positions are plotted against the change in detuning. Here, the system's laser mode follows the main cavity resonance for a wide range of detunings. A jump to another mode occurs at an increased detuning of +25 nm for 300 K or +10 nm for 350 K. Anyway, if the initial detuning between PL and the cavity resonance is too positive (PL peaks at higher wavelength than cavity resonance), there is no lasing on the main cavity resonance.

With this investigation of the detuning and the modal gain, sample #26371-2 is identified as a low-threshold device. For high-power operation a negative detuning, in other words an initial blue shift between PL and cavity resonance, is favorable as different shift rates as function of the temperature apply for the material gain and the cavity resonance. The peak material gain and the cavity resonance would match when increasing the temperature and the excitation density pumping the VECSEL.

3.5 Optimization Capabilities of Type-II Lasers

In contrast to optimizing growth conditions and properties like detuning, slight modifications to the material system can help to improve the laser performance, too. The most crucial property when looking at the RPG is by far the strength of the material gain at the desired emission wavelength. A simple approach is to change the In and Sb content or the size of the quantum wells, while keeping the emission wavelength constant. More sophisticated approaches are the optimization of the interfaces in between the quantum wells or the increase of the quantum confinement by a variation of the barrier material. These two approaches are presented in this section. In addition, an advance to emission wavelength around 1300 nm is discussed, as this would enable the use in optical data transfer.

3.5.1 Graded Interfaces

One possible field of optimization for the material gain strength are the interfaces in between the quantum wells and barriers. Implementing concentration gradients in the simulation of the interfaces enables realistic modeling in comparison to perfect abrupt interfaces which are not very likely to be found in the experiment [135].

Figure 3.15 (a) presents the confinement potentials of an approach to describe the interfaces with concentration gradients. All interfaces are described as linear gradients with length 1 nm in which the concentrations change between the layers. The effective

thickness of each layer is kept constant in comparison to the reference structure from Sec. 3.2. Analyzing the respective gain spectra in Fig. 3.15 (b), it is found that smoothing the interfaces raises the material gain in comparison to the reference with abrupt interfaces by 16%. This is explained by the increased wave function overlap as the innermost interfaces between the Sb and In containing wells are smoother.

In real grown structures the interfaces are far from being perfectly abrupt, thus 1 nm of intermixing between the different layer materials is a realistic approximation [135]. This investigation shows that it could be counterproductive to use perfectly smooth interfaces. In terms of maximizing the material gain, it would be way more worth it to search for a gradient which increases the wave function overlap.

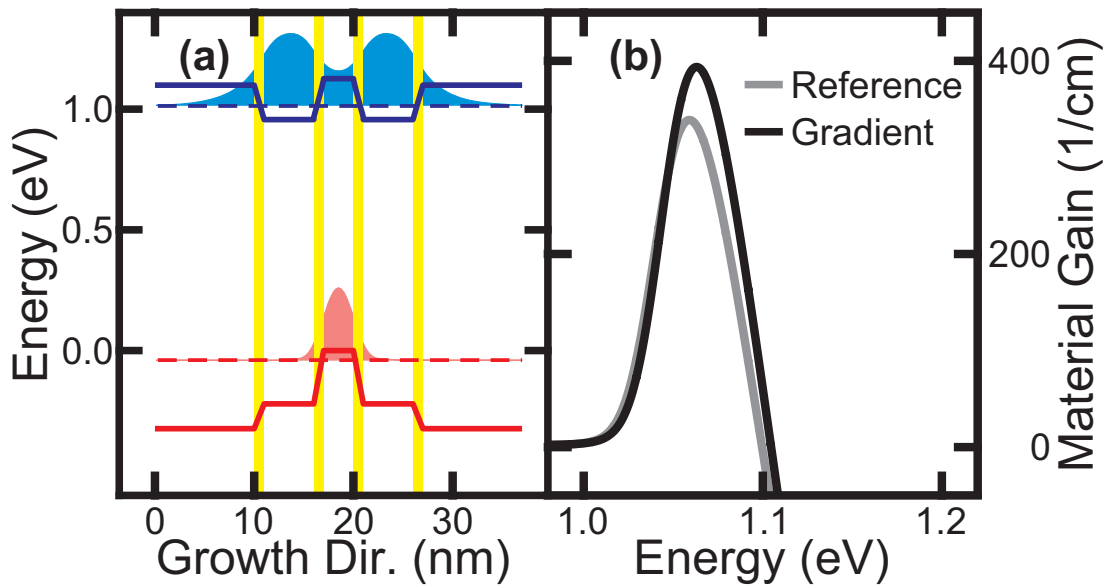


Figure 3.15: Effect of graded interfaces on material gain. (a) Confinement potential (solid lines), wave functions (shaded areas), and first electron and hole levels (dashed lines) are plotted for linear gradients (highlighted) at all interfaces. (b) Induced change to material gain at charge carrier density of $2.5 \cdot 10^{12}/\text{cm}^2$ at 300 K (dark) versus reference spectrum (light) of the structure with abrupt interfaces.

3.5.2 Barrier Height

The leakage of the carriers to the outside of the active region crucially depends on the barrier height. Optimization can either be done by using a different material for the barriers or adding only a few monolayers in between “W”-quantum well and barrier to increase the confinement of the wave functions in the active region.

Replacing GaAs as barrier material by (AlGa)As to increase the barrier height is the first approach. Second, a monolayer of Ga(AsP) is placed in between the In-containing

wells and the GaAs barriers. Both approaches are presented in Fig. 3.16 (a) and (b), respectively. For different Al concentrations of 3.5% and 7.0% it is found that a higher barrier increases the confinement and with this the maximum gain value for a given charge carrier density as shown in Fig. 3.16 (c). An even more drastic increase by 16% is achieved by adding Ga(AsP) monolayers in between the barriers and the “W”-region. The position of the gain maxima are not affected in both approaches in comparison to the reference. A natural limit to the Al concentration is given by the band gap of (AlGa)As, if the optical excitation of carriers is done by the use of an 808 nm pump laser.

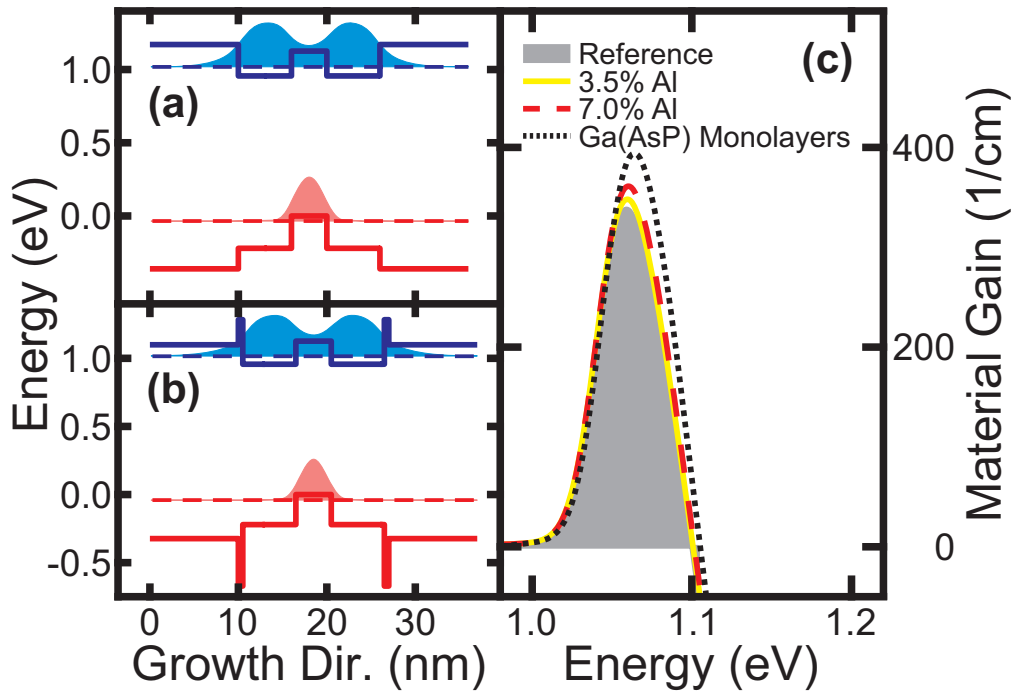


Figure 3.16: Variation of barrier materials. Confinement potentials (solid lines), wave functions (shaded areas), and the first electron and hole levels (dashed lines) for two exemplary barrier configurations with (a) (AlGa)As containing 7% Al and the other with (b) two monolayers of Ga(AsP) with 50% P in between barrier and “W”-region. (c) Calculated material gain for two different Al contents of 3.5% (solid line) and 7% (dashed line) in an (AlGa)As barrier, two monolayers of Ga(AsP) (dotted line) in between the barrier and the “W”-quantum well, and a reference (shaded area) using GaAs barriers for a charge carrier density of $2.5 \cdot 10^{12}/\text{cm}^2$ at a temperature of 300 K

3.5.3 1300 nm Emission Wavelength

So far all investigations were based on 1200 nm emission wavelength. They proved the (GaIn)As/Ga(AsSb)/GaAs material system as working active medium in VECSEL devices, cf. Papers [IV] and [V]. Even if an emission at 1200 nm is in the near-infrared regime, it can be viewed as a proof of principle and test of the material system. For applications in the optical data transfer, emission wavelength of 1300 nm or 1550 nm are needed. This investigation shall provide an idea on how the emission of a laser based on this material system can be tuned to 1300 nm. Therefore, three different suggestions are made with changes in the In and Sb content of the quantum wells.

Table 3.3 presents three suggestions which enable an laser emission around 1300 nm. These compositions of the active regions are all tuned to provide material gain close to 1300 nm as presented in Fig. 3.17. All suggestions have material gain spectra which peak around 0.95 eV, which is roughly 1300 nm, could be achieved. The gain value is highest for the High Sb approach and is of the same size as for the 1200 nm model system, cf. Fig. 3.3.

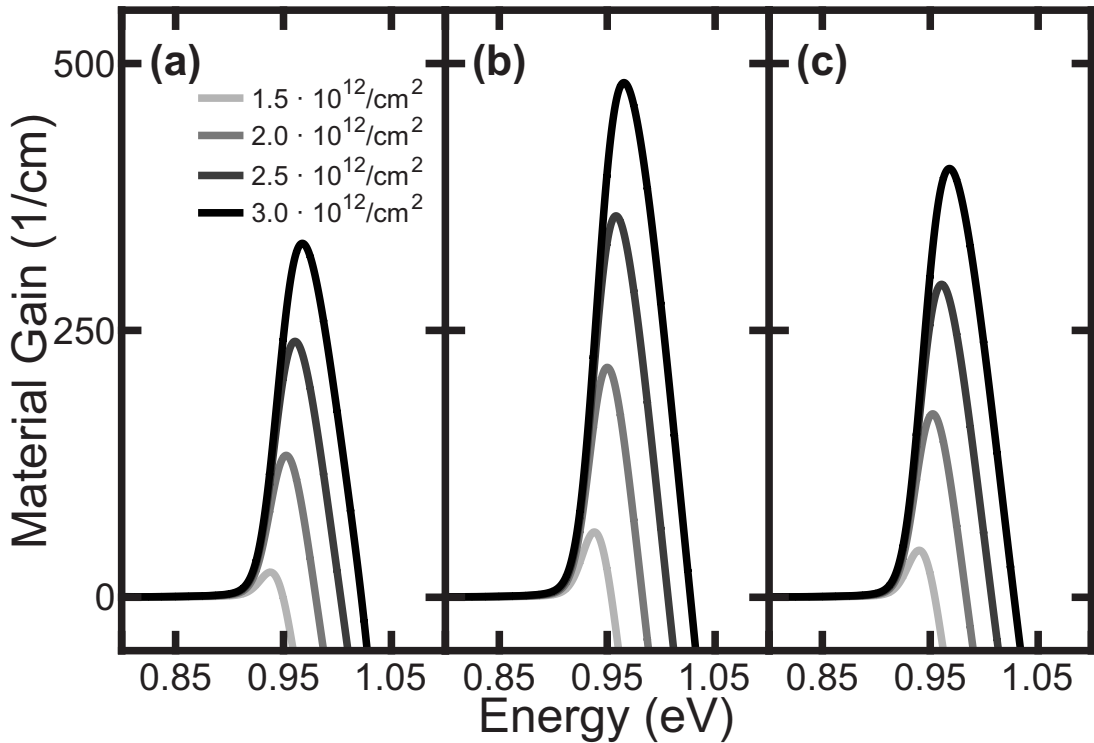


Figure 3.17: Material gain spectra for the 1300 nm suggestions (a) High In, (b) High Sb, and (c) Mix, calculated for carrier densities from $1.5 \cdot 10^{12}/\text{cm}^2$ (bright) to $3.0 \cdot 10^{12}/\text{cm}^2$ (dark) and a temperature of 300 K.

Another property which may change when going to longer emission wavelength is the detuning between the low-density PL emission and the material gain. Figure 3.18 presents a PL to gain maximum shift analysis, as performed for 1200 nm “W”-MQWHs

Name	(GaIn)As (nm)	In (%)	Ga(AsSb) (nm)	Sb (%)
High In	6	35	4	20.0
High Sb	6	20	4	28.5
Mix	6	26	4	25.0

Table 3.3: Quantum-well thickness and composition of “W”-MQWH design suggestions with a material gain tuned to a wavelength of 1300 nm.

in Sec. 3.2.1. The emission to gain shift is actually smaller than for the 1200 nm system. Without increasing the temperature a stronger shift to higher energies is present. This phenomenon was discussed in Sec. 3.2.1 as a consequence of the deformation of the confinement potential due to the presence of charge carriers. Increasing the temperature moves the gain to lower energies which enables an overall shift close to 0 eV for all three suggestions. They mainly differ in their peak height but not in their peak position.

It could be proven that in principle an emission of 1300 nm is achievable with the (GaIn)As/Ga(AsSb)/GaAs material system. All three suggestions are possible designs for a “W”-laser’s active region with 1300 nm emission wavelength and enable chances

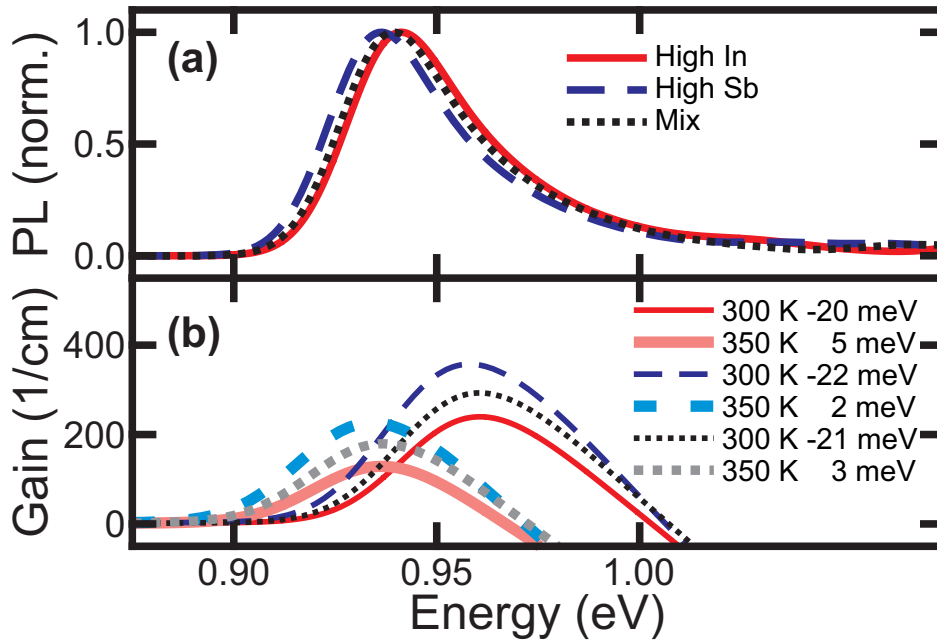


Figure 3.18: Detuning between PL and gain maximum for type-II 1300 nm suggestions. (a) PL spectra for High In (solid line), High Sb (dashed line), and Mix (dotted line) compositions at 300 K. (b) Corresponding material gain for 300 K (thin) and 350 K (thick). The shift of the peak positions is denoted in the legend.

3 Interface-Dominated Laser Structures

to use this material system in devices for optical communication.

Nonlinearities in Quantum-Dot Emission

Quantum-dot microcavities are a versatile system to investigate several quantum phenomena [27–34, 136] and semiconductor-based cavity quantum electrodynamics [20, 24, 26, 137, 138]. Additionally, they are used as laser systems [139–141] and applications like quantum-information processing [142]. As laser they show nearly thresholdless I/O characteristics under off-resonant excitation conditions [25, 143]. Comparable to the pumping into the barrier of the VECSEL structures presented in Sec. 3.4, the off-resonant excitation of quantum dots is done indirectly into the wetting layer and followed by a relaxation of carriers into the dots. Since laser emission produces the most classical form of light, namely the coherent state [144], the detection of new quantum phenomena is challenging. In this study, the excitation was done near-resonant, which disables inversion of the system and thus operation in the regime below lasing is present. Quantum-optical response theory [94] tells us that nonlinearities in the response to an optical excitation are a clear sign for the sensitivity of the matter to the exciting light’s quantum fluctuations.

In this chapter, I/O characteristics of semiconductor quantum dots under near-resonant excitation conditions is investigated by applying a systematic three-step approach to identify a new genuine quantum-optical effect, cf. Paper [I]. First, a nonlinearity in the I/O curves is extracted from the measured response, which were obtained by the group of M. Bayer at Technische Universität Dortmund. Second, the emission characteristics is modeled via a quantum theory which identifies the nonlinearity as a quantum-memory effect related to photon-density correlations. Third, the sensitivity to the quantum-optical properties of the exciting light field is discussed. Quantum-optical spectroscopy can make use of this sensitivity to manipulate the strength of the nonlinearities. This is beyond the scope of this Thesis, information on the results are published in Paper [I] and the technique is explained and applied in Refs. [145–149].

4.1 Extraction of Nonlinear Behavior

The experiments have been performed on self-assembled InP quantum dots in micro-ring cavities made of a 150 nm thick (GaIn)P waveguide [25, 143]. A dot density between $1 \times 10^9/\text{cm}^2$ and $2 \times 10^9/\text{cm}^2$ and a mean dot size of 75 nm is estimated. Because of such a large diameter, the dots host multiple electronic levels which are separated by 3 – 5 meV, and are extracted from the single-dot luminescence spectra in Ref. [25]. The samples were excited quasi-resonantly with a detuning of 30.7 meV above the main cavity mode but below the (GaIn)P band gap, using a laser emitting 2 ps long pulses. At the highest pump power, these pump pulses excite less than 0.26 electrons per electronic level, which is not near to inversion or lasing of the system, cf. Supplemental Material to Paper [I]. Hence, the main cavity mode emission is provided

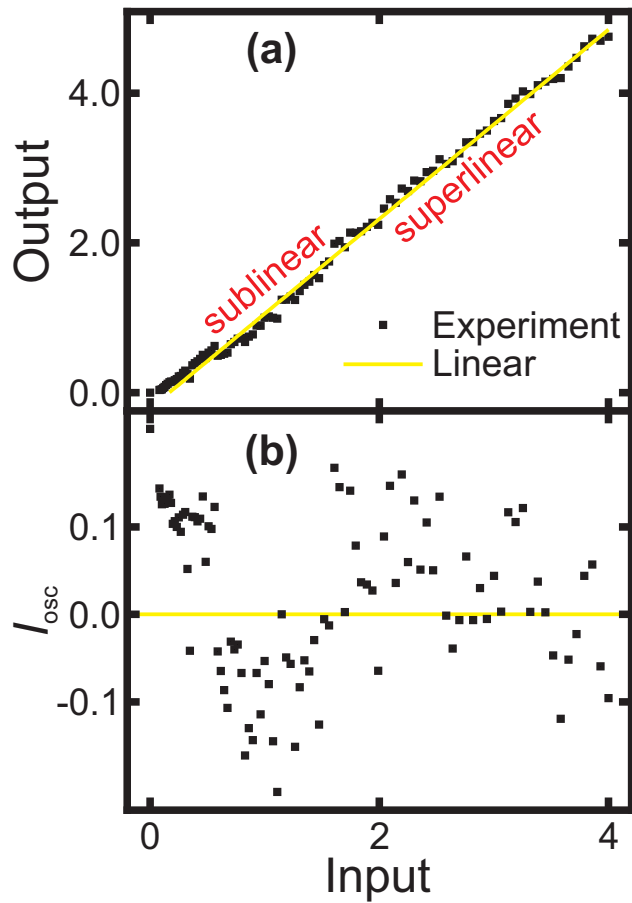


Figure 4.1: Nonlinear oscillations in experimental I/O characteristics. (a) Experimental I/O curve (squares) and linear output (solid line) are plotted. The powers are scaled to 1 at the first sublinear dip. (b) Difference between experiment and linear output, I_{osc} (squares), is presented as function of the input.

by a single dot, while other off-resonant dots contribute to the background emission. Further information on the experiment can be found in Paper [I].

As first step of the systematic three-step approach, the experimental I/O characteristics (squares) for the main cavity mode are presented in Fig. 4.1 (a). Comparing them with a perfect linear output (solid line) reveals an oscillating behavior with sub- and superlinear segments in the emission. By plotting the difference between the experimental I/O curve and the linear output, I_{osc} , Fig. 4.1 (b) highlights the nonlinear oscillation of the quantum-dot emission. It dips at the first minimum by more than 10% of its output power, which exceeds significantly the noise level of 6%. This analysis can be performed with an arbitrary linear output, as the subtraction of a line will only remove linear contributions and never higher orders like the oscillatory nonlinearities. Robustness of the extraction method and the reproducibility with different quantum dots, excitation conditions, and cavity modes are confirmed in the Supplemental Material to Paper [I].

4.2 Modeling and Identification of Sources to Quantum-Dot Emission

The second part of the three-step approach is to model and explain the origin of the experimental observations. For the calculation of the quantum-dot emission properties, the extended JCM presented in Sec. 2.1 is applied. To reproduce the experimental results best, the following parameters are chosen, which are based on the experiment. According to the experimental observations, four quadratically distributed electronic states with a detuning between 2 meV and 8 meV are included. Fully converged results are achieved by including 12 Fock states in the computation. A light-matter coupling strength of $\hbar g = 0.405$ meV is assumed which agrees with typical values for Rabi splitting in comparable quantum-dot experiments [24]. The 2 ps-long pump pulse is set to a detuning of $\hbar\Delta_L = \hbar(\omega_L - \omega_q) = 30.7$ meV with respect to the main cavity mode. Dissipation processes implemented via the Lindbladians in the Liouville-von Neumann equations, Eq. (2.7), are chosen to have a 0.8 ps cavity-photon lifetime and decay times for polarization and occupation of 2.1 ps, each. These lifetimes correspond to $\hbar\kappa = 0.8$ meV and $\hbar\gamma = 0.32$ meV. All values are close to parameters extracted from other experiments [25, 33, 143] and reproduce the emission characteristics.

With this full set of physical parameters the dynamics of the system is solved. The pump amplitude defines the input intensity, $I_{\text{in}} \propto \int |\alpha(t)|^2 dt$, and the photon count inside the cavity defines the output, $I_{\text{out}} \propto \langle B^\dagger B \rangle = \text{Tr} [B^\dagger B \rho]$. For an appropriate comparison to the nonlinear experimental emission, a linear fit with the same slope as for the linear output in Fig. 4.1 (a) is subtracted to obtain I_{osc} , see Supplemental Material of Paper [I] for details. The computed input is scaled to match the experiment at the first sublinear dip. By this the I/O scales are not altered and the oscillations in experiment and theory are qualitatively comparable.

Figure 4.2 (a) presents the resulting I_{osc} for a 2 ps-long pulsed (solid line) and cw

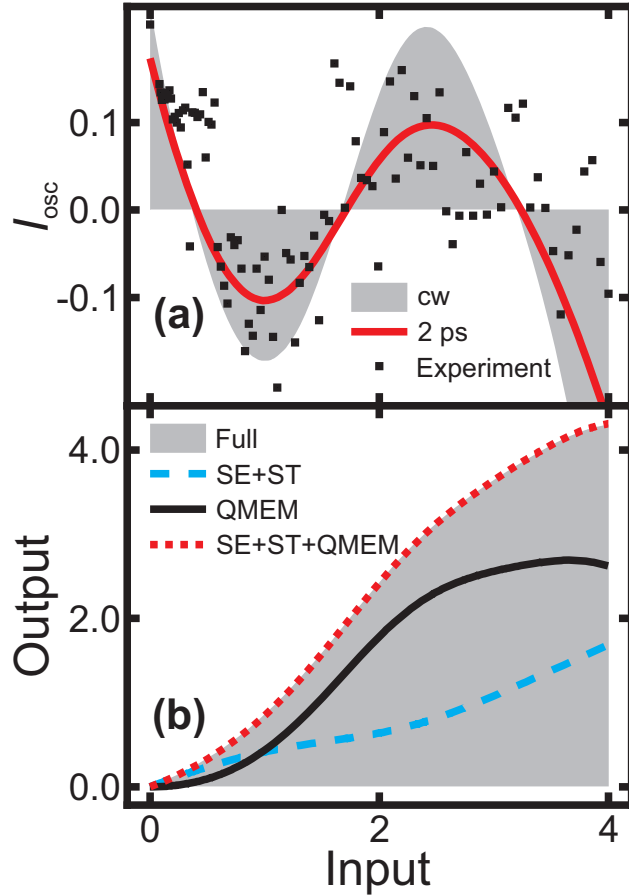


Figure 4.2: Computed I/O oscillations. (a) Difference between experimental and linear output, I_{osc} (squares), is plotted against the input together with computed I_{osc} using a cw (shaded area) and a 2 ps-long pulsed (solid line) excitation. The powers are scaled the same way as in Fig. 4.1. (b) Computed I/O responses using cw excitation. Full model (shaded area) is compared with the emission stemming from the sum of the SE and ST source (dashed line), the QMEM source only (solid line), and the sum of SE, ST, and QMEM source (dotted line).

(shaded area) excitation which are compared to the experimental result (squares). The nonlinear behavior from the experiment is reproduced under both excitation conditions. To show the robustness of this computational results, the laser-cavity detuning, the number of states included, and the pulse duration are varied and analyzed in the Supplemental Material to Paper [I]. It is found that increasing the detuning yields an increase in the size of the sublinear dip, which can be attributed to an higher effective Rabi frequency as explained later in Sec. 4.3. The nonlinear oscillations are found to be slightly, but not critically, dependent on the number of states N included. For the pulse duration, an asymptotical trend towards the cw result is found. A 2 ps-long

pulsed excitation is already sufficiently long to approach the cw result. This is also of interest for further investigations of the nonlinear behavior's origin, as they become significantly simpler if a cw excitation can be assumed.

An identification of the sources to the quantum-dot emission, especially of the nonlinear behavior, is done by deriving the steady-state solution of the photon flux $\Delta\langle B^\dagger B \rangle$. It can be written in terms of the cluster-expansion approach [20, 22], $\Delta\langle B^\dagger B \rangle = \langle B^\dagger B \rangle - |\langle B \rangle|^2$, to be the pure correlated part of the total photon number. The output intensity can be obtained via [I]

$$\frac{\partial}{\partial t} \Delta\langle B^\dagger B \rangle = -2\kappa \Delta\langle B^\dagger B \rangle - 2g \sum_{n=1}^N \text{Im}[\Pi_{-,n}], \quad (4.1)$$

containing the cavity-photon dephasing constant κ and the light-matter coupling constant g . It is driven by the photon-assisted polarizations $\Pi_{-,n} = \Delta\langle B^\dagger P_n \rangle$. The dynamics of the photon-assisted polarizations follow from [I]

$$i \frac{\partial}{\partial t} \Pi_{-,n} = [\delta_n - i(\gamma + \kappa)] \Pi_{-,n} + s_n^{\text{SE}} + s_n^{\text{ST}} + s_n^{\text{QMEM}} + s_n^{\text{tri}}, \quad (4.2)$$

and contain four different source terms. First, the spontaneous-emission (SE) source $s_n^{\text{SE}} = g \sum_{n'=1}^N [\langle P_{n'}^\dagger P_n \rangle - \langle P_{n'}^\dagger \rangle \langle P_n \rangle]$, which is non-vanishing, if at least one state is excited. Spontaneous emission also enables the second source, stimulated emission (ST), $s_n^{\text{ST}} = 2g \langle P_{z,n} \rangle \Delta\langle B^\dagger B \rangle$. It is a product of the population inversion and the photon correlations, and therefore scales with the amount of photons inside the cavity. The third source term generates a quantum-memory (QMEM) contribution via $s_n^{\text{QMEM}} = \Omega \Pi_{z,n}$, including a product of the Rabi frequency $\Omega = 2(g\langle B \rangle + \frac{\alpha_L(t)}{\hbar})$ and the photon-density correlation $\Pi_{z,n} = \Delta\langle B^\dagger P_{z,n} \rangle$. Here, the photon-density correlation stores the dependence of excitation and emitted photons, and therefore gives rise to a quantum memory. As fourth, three-particle correlations, $s_n^{\text{tri}} = 2g \Delta\langle B^\dagger B P_{z,n} \rangle$, contribute to the photon-assisted polarizations.

By integrating Eq. (4.2), an exact solution for the dynamics of the photon-assisted polarizations is found,

$$\Pi_{-,n}(t) = -i \int_{-\infty}^t dt' [s_n^{\text{ST}}(t') + s_n^{\text{QMEM}}(t') + s_n^{\text{SE}}(t') + s_n^{\text{tri}}(t')] e^{-i[\delta_n - i(\gamma + \kappa)](t-t')}. \quad (4.3)$$

It is inserted directly into Eq. (4.1) to obtain

$$\frac{\partial}{\partial t} \Delta\langle B^\dagger B \rangle = 2g \int_{-\infty}^t dt' \text{Re}[S(t, t')] - 2\kappa \Delta\langle B^\dagger B \rangle, \quad (4.4)$$

where all source terms are collected in

$$S(t, t') = S^{\text{SE}}(t, t') + S^{\text{ST}}(t, t') + S^{\text{QMEM}}(t, t') + S^{\text{tri}}(t, t'). \quad (4.5)$$

The individual sources can be accessed via $S^{\text{type}}(t, t') = \sum_n s_n^{\text{type}}(t') e^{-i[\delta_n - i(\gamma + \kappa)](t - t')}$, where type refers to SE, ST, QMEM, or tri. In a steady-state solution of Eq. (4.4) the emission is found to be

$$\Delta \langle B^\dagger B \rangle = \frac{g}{\kappa} \sum_{n=1}^N \text{Im} \left[\frac{s_n^{\text{SE}} + s_n^{\text{ST}} + s_n^{\text{QMEM}} + s_n^{\text{tri}}}{\delta_n - i(\gamma + \kappa)} \right]. \quad (4.6)$$

For this relation a switch-off analysis can be performed to highlight the strength of the different contributions in the overall emission. This analysis is simpler for cw excitation conditions since here Eqs. (4.2) and (4.4) require no integration.

Figure 4.2 (b) presents the switch-off analysis for the different source terms. A computation of I_{out} including all terms (shaded area) is compared to emission from only SE and ST terms (dashed line), emission of SE, ST, and QMEM terms (dotted line), and emission contributed by the QMEM term (solid line). The sum of SE and ST sources shows a monotonically increasing output, which becomes linear for high input powers and is not even half of the size of the full computation. Adding the QMEM contributions, leads to an almost perfect agreement with the full result. Thus, the three-particle correlations have only a minor effect in this regime and can be neglected. The emission from the QMEM source alone shows an oscillation comparable to the nonlinear behavior of the full result. Thus, the nonlinearity can be identified as genuine quantum-memory effect, altering the emission properties.

4.3 Quantum-Optical Sensitivity

As third step of the systematic three-step approach, the quantum-optical sensitivity of the nonlinearities found is demonstrated. Furthermore, the identified quantum-memory effect is discussed.

As worked out in Eq. (4.2), the quantum-memory term contains the Rabi frequency Ω and the photon-density correlation $\Pi_{z,n}$. An intuitive explanation of their contributions to the nonlinear behavior is found in the time domain. The exciting pump generates detuned Rabi oscillations in the quantum dot, which either favor the emission at the peak of the dot excitation or inhibit emission at the dip. Rabi oscillations in the dot contribute to emission processes but also build up quantum-memory contributions to remember excitations earlier in time. This quantum memory involves photons and the oscillating quantum-dot excitation accumulates photon-density correlations. These correlations are nonlinear as function of the pump intensity. Therefore, quantum-memory effects have to be nonlinear in the I/O characteristics.

An analysis of the source terms of the quantum-memory contribution exhibits the quantum-optical sensitivity beyond the dependence on detuned Rabi oscillations and

pump power. The exact dynamics of $\Pi_{z,n}$ is [I]

$$\begin{aligned} i\frac{\partial}{\partial t}\Pi_{z,n} = & -i(\kappa + 2\gamma_a)\Pi_{z,n} + g(\Delta\langle B^\dagger B^\dagger\rangle\langle P_n\rangle - \Delta\langle B^\dagger B\rangle\langle P_n^\dagger\rangle) \\ & + g\sum_{n'}(\langle P_{n'}^\dagger P_{z,n}\rangle - \langle P_{n'}^\dagger\rangle\langle P_{z,n}\rangle) + \frac{\Omega^*\Pi_{-,n} - \Omega\Pi_{+,n}}{2} \\ & + g[\Delta\langle B^\dagger B^\dagger P_n\rangle - \Delta\langle B^\dagger B P_n^\dagger\rangle]. \end{aligned} \quad (4.7)$$

Thus, photon-density correlations are build up by the simultaneous presence of squeezing $\Delta\langle B^\dagger B^\dagger\rangle$ and polarization, as observed from the second term in Eq. (4.7). Furthermore, the third term forms whenever the system has polarization or coherent $\langle P_{n'}^\dagger P_{z,n}\rangle$ contributions. The other source terms need coherences to be non-vanishing as well. Hence, it is clear that the generation of quantum-memory correlations has two main contributors, pure coherence and a combination of squeezing and polarization.

To complete this final step of the three-step approach, quantum-optical spectroscopy [145] is applied which uses the light source's quantum statistics to characterize and control the quantum-dot emission. This enables a spectroscopic analysis with excitations which are not available in present-day experiments, due to the lack of free adjustable quantum-optical light sources. This method has been applied in Paper [I] and in Refs. [149, 150], and will not be explained in detail within the scope of this Thesis. Anyway, the results show that a squeezed light field or one with and without coherences can be used to control the strength of the nonlinear oscillations.

In conclusion, this investigations revealed unexpected oscillations in the I/O curve of quantum dots in a micro-cavity. These oscillations could be identified as a quantum-memory effect by the use of a fully quantum-optical approach. They are driven by photon-density correlations which record emission processes during the excitation of the quantum dot and thus induce nonlinearities to the I/O curve. Additionally, their sensitivity to coherences and squeezing in the pump light field's quantum fluctuations could be shown.

Conclusion

This Thesis summarizes and partially extends the findings from several papers on interface-dominated laser structures and quantum-dot emission characteristics. In these investigations, the aim was to assess the macroscopic properties of both systems by two fully microscopic theories. Therefore, Chapter 2 provides an overview of an extended JCM which is used to model quantum-dot microcavities. Moreover, the well-established SBEs and SLEs are reviewed with the aim to determine the optical properties of type-II semiconductor heterostructures. Both theoretical approaches are applied to perform detailed experiment–theory comparisons in order to increase the physical understanding of novel semiconductor laser material systems.

The main goal of Chapter 3 is to evaluate a novel type-II laser material system and to systematically compare the properties of a type-II band aligned “W”-MQWH arrangement to ordinary type-I systems. Furthermore, all calculations are compared to experimental results for “W”-MQWHs and a type-II based VECSEL. Starting with the concept of a “W”-arranged MQWH, a model system is suggested by theoretical calculations. The systematic comparison to type-I systems reveals a more temperature stable and broader material gain for type-II systems. A more significant finding of this study is that type-II systems have a different sensitivity to increased charge carrier densities. Their material gain shifts to higher energies due to a deformation of the confinement potential induced by an increased charge carrier density in charge separated structures. Besides these fundamental investigations, experimental realization and characterization of “W”-MQWHs are compared to numerical results. In conclusion, they are found to be promising candidates for the use as active medium of a laser, e.g a VECSEL, cf. Papers [II] and [III]. Thus, a “W”-VECSEL was designed, realized, and examined, experimental results are presented in Papers [IV] and [V]. Additionally, a thorough analysis of the VECSEL properties is performed by applying the microscopic theory. A resonant emission around 1180 nm is found which corresponds to the experimental findings. Systematic investigations of the detuning and the modal gain show that a low-threshold laser was built. As type-I systems at 1180 nm [37] exceed output powers of 20 W, compared to 4 W found for the “W”-VECSEL [IV], a more negative detuning is suggested to enable high-power operation for this class of lasers. In the

last part of Chapter 3 possible optimizations of the structural design are discussed. Besides the detuning, which allows to create devices for specific power ranges, this is a versatile approach to increase the material gain. It is found that graded interfaces increase the wave function overlap and thus lead to a 10 % higher gain. Barrier heights are another promising tool to adjust the strength of the gain through a change of the carrier confinement. Last, three possibilities are presented to tune the laser emission to 1300 nm based on the (GaIn)As/Ga(AsSb)/(GaIn)As/GaAs material system. From the calculated suggestions, an increase of the Sb content to 28.5 % is most favorable as it produces the highest material gain at 1300 nm.

A natural progression of this work is to analyze the interfaces using scanning transmission electron microscopy and define the interface roughness and concentration gradients under the growth conditions used. Hence, an optimization of the carrier confinement through variation of growth conditions could be performed. As presented in Paper [VI], edge-emitting lasers were fabricated using this material system recently. They performed well in all investigations and can also be subject of an optimization process. Aiming for devices operating at the telecom wavelengths, the efforts on design suggestions for an emission wavelength of 1300 nm should be intensified. Especially in terms of an increased Sb content, where the hole well's confinement potential gets deeper, the carrier capture dynamics should be studied. Overall, 1300 nm are a realistic goal for this material system, despite having options like incorporating N to the electron wells to reduce the type-II transition energy [38–41]. The even longer 1550 nm telecom wavelength was already investigated in Refs. [40, 42, 43], and seems unlikely to be reachable for the material system discussed in the scope of this Thesis. To the best of my knowledge no type-II device based on the (GaIn)(NAs)/Ga(AsSb)/(GaIn)(NAs)/GaAs material system was produced so far. Nevertheless, type-I 1550 nm devices suffer from heat load [44] and thus it is desirable to have type-II systems as an alternative.

In the second part of this Thesis nonlinear oscillations in the emission of quantum-dot microcavities are studied as presented in Paper [I]. Chapter 4 starts from the experimental I/O curve, which reveals intriguing oscillations in the non-lasing emission of quantum-dot microcavities. An extended JCM reproduces the oscillations and identifies them as quantum-memory effect, which builds up through prior emission and absorption events. It is found that this quantum-memory can be described by photon-density correlations through detuned Rabi flopping. Additional investigations find a sensitivity of the system to quantum-optical fluctuations of the exciting light. They can be used to alter the strength of the nonlinear response by the use of quantum-optical spectroscopy. Even as nowadays no light sources with arbitrary tunable quantum fluctuations are available in experiments, such excitations could be used to control the nonlinear behavior and investigate this effect further.

Overall, two semiconductor laser material systems were studied using microscopic quantum theories. The application of the different theories forms a powerful toolkit, which develops its strength during intense experiment–theory collaborations. It provides immediate feedback on structural information of grown samples and enables the forecast of material properties due to structural changes.

Bibliography

- [1] A. G. Bell, “Selenium and the Photophone”, *Nature* **22**, 500–503 (1880).
- [2] G. P. Agrawal, *Fiber-Optic Communication Systems* (John Wiley & Sons, Nov. 2010).
- [3] J. J. Coleman, “The development of the semiconductor laser diode after the first demonstration in 1962”, *Semiconductor Science and Technology* **27**, 090207 (2012).
- [4] M. Kuznetsov, F. Hakimi, R. Sprague, and A. Mooradian, “High-power (>0.5 -W CW) diode-pumped vertical-external-cavity surface-emitting semiconductor lasers with circular TEM₀₀ beams”, *IEEE Photonics Technology Letters* **9**, 1063–1065 (1997).
- [5] A. C. Tropper, H. D. Foreman, A. Garnache, K. G. Wilcox, and S. H. Hoogland, “Vertical-external-cavity semiconductor lasers”, *Journal of Physics D: Applied Physics* **37**, R75–R85 (2004).
- [6] U. Keller, and A. C. Tropper, “Passively modelocked surface-emitting semiconductor lasers”, *Physics Reports* **429**, 67–120 (2006).
- [7] J. E. Hastie, L. G. Morton, A. J. Kemp, M. D. Dawson, A. B. Krysa, and J. S. Roberts, “Tunable ultraviolet output from an intracavity frequency-doubled red vertical-external-cavity surface-emitting laser”, *Applied Physics Letters* **89**, 061114 (2006).
- [8] S. Calvez, J. E. Hastie, M. Guina, O. G. Okhotnikov, and M. D. Dawson, “Semiconductor disk lasers for the generation of visible and ultraviolet radiation”, *Laser & Photonics Review* **3**, 407–434 (2009).
- [9] M. Scheller, J. M. Yarborough, J. V. Moloney, M. Fallahi, M. Koch, and S. W. Koch, “Room temperature continuous wave milliwatt terahertz source”, *Optics Express* **18**, 27112–27117 (2010).

- [10] E. Murphy, “The semiconductor laser: Enabling optical communication”, *Nature Photonics* **4**, 287–287 (2010).
- [11] A. D. Andreev, and E. P. O’Reilly, “Theoretical study of Auger recombination in a GaInNAs 1.3 μm quantum well laser structure”, *Applied Physics Letters* **84**, 1826–1828 (2004).
- [12] A. R. Adams, M. Silver, and J. Allam, “Semiconductor Optoelectronic Devices”, in *High pressure in semiconductor physics ii* (Elsevier, 1998), pp. 301–352.
- [13] S. J. Sweeney, A. R. Adams, M. Silver, E. P. O’Reilly, J. R. Watling, A. B. Walker, and P. J. A. Thijs, “Dependence of Threshold Current on QW Position and on Pressure in 1.5 μm InGaAs(P) Lasers”, *Physica Status Solidi (b)* **211**, 525–531 (1999).
- [14] T. R. Chen, W. Hsin, and N. Bar-Chaim, “Very high power InGaAsP/InP distributed feedback lasers at 1550 nm wavelength”, *Applied Physics Letters* **72**, 1269–1271 (1998).
- [15] B. Chen, W. Wang, X.-J. Wang, J.-Y. Zhang, and Z. Fan, “A Novel 1.3- μm High T_0 AlGaInAs/InP Strained-Compensated Multi-Quantum Well Complex-Coupled Distributed Feedback Laser Diode”, *Japanese Journal of Applied Physics Part 2-Letters* **38**, 5096–5100 (1999).
- [16] M. Peter, K. Winkler, M. Maier, N. Herres, J. Wagner, D. Fekete, K. H. Bachem, and D. Richards, “Realization and modeling of a pseudomorphic $(\text{GaAs}_{1-x}\text{Sb}_x-\text{In}_y\text{Ga}_{1-y}\text{As})/\text{GaAs}$ bilayer-quantum well”, *Applied Physics Letters* **67**, 2639–2641 (1995).
- [17] G. G. Zegrya, and A. D. Andreev, “Mechanism of suppression of Auger recombination processes in type-II heterostructures”, *Applied Physics Letters* **67**, 2681–2683 (1995).
- [18] G. G. Zegrya, and A. D. Andreev, “Theory of the recombination of nonequilibrium carriers in type-II heterostructures”, *Journal of Experimental and Theoretical Physics* **82**, 328–340 (1996).
- [19] H. Haug, and S. W. Koch, *Quantum Theory of the Optical and Electronic Properties of Semiconductors* (World Scientific Publishing Company Incorporated, Jan. 2009).
- [20] M. Kira, and S. W. Koch, *Semiconductor Quantum Optics* (Cambridge University Press, Nov. 2011).
- [21] L. De Caro, C. Giannini, and L. Tapfer, “Determination of the lattice strain and chemical composition of semiconductor heterostructures by high-resolution x-ray diffraction”, *Journal of Applied Physics* **79**, 4101–4110 (1996).
- [22] M. Kira, and S. W. Koch, “Many-body correlations and excitonic effects in semiconductor spectroscopy”, *Progress in Quantum Electronics* **30**, 155–296 (2006).

- [23] W. W. Chow, and F. Jahnke, “On the physics of semiconductor quantum dots for applications in lasers and quantum optics”, *Progress in Quantum Electronics* **37**, 109–184 (2013).
- [24] G. Khitrova, H. M. Gibbs, M. Kira, S. W. Koch, and A. Scherer, “Vacuum Rabi splitting in semiconductors”, *Nature Physics* **2**, 81–90 (2006).
- [25] Y. Chu, A. M. Mintairov, Y. He, J. L. Merz, N. A. Kalugnyy, V. M. Lantratov, and S. A. Mintairov, “Lasing of whispering-gallery modes in GaInP waveguide micro-discs and rings with InP quantum dots”, *Physica Status Solidi (c)* **8**, 325–327 (2010).
- [26] K. Hennessy, A. Badolato, M. Winger, D. Gerace, M. Atatüre, S. Gulde, S. Fält, E. L. Hu, and A. Imamoglu, “Quantum nature of a strongly coupled single quantum dot–cavity system”, *Nature* **445**, 896–899 (2007).
- [27] T. Yoshie, A. Scherer, J. Hendrickson, G. Khitrova, H. M. Gibbs, G. Rupper, C. Ell, O. B. Shchekin, and D. G. Deppe, “Vacuum Rabi splitting with a single quantum dot in a photonic crystal nanocavity”, *Nature* **432**, 200–203 (2004).
- [28] J. P. Reithmaier, G. Sek, A. Löffler, C. Hofmann, S. Kuhn, S. Reitzenstein, L. V. Keldysh, V. D. Kulakovskii, T. L. Reinecke, and A. Forchel, “Strong coupling in a single quantum dot-semiconductor microcavity system”, *Nature* **432**, 197–200 (2004).
- [29] P. Michler, A. Kiraz, C. Becher, W. V. Schoenfeld, P. M. Petroff, L. Zhang, E. Hu, and A. Imamoglu, “A Quantum Dot Single-Photon Turnstile Device”, *Science* **290**, 2282–2285 (2000).
- [30] Z. Yuan, B. E. Kardynal, R. M. Stevenson, A. J. Shields, C. J. Lobo, K. Cooper, N. S. Beattie, D. A. Ritchie, and M. Pepper, “Electrically Driven Single-Photon Source”, *Science* **295**, 102–105 (2001).
- [31] D. Press, S. Götzinger, S. Reitzenstein, C. Hofmann, A. Löffler, M. Kamp, A. Forchel, and Y. Yamamoto, “Photon Antibunching from a Single Quantum-Dot-Microcavity System in the Strong Coupling Regime”, *Physical Review Letters* **98**, 117402 (2007).
- [32] R. Johne, N. A. Gippius, G. Pavlovic, D. D. Solnyshkov, I. A. Shelykh, and G. Malpuech, “Entangled Photon Pairs Produced by a Quantum Dot Strongly Coupled to a Microcavity”, *Physical Review Letters* **100**, 240404 (2008).
- [33] E. Peter, P. Senellart, D. Martrou, A. Lemaitre, J. Hours, J. M. Gerard, and J. Bloch, “Exciton-photon strong-coupling regime for a single quantum dot embedded in a microcavity”, *Physical Review Letters* **95** (2005).
- [34] J. Kasprzak, S. Reitzenstein, E. A. Muljarov, C. Kistner, C. Schneider, M. Strauss, S. Höfling, A. Forchel, and W. Langbein, “Up on the Jaynes–Cummings ladder of a quantum-dot/microcavity system”, *Nature Materials* **9**, 304–308 (2010).

- [35] E. T. Jaynes, and F. W. Cummings, “Comparison of quantum and semiclassical radiation theories with application to the beam maser”, *Proceedings of the IEEE* **51**, 89–109 (1963).
- [36] M. Cardona, “Modulation Spectroscopy of Semiconductors”, in *Advances in solid state physics* (Elsevier, 1970), pp. 125–173.
- [37] M. Guina, M. Tavast, G. Fetzner, T. Leinonen, S. Ranta, and N. Van Lieu, “1180 nm VECSEL with output power beyond 20 W”, *Electronics Letters* **49**, 59–60 (2013).
- [38] J. Wu, W. Shan, and W. Walukiewicz, “Band anticrossing in highly mismatched III-V semiconductor alloys”, *Semiconductor Science and Technology* **17**, 860–869 (2002).
- [39] I. Vurgaftman, and J. R. Meyer, “Band parameters for nitrogen-containing semiconductors”, *Journal of Applied Physics* **94**, 3675–3696 (2003).
- [40] N. Tansu, and L. J. Mawst, “Design Analysis of 1550-nm GaAsSb-(In)GaAsN Type-II Quantum-Well Laser Active Regions”, *IEEE Journal of Quantum Electronics* **39**, 1205–1210 (2003).
- [41] P. Springer, S. Gies, P. Hens, C. Fuchs, H. Han, J. Hader, J. V. Moloney, W. Stolz, K. Volz, S. W. Koch, and W. Heimbrodt, “Charge transfer luminescence in (GaIn)As/GaAs/Ga(NAs) double quantum wells”, *Journal of Luminescence* **175**, 255–259 (2016).
- [42] I. Vurgaftman, J. R. Meyer, N. Tansu, and L. J. Mawst, “(In)GaAsN-based type-II “W” quantum-well lasers for emission at $\lambda=1.55\ \mu\text{m}$ ”, *Applied Physics Letters* **83**, 2742–2744 (2003).
- [43] J. Y. Yeh, L. J. Mawst, A. A. Khandekar, T. F. Kuech, I. Vurgaftman, J. R. Meyer, and N. Tansu, “Characteristics of InGaAsN-GaAsSb type-II “W” quantum wells”, *Journal of Crystal Growth* **287**, 615–619 (2006).
- [44] V.-M. Korpijarvi, E. L. Kantola, T. Leinonen, R. Isoaho, and M. Guina, “Monolithic GaInNAsSb/GaAs VECSEL Operating at 1550 nm”, *IEEE Journal of Selected Topics in Quantum Electronics* **21**, 480–484 (2015).
- [45] Nonlinear Control Strategies Inc., *SimuLase*, 2014, <http://www.nlcstr.com/simulase.htm>.
- [46] J. Singh, *Electronic and Optoelectronic Properties of Semiconductor Structures* (Cambridge University Press, Cambridge, Mar. 2007).
- [47] C. F. Klingshirn, *Semiconductor Optics*, Graduate Texts in Physics (Springer Berlin Heidelberg, Berlin, Heidelberg, 2012).
- [48] L. Schneebeli, “Microscopic theory of photon-correlation spectroscopy in strong-coupling semiconductors”, PhD thesis (Philipps-Universität Marburg, 2009).
- [49] P. Meystre, and M. Sargent III, *Elements of Quantum Optics* (Springer Science & Business Media, Berlin, Heidelberg, Sept. 2007).

- [50] D. F. Walls, and G. J. Milburn, *Quantum Optics* (Springer Science & Business Media, Berlin, Heidelberg, Jan. 2008).
- [51] M. Lindberg, and S. W. Koch, “Effective Bloch equations for semiconductors”, *Physical Review B* **38**, 3342–3350 (1988).
- [52] C. Schlichenmaier, H. Gruning, A. Thränhardt, P. J. Klar, B. Kunert, K. Volz, W. Stolz, W. Heimbrodt, T. Meier, S. W. Koch, J. Hader, and J. V. Moloney, “Type I-type II transition in InGaAs–GaNAs heterostructures”, *Applied Physics Letters* **86**, 081903 (2005).
- [53] M. Tavis, and F. W. Cummings, “Exact Solution for an N -Molecule—Radiation-Field Hamiltonian”, *Physical Review* **170**, 379–384 (1968).
- [54] B. W. Shore, and P. L. Knight, “The Jaynes-Cummings Model”, *Journal of Modern Optics* **40**, 1195–1238 (1993).
- [55] G. Lindblad, “On the generators of quantum dynamical semigroups”, *Communications in Mathematical Physics* **48**, 119–130 (1976).
- [56] J. Dalibard, Y. Castin, and K. Mølmer, “Wave-function approach to dissipative processes in quantum optics”, *Physical Review Letters* **68**, 580–583 (1992).
- [57] H. J. Carmichael, “Quantum trajectory theory for cascaded open systems”, *Physical Review Letters* **70**, 2273–2276 (1993).
- [58] Y. Kaluzny, P. Goy, M. Gross, J. M. Raimond, and S. Haroche, “Observation of Self-Induced Rabi Oscillations in Two-Level Atoms Excited Inside a Resonant Cavity: The Ringing Regime of Superradiance”, *Physical Review Letters* **51**, 1175–1178 (1983).
- [59] R. J. Thompson, G. Rempe, and H. J. Kimble, “Observation of normal-mode splitting for an atom in an optical cavity”, *Physical Review Letters* **68**, 1132–1135 (1992).
- [60] M. Brune, F. Schmidt-Kaler, A. Maali, J. Dreyer, E. Hagley, J. M. Raimond, and S. Haroche, “Quantum Rabi Oscillation: A Direct Test of Field Quantization in a Cavity”, *Physical Review Letters* **76**, 1800–1803 (1996).
- [61] P. G. Kwiat, K. Mattle, H. Weinfurter, A. Zeilinger, A. V. Sergienko, and Y. Shih, “New High-Intensity Source of Polarization-Entangled Photon Pairs”, *Physical Review Letters* **75**, 4337–4341 (1995).
- [62] D. Bouwmeester, J.-W. Pan, K. Mattle, M. Eibl, H. Weinfurter, and A. Zeilinger, “Experimental quantum teleportation”, *Nature* **390**, 575–579 (1997).
- [63] A. Furusawa, J. L. Sørensen, S. L. Braunstein, C. A. Fuchs, H. J. Kimble, and E. S. Polzik, “Unconditional Quantum Teleportation”, *Science* **282**, 706–709 (1998).
- [64] J. M. Raimond, M. Brune, and S. Haroche, “Manipulating quantum entanglement with atoms and photons in a cavity”, *Reviews of Modern Physics* **73**, 565–582 (2001).

- [65] M. Riebe, H. Häffner, C. F. Roos, W. Hänsel, J. Benhelm, G. P. T. Lancaster, T. W. Körber, C. Becher, F. Schmidt-Kaler, D. F. V. James, and R. Blatt, “Deterministic quantum teleportation with atoms”, *Nature* **429**, 734–737 (2004).
- [66] M. D. Barrett, J. Chiaverini, T. Schaetz, J. Britton, W. M. Itano, J. D. Jost, E. Knill, C. Langer, D. Leibfried, R. Ozeri, and D. J. Wineland, “Deterministic quantum teleportation of atomic qubits”, *Nature* **429**, 737–739 (2004).
- [67] T. Feldtmann, L. Schneebeli, M. Kira, and S. W. Koch, “Quantum theory of light emission from a semiconductor quantum dot”, *Physical Review B* **73**, 155319 (2006).
- [68] F. Schwabl, *Quantenmechanik (QM I)*, Eine Einführung (Springer, Berlin, Heidelberg, Sept. 2007).
- [69] W. P. Schleich, *Quantum Optics in Phase Space* (John Wiley & Sons, Weinheim, Feb. 2011).
- [70] F. Schwabl, *Statistische Mechanik* (Springer-Verlag, Berlin/Heidelberg, 2006).
- [71] W. H. Press, B. P. Flannery, S. A. Teukolsky, and W. T. Vetterling, *Numerical Recipes in FORTRAN 77: Volume 1, Volume 1 of Fortran Numerical Recipes*, The Art of Scientific Computing (Cambridge University Press, Sept. 1992).
- [72] W. W. Chow, and S. W. Koch, *Semiconductor-Laser Fundamentals*, Physics of the Gain Materials (Springer Science & Business Media, July 1999).
- [73] S. W. Koch, M. Kira, G. Khitrova, and H. M. Gibbs, “Semiconductor excitons in new light”, *Nature Materials* **5**, 523–531 (2006).
- [74] R. P. Smith, J. K. Wahlstrand, A. C. Funk, R. P. Mirin, S. T. Cundiff, J. T. Steiner, M. Schafer, M. Kira, and S. W. Koch, “Extraction of Many-Body Configurations from Nonlinear Absorption in Semiconductor Quantum Wells”, *Physical Review Letters* **104**, 247401 (2010).
- [75] C. N. Böttge, “On the Phonon Interactions and Terahertz Excitations Among Coulomb-correlated Charge Carriers of Semiconductors”, PhD thesis (Philipps-Universität Marburg, 2013).
- [76] J. Hader, N. Linder, and G. H. Döhler, “k·p theory of the Franz-Keldysh effect”, *Physical Review B* **55**, 6960–6974 (1997).
- [77] S. Chuang, “Efficient band-structure calculations of strained quantum wells”, *Physical Review B* **43**, 9649–9661 (1991).
- [78] D. Ahn, and S. Chuang, “Model of the field-effect quantum-well laser with free-carrier screening and valence band mixing”, *Journal of Applied Physics* **64**, 6143–6149 (1988).
- [79] J. Hader, S. W. Koch, and J. V. Moloney, “Microscopic theory of gain and spontaneous emission in GaInNAs laser material”, *Solid-State Electronics* **47**, 513–521 (2003).

- [80] J. Steiner, “Microscopic Theory of Linear and Nonlinear Terahertz Spectroscopy in Semiconductors”, PhD thesis (Philipps-Universität Marburg, 2008).
- [81] P. Y. Yu, and M. Cardona, *Fundamentals of Semiconductors*, Graduate Texts in Physics (Springer Berlin Heidelberg, Berlin, Heidelberg, 2010).
- [82] A. Girndt, F. Jahnke, A. Knorr, S. W. Koch, and W. W. Chow, “Multi-Band Bloch Equations and Gain Spectra of Highly Excited II–VI Semiconductor Quantum Wells”, *Physica Status Solidi (b)* **202**, 725–739 (1997).
- [83] J. V. Moloney, J. Hader, and S. W. Koch, “Quantum design of semiconductor active materials: laser and amplifier applications”, *Laser & Photonics Reviews* **1**, 24–43 (2007).
- [84] J. Hader, J. V. Moloney, S. W. Koch, and W. W. Chow, “Microscopic modeling of gain and luminescence in semiconductors”, *IEEE Journal of Selected Topics in Quantum Electronics* **9**, 688–697 (2003).
- [85] E. Fermi, “Zur Quantelung des idealen einatomigen Gases”, *Zeitschrift für Physik* **36**, 902–912 (1926).
- [86] P. A. M. Dirac, “On the Theory of Quantum Mechanics”, *Proceedings of the Royal Society of London A: Mathematical, Physical and Engineering Sciences* **112**, 661–677 (1926).
- [87] H. Haug, *Statistische Physik, Gleichgewichtstheorie und Kinetik* (Springer-Verlag, Berlin/Heidelberg, 2006).
- [88] R. W. Boyd, *Nonlinear Optics* (Academic Press, May 2008).
- [89] W. Hoyer, M. Kira, S. W. Koch, J. Hader, and J. V. Moloney, “Coulomb effects on quantum-well luminescence spectra and radiative recombination times”, *Journal of the Optical Society of America B* **24**, 1344–1353 (2007).
- [90] C. Bückers, “Mikroskopische Analyse optoelektronischer Eigenschaften von Halbleiterverstärkungsmedien für Laseranwendungen”, PhD thesis (Philipps-Universität Marburg, 2010).
- [91] J. Hader, P. Thomas, and S. W. Koch, “Optoelectronics of semiconductor superlattices”, *Progress in Quantum Electronics* **22**, 123–209 (1998).
- [92] M. Kira, F. Jahnke, W. Hoyer, and S. W. Koch, “Quantum theory of spontaneous emission and coherent effects in semiconductor microstructures”, *Progress in Quantum Electronics* **23**, 189–279 (1999).
- [93] C. Schlichenmaier, “Modeling of Optical Properties of Semiconductor Heterostructures”, PhD thesis (Philipps-Universität Marburg, 2005).
- [94] M. Kira, S. W. Koch, R. P. Smith, A. E. Hunter, and S. T. Cundiff, “Quantum spectroscopy with Schrödinger-cat states”, *Nature Physics* **7**, 799–804 (2011).
- [95] C. Karcher, “Über den Einfluss von isoelektronischen Störstellen auf Bandbiegung und Unordnung in Verbindungshalbleitern”, PhD thesis (Philipps-Universität Marburg, 2012).

- [96] E. Hecht, *Optics* (Addison-Wesley, July 2015).
- [97] I. Vurgaftman, J. R. Meyer, and L. R. Ra-Mohan, “Band Parameters for III-V Compound Semiconductors and Their Alloys”, *Journal of Applied Physics* **89**, 5815–5875 (2001).
- [98] C. H. Grein, P. M. Young, and H. Ehrenreich, “Theoretical Performance of InAs/In_xGa_{1-x}Sb Superlattice-Based Midwave Infrared-Lasers”, *Journal of Applied Physics* **76**, 1940–1942 (1994).
- [99] J. I. Malin, J. R. Meyer, C. L. Felix, J. R. Lindle, L. Goldberg, C. A. Hoffman, F. J. Bartoli, C. H. Lin, P. C. Chang, S. J. Murry, R. Q. Yang, and S. S. Pei, “Type II mid-infrared quantum well lasers”, *Applied Physics Letters* **68**, 2976–2978 (1996).
- [100] M. Peter, R. Kiefer, F. Fuchs, N. Herres, K. Winkler, K. H. Bachem, and J. Wagner, “Light-emitting diodes and laser diodes based on a Ga_{1-x}In_xAs/GaAs_{1-y}Sb_y type II superlattice on InP substrate”, *Applied Physics Letters* **74**, 1951–1953 (1999).
- [101] O. Vänskä, I. Tittonen, S. W. Koch, and M. Kira, “Coherent Terahertz Control of Vertical Transport in Semiconductor Heterostructures”, *Physical Review Letters* **114**, 116802 (2015).
- [102] K. Thyagarajan, and A. Ghatak, *Lasers, Fundamentals and Applications* (Springer, Boston, MA, Oct. 2010).
- [103] J. R. Meyer, C. L. Felix, W. W. Bewley, I. Vurgaftman, E. H. Aifer, L. J. Olafsen, J. R. Lindle, C. A. Hoffman, M. J. Yang, B. R. Bennett, B. V. Shanabrook, H. Lee, C. H. Lin, S. S. Pei, and R. H. Miles, “Auger coefficients in type-II InAs/Ga_{1-x}In_xSb quantum wells”, *Applied Physics Letters* **73**, 2857–2859 (1998).
- [104] R. Fehse, S. Tomic, A. R. Adams, S. J. Sweeney, E. P. O’Reilly, A. Andreev, and H. Riechert, “A quantitative study of radiative, Auger, and defect related recombination processes in 1.3- μ m GaInNAs-based quantum-well lasers”, *IEEE Journal of Selected Topics in Quantum Electronics* **8**, 801–810 (2002).
- [105] R. H. Miles, D. H. Chow, Y.-H. Zhang, P. D. Brewer, and R. G. Wilson, “Mid-wave Infrared Stimulated-Emission From a GaInSb/InAs Superlattice”, *Applied Physics Letters* **66**, 1921–1923 (1995).
- [106] T. C. Hasenberg, D. H. Chow, A. R. Kost, R. H. Miles, and L. West, “Demonstration of 3.5 μ m Ga_{1-x}In_xSb/InAs superlattice diode laser”, *Electronics Letters* **31**, 275–276 (1995).
- [107] R. Q. Yang, “Infrared laser based on intersubband transitions in quantum wells”, *Superlattices and Microstructures* **17**, 77–83 (1995).
- [108] C. L. Felix, W. W. Bewley, I. Vurgaftman, J. R. Meyer, D. Zhang, C. H. Lin, R. Q. Yang, and S. S. Pei, “Interband cascade laser emitting >1 photon per injected electron”, *IEEE Photonics Technology Letters* **9**, 1433–1435 (1997).

- [109] C.-H. Lin, R. Q. Yang, D. Zhang, S. J. Murry, S. S. Pei, A. A. Allerman, and S. R. Kurtz, “Type-II interband quantum cascade laser at 3.8 μm ”, *Electronics Letters* **33**, 598 (1997).
- [110] J. F. Klem, O. Blum, S. R. Kurtz, I. J. Fritz, and K. D. Choquette, “GaAsSb/InGaAs type-II quantum wells for long-wavelength lasers on GaAs substrates”, *Journal of Vacuum Science & Technology B: Microelectronics and Nanometer Structures* **18**, 1605–1608 (2000).
- [111] J. R. Meyer, C. A. Hoffman, F. J. Bartoli, and L. R. Ram-Mohan, “Type-II quantum-well lasers for the mid-wavelength infrared”, *Applied Physics Letters* **67**, 757 (1995).
- [112] P. Dowd, W. Braun, D. J. Smith, C. M. Ryu, C. Z. Guo, S. L. Chen, U. Koelle, S. R. Johnson, and Y.-H. Zhang, “Long wavelength (1.3 and 1.5 μm) photoluminescence from InGaAs/GaPAsSb quantum wells grown on GaAs”, *Applied Physics Letters* **75**, 1267–1269 (1999).
- [113] W. Braun, P. Dowd, C. Z. Guo, S. L. Chen, C. M. Ryu, U. Koelle, S. R. Johnson, Y.-H. Zhang, J. W. Tomm, T. Elsässer, and D. J. Smith, “Strained InGaAs/GaPAsSb heterostructures grown on GaAs (001) for optoelectronic applications in the 1100–1550 nm range”, *Journal of Applied Physics* **88**, 3004–3014 (2000).
- [114] J. Y. Yeh, L. J. Mawst, A. A. Khandekar, T. F. Kuech, I. Vurgaftman, J. R. Meyer, and N. Tansu, “Long wavelength emission of InGaAsN/GaAsSb type II “W” quantum wells”, *Applied Physics Letters* **88**, 051115 (2006).
- [115] L. J. Mawst, J. Y. T. Huang, D. P. Xu, J.-Y. Yeh, G. Tsvid, T. F. Kuech, and N. Tansu, “MOCVD-Grown Dilute Nitride Type II Quantum Wells”, *IEEE Journal of Selected Topics in Quantum Electronics* **14**, 979–991 (2008).
- [116] A. A. Khandekar, B. E. Hawkins, T. F. Kuech, J. Y. Yeh, L. J. Mawst, J. R. Meyer, I. Vurgaftman, and N. Tansu, “Characteristics of GaAsN/GaAsSb type-II quantum wells grown by metalorganic vapor phase epitaxy on GaAs substrates”, *Journal of Applied Physics* **98**, 123525 (2005).
- [117] W. W. Chow, and H. C. Schneider, “Charge-separation effects in 1.3 μm GaAsSb type-II quantum-well laser gain”, *Applied Physics Letters* **78**, 4100 (2001).
- [118] W. W. Chow, O. B. Spahn, H. C. Schneider, and J. F. Klem, “Contributions to the large blue emission shift in a GaAsSb type-II laser”, *IEEE Journal of Quantum Electronics* **37**, 1178–1182 (2001).
- [119] M. Kudo, K. Ouchi, J.-i. Kasai, and T. Mishima, “Low-Lattice-Strain Long-Wavelength GaAsSb/GaInAs Type-II Quantum Wells Grown on GaAs Substrates”, *Japanese Journal of Applied Physics Part 2-Letters* **41**, L1040–L1042 (2002).

Bibliography

- [120] I. Vurgaftman, C. L. Felix, W. W. Bewley, D. W. Stokes, R. E. Bartolo, and J. R. Meyer, “Mid-infrared ‘W’ lasers”, *Philosophical Transactions of the Royal Society A: Mathematical, Physical and Engineering Sciences* **359**, 489–503 (2001).
- [121] C. L. Canedy, W. W. Bewley, J. R. Lindle, C. S. Kim, M. Kim, I. Vurgaftman, and J. R. Meyer, “Investigation of mid-infrared type-II “W” diode lasers”, *Journal of Electronic Materials* **35**, 453–461 (2006).
- [122] E. H. Aifer, J. G. Tischler, J. H. Warner, I. Vurgaftman, W. W. Bewley, J. R. Meyer, J. C. Kim, L. J. Whitman, C. L. Canedy, and E. M. Jackson, “W-structured type-II superlattice long-wave infrared photodiodes with high quantum efficiency”, *Applied Physics Letters* **89**, 053519 (2006).
- [123] C.-H. Pan, C.-H. Chang, and C.-P. Lee, “Room Temperature Optically Pumped 2.56- μm Lasers With “W” Type InGaAs/GaAsSb Quantum Wells on InP Substrates”, *IEEE Photonics Technology Letters* **24**, 1145–1147 (2012).
- [124] C. Grasse, P. Wiecha, T. Gruendl, S. Sprengel, R. Meyer, and M.-C. Amann, “InP-based 2.8–3.5 μm resonant-cavity light emitting diodes based on type-II transitions in GaInAs/GaAsSb heterostructures”, *Applied Physics Letters* **101**, 221107 (2012).
- [125] S. Sprengel, C. Grasse, P. Wiecha, A. Andrejew, T. Gruendl, G. Boehm, R. Meyer, and M. Amann, “InP-Based Type-II Quantum-Well Lasers and LEDs”, *IEEE Journal of Selected Topics in Quantum Electronics* **19**, 1900909–1900909 (2013).
- [126] C.-H. Chang, Z.-L. Li, H.-T. Lu, C.-H. Pan, C.-P. Lee, G. Lin, and S.-D. Lin, “Low-Threshold Short-Wavelength Infrared InGaAs/GaAsSb ‘W’ -Type QW Laser on InP Substrate”, *IEEE Photonics Technology Letters* **27**, 225–228 (2015).
- [127] S. Sprengel, A. Andrejew, F. Federer, G. K. Veerabathran, G. Boehm, and M. C. Amann, “Continuous wave vertical cavity surface emitting lasers at 2.5 μm with InP-based type-II quantum wells”, *Applied Physics Letters* **106**, 151102 (2015).
- [128] S. Sato, and S. Satoh, “1.21 μm continuous-wave operation of highly strained GaInAs quantum well lasers on GaAs substrates”, *Japanese Journal of Applied Physics Part 2-Letters* **38**, L990–L992 (1999).
- [129] N. Tansu, J.-Y. Yeh, and L. J. Mawst, “Extremely low threshold-current-density InGaAs quantum-well lasers with emission wavelength of 1215–1233 nm”, *Applied Physics Letters* **82**, 4038–4040 (2003).
- [130] P. Sundgren, J. Berggren, P. Goldman, and M. Hammar, “Highly strained InGaAs/GaAs multiple quantum-wells for laser applications in the 1200–1300 nm wavelength regime”, *Applied Physics Letters* **87**, 071104 (2005).
- [131] J. Hader, G. Hardesty, T.-L. Wang, M. J. Yarborough, Y. Kaneda, J. V. Moloney, B. Kunert, W. Stolz, and S. W. Koch, “Predictive Microscopic Modeling of VECSELs”, *IEEE Journal of Quantum Electronics* **46**, 810–817 (2010).

- [132] B. Heinen, F. Zhang, M. Sparenberg, B. Kunert, M. Koch, and W. Stolz, “On the Measurement of the Thermal Resistance of Vertical-External-Cavity Surface-Emitting Lasers (VECSELs)”, *IEEE Journal of Quantum Electronics* **48**, 934–940 (2012).
- [133] M. Born, E. Wolf, and A. B. Bhatia, *Principles of Optics*, Electromagnetic Theory of Propagation, Interference and Diffraction of Light (Cambridge University Press, Oct. 1999).
- [134] M. Schafer, W. Hoyer, M. Kira, S. W. Koch, and J. V. Moloney, “Influence of dielectric environment on quantum-well luminescence spectra”, *Journal of the Optical Society of America B* **25**, 187–195 (2008).
- [135] H. Han, A. Beyer, K. Jandieri, K. I. Gries, L. Duschek, W. Stolz, and K. Volz, “Quantitative characterization of the interface roughness of (GaIn)As quantum wells by high resolution STEM”, *Micron* **79**, 1–7 (2015).
- [136] A. Badolato, K. Hennessy, M. Atatüre, J. Dreiser, E. Hu, P. M. Petroff, and A. Imamoglu, “Deterministic coupling of single quantum dots to single nanocavity modes.”, *Science* **308**, 1158–1161 (2005).
- [137] A. Kiraz, P. Michler, C. Becher, B. Gayral, A. Imamoglu, L. Zhang, E. Hu, W. V. Schoenfeld, and P. M. Petroff, “Cavity-quantum electrodynamics using a single InAs quantum dot in a microdisk structure”, *Applied Physics Letters* **78**, 3932–3934 (2001).
- [138] G. Sek, C. Hofmann, J. P. Reithmaier, A. Löffler, S. Reitzenstein, M. Kamp, L. V. Keldysh, V. D. Kulakovskii, T. L. Reinecke, and A. Forchel, “Investigation of strong coupling between single quantum dot excitons and single photons in pillar microcavities”, *Physica E: Low-dimensional Systems and Nanostructures* **32**, 471–475 (2006).
- [139] Z. Xie, S. Götzinger, W. Fang, H. Cao, and G. Solomon, “Influence of a Single Quantum Dot State on the Characteristics of a Microdisk Laser”, *Physical Review Letters* **98**, 117401 (2007).
- [140] J. Wiersig, C. Gies, F. Jahnke, M. Aßmann, T. Berstermann, M. Bayer, C. Kistner, S. Reitzenstein, C. Schneider, S. Höfling, A. Forchel, C. Kruse, J. Kalden, and D. Hommel, “Direct observation of correlations between individual photon emission events of a microcavity laser”, *Nature* **460**, 245–249 (2009).
- [141] F. Albert, C. Hopfmann, A. Eberspächer, F. Arnold, M. Emmerling, C. Schneider, S. Höfling, A. Forchel, M. Kamp, J. Wiersig, and S. Reitzenstein, “Directional whispering gallery mode emission from Limaçon-shaped electrically pumped quantum dot micropillar lasers”, *Applied Physics Letters* **101**, 021116 (2012).
- [142] D. D. Awschalom, L. C. Bassett, A. S. Dzurak, E. L. Hu, and J. R. Petta, “Quantum Spintronics: Engineering and Manipulating Atom-Like Spins in Semiconductors”, *Science* **339**, 1174–1179 (2013).

Bibliography

- [143] Y. Chu, A. M. Mintairov, Y. He, J. L. Merz, N. A. Kalyuzhnyy, V. M. Lantratov, and S. A. Mintairov, “Lasing of whispering-gallery modes in asymmetric waveguide GaInP micro-disks with InP quantum dots”, *Physics Letters A* **373**, 1185–1188 (2009).
- [144] S. M. Ulrich, C. Gies, S. Ates, J. Wiersig, S. Reitzenstein, C. Hofmann, A. Löffler, A. Forchel, F. Jahnke, and P. Michler, “Photon Statistics of Semiconductor Microcavity Lasers”, *Physical Review Letters* **98**, 043906 (2007).
- [145] M. Kira, and S. W. Koch, “Quantum-optical spectroscopy of semiconductors”, *Physical Review A* **73**, 013813 (2006).
- [146] M. Kira, and S. W. Koch, “Cluster-expansion representation in quantum optics”, *Physical Review A* **78**, 022102 (2008).
- [147] M. Mootz, M. Kira, S. W. Koch, A. E. Almand-Hunter, and S. T. Cundiff, “Characterizing biexciton coherences with quantum spectroscopy”, *Physical Review B* **89** (2014).
- [148] A. E. Almand-Hunter, H. Li, S. T. Cundiff, M. Mootz, M. Kira, and S. W. Koch, “Quantum droplets of electrons and holes”, *Nature* **506**, 471–475 (2014).
- [149] M. Mootz, “Quantum-Spectroscopy Studies on Semiconductor Nanostructures”, PhD thesis (Philipps-Universität Marburg, 2014).
- [150] U. Huttner, “Influence of Pump-Laser Quantum Statistics on Quantum-Dot Lasing”, MA thesis (Philipps-Universität Marburg, 2013).

This appendix contains all publications described in this Thesis. An overview of the articles is provided by their abstracts first.

Paper I: *Quantum-Memory Effects in the Emission of Quantum-Dot Microcavities*

The experimentally measured input-output characteristics of optically pumped semiconductor microcavities exhibits unexpected oscillations modifying the fundamentally linear slope in the excitation power regime below lasing. A systematic microscopic analysis reproduces these oscillations, identifying them as a genuine quantum-memory effect, i.e., a photon-density correlation accumulated during the excitation. With the use of projected quantum measurements, it is shown that the input-output oscillations can be controlled and enhanced by an order of magnitude when the quantum fluctuations of the pump are adjusted.

Paper II: *Novel type-II material system for laser applications in the near-infrared regime*

The design and experimental realization of a type-II “W”-multiple quantum well heterostructure for emission in the $\lambda > 1.2 \mu\text{m}$ range is presented. The experimental photoluminescence spectra for different excitation intensities are analyzed using microscopic quantum theory. On the basis of the good theory–experiment agreement, the gain properties of the system are computed using the semiconductor Bloch equations. Gain values comparable to those of type-I systems are obtained.

Paper III: *Excitonic transitions in highly efficient (GaIn)As/Ga(AsSb) type-II quantum-well structures*

The excitonic transitions of the type-II (GaIn)As/Ga(AsSb) gain medium of a “W”-laser structure are characterized experimentally by modulation spectroscopy and analyzed using microscopic quantum theory. On the basis of the very good agreement between the measured and calculated photorefectivity, the type-I or type-II character of the observable excitonic transitions is identified.

Whereas the energetically lowest three transitions exhibit type-II character, the subsequent energetically higher transitions possess type-I character with much stronger dipole moments. Despite the type-II character, the quantum-well structure exhibits a bright luminescence.

Paper IV: *Type-II vertical-external-cavity surface emitting laser with Watt level output powers at $1.2\ \mu\text{m}$*

Semiconductor laser characteristics based on type-II band-aligned quantum well heterostructures for the emission at $\lambda > 1.2\ \mu\text{m}$ are presented. Ten “W”-quantum wells consisting of GaAs/(GaIn)As/ Ga(AsSb)/(GaIn)As/GaAs are arranged as resonant periodic gain in a vertical-external-cavity surface-emitting laser. Its structure is analyzed by X-ray diffraction, photoluminescence, and reflectance measurements. The laser’s power curves and spectra are investigated. Output powers at Watt level are achieved, with a maximum output power of 4 W. It is confirmed that laser operation only involves the type-II transition. A blue shift of the material gain is observed while the modal gain exhibits a red shift.

Paper V: *$1.2\ \mu\text{m}$ emitting VECSEL based on type-II aligned QWs*

Since the invention of VECSELs, their great spectral coverage has been demonstrated and emission wavelengths in the range from UV to almost MIR have been achieved. However, in the infrared regime the laser performance is affected by Auger losses which become significant at large quantum defects. In order to reduce the Auger losses and to develop more efficient devices in the IR, type-II aligned QWs have been suggested as alternative gain medium for semiconductor lasers.

We present the first room temperature VECSEL containing type-II aligned quantum wells arranged as resonant periodic gain. The quantum wells consist of (GaIn)As/Ga(AsSb)/(GaIn)As heterostructures. The structure was grown bottom-up on GaAs substrate and flip-chip bonded onto a diamond heat spreader. The device, pumped at 808 nm, emits $> 1\ \text{W}$ of cw output power at an emission wavelength of $\lambda > 1.2\ \mu\text{m}$. A detailed study of the device is performed in order to investigate the potential of such novel type-II gain media for future applications. These investigations include the determination of the power and temperature dependent shift rates. The gain temperatures at laser threshold and at maximum output power are determined.

Paper VI: *Electrical Injection Type-II (GaIn)As/Ga(AsSb)/(GaIn)As Single “W”-Quantum Well Laser at $1.2\ \mu\text{m}$*

Highly efficient interface-dominated electrical injection lasers in the near-infrared regime based on the type-II band alignment in (GaIn)As/Ga(AsSb)/(GaIn)As single “W”-quantum wells are verified. The structure is designed by applying a fully microscopic theory, realized by employing metal organic vapor phase

epitaxy, and characterized using electroluminescence measurements and broad-area laser studies. The characteristic blue shift of type-II material systems with increasing charge carrier density is observed and compared to theoretical investigations. The experimental data yields a shift of $93 \text{ meV}/(\text{kA}/\text{cm}^2)$. Low threshold current densities of $0.4 \text{ kA}/\text{cm}^2$, high differential efficiencies of 66 %, optical output powers of 1.4 W per facet, and internal losses of only 1.9 cm^{-1} are observed at a wavelength of $1.16 \mu\text{m}$. No indication for type-I related transitions for current densities up to $4.5 \text{ kA}/\text{cm}^2$ is observed. A detailed atomic scale chemical analysis forms the basis for future improvements in laser performance.

Paper VII: *Gain spectroscopy of a type-II VECSEL chip*

In this work, gain dynamics of a novel VECSEL chip design based on type-II heterostructures is analyzed both theoretically as well as experimentally. For such a chip consisting of a GaAs/(GaIn)As/Ga(AsSb)/(GaIn)As/GaAs multi-quantum-well active region, optical transitions for laser operation take place across the interface of the heterostructure, with holes and electrons separately confined. In order to study the temporal evolution of gain in a type-II chip in comparison to conventional type-I structures, optical pump-probe spectroscopy is used. Our measurements in reflection geometry reveal a maximum reflectance of 1.008 at 1168 nm for a delay of 1.3 ns between pump and probe pulse. Starting at 0.6 ns after excitation, gain lasts for 1.5 ns. Here, the observed dynamics deviates from the earlier but shorter gain evolution in a comparable type-I structure. Gain spectra of the laser chip are predicted by a fully microscopic approach using the semiconductor Bloch equations, showing remarkable agreement with the obtained results.

Paper I

C. Berger, U. Huttner, M. Mootz, M. Kira, S. W. Koch,
J.-S. Tempel, M. Aßmann, M. Bayer, A. M. Mintairov, and J. L. Merz

*Quantum-Memory Effects in the Emission of Quantum-Dot
Microcavities*

Physical Review Letters **113**, 093902 (2014)

DOI: 10.1103/PhysRevLett.113.093902

Quantum-Memory Effects in the Emission of Quantum-Dot Microcavities

C. Berger,^{1,*} U. Huttner,¹ M. Mootz,¹ M. Kira,¹ S. W. Koch,¹ J.-S. Tempel,² M. Aßmann,²
M. Bayer,^{2,3} A. M. Mintairov,^{3,4} and J. L. Merz⁴

¹Department of Physics, Philipps-Universität Marburg, Renthof 5, D-35032 Marburg, Germany

²Experimentelle Physik 2, Technische Universität Dortmund, D-44221 Dortmund, Germany

³Ioffe Physical-Technical Institute of the Russian Academy of Sciences, Saint Petersburg, 194021, Russia

⁴Department of Electrical Engineering, University of Notre Dame, Notre Dame, Indiana 46556, USA

(Received 20 December 2013; published 29 August 2014)

The experimentally measured input-output characteristics of optically pumped semiconductor microcavities exhibits unexpected oscillations modifying the fundamentally linear slope in the excitation power regime below lasing. A systematic microscopic analysis reproduces these oscillations, identifying them as a genuine quantum-memory effect, i.e., a photon-density correlation accumulated during the excitation. With the use of projected quantum measurements, it is shown that the input-output oscillations can be controlled and enhanced by an order of magnitude when the quantum fluctuations of the pump are adjusted.

DOI: 10.1103/PhysRevLett.113.093902

PACS numbers: 42.55.Px, 42.50.Pq, 78.55.-m

Quantum-dot microcavities have been used to demonstrate a number of intriguing quantum phenomena such as the Purcell effect [1], vacuum Rabi splitting [2,3], strong light-matter coupling [3–5], and single-photon [6–8] as well as entangled photon-pair [9] emission. These systems are, thus, prototypical for semiconductor-based cavity quantum electrodynamic (QED) studies [10–12] exploring the foundations of quantum mechanics. Moreover, microcavity structures can be utilized to produce new components and algorithms for quantum-information processing [13] and they can be used as high-quality lasers [14–16] that show a nearly thresholdless input-output (I/O) characteristics.

In the lasing regime, the system's output approaches a coherent state [17], which as the most classical form of light, is not interesting for QED studies. However, true QED effects can still be observed in the regime of low output power [18] where they may even become strong enough to produce visible deviations from the expected linear I/O behavior. According to the quantum-optical response theory developed in Ref. [19], any form of optical nonlinearity in the matter's response to classical light implies that the response must necessarily be sensitive to the light's quantum fluctuations. This completely general result implies that one should be able to find quantum-fluctuation signatures in the light-matter correlations even when the nonlinearity was originally identified completely classically.

In this Letter, we analyze the quantum-optical sensitivity of quantum-dot microcavities with a three-step approach: (i) We present the experimental observation of well-defined I/O oscillations as the nonlinear response; (ii) we use a quantum analysis to show that these oscillations originate from quantum-memory effects related to photon-density correlations; (iii) we demonstrate that the quantum-optical sensitivity of the I/O curve exhibits the predicted signatures for the identified quantum-memory correlation.

Our sample contains microring cavities [20,21] fabricated from a 150 nm thick $\text{Ga}_{0.52}\text{In}_{0.48}\text{P}$ waveguide including self-assembled InP quantum dots with a dot density of $(1-2) \times 10^9/\text{cm}^2$ and a mean dot size of 75 nm. Because of the large diameter, the dots host multiple confined levels with level spacings on the order of 3–5 meV, as demonstrated in single-dot luminescence spectra [21]. The central emission wavelength of the dot ensemble is close to 720 nm, and the inhomogeneous linewidth is 25 nm at cryogenic temperatures. The inset to Fig. 1 shows a scanning electron micrograph of the used ring cavity with a 2.2 μm outer and 1.5 μm inner diameter. The sample is kept in a helium-flow cryostat at 10 K temperature and excited using a Ti-sapphire laser emitting pulses with 2 ps duration at 75.39 MHz repetition rate. The linearly polarized pump beam is focused onto the cavity using a 100 \times microscope objective with a numerical aperture of 0.55, resulting in a spot size of 2–3 μm covering the ring. We excite the dots quasiresonantly by detuning the photon energy 30.7 meV above the $M1$ main cavity mode

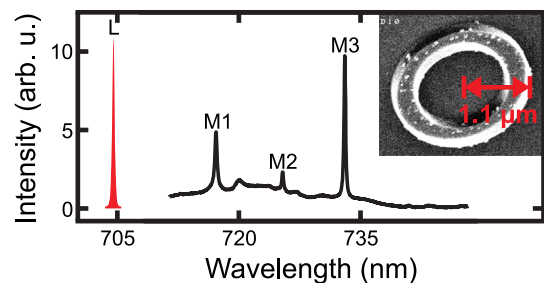


FIG. 1 (color online). μPL spectrum of the investigated microring cavity. The excitation laser was tuned to the wavelength of 705 nm. Inset: Scanning electron micrograph (side view) of the microring cavity used.

energy (see Fig. 1) but below the GaInP band gap. For this detuning, the highest excitation power generates less than 0.26 electrons per electronic level, as shown in the Supplemental Material [22]. This is well below inversion and lasing even though these structures have extremely low lasing thresholds for strongly nonresonant excitations [21]. From the dot density and the ring area in combination with the quasiresonant excitation, we estimate that the $M1$ mode emission can basically be attributed to a single dot [21], while off-resonant dots only contribute to the broad background.

The emission is collected using the same $100\times$ microscope objective that is used for the pump focusing. To minimize stray light from the excitation laser, a cross-polarized Glan prism is inserted in the detection path. Microphotoluminescence (μ PL) spectra are measured using a 500 mm focal length spectrometer equipped with a liquid-nitrogen-cooled CCD camera. A μ PL spectrum of the investigated microring cavity is shown in Fig. 1. Three main whispering-gallery modes labeled $M1$ - $M3$ are observed.

Our three-step approach starts with Fig. 2(a) that presents the measured output power at the $M1$ cavity mode as a function of the input power. While the I/O curve at first sight appears to show a linear behavior, a closer look at the data reveals small but systematic deviations from a perfect linear I/O dependence (solid line). To clearly visualize the nonlinearities, we subtract the linear straight line from the I/O data and plot in Fig. 2(b) the difference I_{osc} ; this procedure nicely highlights the oscillatory deviations. We see that the first minimum dips down to -0.1 , i.e., 10%, below the expected linear output, which significantly exceeds the 6% noise level. As discussed in the Supplemental Material [22], we have verified that the I_{osc} oscillations are reproduced for a large variety of experimental conditions.

In the second step of our analysis, we want to identify a particular quantum correlation that is responsible for the experimentally observed oscillatory nonlinearity. For this purpose, we extend the standard Jaynes-Cummings model [28] to include the four relevant electronic states in our large dot. Denoting the polarization operator for the state n by \hat{P}_n , the cavity-dot interaction follows from $\hat{H}_{\text{int}} = -\hbar g \sum_n (\hat{B} \hat{P}_n^\dagger + \hat{B}^\dagger \hat{P}_n)$, containing an effective coupling strength g and the Boson operator \hat{B} for the cavity mode. We use $\hbar g = 0.405$ meV that agrees with the typical Rabi splitting in similar quantum-dot experiments [11]. The experimental emission is best reproduced when the four states have a detuning δ_n between 2 and 8 meV above the cavity mode, comparable with the dot energetics identified in Ref. [21]. These states contribute to the Hamiltonian via $\sum_n \hbar \delta_n \hat{P}_{z,n}$ where $\hat{P}_{z,n}$ is the inversion operator for the state n .

The dot is optically driven by a classical pump pulse $\alpha(t) = \alpha_0 e^{-(t^2/\tau^2)} e^{-i\Delta_L t}$ where α_0 is the amplitude, τ gives

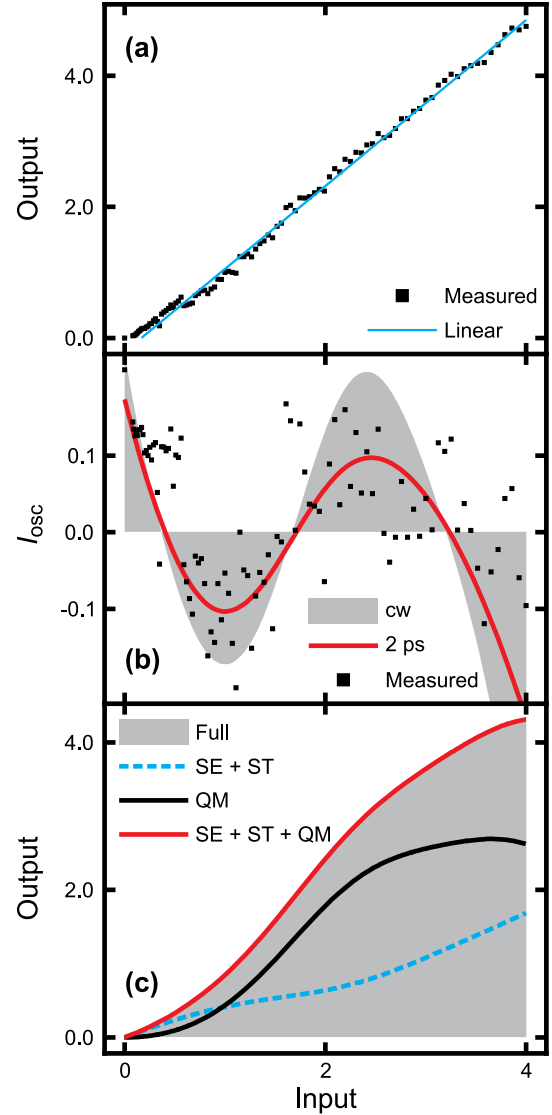


FIG. 2 (color online). Characterizing the I/O oscillations. (a) Measured I/O curve (squares) is compared with a linear output (solid line). The powers are scaled to 1 at the first sublinear dip, which corresponds to an input power of $7.6 \mu\text{W}$ resulting in 500 photons per dot in the experiment. (b) Difference of measured and linear output I_{osc} (squares) is shown as function of the input together with computed I_{osc} using a cw (shaded area) and a pulsed 2-ps-long (solid line) excitation. (c) Computed I/O responses for a cw excitation. Full computation (shaded area) is compared with the emission stemming from the sum of the spontaneous-emission (SE) and stimulated-emission (ST) sources (dashed line), the quantum-memory (QM) source only (black solid line), and the sum of SE, ST, and QM sources (red solid line).

the duration, and $\hbar\Delta_L$ defines the laser detuning with respect to the cavity. The pump-dot interaction follows from $\hat{H}_{\text{pump}} = -\sum_n [\alpha^*(t) \hat{P}_n + \alpha(t) \hat{P}_n^\dagger]$. We set $\hbar\Delta_L = 30.7$ meV as in the experiment and use the Lindbladian [29] to systematically introduce dephasing for the dot

excitation and the cavity photons. The dephasing parameters are chosen to reproduce the 0.8 ps cavity-photon lifetime as well as the $T_1 = 2.1$ ps polarization and $T_2 = 2.1$ ps occupation decay times. These values not only reproduce the correct emission linewidth in our system but are also very close to the parameters deduced from other experiments [4,20,21].

We solve the full quantum dynamics exactly by evolving the dot-cavity mode density matrix $\hat{\rho}$ in time. The input intensity is defined by the pump amplitude, i.e., $I_{\text{in}} \propto \int |\alpha(t)|^2 dt$, while the dot emits the output intensity $I_{\text{out}} \propto \langle \hat{B}^\dagger \hat{B} \rangle = \text{Tr}[\hat{B}^\dagger \hat{B} \hat{\rho}]$. We scale the computed input power to match the experiment at the first sublinear dip. We then find the linear fit $I_{\text{in}} = aI_{\text{in}} + b$ for both experiment and theory and fix the scale of I_{out} so that it has the same linear coefficient a as the experiment. This procedure only matches the I/O scales while the relative magnitude of the I_{osc} oscillations is not *a priori* fixed.

The resulting computed I_{osc} is shown in Fig. 2(b) for a 2-ps-long (solid line) and a continuous-wave (cw) pump (shaded area) as function of pump power. We see that the computed I_{osc} reproduces the experimentally observed nonlinearities. We also conclude that the 2-ps-long pump pulse is sufficiently long such that the I_{osc} oscillations approach the cw result.

In our experiment, the pump generates detuned Rabi oscillations that favor (inhibit) emission at the peak (dip) of the dot excitation. For the chosen detuning, the dot excitation both remains very small and oscillates more than five times during a photon emission. Such oscillations not only regulate the instantaneous emission but also induce quantum-memory contributions that remember excitations prior to the emission. Intuitively, the quantum memory must then involve both photons and the oscillating excitation density, yielding an accumulation of photon-density correlations. Since any photon-density correlation must be nonlinear in the pump, the quantum-memory effects must contribute nonlinearly to the I/O curve.

To verify this intuitive interpretation, we express the emitted photon flux exactly via [10]

$$\frac{\partial}{\partial t} \Delta \langle \hat{B}^\dagger \hat{B} \rangle = 2g \int_{-\infty}^t dt' \text{Re}[S(t, t')] - 2\kappa \Delta \langle \hat{B}^\dagger \hat{B} \rangle, \quad (1)$$

that is driven by a kernel $S = S^{\text{SE}} + S^{\text{QM}} + S^{\text{ST}} + S^{\text{tri}}$, as discussed in the Supplemental Material [22]. The emission is initiated by the spontaneous source $S^{\text{SE}} = g \sum_{n,n'} [\langle \hat{P}_n^\dagger \hat{P}_n \rangle - \langle \hat{P}_n^\dagger \rangle \langle \hat{P}_n \rangle]$ that is nonvanishing whenever one or more states are excited. The stimulated contribution $S^{\text{ST}} = 2g \sum_n \langle \hat{P}_{z,n} \rangle \Delta \langle \hat{B}^\dagger \hat{B} \rangle$ modifies the emission via the photon correlations inside the cavity. The quantum-memory contribution $S^{\text{QM}} = \Omega \Delta \langle \hat{B}^\dagger \hat{P}_{z,n} \rangle$ contains a product of the classical Rabi frequency Ω and $\Delta \langle \hat{B}^\dagger \hat{P}_{z,n} \rangle$ that describes a photon-density correlation. In addition, S^{tri} defines a three-particle correlation.

The relative influences of the different source terms on the emission are identified via a straightforward switch-off analysis. Figure 2(c) compares I_{out} of the full computation (shaded area) with the emission stemming from $S^{\text{SE}} + S^{\text{ST}}$ (dashed line) and from the sum of spontaneous, stimulated, and quantum-memory sources (red solid line). We observe that $S^{\text{SE}} + S^{\text{ST}}$ produces a monotonically increasing output. For larger I_{in} , I_{out} becomes essentially a linear function of I_{in} , while it still deviates significantly from the full computation result. However, combining $S^{\text{SE}} + S^{\text{ST}}$ with S^{QM} results in an almost perfect reproduction of the full I_{out} . Especially, S^{QM} (black solid line) alone contains large oscillations that remain visible also in the full I_{out} , verifying our intuitive explanation above. Since the calculated results for $S^{\text{SE}} + S^{\text{ST}} + S^{\text{QM}}$ are very close to the experimentally observed emission, we can conclude that S^{tri} has a minor effect on I_{out} in our experiment. In the Supplemental Material [22], we discuss that different coupling strengths for each emitting state and modified dot energetics do not produce quantitative changes of the scaled I/O characteristics. The further analysis also indicates that the quantum-memory effect can be enhanced by changing the detuning and engineering the coupling strength.

The third step of our analysis verifies that I_{osc} and S^{QM} have the same quantum-optical sensitivity. The detailed analysis in the Supplemental Material [22] shows that S^{QM} is driven by coherences involving a product of Ω and the squeezing of the light emission. Consequently, according to the principles of quantum-optical spectroscopy [10,30–34], I_{osc} should also depend on the pump field's quantum fluctuations following the same control rules as the quantum memory does. To fully demonstrate this experimentally, one would need to adjust the quantum fluctuations of the source. Unfortunately, this level of control is not yet possible in present-day experiments. However, a set of classical measurements can be projected to any quantum-optical response to access the quantum-optical dependence of I_{osc} , as demonstrated in Ref. [19] and utilized in Refs. [35,36] to realize a superior characterization of different quasiparticles. The projection algorithm is discussed in the Supplemental Material [22] together with all quantum-light sources studied.

Since S^{QM} is generated via the simultaneous presence of coherences and squeezing of the emission, we test if we can quench the I/O oscillations by a pump field that has either no coherences or does not produce squeezed emission. Figure 3(a) compares the classical measurement (squares) with the quantum (solid line) I/O curve when we use a squeezed vacuum state as quantum source in the projection. Since the squeezed vacuum lacks first-order coherences, it cannot induce a coherent Ω . As a result, it produces an output response *without* the oscillations, simply, because it does not generate the required quantum-memory correlations. In contrast to this, a coherent state has a nonvanishing Ω while it generates squeezing as a natural part of

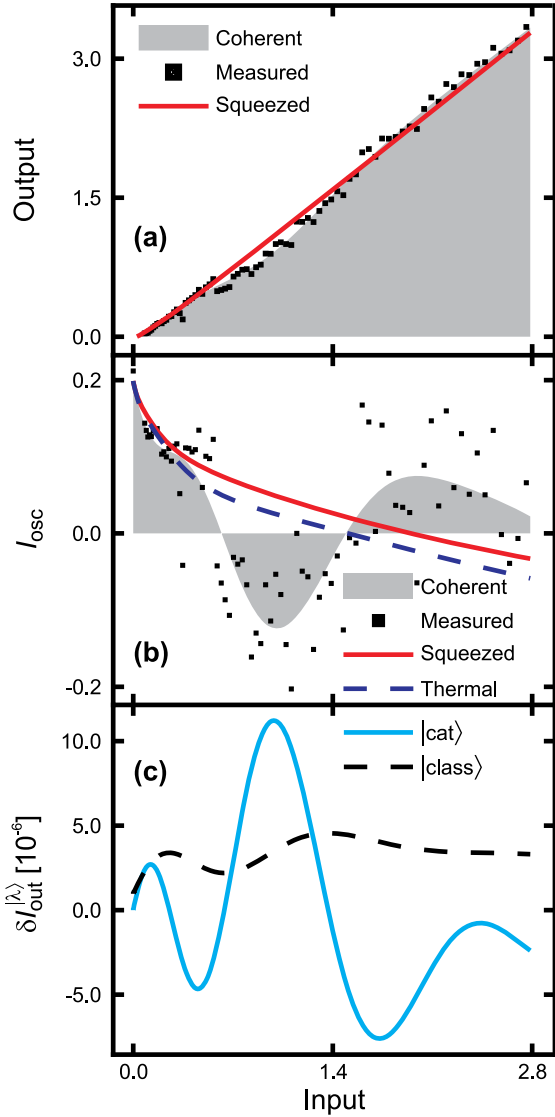


FIG. 3 (color online). Quantum-optical control of I/O oscillations. (a) Measured I/O curve (squares) is compared with the projected coherent-state (shaded area) and squeezed-vacuum output (solid line). (b) Corresponding I_{osc} and thermal-state I_{osc} (dashed line) values are shown. (c) Differential response as function of input power. The classical differential (dashed line) is compared with the stretching-cat state's differential (solid line).

resonance fluorescence emission [37]. For a consistency check, we have also projected the coherent-state response (shaded area) and, as expected, it reproduces the measured I/O oscillations.

The quantum-optical control of the I/O oscillations becomes particularly clear when we construct I_{osc} as in Fig. 2(b) by removing the line from the I/O curve. Figure 3(b) compares the measured I_{osc} (squares) with the projected coherent-state (shaded area), squeezing (solid line), and thermal-state (dashed line) source outputs. The thermal source has neither coherences nor does it generate

squeezed emission such that it produces essentially the same output as the squeezed-state source. In other words, we have verified that I_{osc} indeed stems from the quantum-memory correlations because they obey the same, non-trivial, control rules.

The dependence of the output super- or sublinearity on the quantum fluctuations of the source can be directly characterized by defining an output differential,

$$\delta I_{out}^{|\lambda\rangle} \equiv I_{out}^{|\lambda\rangle} - I_{out}, \quad (2)$$

when one changes the laser's fluctuations from a classical source (giving I_{out}) to a quantum state $|\lambda\rangle$; we project $I_{out}^{|\lambda\rangle}$ from the measured I/O curve. For the classical differentials, we use $|\lambda\rangle = |\text{class}\rangle$ that is a coherent state having one more photon than when measuring I_{out} . For the quantum differentials, we use the so-called stretching-cat state [19] $|\lambda\rangle = |\text{cat}\rangle$ that consists of a superposition of two *different* coherent states displaced along the direction of the classical field's original displacement. We adjust $|\text{cat}\rangle$ such that its quantum fluctuations add one photon to the source while its coherences are reduced so that its average photon number is equal to that of the classical reference I_{out} . As a result, $\delta I_{out}^{|\lambda\rangle}$ measures the effects generated by pure quantum fluctuations. The cat state is expected to enhance the oscillatory nonlinearities because it contains both coherences and squeezing.

Figure 3(c) compares the projected $\delta I_{out}^{|\text{class}\rangle}$ (dashed line) with the differential $\delta I_{out}^{|\text{cat}\rangle}$ (solid line). We see that the classical differential response is always positive valued and oscillatory. The maxima and minima of $\delta I_{out}^{|\text{class}\rangle}$ match with the nodes of the measured I_{osc} oscillations in Fig. 3(b). At the same time, $|\text{cat}\rangle$ produces a differential $\delta I_{out}^{|\text{cat}\rangle}$ whose oscillation amplitude is an order of magnitude greater than the result of classical spectroscopy, verifying that a suitable quantum source can indeed amplify the quantum-memory effects. By comparing this result with I_{osc} in Fig. 3(b), we also see that the used $|\text{cat}\rangle$ produces a *superlinear* increase (sublinear decrease) when the classical pump yields *sublinear* (superlinear) output. Since the super- or sublinear oscillations have an opposite phase, one can control the super- or sublinear nature of quantum-memory effects completely via the quantum fluctuations of the pump.

In conclusion, our measurements identify nontrivial I/O oscillations for a quantum dot in a microcavity. Using the methodology of quantum-optical spectroscopy, we show that the I/O oscillations are initiated by the simultaneous presence of coherences and squeezed-light emission. Physically, the excitation drives photon-density correlations that act as a quantum memory for the Rabi oscillations and, thus, induce the oscillatory nonlinearities in the I/O curve. Our projected measurements demonstrate that the super- and sublinear variations can be controlled by modifying the quantum statistics of the pump.

The Marburg group is partially funded by the Deutsche Forschungsgemeinschaft (DFG) via Grants No. KI 917/2-1 and No. SFB 1083. The Dortmund group acknowledges support by the DFG through research Grant No. DFG 1549/19-1. M. B. and A. M. M. acknowledge support from the Russian Ministry of Science and Education (Contract No. 14.Z50.31.0021).

*Corresponding author.

christian.berger@physik.uni-marburg.de

- [1] A. Badolato, K. Hennessy, M. Atatüre, J. Dreiser, E. Hu, P. M. Petroff, and A. Imamoglu, *Science* **308**, 1158 (2005).
- [2] T. Yoshie, A. Scherer, J. Hendrickson, G. Khitrova, H. M. Gibbs, G. Rupper, C. Ell, O. B. Shchekin, and D. G. Deppe, *Nature (London)* **432**, 200 (2004).
- [3] J. P. Reithmaier, G. Şek, A. Löffler, C. Hofmann, S. Kuhn, S. Reitzenstein, L. V. Keldysh, V. D. Kulakovskii, T. L. Reinecke, and A. Forchel, *Nature (London)* **432**, 197 (2004).
- [4] E. Peter, P. Senellart, D. Martrou, A. Lemaître, J. Hours, J. M. Gérard, and J. Bloch, *Phys. Rev. Lett.* **95**, 067401 (2005).
- [5] J. Kasprzak, S. Reitzenstein, E. A. Muljarov, C. Kistner, C. Schneider, M. Strauss, S. Höfling, A. Forchel, and W. Langbein, *Nat. Mater.* **9**, 304 (2010).
- [6] P. Michler, A. Kiraz, C. Becher, W. V. Schoenfeld, P. M. Petroff, L. Zhang, E. Hu, and A. Imamoglu, *Science* **290**, 2282 (2000).
- [7] Z. Yuan, B. E. Kardynal, R. M. Stevenson, A. J. Shields, C. J. Lobo, K. Cooper, N. S. Beattie, D. A. Ritchie, and M. Pepper, *Science* **295**, 102 (2002).
- [8] D. Press, S. Götzinger, S. Reitzenstein, C. Hofmann, A. Löffler, M. Kamp, A. Forchel, and Y. Yamamoto, *Phys. Rev. Lett.* **98**, 117402 (2007).
- [9] R. Johne, N. A. Gippius, G. Pavlovic, D. D. Solnyshkov, I. A. Shelykh, and G. Malpuech, *Phys. Rev. Lett.* **100**, 240404 (2008).
- [10] M. Kira and S. W. Koch, *Semiconductor Quantum Optics* (Cambridge University Press, Cambridge, England, 2012).
- [11] G. Khitrova, H. M. Gibbs, M. Kira, S. W. Koch, and A. Scherer, *Nat. Phys.* **2**, 81 (2006).
- [12] K. Hennessy, A. Badolato, M. Winger, D. Gerace, M. Atatüre, S. Gulde, S. Fält, E. L. Hu, and A. Imamoglu, *Nature (London)* **445**, 896 (2007).
- [13] D. D. Awschalom, L. C. Bassett, A. S. Dzurak, E. L. Hu, and J. R. Petta, *Science* **339**, 1174 (2013).
- [14] Z. G. Xie, S. Götzinger, W. Fang, H. Cao, and G. S. Solomon, *Phys. Rev. Lett.* **98**, 117401 (2007).
- [15] J. Wiersig, C. Gies, F. Jahnke, M. Aßmann, T. Berstermann, M. Bayer, C. Kistner, S. Reitzenstein, C. Schneider, S. Höfling, A. Forchel, C. Kruse, J. Kalden, and D. Hommel, *Nature (London)* **460**, 245 (2009).
- [16] F. Albert, C. Hopfmann, A. Eberspächer, F. Arnold, M. Emmerling, C. Schneider, S. Höfling, A. Forchel, M. Kamp, J. Wiersig, and S. Reitzenstein, *Appl. Phys. Lett.* **101**, 021116 (2012).
- [17] S. M. Ulrich, C. Gies, S. Ates, J. Wiersig, S. Reitzenstein, C. Hofmann, A. Löffler, A. Forchel, F. Jahnke, and P. Michler, *Phys. Rev. Lett.* **98**, 043906 (2007).
- [18] M. Nomura, N. Kumagai, S. Iwamoto, Y. Ota, and Y. Arakawa, *Nat. Phys.* **6**, 279 (2010).
- [19] M. Kira, S. W. Koch, R. P. Smith, A. E. Hunter, and S. T. Cundiff, *Nat. Phys.* **7**, 799 (2011).
- [20] Y. Chu, A. M. Mintairov, Y. He, J. L. Merz, N. A. Kalyuzhnyy, V. M. Lantratov, and S. A. Mintairov, *Phys. Lett. A* **373**, 1185 (2009).
- [21] Y. Chu, A. M. Mintairov, Y. He, J. L. Merz, N. A. Kalugnyy, V. M. Lantratov, and S. A. Mintairov, *Phys. Status Solidi C* **8**, 325 (2011).
- [22] See the Supplemental Material at <http://link.aps.org/supplemental/10.1103/PhysRevLett.113.093902>, which includes Refs. [23–27].
- [23] D. F. Walls and G. J. Milburn, *Quantum Optics*, 2nd ed. (Springer, Berlin, 2008).
- [24] R. J. Glauber, *Phys. Rev.* **131**, 2766 (1963).
- [25] E. C. G. Sudarshan, *Phys. Rev. Lett.* **10**, 277 (1963).
- [26] M. Kira and S. W. Koch, *Prog. Quantum Electron.* **30**, 155 (2006).
- [27] M. Kira, F. Jahnke, W. Hoyer, and S. W. Koch, *Prog. Quantum Electron.* **23**, 189 (1999).
- [28] E. T. Jaynes and F. W. Cummings, *Proc. IEEE* **51**, 89 (1963).
- [29] G. Lindblad, *Commun. Math. Phys.* **48**, 119 (1976).
- [30] M. Kira and S. W. Koch, *Phys. Rev. A* **73**, 013813 (2006).
- [31] S. W. Koch, M. Kira, G. Khitrova, and H. M. Gibbs, *Nat. Mater.* **5**, 523 (2006).
- [32] M. Kira and S. W. Koch, *Phys. Rev. A* **78**, 022102 (2008).
- [33] M. Aßmann and M. Bayer, *Phys. Rev. A* **84**, 053806 (2011).
- [34] A. Carmele, A. Knorr, and M. Richter, *Phys. Rev. B* **79**, 035316 (2009).
- [35] M. Mootz, M. Kira, S. W. Koch, A. E. Almand-Hunter, and S. T. Cundiff, *Phys. Rev. B* **89**, 155301 (2014).
- [36] A. E. Almand-Hunter, H. Li, S. T. Cundiff, M. Mootz, M. Kira, and S. W. Koch, *Nature (London)* **506**, 471 (2014).
- [37] M. Kira, F. Jahnke, and S. W. Koch, *Phys. Rev. Lett.* **82**, 3544 (1999).

Supplementary Material to Paper I

Supplemental Material:

Quantum-memory effects in the emission of quantum-dot microcavities

C. Berger,^{1,*} U. Huttner,¹ M. Mootz,¹ M. Kira,¹ S. W. Koch,¹ J.-S. Tempel,²
M. Aßmann,² M. Bayer,^{2,3} A. M. Mintairov,^{3,4} and J. L. Merz⁴

¹*Department of Physics, Philipps-Universität Marburg, Renthof 5, D-35032 Marburg, Germany*

²*Experimentelle Physik 2, Technische Universität Dortmund, D-44221 Dortmund, Germany*

³*Ioffe Physical-Technical Institute of the Russian Academy of Sciences, St. Petersburg, 194021, Russia*

⁴*Department of Electrical Engineering, University of Notre Dame, Notre Dame, IN, 46556, USA*

I. GENERAL IMPLICATIONS OF QUANTUM-OPTICAL RESPONSE THEORY

Classical spectroscopy measures matter's response as a function of pump field's amplitude, frequency, duration, or carrier envelope phase, i. e. the classical aspects of light. Quantum mechanically, the light field fluctuates around its classical value defined by the expectation value of the electric field. We call a distribution that uniquely defines these intrinsic fluctuations *quantum statistics*. For any fixed classical aspect of light, there exist infinitely many quantum-statistical forms that all correspond to different quantum fluctuations, cf. Refs. [10, 23]. Our analysis is guided by the rigorous steps one must undertake in order to find which aspects of matter's (optical) response are sensitive to quantum fluctuations of the light source. More specifically, Ref. [19] formulates a quantum-optical response theory that is based on a completely general argumentation; we next summarize its main points.

As defined by Glauber [24], quantum statistics of a high-quality pump laser is described by a coherent state $|\beta\rangle$ where β labels the complex-valued amplitude of the field. The optical response of any matter to $|\beta\rangle$ can be uniquely identified by a function $R_{|\beta\rangle}$; in other words, $R_{|\beta\rangle}$ labels all responses measured with classical spectroscopy by adjusting the pump laser's amplitude. We denote the matter's response to a real quantum-light source by $R_{|\text{QM}\rangle}$. As formulated by Sudershan [25], the $R_{|\beta\rangle}$ and $R_{|\text{QM}\rangle}$ are uniquely connected via a general relation

$$R_{|\text{QM}\rangle} = \int d^2\beta P^{|\text{QM}\rangle}(\beta) R_{|\beta\rangle}, \quad (\text{S1})$$

where $P^{|\text{QM}\rangle}(\beta)$ is the Glauber-Sudarshan function [24, 25] of the quantum source.

A classical field $|\beta\rangle$ has intensity $I_{\text{in}} \propto |\beta|^2$ defined by the average photon number $N = |\beta|^2$. In case the classical measured $R_{|\beta\rangle}$ depends linearly on N , i. e. $R_{|\beta\rangle} = a|\beta|^2 + b$, we find $R_{|\text{QM}\rangle} = \int d^2\beta (a|\beta|^2 + b) P^{|\text{QM}\rangle}(\beta) = aN + b$ for all sources because $P^{|\text{QM}\rangle}(\beta)$ is normalized and $\int d^2\beta P^{|\text{QM}\rangle}(\beta) |\beta|^2 = N$ produces the average photon number for all quantum sources. Therefore, the linear classical response is completely insensitive to the quantum fluctuations of the pump. Consequently, *the quantum-optical sensitivity must reside within the nonlinear contributions of $R_{|\beta\rangle}$* . In complex systems, such nonlinearities are related to many-body and/or quantum-optical correlations. As a key element of quantum-optical spectroscopy [26, 30, 31], specific forms of $R_{|\text{QM}\rangle}$ nonlinearities can be directly excited via suitably tailored quantum sources. As a result, quantum sources can characterize and control complicated processes much more accurately than the conventional classical spectroscopy does. Especially, this quantum-optical sensitivity is a gateway to identify individual quantum correlations in matter [19, 35, 36].

We seek for unexpected nonlinear responses to discover new quantum-optical effects in quantum-dot (QD) microcavities in the Letter. Since a linear response is uninteresting from a quantum-optical point of view, we remove it from the input/output (I/O) curves to isolate the true nonlinearity. When the I/O curve exhibits the oscillatory nonlinearities a linear fit contains also a constant contribution depending on the oscillation period which is unknown due to the unknown nature of the nonlinearities. In general, the line-removal does not affect the identification of the nonlinearities because they cannot be removed by a line. In this sense, removing a line from the I/O curve is just a visual aid that allows us to exclusively see the most interesting part of the data, i. e. the oscillatory nonlinearities. Since the quantum-optical sensitivity of the response is caused exclusively by the nonlinear response, the line-removal does also not affect the projection results presented in Fig. 3.

* Corresponding author.
christian.berger@physik.uni-marburg.de

II. QUANTUM-MEMORY OSCILLATIONS IN DIFFERENT EXPERIMENTS

To compare different measurements systematically, we introduce the following iterative procedure for the measured I/O intensities $I_{\text{in}}^{\text{org}}$ and $I_{\text{out}}^{\text{org}}$, respectively; superscript ‘‘org’’ denotes that the original intensities without any normalization procedure are used. We first define the region of interest (ROI) for $I_{\text{in}}^{\text{org}}$ where a linear fit $I_{\text{in}}^{\text{org}} = a I_{\text{in}}^{\text{org}} + b$ is performed to extract the linear part of $I_{\text{out}}^{\text{org}}$. As the second step, we determine $I_{\text{osc}}^{\text{org}} = I_{\text{out}}^{\text{org}} - I_{\text{in}}^{\text{org}}$ as the difference of the measured data and its linear fit. As the third step, we determine which input intensity $I_{\text{in}}^{\text{dip}}$ produces the first oscillation dip in $I_{\text{osc}}^{\text{org}}$. In other words, we find a unique I/O value $(I_{\text{in}}^{\text{dip}}, I_{\text{out}}^{\text{dip}})$ of the first oscillation dip. Since the I/O data has experimental noise, we low-pass filter the $I_{\text{osc}}^{\text{org}}$ data to determine the $(I_{\text{in}}^{\text{dip}}, I_{\text{out}}^{\text{dip}})$ point more accurately, which constitutes the fourth step of our algorithm. Since the $(I_{\text{in}}^{\text{dip}}, I_{\text{out}}^{\text{dip}})$ outcome depends slightly on the ROI choice we iterate steps 1-4 by setting the ROI to extend from $0.33 \times I_{\text{in}}^{\text{dip}}$ to $6 \times I_{\text{in}}^{\text{dip}}$ in step 1.

We iterate steps 1-4 until the dip position becomes stable to find a unique linear fit $I_{\text{in}}^{\text{org}}$ and dip positions for each measured data. These positions are used to scale input and output with $I_{\text{in}} = I_{\text{in}}^{\text{org}}/I_{\text{in}}^{\text{dip}}$ and $I_{\text{out}} = I_{\text{out}}^{\text{org}}/I_{\text{out}}^{\text{dip}}$. For later reference, we denote the linear fit of the scaled output as

$$I_{\text{lin}} = a_{\text{exp}} I_{\text{in}} + b_{\text{exp}}, \quad (\text{S2})$$

where the scaling coefficients follow from the linear fit of step 2, i. e. $a_{\text{exp}} = a I_{\text{in}}^{\text{dip}}/I_{\text{out}}^{\text{dip}}$ and $b_{\text{exp}} = b/I_{\text{out}}^{\text{dip}}$.

Computed I/O results are processed analogously as experiments. Since the computations do not contain random noise, iterations are not needed to locate the position of the first oscillation dip $(I_{\text{in}}^{\text{dip}}, I_{\text{out}}^{\text{dip}})$. However, the computed $I_{\text{out}}^{\text{org}}$ saturates faster than in the experiment such that the computational ROI includes some saturation aspects. To eliminate such saturation effects from the $I_{\text{osc}}^{\text{org}}$ identification, we use the same linear a_{exp} coefficient as in the experiment to describe the normalized linear computation $I_{\text{lin}} = a_{\text{exp}} I_{\text{in}} + b_{\text{num}}$. Technically, this is obtained by scaling the output with a slightly modified value $\tilde{I}_{\text{out}}^{\text{dip}}$, compared with $I_{\text{out}}^{\text{dip}}$, yielding $I_{\text{out}} = I_{\text{out}}^{\text{org}}/\tilde{I}_{\text{out}}^{\text{dip}}$. Typically, $\tilde{I}_{\text{out}}^{\text{dip}}$ is very close to $I_{\text{out}}^{\text{dip}}$ with only 1% difference.

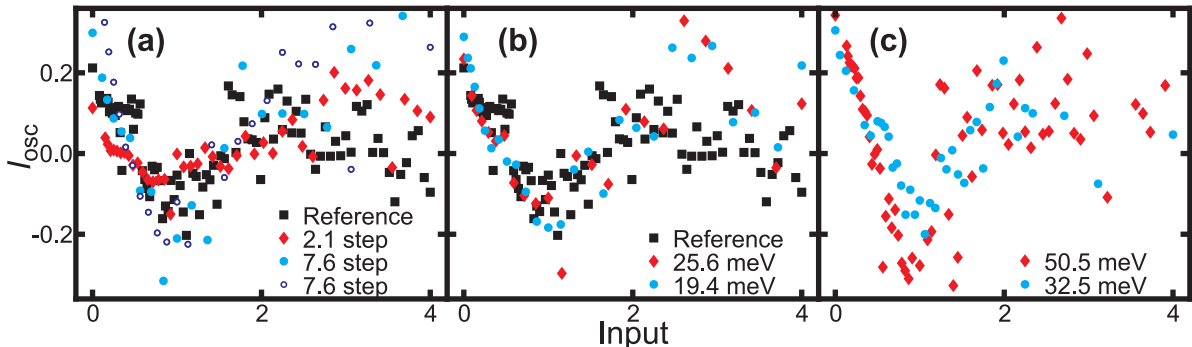


FIG. S1. Scaled experimental output after the subtraction of the linear part. (a) Dependence of output on intensity steps in input. Reference (squares) is compared with measurements having 2.1 (diamonds), 7.6 (filled circles), and 7.6 (open circles) times larger intensity steps than the reference. (b) Dependence on cavity detuning. Reference (squares) has 30.7 meV detuning while two other measurements have 25.6 meV (diamonds) and 19.4 meV (circles) detuning. (c) Effect of cavity mode. Output to cavity mode M2 (see Fig. 1) is measured for 50.5 meV (diamonds) and 32.5 meV (circles) detuning. Frames (a) and (b) were measured for cavity mode M1.

We check the repeatability of the I_{osc} oscillations by performing experiments under nominally the same conditions as the data shown in Fig. 2. Figure S1(a) presents the input dependence of I_{osc} that is constructed with the algorithm above; the squares are exactly the same data as presented in the Letter. We also have performed the I/O measurements with two different intensity steppings in the pump. The filled diamonds correspond to data measured with roughly 2.1 times larger intensity steps than for the reference while the intensity steps are 7.6 times the reference value for both open and filled circles. Since the different measurements have different noise levels the individual measurement points scatter quite differently and cannot be directly compared. However, the mean I/O curves coincide within the experimental scatter, verifying the repeatability of quantum-memory oscillations. In other words, all step sizes indeed reproduce essentially the same oscillatory nonlinearity, dipping roughly to 10% at the dip.

We also can change the detuning of the pump laser with respect to the emission energy. Figure S1(b) shows the measured I_{osc} when the detuning is 30.7 meV (squares), 25.6 meV (diamonds), and 19.4 meV (circles). As before, the squares correspond to the same data presented in Fig. 2. The mean curves still produce qualitatively similar

oscillatory nonlinearities, which verifies that quantum-memory effects emerge for a broad range of experimentally relevant situations. Since our photoluminescence spectrum shows three main emission resonances (M1-M3 see Fig. 1), we may directly analyze the cavity-mode dependence of the I_{osc} oscillations. Figure S1(c) shows the measured I_{osc} for the M2 mode. Diamonds correspond to 50.5 meV detuning while circles are measured with 32.5 meV. In both cases, the quantum-memory oscillations appear in the same way as for the M1 mode (compare Fig. S1(a)-(b)), but only the mean of 32.5 meV has a similar amplitude than the M1 data because 50.5 meV detuning produces roughly 40% increase in the nonlinear dip depth. We attribute this to a rather large change in the detuning, as discussed in more detail in connection with Fig. S2(a).

Our QD is so large that it hosts several close-by single-electron levels that can be independently excited. Therefore, it is straight forward to estimate the QD excitation for each level separately. In more detail, we estimate the inversion level by computing how much a single dot level is excited by our detuned pump laser. The maximum occupation of the excited state becomes then

$$f_{\text{max}} = \frac{1}{1 + \left| \frac{\Delta}{\Omega} \right|^2}, \quad (\text{S3})$$

based on Eq. (18.70) in Ref. [10], which presents f_{max} of an ideal two-level system without further coupling to a reservoir or other states. In other words, f_{max} estimates the upper limit of excitation for the most resonant dot level. In general, f_{max} depends on the detuning Δ between the two-level system and the exciting laser and the Rabi frequency Ω . In the study of our Letter, the pump laser is $\hbar\Delta = 28.7$ meV above this dot level. To estimate Ω , we measured the excitation power P of the pump at 75.4 MHz repetition rate and central photon energy $\hbar\omega = 1.76$ eV; it was $P = 30.4$ μ W for the maximum excitation used in Fig. 2 and four times lower at the first nonlinear dip. For a 2 μ m excitation spot, this gives 33.7 kV/cm as peak electric field for the 2 ps-long pump pulse. In principle, only a fraction of this pulse reaches the QD due to reflection at the cavity and features in the optical path such as microscope objective and cryostat windows. We ignore this ‘‘loss’’ and use $E = 33.7$ kV/cm as the upper limit. The Rabi frequency is determined by $\hbar\Omega = 2dE$ where d is the dipole of the transition. For the InP QDs, the upper limit of d is roughly 25e \AA , which yields $\hbar\Omega = 16.8$ meV as peak Rabi energy. By inserting Ω and Δ into Eq. (S3), we find $f_{\text{max}} = 0.26$ as the upper limit of excitation. At the nonlinear dip, the same estimate yields $f_{\text{max}} = 0.08$. Since this number is so small, it is impossible that other higher excited states could invert the system. In other words, this estimate shows convincingly that the system is certainly not inverted.

We also have computed the maximum occupation based on our microscopic model discussed in Sec. III. Including all dot levels, the actual computations yield $f_{\text{max}} = 0.07$ and 0.24 at the nonlinear dip and maximum power, respectively. These numbers agree well with the experimental estimate, showing that the oscillatory nonlinearities indeed appear in the excitation power regime well below inversion, (i. e. f_{max} remains smaller than 0.5). The detuned Rabi frequency $\Upsilon = \sqrt{|\Delta|^2 + |\Omega|^2}$ produces Rabi flopping faster than 144 fs for all pump intensities. Therefore the dot level oscillates at least 5 times during each radiative process, defined by the 0.8 ps radiative decay. In other words, quantum memory accumulated during many detuned Rabi flops contributes to emission even though the maximum excitation remains low. That the QD occupation at the used excitation powers stays well below unity is also suggested by the background emission, that is contributed by QDs off-resonant with the cavity modes, which scales linearly with excitation power, so that any effects from biexcitons can be excluded.

In addition, despite of the low lasing threshold, the output intensity still undergoes a jump by an order of magnitude when crossing the threshold. In our experiment we use excitation power densities which are well below those at which this jump occurs, so that it does not occur in the scanned power range.

III. THEORY OF QUANTUM-MEMORY EFFECTS

We explain the quantum-memory effects using the standard Jaynes–Cummings Hamiltonian [28] for a detuned QD with N electronic states inside a cavity. Each of the states can either be excited or unexcited defining 2^N different basis states $|S\rangle$. Additionally, the Hamiltonian contains classical pumping of the two-level system, yielding

$$\hat{H} = \hbar\omega(\hat{B}^\dagger\hat{B} + \frac{1}{2}) + \sum_{n=1}^N \hbar\omega_{21,n}\hat{P}_{z,n} - \hbar g \sum_{n=1}^N (\hat{B}^\dagger\hat{P}_n + \hat{B}\hat{P}_n^\dagger) - \sum_{n=1}^N (\alpha_L^*(t)\hat{P}_n + \alpha_L(t)\hat{P}_n^\dagger), \quad (\text{S4})$$

where \hat{B} and \hat{B}^\dagger are photon operators for a single-mode light field with energy $\hbar\omega$. The QD population is described by the population-inversion operator $\hat{P}_{z,n}$ while \hat{P}_n and \hat{P}_n^\dagger are the corresponding polarization operators for the dot state n . Mathematically, \hat{P}_n and \hat{P}_n^\dagger are the usual lowering and rising Pauli operators. The energy differences of the states $\hbar\omega_{21,n}$ are detuned against the cavity mode. The effective coupling strength between light and matter is chosen

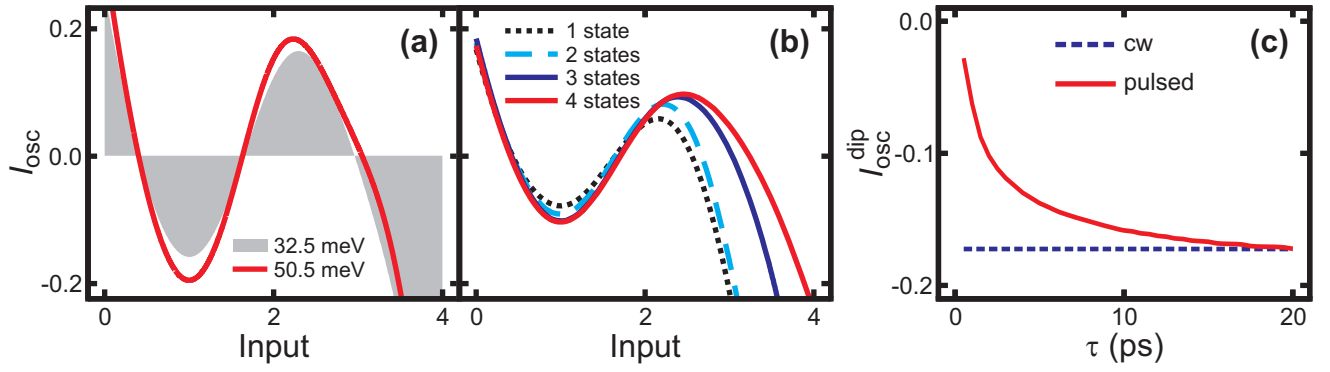


FIG. S2. Effect of detuning and state-number on oscillatory nonlinearities and normalized oscillation amplitude as function of pulse duration τ . (a) Normalized I_{osc} is plotted for $\hbar\Delta_L = 32.5$ meV (shaded area) and $\hbar\Delta_L = 50.5$ meV (solid line). (b) Normalized I_{osc} is presented for $N = 1$ (dotted line), $N = 2$ (dashed line), $N = 3$ (blue-solid line), and $N = 4$ (red-solid line) states. (c) Pulsed result (solid line) is compared with the cw computation (dashed line).

g for all states. In the Letter, we use the interaction picture that replaces $\hbar\omega_{21,n}$ in Eq. (S4) by the detuned energy $\hbar\delta_n = \hbar(\omega_{21,n} - \omega)$ and eliminates the pure photon part from the Hamiltonian.

The classical pump field is described by a complex-valued amplitude $\alpha_L(t)$. We use either a continuous wave (cw) or pulsed, $\alpha_L(t) = \alpha_0 e^{-\frac{t^2}{\tau^2}} e^{-i\omega_L t}$, where $\hbar\omega_L$ is the pump-photon energy and τ determines the pulse width. We then solve the time dynamics via the density matrix $\hat{\rho} = \sum_{n_1, n_2} \sum_{S_1, S_2} |S_1\rangle |n_1\rangle C_{n_2, S_2}^{n_1, S_1} \langle n_2| \langle S_2|$, where $|n_j\rangle$ is a Fock state of the quantized light and $|S_j\rangle$ denotes the basis states of the dot. The quantum dynamics of $\hat{\rho}$ is solved from the Liouville–von Neumann equation

$$i\hbar \frac{\partial}{\partial t} \hat{\rho}(t) = [\hat{H}, \hat{\rho}]_- + i\hbar \left(\gamma_z \sum_{n=1}^N \mathcal{L}[\hat{P}_{z,n}] + \gamma_a \sum_{n=1}^N \mathcal{L}[\hat{P}_n] + \kappa \mathcal{L}[\hat{B}] \right), \quad (\text{S5})$$

where we have added the Lindbladian, $\mathcal{L}[\hat{O}] = 2\hat{O}\hat{\rho}\hat{O}^\dagger - \hat{O}^\dagger\hat{O}\hat{\rho} - \hat{\rho}\hat{O}^\dagger\hat{O}$ [29], to account for the dephasing of polarization, population, and cavity photons with dephasing constants $\gamma = \gamma_z + \gamma_a$, $2\gamma_a$, and κ , respectively. The usual T_1 - and T_2 -decay times become equal when we set $\gamma_z = \gamma_a$, as it is done in our Letter.

We solve Eq. (S5) numerically, to compute the output intensity $I_{\text{out}}^{\text{org}} = \langle \hat{B}^\dagger \hat{B} \rangle$ defined at the steady state. In the same way, we compute numerically the correlations

$$\begin{aligned} \Pi_{-,n} &\equiv \Delta\langle \hat{B}^\dagger \hat{P}_n \rangle = \langle \hat{B}^\dagger \hat{P}_n \rangle - \langle \hat{B}^\dagger \rangle \langle \hat{P}_n \rangle, & \Pi_{z,n} &\equiv \Delta\langle \hat{B}^\dagger \hat{P}_{z,n} \rangle = \langle \hat{B}^\dagger \hat{P}_{z,n} \rangle - \langle \hat{B}^\dagger \rangle \langle \hat{P}_{z,n} \rangle, \\ \Delta\langle \hat{B}^\dagger \hat{B} \rangle &= \langle \hat{B}^\dagger \hat{B} \rangle - \langle \hat{B}^\dagger \rangle \langle \hat{B} \rangle, & & \\ \Delta\langle \hat{B}^\dagger \hat{B} \hat{P}_{z,n} \rangle &= \langle \hat{B}^\dagger \hat{B} \hat{P}_{z,n} \rangle - \langle \hat{B}^\dagger \rangle \Delta\langle \hat{B} \hat{P}_{z,n} \rangle - \langle \hat{B} \rangle \Delta\langle \hat{B}^\dagger \hat{P}_{z,n} \rangle - \langle \hat{P}_{z,n} \rangle \Delta\langle \hat{B}^\dagger \hat{B} \rangle - \langle \hat{B}^\dagger \rangle \langle \hat{B} \rangle \langle \hat{P}_{z,n} \rangle, \end{aligned} \quad (\text{S6})$$

that are used this Section and Fig. 2 to reveal the source of I_{osc} oscillations.

The density-matrix computation produces fully converging results when it contains 12 Fock states for the conditions studied. As system parameters, we use $\hbar g = 0.405$ meV, $\hbar\gamma = 0.32$ meV, and $\hbar\kappa = 0.8$ meV that are very typical values [11, 20, 21] for similar samples like ours. To explain the experimental observations in our Letter, we use the experimental parameters $\hbar\Delta_L = 30.7$ meV and $\tau = 2$ ps (pulsed) or $\tau = \infty$ (cw) for the pump. The individual $\delta_n = \omega_{21,n} - \omega$ define the state-cavity detuning. The experimental emission is best reproduced when we use $N = 4$ states that are detuned $\hbar\delta_1 = 2$ meV, $\hbar\delta_2 = 2.6$ meV, $\hbar\delta_3 = 4.58$ meV, and $\hbar\delta_4 = 8$ meV above the cavity mode, which yields a similar dot energetics as observed in a comparable system in Ref. [21]. The four dot states are either excited or unexcited, producing $2^4 = 16$ basis states. Altogether, $\hat{\rho}$ contains $(12 \times 16)^2 = 36864$ elements. The energy splitting $\hbar\omega \approx 2.5$ meV and exciton mass $m = 0.135$ predict a QD diameter very close to the estimated dot size of 75 nm when the dot is assumed spherical. Therefore, the chosen energy levels are consistent with the dot size.

Motivated by the measured Δ_L dependence of amplitude in oscillatory nonlinearities (Fig. S1(c)), it is interesting to check whether the computations explain this tendency. Figure S2(a) presents the computed I_{osc} for $\hbar\Delta_L = 32.5$ meV (shaded area) and $\hbar\Delta_L = 50.5$ meV (solid line). Increasing Δ_L yields 25% increase in the I_{osc} dip amplitude, which confirms the experimental change in Fig. S1(c). As explained in our Letter, I_{osc} results from the quantum memory accumulated during each pump-induced Rabi flop. Since the effective Rabi frequency Υ increases with growing detuning, higher Δ_L induces more flops and, thus, a larger quantum-memory accumulation, which provides an intuitive explanation for the detected Δ_L dependence. Naturally, a too large Δ_L will eventually decrease the

excitation emission when it becomes too nonresonant, which sets physical limits how much I_{osc} can be enhanced by Δ_L .

We also have investigated the effect of the coupling strength g on the oscillatory nonlinearities. We find that the scaled oscillation amplitude increases with decreasing coupling strength and scales as $\frac{1}{g}$, which again has a simple connection to the intuitive quantum-memory source. More specifically, lowering g means that the relative effect of pumping induced Rabi flopping, scaling with the pump (not g), becomes more prominent in the QD emission that scales with g . Therefore, the relative strength of quantum-memory effects increases with decreasing g . However, this argument holds only until g is large enough to favor single-mode emission. We also have verified that changing each g separately does not alter the overall I_{osc} behavior. In summary, the pump-dot detuning and g provide most control for the magnitude of I_{osc} .

It is also interesting to study how the quantum-memory oscillations are modified by the state number N included to the model. Therefore, we perform a computation where one, two, or three highest-energy states are eliminated from the computation. The full computation is solved with $N = 4$ states. Figure S2(b) shows the normalized I_{osc} for $N = 1$ (dotted line), $N = 2$ (dashed line), $N = 3$ (blue-solid line), and $N = 4$ (red-solid line) states. We see that the oscillation amplitude increases with elevated N . In addition, higher N yields an extended range for the second oscillation. Therefore, we conclude that the quantum-memory effects are slightly enhanced when the number of emitting states increases, but are not critically dependent on N . Additional numerical studies show that I_{osc} has only a weak dependence on the specific energy values of the dot states.

Even though the experiment is performed with a pulsed excitation, the switch-off analysis shown in Fig. 2(c) becomes significantly simpler when the steady-state emission of the cw pumping is analyzed. Therefore, we studied how I_{osc} of the pulsed excitation approaches the cw result by increasing the pulse duration τ . Figure S2(c) presents the magnitude of the normalized I_{osc} dip (solid line) as function of τ . As a clear trend, the pulsed excitation approaches the cw result. In particular, the $\tau = 2$ ps pulsed result is sufficiently close to the cw-case such that the basic features of quantum-memory oscillations can be studied with a cw computation.

A. Sources to quantum-dot emission

The quantum-emission dynamics of the Jaynes–Cummings model is already worked out, e. g., in a textbook [10] such that we only need to collect here the central equations. The light emission to the cavity mode is defined by the correlated intensity $\Delta\langle\hat{B}^\dagger\hat{B}\rangle$. As we generalize Eq. (23.42) of Ref. [10], we find that the output intensity follows from

$$\frac{\partial}{\partial t}\Delta\langle\hat{B}^\dagger\hat{B}\rangle = -2\kappa\Delta\langle\hat{B}^\dagger\hat{B}\rangle - 2g\sum_{n=1}^N\text{Im}[\Pi_{-,n}], \quad (\text{S7})$$

that contains the decay constant κ and couples to photon-assisted polarizations $\Pi_{-,n}$. The emission is driven by $\Pi_{-,n}$ whose dynamics becomes [10]

$$i\frac{\partial}{\partial t}\Pi_{-,n} = [\delta_n - i(\gamma + \kappa)]\Pi_{-,n} + s_n^{\text{SE}} + s_n^{\text{ST}} + s_n^{\text{QM}} + s_n^{\text{tri}}, \quad (\text{S8})$$

that contains four different sources. The $\Pi_{-,n}$ correlation is initiated by the *spontaneous-emission* source $s_n^{\text{SE}} = g\sum_{n'=1}^N\left[\langle\hat{P}_{n'}^\dagger\hat{P}_n\rangle - \langle\hat{P}_{n'}^\dagger\rangle\langle\hat{P}_n\rangle\right]$, whose diagonal part, i. e. $g[\langle\hat{P}_n^\dagger\hat{P}_n\rangle - \langle\hat{P}_n^\dagger\rangle\langle\hat{P}_n\rangle]$, is proportional to the incoherent occupation at the excited state of level n . The nondiagonal ($n' \neq n$) contributions result from the collective recombination processes where state n' is excited by recombining state n . These processes describe either sub- or super-radiant effects when N states collectively emit light to a single mode [27].

The spontaneous emission also enables the *stimulated contribution* $s_n^{\text{ST}} = 2g\langle\hat{P}_{z,n}\rangle\Delta\langle\hat{B}^\dagger\hat{B}\rangle$, that is a product of the population inversion of state n and correlated photon intensity. In other words, the more photons remain inside the cavity, the more stimulation of $\Pi_{-,n}$ processes emerges in the system. Besides stimulation, each emission also generates a *quantum-memory contribution* $s_n^{\text{QM}} = \Omega\Pi_{z,n}$, that is a product of a Rabi frequency $\Omega = 2(g\langle\hat{B}\rangle + \frac{\alpha_L(t)}{\hbar})$ and the photon-density correlation $\Pi_{z,n} = \Delta\langle\hat{B}^\dagger\hat{P}_{z,n}\rangle$. Intuitively, $\Pi_{z,n}$ records dot's previous emission events giving rise to quantum memory because it defines how excitation depends on the emitted photons; the exact form of quantum-memory accumulations is studied below. Also correlations involving three operators, $s_n^{\text{tri}} = 2g\Delta\langle\hat{B}^\dagger\hat{B}\hat{P}_{z,n}\rangle$, act as a source.

Equation (S8) can be solved exactly, $\Pi_{-,n}(t) = -i\int_{-\infty}^t dt' [s_n^{\text{ST}}(t') + s_n^{\text{QM}}(t') + s_n^{\text{SE}}(t') + s_n^{\text{tri}}(t')] e^{-i[\delta_n - i(\gamma + \kappa)](t-t')}$, in terms of its source terms. When this is inserted into Eq. (S7), we find

$$\frac{\partial}{\partial t}\Delta\langle\hat{B}^\dagger\hat{B}\rangle = 2g\int_{-\infty}^t dt'\text{Re}[S(t,t')] - 2\kappa\Delta\langle\hat{B}^\dagger\hat{B}\rangle, \quad (\text{S9})$$

where we have identified $S(t, t') = S^{\text{SE}}(t, t') + S^{\text{ST}}(t, t') + S^{\text{QM}}(t, t') + S^{\text{tri}}(t, t')$. Each of the macroscopic sources that appear are obtained from $S^{\text{type}}(t, t') = \sum_n s_n^{\text{type}}(t') e^{-i[\delta_n - i(\gamma + \kappa)](t - t')}$, where type refers to SE, ST, QM, or tri.

By solving Eq. (S9) in steady state, the emission becomes

$$\Delta\langle\hat{B}^\dagger\hat{B}\rangle = \frac{g}{\kappa} \sum_{n=1}^N \text{Im} \left[\frac{s_n^{\text{SE}} + s_n^{\text{ST}} + s_n^{\text{QM}} + s_n^{\text{tri}}}{\delta_n - i(\gamma + \kappa)} \right]. \quad (\text{S10})$$

This relation can be applied to determine the effect of spontaneous emission, stimulated emission, quantum memory, and three-particle correlations output, as done in Fig. 2(c) in our Letter. This cw analysis is simpler than the corresponding switch-off study with the pulsed excitation, because one does not need to integrate Eqs. (S8) and (S9). Also the $\Pi_{z,n}$ dynamics is worked out in Ref. [10] for $N = 1$ state so that we can directly study how the quantum memory is generated. By generalizing Eq. (23.42) of Ref. [10] for N states, we find an exact dynamics,

$$\begin{aligned} i\frac{\partial}{\partial t}\Pi_{z,n} = & -i(\kappa + 2\gamma_a)\Pi_{z,n} + g(\Delta\langle\hat{B}^\dagger\hat{B}^\dagger\rangle\langle\hat{P}_n\rangle - \Delta\langle\hat{B}^\dagger\hat{B}\rangle\langle\hat{P}_n^\dagger\rangle) \\ & + g\sum_{n'}(\langle\hat{P}_{n'}^\dagger\hat{P}_{z,n}\rangle - \langle\hat{P}_{n'}^\dagger\rangle\langle\hat{P}_{z,n}\rangle) + \frac{\Omega^*\Pi_{-,n} - \Omega\Pi_{+,n}}{2} + g[\Delta\langle\hat{B}^\dagger\hat{B}^\dagger\hat{P}_n\rangle - \Delta\langle\hat{B}^\dagger\hat{B}\hat{P}_n^\dagger\rangle]. \end{aligned} \quad (\text{S11})$$

The second term induces $\Pi_{z,n}$ when the system simultaneously contains squeezing correlation $\Delta\langle\hat{B}^\dagger\hat{B}^\dagger\rangle$ and polarization. The third term generates $\Pi_{z,n}$ spontaneously whenever the system has polarization or coherent $\langle\hat{P}_{n'}^\dagger\hat{P}_{z,n}\rangle$ contributions. Also the remaining sources exist only when coherences are present. In particular, Eq. (S11) identifies two main mechanisms for generating quantum-memory correlations; either pure coherence or a combination of polarization and squeezing induces $\Pi_{z,n}$.

IV. QUANTUM-OPTICAL SPECTROSCOPY

In our Letter, we measure the output intensity $I_{\text{out}}(\beta)$ as function of the input-laser's amplitude β or equivalent as function of photon number $N = |\beta|^2$ because our measurement is not phase sensitive. Unfortunately, lasers with arbitrary quantum statistics are not yet available in order to measure the output intensity $I_{\text{out}}^{|\lambda\rangle}$ as function of an arbitrary quantum state $|\lambda\rangle$. However,

$$I_{\text{out}}^{|\lambda\rangle} = \int d^2\beta P^{|\lambda\rangle}(\beta) I_{\text{out}}(\beta) \quad (\text{S12})$$

establishes a fundamental connection [25] between $I_{\text{out}}^{|\lambda\rangle}$ and a set of classical responses $I_{\text{out}}(\beta)$, where the Glauber–Sudarshan $P^{|\lambda\rangle}(\beta)$ function represents the quantum statistics of the desired light source. As demonstrated in Ref. [19], the projection (S12) can be efficiently implemented with the help of the so-called cluster-expansion transformation (CET), even when the measurement contains noise and is performed in a limited phase space $\beta \in \Gamma$. In particular, this work introduces an experimentally robust algorithm to project a set of measured I_{out} to any desired quantum response $I_{\text{out}}^{|\lambda\rangle}$. The extreme accuracy of this method is demonstrated by the high-precision characterization of biexcitons [35] and the discovery of a new quasiparticle, the dropletion [36].

Technically, the CET finds correlation coefficients $a_R(J)$ based on the set of measured $I_{\text{out}}(\beta)$. They are connected to physical correlations like mean, variance, and higher order cumulants. The explicit algorithm from measurement-to- $a_R(J)$ is provided in Appendix B of Ref. [35] for the phase insensitive measurements studied here. Once the $a_R(J)$ coefficients are known, they uniquely define any quantum response. As a consistency check, we first analyze the CET projection to a classical source $|\beta_0\rangle$, yielding [19]

$$I_{\text{CET}}(\beta) = \frac{\mathcal{N}_R}{4\Delta x_R^2} \sum_{J=0}^{C/2} (-1)^J a_R(J) W_J \left(\frac{|\beta|^2}{4\Delta x_R^2} \right), \quad W_J(x) = \frac{2}{\pi} e^{-2x} \sum_{k=0}^J \frac{2^{2J-k} (-x)^{J-k}}{k!(J-k)!(J-k)!}, \quad (\text{S13})$$

where $\mathcal{N}_R = \int_\Gamma d^2\beta I_{\text{out}}(|\beta|)$ is the norm and $\Delta x_R^2 \equiv \frac{1}{2\mathcal{N}_R} \int_\Gamma d^2\beta |\beta|^2 I_{\text{out}}(|\beta|)$ is the normalized variance. Both Δx_R^2 and $a_R(j)$ can be accurately determined from the high-precision measurements shown in our Letter. In practice, one adjusts the maximum number of clusters C such that $I_{\text{CET}}(\beta)$ reproduces the experimental input accurately. We use $C = 192$ clusters to project the data in the Letter and produce I/O curves resulting from pumping a QD with different quantum-light sources.

A. Projection to quantum sources

A thermal state is completely defined by its photon-number fluctuations $\Delta\langle B^\dagger B \rangle_{\text{th}} = \langle B^\dagger B \rangle_{\text{th}} \equiv \bar{n}$ which are equal to the average photon number since the first-order coherences $\langle B \rangle_{\text{th}}$ vanish [23]. The CET projection algorithm (S12) with a thermal state yields [19]

$$I_{\text{out}}^{|\text{th}\rangle} = \frac{\mathcal{N}_R}{\pi(2\Delta x_R^2 + \bar{n})} \sum_{J=0}^{C/2} \frac{a_R(J)}{J!} \left(\frac{-4\Delta x_R^2}{2\Delta x_R^2 + \bar{n}} \right)^J. \quad (\text{S14})$$

A squeezed vacuum state is characterized by the two-photon correlation $|\Delta\langle BB \rangle_{\text{sqz}}| = s$ that defines the average photon number N_{sqz} via $s \equiv \sqrt{N_{\text{sqz}}^2 + N_{\text{sqz}}}$. The CET projection of Eq. (S12) with squeezed vacuum produces [19]

$$I_{\text{out}}^{|\text{sqz}\rangle} = \frac{\mathcal{N}_R}{\pi\sqrt{S^2 - s^2}} \sum_{J=0}^{C/2} a_R(J) \left(\frac{-2\Delta x_R^2}{S^2 - s^2} \right)^J \sum_{k=0}^{J/2} \frac{[2S]^{J-2k} s^{2k}}{k!(J-2k)!}, \quad (\text{S15})$$

where we have identified $S \equiv 2\Delta x_R^2 + N_{\text{sqz}}$.

A Schrödinger-cat state is a superposition of two coherent states with common displacement β_0 along the x -quadrature and separation determined by γ . By choosing γ to be aligned parallel to β_0 , we obtain the so-called *stretching-cat* state [19]. The wave function is then $|\text{cat}\rangle \equiv \mathcal{N}_{\text{cat}} (|\beta_0 - \gamma\rangle + |\beta_0 + \gamma\rangle)$ with coherent states $|\beta_0 \pm \gamma\rangle$ and the normalization constant $\mathcal{N}_{\text{cat}} = (2 + 2e^{-2|\gamma|^2})^{-\frac{1}{2}}$. The average coherent displacement of the cat state becomes then $\langle B \rangle_{\text{cat}} = \beta_0$, while its squeezing correlation is $\Delta\langle BB \rangle_{\text{cat}} = \gamma^2$. As a result, this stretching-cat state is squeezed while having also coherence. The CET projection of Eq. (S12) with $|\text{cat}\rangle$ yields [19]

$$I_{\text{out}}^{|\text{cat}\rangle} = \frac{\mathcal{N}_R}{4\Delta x_R^2} \sum_{J=0}^{C/2} (-1)^J a_R(J) \mathcal{N}_{\text{cat}}^2 \left[W_J \left(\frac{|\beta_0 + \gamma|^2}{4\Delta x_R^2} \right) + W_J \left(\frac{|\beta_0 - \gamma|^2}{4\Delta x_R^2} \right) + 2e^{-2|\gamma|^2} \text{Re} \left[W_J \left(\frac{(\beta_0 + \gamma)^* (\beta_0 - \gamma)}{4\Delta x_R^2} \right) \right] \right]. \quad (\text{S16})$$

In the Letter, we choose β_0 and γ so that $|\text{cat}\rangle$ has the *same* average photon number as the coherent state $|\beta = \sqrt{|\beta_0|^2 + 1}\rangle$ while the $|\text{cat}\rangle$ state's fluctuations correspond to the addition of a single photon.

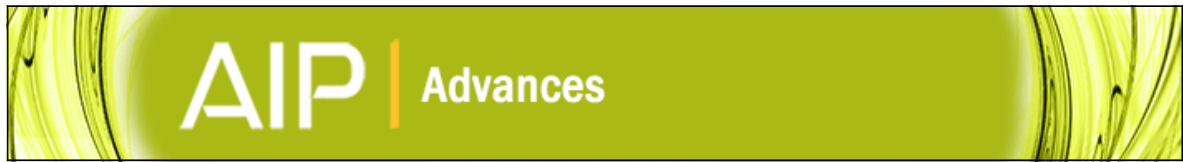
Paper II

C. Berger, C. Möller, P. Hens, C. Fuchs, W. Stolz, S. W. Koch,
A. Ruiz Perez, J. Hader, and J. V. Moloney

*Novel type-II material system for laser applications in the
near-infrared regime*

AIP Advances **5**, 047105 (2015)

DOI: 10.1063/1.4917180



Novel type-II material system for laser applications in the near-infrared regime

C. Berger, C. Möller, P. Hens, C. Fuchs, W. Stolz, S. W. Koch, A. Ruiz Perez, J. Hader, and J. V. Moloney

Citation: *AIP Advances* **5**, 047105 (2015); doi: 10.1063/1.4917180

View online: <http://dx.doi.org/10.1063/1.4917180>

View Table of Contents: <http://scitation.aip.org/content/aip/journal/adva/5/4?ver=pdfcov>

Published by the *AIP Publishing*

Articles you may be interested in

[GaSb-based composite quantum wells for laser diodes operating in the telecom wavelength range near 1.55- \$\mu\text{m}\$](#)

Appl. Phys. Lett. **106**, 101102 (2015); 10.1063/1.4914884

[Microscopic analysis of mid-infrared type-II “W” diode lasers](#)

Appl. Phys. Lett. **94**, 061106 (2009); 10.1063/1.3080216

[Strong near-infrared photoluminescence and absorption from Si/Si \$1-x\$ Ge \$x\$ type-II multiple quantum wells on bulk crystal SiGe substrates](#)

Appl. Phys. Lett. **83**, 2790 (2003); 10.1063/1.1615310

[GaAs-substrate-based long-wave active materials with type-II band alignments](#)

J. Vac. Sci. Technol. B **19**, 1501 (2001); 10.1116/1.1386380

[Optimum growth parameters for type-II infrared lasers](#)

J. Appl. Phys. **86**, 1796 (1999); 10.1063/1.370971

An advertisement for AIP's journal. It features a row of computer monitors in a library or office setting, each displaying the journal's cover. The cover shows a colorful, abstract image with the title 'computing' and 'SCIENCE ENGINEERING'. The text 'AIP'S JOURNAL OF COMPUTATIONAL TOOLS AND METHODS. AVAILABLE AT MOST LIBRARIES.' is overlaid on the bottom right of the image. The AIP logo is also visible in the bottom right corner of the image.

computing
SCIENCE ENGINEERING

AIP'S JOURNAL OF COMPUTATIONAL TOOLS AND METHODS.
AVAILABLE AT MOST LIBRARIES.

Novel type-II material system for laser applications in the near-infrared regime

C. Berger,^{1,a} C. Möller,¹ P. Hens,¹ C. Fuchs,¹ W. Stolz,¹ S. W. Koch,¹
A. Ruiz Perez,² J. Hader,³ and J. V. Moloney³

¹Department of Physics and Material Sciences Center, Philipps-Universität Marburg,
Renthof 5, 35032 Marburg, Germany

²NAsP_{III/V} GmbH, Am Knechtacker 19, 35041 Marburg, Germany

³Nonlinear Control Strategies Inc, 3542 N. Geronimo Ave., Tucson, AZ 85705, USA

(Received 10 March 2015; accepted 26 March 2015; published online 3 April 2015)

The design and experimental realization of a type-II “W”-multiple quantum well heterostructure for emission in the $\lambda > 1.2 \mu\text{m}$ range is presented. The experimental photoluminescence spectra for different excitation intensities are analyzed using microscopic quantum theory. On the basis of the good theory–experiment agreement, the gain properties of the system are computed using the semiconductor Bloch equations. Gain values comparable to those of type-I systems are obtained. © 2015 Author(s). All article content, except where otherwise noted, is licensed under a Creative Commons Attribution 3.0 Unported License. [<http://dx.doi.org/10.1063/1.4917180>]

Semiconductor laser systems in the near-infrared regime have a wide range of applications, especially in optical data transfer and telecommunication.^{1,2} Due to the absorption properties of optical fibers, wavelengths greater than $1.2 \mu\text{m}$ are particularly important. More recently, vertical-external-cavity surface-emitting lasers (VECSELs) with high output power, the possibility of intra cavity frequency conversion via nonlinear crystals, and their ability of short-pulse generation have become increasingly important for a wide range of applications.^{3–5}

While the flexibility of using different semiconductor alloys, quantum confinement and/or strain allows the sample designers to access a wide variety of emission wavelengths, it is often difficult to optimize the gain and simultaneously reduce the intrinsic losses. Especially for longer wavelength applications, Auger losses lead to prominent non-radiative carrier recombination and introduce significant heating in the structures.^{6,7} Therefore, it can become desirable to utilize a somewhat more complex design, which combines two materials with relatively large band gaps in a type-II setup, where electrons and holes are spatially separated in neighboring quantum wells and the optical recombination occurs across the interfaces.⁸ In such type-II systems, more degrees of freedom are available in the design process than in a traditional type-I configuration. Thus, the gain can be optimized while, at the same time, Auger losses can be controlled.⁹

Pioneering work in this field has been presented by Meyer et al., Kudo et al., and Vurgaftman et al. who introduced type-II “W”-material systems as active region of a laser setup.^{10–12} These structures consist of a sandwich configuration involving two different materials (see Fig. 1) whose composition and well width can be adjusted independently to achieve the desired type-II transition energy. Making use of the possibilities to independently adjust the individual band gaps and to some degree also the band alignment the resulting type-II energy difference can be tailored.

In this paper, we report on the experimental realization, the luminescence properties and the theoretical modeling of a gain structure that can be used in an optically pumped VECSEL with an emission wavelength of $\lambda > 1.2 \mu\text{m}$. For this purpose, we construct a type-II “W”-design for

^aElectronic mail: christian.berger@physik.uni-marburg.de



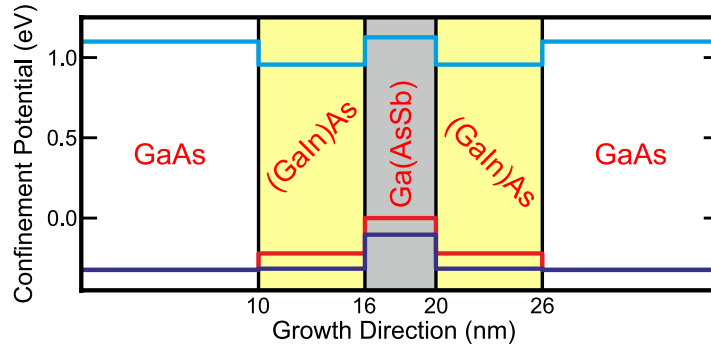


FIG. 1. Typical confinement potentials of electrons and holes for type-II alignment. In growth direction the layers of the semiconductor heterostructure consist of GaAs, $(\text{Ga}_{1-x}\text{In}_x)\text{As}$, $\text{Ga}(\text{As}_{1-y}\text{Sb}_y)$, $(\text{Ga}_{1-x}\text{In}_x)\text{As}$, and GaAs.

a material system consisting of $(\text{Ga}_{1-x}\text{In}_x)\text{As}$ and $\text{Ga}(\text{As}_{1-y}\text{Sb}_y)$ quantum wells. The growth of these samples is analyzed by high resolution X-ray diffraction (HR-XRD) measurements. Their experimentally obtained photoluminescence (PL) spectra for various optical excitation densities are compared to those predicted by a fully microscopic theory. This many-body theory is based on the multi-band semiconductor luminescence^{13,14} and Bloch^{14,15} equations as implemented in the software SimuLase.¹⁶ The predictive abilities of this theory allow us to present absorption spectra by utilizing independently determined material parameters only.

Samples of the type-II “W”-multiple quantum well heterostructure (MQWH) were grown by metal organic vapor phase epitaxy (MOVPE) using a commercial Aixtron horizontal Aix 200-gas foil rotation (GFR) reactor system. We held the reactor pressure at 50 mbar under H_2 -carrier gas. The standard group-III precursors triethylgallium (TEGa) and trimethylindium (TMIn) in combination with tertiarybutylarsine (TBAs), tertiarybutylphosphine (TBP), and triethylantimony (TESb) were applied. Typical growth rates were chosen at 0.4 nm/s. All structures were grown on semi-insulating GaAs substrates with exact (001) ($\pm 0.1^\circ$) orientation. Prior to epitaxial growth we prepared the substrates in a TBAs-stabilized bake-out step to remove the oxide layer. The 250 nm thick GaAs buffer layer was grown at 600 °C, while the highly strained type-II “W”-layer stack was deposited at 550 °C. To allow for strain compensation of the active compressively strained “W”-MQWH stack, additional tensile-strained $\text{Ga}(\text{AsP})$ -barrier layers with small P contents were incorporated in the layer stack.

The HR-XRD pattern ((004)-reflection) of two samples with different active type-II “W”-MQWH are shown in Fig. 2. We obtained the simulated HR-XRD pattern by applying a full dynamical description as detailed in Ref. 17. The evaluated sample parameters (thicknesses and respective compositions) are indicated in the inset of Fig. 2 for the sample A and B, respectively.

In order to record spectrally resolved photoluminescence measurements, we used a germanium detector in combination with a monochromator. A continuous-wave argon ion laser was employed for optical excitation at 514 nm. The spot size on the sample was approximately 160 μm (full width at half maximum) in diameter. All our measurements were performed with excitation powers varying over several orders of magnitude. Their respective spectra are shown in Fig. 3 (a) (sample A) and 3 (b) (sample B). Sample A exhibits its peak intensity at about 1.06 eV corresponding to a wavelength of 1170 nm. Due to the higher Sb content in the $\text{Ga}(\text{As}_{1-y}\text{Sb}_y)$ hole-confining wells, sample B exhibits its peak intensity at about 1.01 eV corresponding to a wavelength of 1228 nm. A slight blue shift is observed for intermediate excitation densities until a red shift occurs due to saturation, which involves excessive heating of the sample.

To analyze the experimental results, we use the fully microscopic semiconductor luminescence and Bloch equations. The single-particle properties are obtained by evaluating an 8×8 Luttinger $\mathbf{k} \cdot \mathbf{p}$ model for the designed heterostructure to determine the band structure and the electron and hole wave-functions.^{18,19} Strain effects between the different layers of the semiconductor heterostructure are treated as described in Ref. 20.

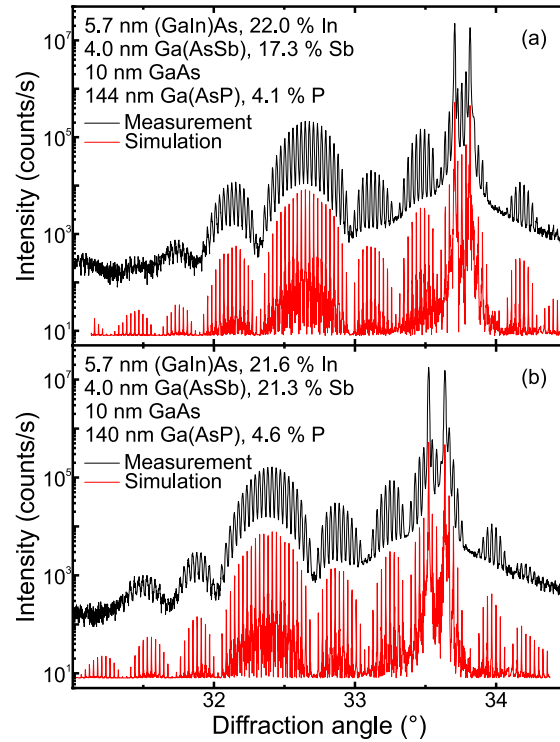


FIG. 2. HR-XRD pattern of sample A/B with simulation fit is presented in frame (a)/(b). The measurement is offset by a factor 10 for better visibility.

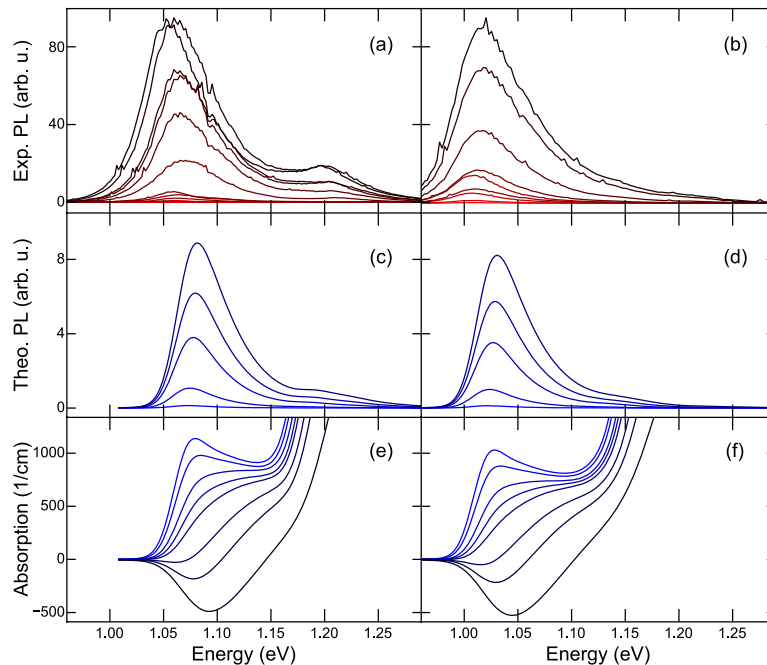


FIG. 3. Experimental and theoretical PL and theoretical absorption spectra. The left/right column shows results of sample A/B. (a) and (b) Experimental PL spectra are shown for excitation powers ranging from 0.1 to 400 mW (bottom to top) for sample A and from 0.5 to 150 mW (bottom to top) for sample B. (c) and (d) Corresponding theoretical PL spectra for carrier densities of $0.1 - 1 \times 10^{12}/\text{cm}^2$ (bottom to top) are plotted. (e) and (f) The respective theoretical absorption spectra for carrier densities of $0.1 - 3 \times 10^{12}/\text{cm}^2$ (top to bottom) are depicted.

In the next step, we calculate the dipole matrix elements $d_{\lambda,\nu}(\mathbf{k})$ between different sub bands λ and ν and the Coulomb matrix elements,²¹

$$V_{|\mathbf{k}-\mathbf{q}|}^{\lambda,\lambda',\lambda'',\lambda'''} = \frac{2\pi e^2}{\epsilon_0} \int dz dz' \psi_{\lambda'}^*(z) \psi_{\lambda}^*(z') \frac{e^{-|\mathbf{k}-\mathbf{q}||z-z'|}}{|\mathbf{k}-\mathbf{q}|} \times \psi_{\lambda''}(z') \psi_{\lambda'''}(z), \quad (1)$$

where ϵ_0 is the background refractive index. Changes in the confinement potential due to local charge inhomogeneities are included by solving the microscopic Schrödinger–Poisson equation.²²

Using these results, we calculate the PL via the semiconductor luminescence equations,^{13,14} assuming thermal equilibrium for the carrier distributions $f_{\lambda,\mathbf{k}}^{e/h}$ of electrons and holes in their respective bands. Since the spontaneous emission is a purely quantum-optical effect, we have to quantize the light field and introduce the creation and annihilation operator for photons of light mode with frequency $\omega_q = cq$ as \hat{B}_q^\dagger and \hat{B}_q .¹⁴ We now examine the dynamics of the following quantities: The photon-assisted polarization $\Pi_{\lambda,\nu,\mathbf{k},q} \equiv \langle \hat{B}_q^\dagger p_{\lambda,\nu,\mathbf{k}} \rangle$, where $p_{\lambda,\nu,\mathbf{k}}$ is the microscopic polarization, and the photon-number-like correlations $N_{q',q} \equiv \langle \hat{B}_q^\dagger \hat{B}_{q'} \rangle$,

$$\begin{aligned} i\hbar \frac{\partial}{\partial t} \Pi_{\lambda,\nu,\mathbf{k},q} &= (\mathcal{E}_{\lambda,\lambda,\mathbf{k}}^e + \mathcal{E}_{\nu,\nu,\mathbf{k}}^h - \hbar\omega_q) \Pi_{\lambda,\nu,\mathbf{k},q} \\ &\quad + \Omega_{\lambda,\nu,\mathbf{k},q}^{\text{sp}} - (1 - f_{\lambda,\mathbf{k}}^e - f_{\nu,\mathbf{k}}^h) \Omega_{\lambda,\nu,\mathbf{k},q}^{\text{st}}, \\ \frac{\partial}{\partial t} N_{q',q} &= i(\omega_q - \omega_{q'}) N_{q',q} + \sum_{\lambda,\nu,\mathbf{k}} (d_{\lambda,\nu}(\mathbf{k},q) \Pi_{\lambda,\nu,\mathbf{k},q'}^* \\ &\quad + d_{\lambda,\nu}(\mathbf{k},q')^* \Pi_{\lambda,\nu,\mathbf{k},q}), \end{aligned} \quad (2)$$

with the Coulomb renormalized energies $\mathcal{E}_{\lambda,\lambda,\mathbf{k}}^{e/h}$. The photon-assisted polarization is driven by two source terms representing the spontaneous emission $\Omega_{\lambda,\nu,\mathbf{k},q}^{\text{sp}}$ and the stimulated emission $\Omega_{\lambda,\nu,\mathbf{k},q}^{\text{st}}$, respectively. The electrons and holes in the structure are assumed to be in a quasi-equilibrium Fermi-Dirac configuration with the density $n_{e/h} = \sum_{\lambda,\mathbf{k}} f_{\lambda,\mathbf{k}}^{e/h}$.

While the microscopic modeling is based on the assumption that the structures are perfect, the real systems have unavoidable growth-related impurities and imperfections, e.g. thickness fluctuations of layers and/or small changes in the material composition. We model these effects phenomenologically by convolving our computed spectra with a Gaussian distribution of a fitted width.²³ In a way, we can interpret the resulting inhomogeneous broadening as a measure for the experimentally realized sample quality.

Figures 3(c) and 3(d) present the computed PL calculations for both samples assuming carrier densities of $0.1 - 1 \times 10^{12}/\text{cm}^2$ at room temperature. Using an inhomogeneous broadening of 25 meV for both samples, we obtain very good agreement with the experimental results. In particular, the main peaks have the same shape and also the shoulder around 1.2 eV with its relative decrease for increasing Sb content agrees well with the experiments. Looking at the theory–experiment comparison for sample A with an Sb content of 17.3 % in Figs. 3(a) and 3(c), we notice a slight difference in the energetic position of the main peak. This difference could be due to a 1.7 % higher Sb content using the nominal well width or a 0.3 % higher In content when the (GaIn)As well thickness is simultaneously increased by 1 nm. However, these deviations are well within the typical uncertainties for real samples. Remarkably, for sample B, Figs. 3(b) and 3(d), we find an excellent agreement with the nominal structure parameters even without any adjustments.

On the basis of our accurate reproduction of experimental PL, we can now use the optimized structure parameters to compute the expected gain properties. For this purpose, we evaluate the semiconductor Bloch equations,^{14,15}

$$\begin{aligned} \frac{d}{dt} p_{\lambda,\nu,\mathbf{k}}(t) &= -\frac{i}{\hbar} \sum_{\lambda',\nu'} [\mathcal{E}_{\lambda,\lambda',\mathbf{k}}^e \delta_{\nu,\nu'} + \mathcal{E}_{\nu,\nu',\mathbf{k}}^h \delta_{\lambda,\lambda'}] p_{\lambda',\nu',\mathbf{k}}(t) \\ &\quad - \frac{i}{\hbar} [1 - f_{\lambda,\mathbf{k}}^e - f_{\nu,\mathbf{k}}^h] \mathcal{U}_{\lambda,\nu,\mathbf{k}}(t) + \frac{d}{dt} p_{\lambda,\nu,\mathbf{k}}(t) \Big|_{\text{corr}}, \end{aligned} \quad (3)$$

with the microscopic polarization $p_{\lambda,\nu,\mathbf{k}}$, the Coulomb renormalized energies \mathcal{E} , and the Coulomb renormalized field \mathcal{U} ,

$$\mathcal{E}_{\lambda,\lambda',\mathbf{k}}^e = e_{\lambda,\mathbf{k}}^e \delta_{\lambda,\lambda'} - \sum_{\lambda'',q} V_{|\mathbf{k}-\mathbf{q}|}^{\lambda,\lambda'',\lambda',\lambda''} f_{\lambda'',q}^e, \quad (4)$$

$$\mathcal{E}_{\nu,\nu',\mathbf{k}}^h = e_{\nu,\mathbf{k}}^h \delta_{\nu,\nu'} - \sum_{\nu'',q} V_{|\mathbf{k}-\mathbf{q}|}^{\nu,\nu'',\nu,\nu''} f_{\nu'',q}^h, \quad (5)$$

$$\mathcal{U}_{\lambda,\nu,\mathbf{k}} = -d_{\lambda,\nu}(\mathbf{k})E(t) - \sum_{\lambda',\nu'} \sum_q V_{|\mathbf{k}-\mathbf{q}|}^{\lambda,\nu',\lambda',\nu'} p_{\lambda',\nu',q}. \quad (6)$$

$E(t)$ describes a weak probe pulse. Higher order scattering processes are summarized inside the last term of Eq. (3). We treat electron–electron and electron–phonon scattering at the level of the second Born approximation.^{19,21} From the microscopic polarization, we obtain the absorption/gain spectra of the system via $\alpha(\omega) \propto \omega \text{Im} [\sum_{\lambda,\nu,\mathbf{k}} d_{\lambda,\nu}(\mathbf{k}) p_{\lambda,\nu,\mathbf{k}}(\omega) / E(\omega)]$.

Examples of the results are shown in Figs. 3(e) and 3(f) for carrier densities ranging from 0.1 to $3 \times 10^{12}/\text{cm}^2$. We obtain gain for carrier densities above $2 - 3 \times 10^{12}/\text{cm}^2$ with the gain maxima reaching 500/cm for a carrier density of $3 \times 10^{12}/\text{cm}^2$. These values are in the same order of magnitude as those of typical type-I structures²⁴ indicating that the designed “W”-structures should perform well in laser applications.

In conclusion, we designed and experimentally realized a type-II gain medium and theoretically analyzed the measured PL spectra. On the basis of these results, we can conclude that this material system is very promising for laser applications.

ACKNOWLEDGMENTS

The Marburg work is a project of the Sonderforschungsbereich 1083 funded by the Deutsche Forschungsgemeinschaft (DFG). The work at Nonlinear Control Strategies Inc. is supported via STTR Phase II, Contract # FA9550-13-C-0009.

- ¹ E. Murphy, “The semiconductor laser: Enabling optical communication,” *Nature Photon.* **4**, 287–287 (2010).
- ² G. P. Agrawal, *Fiber-Optic Communication Systems*, 4th ed. (John Wiley & Sons, Hoboken, NJ, 2010).
- ³ M. Kuznetsov, F. Hakimi, R. Sprague, and A. Mooradian, “High-power (>0.5-W CW) diode-pumped vertical-external-cavity surface-emitting semiconductor lasers with circular TEM/sub 00/beams,” *IEEE Photon. Technol. Lett.* **9**, 1063–1065 (1997).
- ⁴ A. C. Tropper, H. D. Foreman, A. Garnache, K. G. Wilcox, and S. H. Hoogland, “Vertical-external-cavity semiconductor lasers,” *J. Phys. D: Appl. Phys.* **37**, R75–R85 (2004).
- ⁵ U. Keller and A. C. Tropper, “Passively modelocked surface-emitting semiconductor lasers,” *Phys. Rep.* **429**, 67–120 (2006).
- ⁶ A. R. Adams, M. Silver, and J. Allam, “Semiconductor optoelectronic devices,” in *High Pressure in Semiconductor Physics II* (Elsevier, San Diego, CA, London, 1998), pp. 301–352.
- ⁷ A. D. Andreev and E. P. O’Reilly, “Theoretical study of Auger recombination in a GaInNAs 1.3 μm quantum well laser structure,” *Appl. Phys. Lett.* **84**, 1826–1828 (2004).
- ⁸ M. Peter, K. Winkler, M. Maier, N. Herres, J. Wagner, D. Fekete, K. H. Bachem, and D. Richards, “Realization and modeling of a pseudomorphic (GaAs1-xSbx–InyGa1-yAs)/GaAs bilayer-quantum well,” *Appl. Phys. Lett.* **67**, 2639–2641 (1995).
- ⁹ G. G. Zegrya and A. D. Andreev, “Mechanism of suppression of Auger recombination processes in type-II heterostructures,” *Appl. Phys. Lett.* **67**, 2681–2683 (1995).
- ¹⁰ J. R. Meyer, C. A. Hoffman, F. J. Bartoli, and L. R. Ram-Mohan, “Type-II quantum-well lasers for the mid-wavelength infrared,” *Appl. Phys. Lett.* **67**, 757 (1995).
- ¹¹ M. Kudo, K. Ouchi, J.-i. Kasai, and T. Mishima, “Low-lattice-strain long-wavelength GaAsSb/GaInAs type-II quantum wells grown on GaAs substrates,” *Jpn. J. Appl. Phys.* **41**, L1040–L1042 (2002).
- ¹² I. Vurgaftman, W. W. Bewley, C. L. Canedy, C. S. Kim, J. R. Lindle, M. Kim, and J. R. Meyer, “Antimonide type-II “W” lasers,” in *Mid-infrared Semiconductor Optoelectronics* (Springer, London, 2006), pp. 189–217.
- ¹³ M. Kira and S. W. Koch, “Many-body correlations and excitonic effects in semiconductor spectroscopy,” *Prog. Quantum Electron.* **30**, 155–296 (2006).
- ¹⁴ M. Kira and S. W. Koch, *Semiconductor Quantum Optics* (Cambridge University Press, Cambridge, 2012).
- ¹⁵ H. Haug and S. W. Koch, *Quantum Theory of the Optical and Electronic Properties of Semiconductors*, 5th ed. (World Scientific Publ., Singapore, 2009).
- ¹⁶ Nonlinear Control Strategies Inc., <http://www.nlcstr.com/simulase.htm>.
- ¹⁷ L. De Caro, C. Giannini, and L. Tapfer, “Determination of the lattice strain and chemical composition of semiconductor heterostructures by high-resolution x-ray diffraction,” *J. Appl. Phys.* **79**, 4101–4110 (1996).
- ¹⁸ J. Hader, N. Linder, and G. H. Döhler, “k·p theory of the Franz-Keldysh effect,” *Phys. Rev. B* **55**, 6960–6974 (1997).
- ¹⁹ W. W. Chow and S. W. Koch, *Semiconductor-Laser Fundamentals: Physics of the Gain Materials* (Springer, Berlin, Heidelberg, New York, 1999).

- ²⁰ S. Chuang, "Efficient band-structure calculations of strained quantum wells," *Phys. Rev. B* **43**, 9649–9661 (1991).
- ²¹ J. Hader, S. W. Koch, and J. V. Moloney, "Microscopic theory of gain and spontaneous emission in GaInNAs laser material," *Solid-State Electron.* **47**, 513–521 (2003).
- ²² D. Ahn and S. L. Chuang, "Model of the field-effect quantum-well laser with free-carrier screening and valence band mixing," *J. Appl. Phys.* **64**, 6143–6149 (1988).
- ²³ J. Hader, J. V. Moloney, S. W. Koch, and W. W. Chow, "Microscopic modeling of gain and luminescence in semiconductors," *IEEE J. Select. Topics Quantum Electron.* **9**, 688–697 (2003).
- ²⁴ J. V. Moloney, J. Hader, and S. W. Koch, "Quantum design of semiconductor active materials: laser and amplifier applications," *Laser Photon. Rev.* **1**, 43 (2007).

Paper III

S. Gies, C. Kruska, **C. Berger**, P. Hens, C. Fuchs, A. Ruiz Perez,
N. W. Rosemann, J. Veletas, S. Chatterjee, W. Stolz, S. W. Koch,
J. Hader, J. V. Moloney, and W. Heimbrodt

*Excitonic transitions in highly efficient (GaIn)As/Ga(AsSb) type-II
quantum-well structures*

Applied Physics Letters **107**, 182104 (2015)

DOI: 10.1063/1.4935212



Excitonic transitions in highly efficient (GaIn)As/Ga(AsSb) type-II quantum-well structures

S. Gies, C. Kruska, C. Berger, P. Hens, C. Fuchs, A. Ruiz Perez, N. W. Rosemann, J. Veletas, S. Chatterjee, W. Stolz, S. W. Koch, J. Hader, J. V. Moloney, and W. Heimbrodt

Citation: *Applied Physics Letters* **107**, 182104 (2015); doi: 10.1063/1.4935212

View online: <http://dx.doi.org/10.1063/1.4935212>

View Table of Contents: <http://scitation.aip.org/content/aip/journal/apl/107/18?ver=pdfcov>

Published by the *AIP Publishing*

Articles you may be interested in

Type II InAs/GaAsSb quantum dots: Highly tunable exciton geometry and topology
Appl. Phys. Lett. **107**, 183101 (2015); 10.1063/1.4934841

Signature of optical absorption in highly strained and partially relaxed InP/GaAs type-II quantum well superlattice structures
J. Appl. Phys. **112**, 093505 (2012); 10.1063/1.4758472

Quantum beats of type-I and type-II excitons in an $\text{In}_x\text{Ga}_{1-x}\text{As}/\text{GaAs}$ strained single quantum well
J. Appl. Phys. **112**, 043522 (2012); 10.1063/1.4748339

Optical studies of type-I GaAs $1 - x\text{Sb}_x / \text{GaAs}$ multiple quantum well structures
J. Appl. Phys. **105**, 123523 (2009); 10.1063/1.3153975

Modeling and analysis of photomodulated reflectance and double crystal x-ray diffraction measurements of tensilely strained InGaAs/InGaAsP quantum well structures
J. Appl. Phys. **83**, 4909 (1998); 10.1063/1.367292

An advertisement for COMSOL Multiphysics simulation. The background is a dark image of a car's front end. On the left, the text 'MULTIPHYSICS SIMULATION' is written in large, bold, white letters, with 'Modeling and App Design Stories' below it. A green lightning bolt icon is positioned to the right of the text. On the right side, there are two small inset images showing simulation results: one with a color-coded stress or temperature distribution on a mechanical part, and another showing a blue and yellow field on a curved surface. At the bottom right, a blue button with white text says 'READ LATEST ISSUE >>'. The COMSOL logo is in the bottom left corner.

**MULTIPHYSICS
SIMULATION**
Modeling and App Design Stories

READ LATEST ISSUE >>

COMSOL

Excitonic transitions in highly efficient (GaIn)As/Ga(AsSb) type-II quantum-well structures

S. Gies,¹ C. Kruska,¹ C. Berger,¹ P. Hens,¹ C. Fuchs,¹ A. Ruiz Perez,² N. W. Rosemann,¹ J. Veletas,¹ S. Chatterjee,^{1,3} W. Stolz,¹ S. W. Koch,¹ J. Hader,⁴ J. V. Moloney,⁴ and W. Heimbrod^{1,a)}

¹Department of Physics and Material Sciences Center, Philipps-Universität Marburg, Renthof 5, 35032 Marburg, Germany

²NAsP_{III/IV} GmbH, Am Knechtacker 19, 35041 Marburg, Germany

³I. Physikalisches Institut, Justus-Liebig-Universität Gießen, Heinrich-Buff-Ring 16, 35392 Gießen, Germany

⁴College of Optical Sciences, University of Arizona, Tucson, Arizona 85721, USA

(Received 17 August 2015; accepted 24 October 2015; published online 3 November 2015)

The excitonic transitions of the type-II (GaIn)As/Ga(AsSb) gain medium of a “W”-laser structure are characterized experimentally by modulation spectroscopy and analyzed using microscopic quantum theory. On the basis of the very good agreement between the measured and calculated photoreflectivity, the type-I or type-II character of the observable excitonic transitions is identified. Whereas the energetically lowest three transitions exhibit type-II character, the subsequent energetically higher transitions possess type-I character with much stronger dipole moments. Despite the type-II character, the quantum-well structure exhibits a bright luminescence. © 2015 AIP Publishing LLC.

[<http://dx.doi.org/10.1063/1.4935212>]

Semiconductor lasers are essential devices for telecommunications and optical data transfer.^{1,2} In particular, the near infrared spectral region with wavelengths exceeding 1.2 μm is of particular interest for data transfer through optical fibers. Unfortunately, devices emitting in this spectral window typically suffer from significant Auger losses.^{3,4} In an attempt to suppress this intrinsic loss mechanism, type-II heterostructure designs can be utilized as the active region of an infrared “W”-laser configuration.^{5,6} Here, the electrons and holes are spatially separated into adjacent layers of rather large bandgap materials and recombine across the interfaces (see Fig. 1). Through proper choice of the constituent materials, the “W”-design allows for an increased flexibility in the design of devices with reduced Auger losses, high gain, and an emission wavelength of $\lambda > 1.2 \mu\text{m}$.⁷

In this paper, we present a (GaIn)As/Ga(AsSb)-based “W”-multiple quantum well heterostructure (MQWH) desired for use as active medium in a vertical-external-cavity surface emitting laser (VECSEL) for the application in the near infrared. The “W”-MQWH is investigated using photoluminescence (PL) spectroscopy and photomodulation reflectance (PR) spectroscopy. The results are analyzed using a fully microscopic theory to reveal the complex structure of electron and hole states and their type-I or type-II character upon excitation.

The samples were grown by metal organic vapor-phase epitaxy (MOVPE) on semi-insulating GaAs(001) substrates with a growth rate of approximately 0.4 nm/s. A 250 nm thick GaAs buffer layer was deposited on the substrate at 600 °C, while the “W”-MQWH was grown at 550 °C. The “W”-MQWH is made up of a Ga(As_{1-y}Sb_y)-quantum well (QW) surrounded by two identical (Ga_{1-x}In_x)As-QWs and enclosed by a barrier consisting of GaAs and Ga(As_{1-z}P_z) for strain compensation. This unit is repeated ten times.

Here, we investigate two samples. Layer thicknesses and respective compositions presented in the following were determined very accurately using high resolution X-ray diffraction (HR-XRD).^{8,9} The first sample has a Sb and In content of 17.3% Sb and 22.0% In and the respective layer thicknesses are 4.0 nm and 5.7 nm. A 10 nm GaAs layer and a 144 nm Ga(As_{0.959}P_{0.041}) layer form the barriers. The second sample contains 21.3% Sb and 21.6% In in the “W”-MQWH layers, which are of the same thickness as in the first sample. Its barriers are composed of a 10 nm GaAs layer and a 140 nm Ga(As_{0.954}P_{0.046}) layer. In the following, the samples will be identified by their Sb content. The structure and the resulting confinement potentials for electrons and holes are depicted schematically in Fig. 1.

The PL was measured using a diode pumped solid-state laser to excite the samples at 532 nm. The excitation laser was chopped; so, the PL could be amplified using lock-in technique. The detection was done by a standard setup consisting of a 0.5 m grating spectrometer and a liquid-nitrogen cooled germanium detector.

PR measurements are used to reveal the excitonic states. This is advantageous, because in modulation spectroscopy

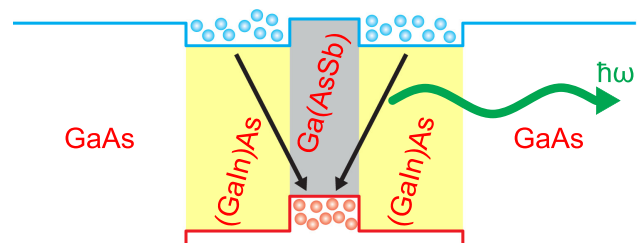


FIG. 1. Schematic depiction of the samples valence band and conduction band edge over real space. The electrons (blue) are confined in the (GaIn)As and the holes (red) are confined in the Ga(AsSb). This type-II band alignment leads to a radiative recombination across the interface in the infrared (black and green arrow).

^{a)}Electronic mail: wolfram.heimbrod@physik.uni-marburg.de

the derivatives of the transition bands are enhanced compared to conventional reflectance spectroscopy due to the largely disappearing background. Furthermore, very weak structures, such as type-II excitations, can be observed.^{10,11} The PR is measured in line-scan mode at room temperature. The light from a standard tungsten-halogen lamp is dispersed by a 1 m Czerny–Turner grating monochromator. The spectral resolution of the system is set to 1.5 nm. Higher diffraction orders are suppressed by either a color glass long-pass filter or a Si-wafer. The setup features metal-coated all-reflective optics to eliminate any chromatic errors. In particular, off-axis parabolic mirrors were used for all focusing optics minimizing astigmatism. The light is focused on to the sample to a diameter of about 0.5 mm under an angle of about 30° to the sample’s surface normal. All reflected light is then relayed on single-stage thermoelectrically cooled (GaIn)As photodiode operating with a small bias. The sample was modulated by a weakly focused 532 nm diode-pumped solid-state laser at a photon flux of approximately $1 \times 10^8/\text{cm}^2$, which was mechanically chopped. Due to the above bandgap excitation, the modulation results from both, a modulation of the built-in electric field near the surface of the crystal^{12,13} as well as from changes in the population of the conduction and valence bands.¹⁴ The absolute reflectance and the modulated signal were electronically separated by a passive frequency crossover and acquired simultaneously by the same lock-in amplifier. Additionally, a background including PL was recorded and subtracted from the signal. The normalized differential reflectance $\Delta R/R$ is then calculated straight forwardly from the in-phase part of the differential reflectance (ΔR) and the unmodulated absolute reflectance ($R = R^* - PL$) corrected for the background PL.

In Fig. 2, the room-temperature PL (red lines) and the PR (black lines) are depicted. Below 1.2 eV, the PR spectra are scaled by a factor of 3 for better visibility. For both, the 17.3% Sb and the 21.3% Sb sample, several signatures in the PR can be seen as indicated by the arrows. We can distinguish two energy ranges with very different oscillator strengths. As we will elucidate below, the PR spectra below about 1.2 eV (range “indirect”) are dominated by excitations across the (GaIn)As/Ga(AsSb) interface, whereas range “direct” is dominated by spatially direct transitions.

The strong features around 1.435 eV and 1.470 eV in both samples can be attributed to the GaAs barrier and substrate¹⁵ and the Ga(AsP) cladding layers, respectively.¹⁶ Furthermore, for both samples, a very strong type-II luminescence is observed in the infrared, due to the recombination of electrons in the (GaIn)As and holes in the Ga(AsSb). Remarkably, the PR measurements allow for observing the corresponding type-II excitation at 1.066 eV for the 17.3% Sb sample and at 1.010 eV for the 21.3% Sb sample. This is astonishing because the oscillator strength of the type-II transition is rather weak. It is most interesting to note that even further excited type-II states marked by the blue arrows in Fig. 2 in the “indirect” range could be identified. For the 17.3% Sb sample, one state can be observed at an approximately 1.180 eV, whereas the 21.3% Sb sample exhibits two excited states around 1.112 eV and 1.160 eV, respectively.

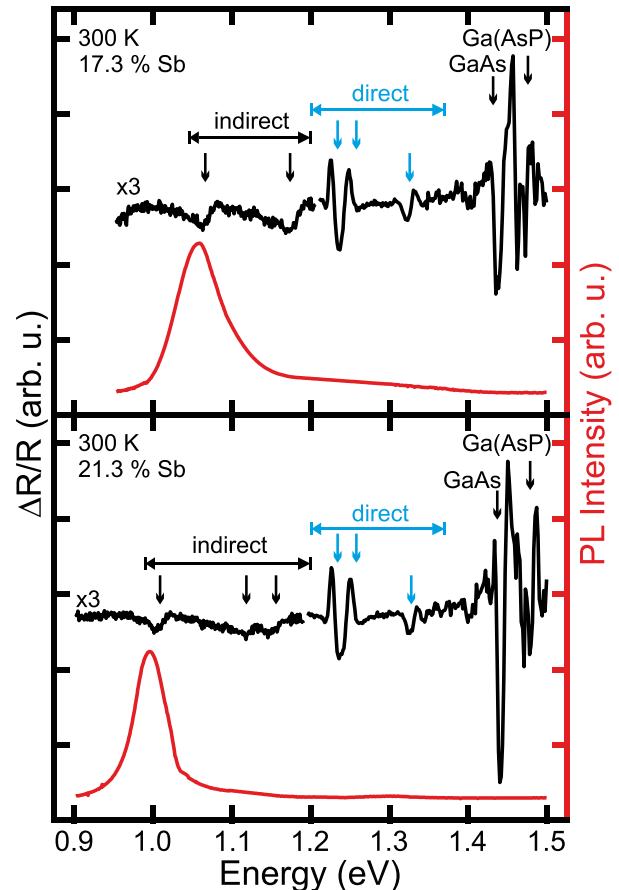


FIG. 2. Room temperature PR (black) and PL (red) spectra for the samples containing 17.3% Sb (top) and 21.3% Sb (bottom). The PR spectrum is multiplied by a factor of 3 below 1.2 eV to ensure visibility of the signals. Observed signals are marked with arrows.

For both the samples, three further transitions around 1.230 eV, 1.255 eV, and 1.325 eV can be observed, as indicated by the blue arrows in Fig. 2. With the help of the theoretical analysis discussed below, these signatures can be assigned to type-I transitions in the (GaIn)As. We will discuss the oscillator strength of the transitions in the framework of the microscopic theory. In both samples, the direct excitonic transitions are located almost at the same energy, which can be explained by the fact that the In content in the (GaIn)As differs only by 0.4%. The type-II transitions exhibit different energies in both samples, because the Sb content is different by about 4%. This strongly influences the bandgap and the respective valence-band energy of the Ga(AsSb)¹⁷ and therefore eventually the type-II transitions.

To support the identification of the observed transitions, we compare the experimental findings with the results obtained from a fully microscopic model. To compute the change of the reflectivity between excited and unexcited semiconductor heterostructures, we apply the semiconductor Bloch equations (SBE).^{18–20} This way, we access the complex optical susceptibility $\chi(\omega)$ whose imaginary part is directly proportional to the absorption and the real part yields the refractive index change. The SBE are evaluated at the second Born level to properly account for the intrinsic microscopic carrier scattering effects.^{21,22} To model the sample inhomogeneities of the experimental samples, we apply an

inhomogeneous broadening to our theoretical spectra by convolving them with a Gaussian distribution of the bandgap energies.²³

After computing the refractive index spectra, we use Fresnel's formula to calculate the reflectivity.²⁴ To obtain the PR, we then use the reflectivity derived under unexcited conditions and a second one where we take the modulation via optical excitation into account.²⁵ In addition to the PR, our calculations yield the eigenenergies and the carrier wave functions within the active region of the semiconductor heterostructure. Thus, we can identify whether a transition is of type-I or type-II character.

In all our calculations, we use 8×8 multiband $\mathbf{k} \cdot \mathbf{p}$ theory for the band structure.^{21,26} To take care of local charge separation, we solve the microscopic Schrödinger–Poisson equation.²⁷ The confinement potentials, wave functions, and band structure details are used to compute the optical and Coulomb matrix elements needed in the evaluation of the SBE. The material parameters used to evaluate the microscopic and macroscopic response of the semiconductor sample can be found in Ref. 8.

In the following, we perform a systematic comparison of the experimental PR results with calculated spectra. Figure 3 presents the PR spectra for both samples, where the calculations were performed at low excitation carrier density conditions of $1 \times 10^{-9}/\text{cm}^2$ and a temperature of 300 K. For the unexcited sample, we use an inhomogeneous broadening

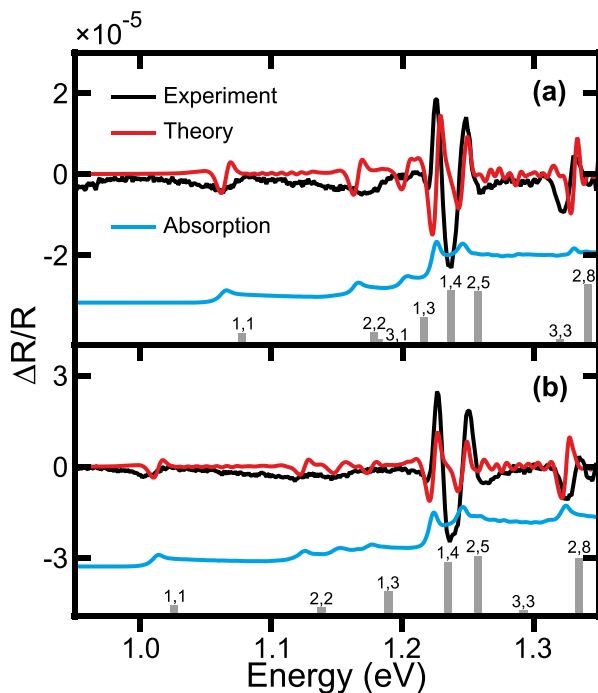


FIG. 3. Experimental and theoretical PR and theoretical absorption spectra. Frame (a) presents the spectra for sample with 17.3% Sb and frame (b) for sample with 21.3% Sb. Experimental PR spectra are plotted as black solid lines. Corresponding theoretical PR spectra are plotted as red solid lines. The respective theoretical absorption spectra are depicted as blue solid lines. Vertical bars mark the single particle excitations between electron and hole states. The numbers at the bars indicate the quantum number of the participating electron and hole states, respectively. Their size presents their relative strength; only excitations with at least 10% strength with respect to the strongest one are plotted.

of 4 meV. Due to excitation induced dephasing, the inhomogeneous broadening is increased to 12 meV for the excited sample. For illustration, we also show the calculated absorption spectra for both samples. We notice a very good overall theory–experiment agreement of the excitation peak positions. All of the main signatures in the PR have a corresponding peak in the calculated absorption. Our theory reproduces all small signals in “indirect” region between 1 eV and 1.2 eV very well, both in position and relative size. Only the signatures for energies higher than 1.2 eV (“direct” region) are slightly off with respect to the size of the experimental signal. We believe that the origin of this deviation is due to the assumption made in our theoretical evaluation that the carriers are in fully relaxed quasi equilibrium Fermi distributions, whereas in the experiment, some of the carriers are probably still in energetically higher states.

Based on the good agreement for the peak positions, we use the corresponding electron and hole wave functions to identify the nature of the observed signatures (see Fig. 4). Electrons confined in the two (GaIn)As wells can be in one of the two almost degenerate states e1 and e2. A type-II transition appears when the respective hole which recombines with an electron from state e1 or e2 is confined in the Ga(AsSb) well. Both samples with their different Sb concentrations in the quantum wells have three confined hole states h1, h2, and h3 in the Ga(AsSb) well (see Fig. 4(a)). Every possible transition between one of the first two electron states and one of the first three hole states is, therefore, a type-II transition through the interface between the (GaIn)As and Ga(AsSb).

All possible type-I transitions are energetically higher and exhibit also a higher dipole transition strength, as can be seen in Fig. 3. Figure 4(b) presents the hole wave functions participating in the transitions producing the strong features in Fig. 3. All of them have a very similar shape belonging to

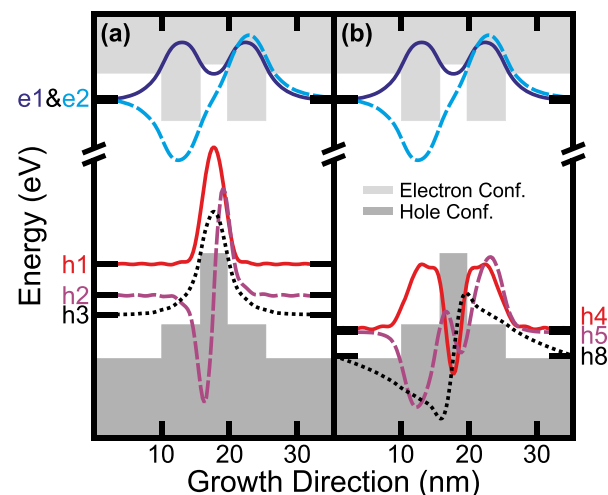


FIG. 4. Confinement potentials of electrons and holes and their respective wave functions of the 21.3% Sb sample. (a) All wave functions needed for type-II transitions are presented. (b) The wave functions of the strongest type-I transitions are plotted. Electron and hole confinement are plotted as grey shaded areas. The electron wave functions are plotted as blue solid (dashed) lines for the first (second) electron state. Hole wave functions are presented as solid, dashed, and dotted line for the first, second, and third state in frame (a) and for the fourth, fifth, and eighth state in frame (b).

either e_1 or e_2 , which explains that the respective dipole transition probability is high and result in a significant contributions to the PR spectrum. We marked all transition with a relative strength of at least 10% in Fig. 3; the height of the corresponding gray lines depicts the relative dipole transition strength.

An interesting difference between both samples is caused by the 4% difference in their Sb concentration. On one hand, all type-II transitions have higher energies for the sample containing 17.3% Sb due to a smaller valence band offset. On the other hand, the type-II transitions are weaker compared to the type-I transitions due to a stronger hole localization for the sample with an Sb content of 21.3%.

In conclusion, we were able to explain the complex structure of electron and hole states involved in the excitonic PR spectra of (GaIn)As/Ga(AsSb) “W”-shape quantum-well heterostructures. The energetically lowest three transitions observed in the PR experiments all clearly exhibit a type-II character with the holes in the Ga(AsSb) well and the electrons in the cladding (GaIn)As wells. The comparison of experimental PR measurements and microscopic model calculations reveals the first clear direct transition to be caused by the h_4 and h_5 hole states. The dipole transitions of the type-II signals are much smaller in comparison to the direct transitions due to the reduced wave function overlap, which explains the weaker experimental signatures. We could also show that the type-II character can be varied by changing the Sb concentration in the innermost Ga(AsSb) quantum well. It is worth mentioning that the quantum efficiency of these structures is very high despite the type-II character, which makes this quantum well system a promising material for laser application in the near infrared.

The Marburg work was a project of the Sonderforschungsbereich 1083 funded by the Deutsche Forschungsgemeinschaft (DFG). S.G., N.W.R., and J.V. gratefully acknowledge the financial support of the DFG in the framework of the GRK 1782. The work at the University of Arizona was supported by the AFOSR BRI Grant FA9550-14-1-0062.

- ¹E. Murphy, *Nat. Photonics* **4**, 287 (2010).
- ²K. Thyagarajan and A. Ghatak, *Lasers, Graduate Texts in Physics* (Springer US, 2011), pp. 323–362.
- ³A. D. Andreev and E. P. O'Reilly, *Appl. Phys. Lett.* **84**, 1826 (2004).
- ⁴S. J. Sweeney, A. R. Adams, M. Silver, E. P. O'Reilly, J. R. Watling, A. B. Walker, and P. J. A. Thijs, *Phys. Status Solidi B* **211**, 525 (1999).
- ⁵J. R. Meyer, C. A. Hoffman, F. J. Bartoli, and L. R. Ram-Mohan, *Appl. Phys. Lett.* **67**, 757 (1995).
- ⁶G. G. Zegrya and A. D. Andreev, *J. Exp. Theor. Phys.* **82**, 328 (1996).
- ⁷G. G. Zegrya and A. D. Andreev, *Appl. Phys. Lett.* **67**, 2681 (1995).
- ⁸C. Berger, C. Möller, P. Hens, C. Fuchs, W. Stolz, S. W. Koch, A. Ruiz Perez, J. Hader, and J. V. Moloney, *AIP Adv.* **5**, 047105 (2015).
- ⁹L. De Caro, C. Giannini, and L. Tapfer, *J. Appl. Phys.* **79**, 4101 (1996).
- ¹⁰M. Cardona, *Festkörperprobleme, Advances in Solid State Physics*, Vol. 10, edited by O. Madelung (Springer, Berlin, Heidelberg, 1970), pp. 125–173.
- ¹¹P. J. Klar, H. Grüning, W. Heimbrod, G. Weiser, J. Koch, K. Volz, W. Stolz, S. W. Koch, S. Tomic, S. A. Choulis, T. J. C. Hosea, E. P. O'Reilly, M. Hofmann, J. Hader, and J. V. Moloney, *Semicond. Sci. Technol.* **17**, 830 (2002).
- ¹²J. L. Shay, R. E. Nahory, and C. K. N. Patel, *Phys. Rev.* **184**, 809 (1969).
- ¹³R. E. Nahory and J. L. Shay, *Phys. Rev. Lett.* **21**, 1569 (1968).
- ¹⁴J. G. Gay and L. T. Klauder, *Phys. Rev.* **172**, 811 (1968).
- ¹⁵M. D. Sturge, *Phys. Rev.* **127**, 768 (1962).
- ¹⁶A. G. Thompson, M. Cardona, K. L. Shaklee, and J. C. Woolley, *Phys. Rev.* **146**, 601 (1966).
- ¹⁷R. M. Cohen, M. J. Cherng, R. E. Benner, and G. B. Stringfellow, *J. Appl. Phys.* **57**, 4817 (1985).
- ¹⁸M. Lindberg and S. W. Koch, *Phys. Rev. B* **38**, 3342 (1988).
- ¹⁹H. Haug and S. W. Koch, *Quantum Theory of the Optical and Electronic Properties of Semiconductors*, 5th ed. (World Scientific Publishing, Singapore, 2009).
- ²⁰M. Kira and S. W. Koch, *Semiconductor Quantum Optics* (Cambridge University Press, Cambridge, 2012).
- ²¹W. W. Chow and S. W. Koch, *Semiconductor-Laser Fundamentals: Physics of the Gain Materials* (Springer, Berlin, Heidelberg, New York, 1999).
- ²²J. Hader, S. W. Koch, and J. V. Moloney, *Solid-State Electron.* **47**, 513 (2003).
- ²³J. Hader, J. V. Moloney, S. W. Koch, and W. W. Chow, *IEEE J. Sel. Top. Quantum Electron.* **9**, 688 (2003).
- ²⁴E. Hecht, *Optics*, 4th ed. (Addison-Wesley, Boston, MA, 2002).
- ²⁵C. Schlichenmaier, H. Grüning, A. Thränhardt, P. J. Klar, B. Kunert, K. Volz, W. Stolz, W. Heimbrod, T. Meier, S. W. Koch, J. Hader, and J. V. Moloney, *Appl. Phys. Lett.* **86**, 081903 (2005).
- ²⁶J. Hader, N. Linder, and G. H. Döhler, *Phys. Rev. B* **55**, 6960 (1997).
- ²⁷D. Ahn and S. L. Chuang, *J. Appl. Phys.* **64**, 6143 (1988).

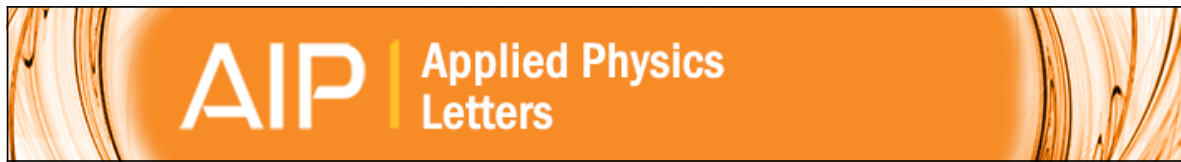
Paper IV

C. Möller, C. Fuchs, **C. Berger**, A. Ruiz Perez, M. Koch, J. Hader,
J. V. Moloney, S. W. Koch, and W. Stolz

*Type-II vertical-external-cavity surface emitting laser with Watt level
output powers at 1.2 μm*

Applied Physics Letters **108**, 071102 (2016)

DOI: 10.1063/1.4942103



Type-II vertical-external-cavity surface-emitting laser with Watt level output powers at $1.2\mu\text{m}$

C. Möller, C. Fuchs, C. Berger, A. Ruiz Perez, M. Koch, J. Hader, J. V. Moloney, S. W. Koch, and W. Stolz

Citation: *Applied Physics Letters* **108**, 071102 (2016); doi: 10.1063/1.4942103

View online: <http://dx.doi.org/10.1063/1.4942103>

View Table of Contents: <http://scitation.aip.org/content/aip/journal/apl/108/7?ver=pdfcov>

Published by the [AIP Publishing](#)

Articles you may be interested in

[GaInNAs\(Sb\) vertical-cavity surface-emitting lasers at \$1.460\mu\text{m}\$](#)

J. Vac. Sci. Technol. B **22**, 1562 (2004); 10.1116/1.1714940

[Differential surface photovoltage spectroscopy characterization of a \$1.3\mu\text{m}\$ InGaAlAs/InP vertical-cavity surface-emitting laser structure](#)

J. Appl. Phys. **93**, 1874 (2003); 10.1063/1.1538323

[Surface photovoltage spectroscopy and normal-incidence reflectivity characterization of a \$1.3\mu\text{m}\$ InGaAlAs/InP vertical-cavity surface-emitting laser structure](#)

J. Appl. Phys. **91**, 6203 (2002); 10.1063/1.1467396

[\(GaIn\)\(NAs\)/GaAs vertical-cavity surface-emitting laser with ultrabroad temperature operation range](#)

Appl. Phys. Lett. **76**, 271 (2000); 10.1063/1.125744

[Ground state lasing from a quantum-dot oxide-confined vertical-cavity surface-emitting laser](#)

Appl. Phys. Lett. **75**, 22 (1999); 10.1063/1.124264

A promotional banner for Applied Physics Reviews. On the left is a small image of a journal cover titled 'AIP Applied Physics Reviews' showing a 3D diagram of a layered structure. The main background is blue with a bright light source on the right. The text 'NEW Special Topic Sections' is prominently displayed in white. Below this, it says 'NOW ONLINE' in yellow, followed by 'Lithium Niobate Properties and Applications: Reviews of Emerging Trends' in white. The AIP Applied Physics Reviews logo is in the bottom right corner.

NEW Special Topic Sections

NOW ONLINE
Lithium Niobate Properties and Applications:
Reviews of Emerging Trends

AIP Applied Physics Reviews

Type-II vertical-external-cavity surface-emitting laser with Watt level output powers at 1.2 μm

C. Möller,^{1,a)} C. Fuchs,¹ C. Berger,¹ A. Ruiz Perez,² M. Koch,¹ J. Hader,³ J. V. Moloney,³ S. W. Koch,¹ and W. Stolz^{1,2}

¹*Department of Physics and Material Sciences Center, Philipps-Universität Marburg, Renthof 5, 35032 Marburg, Germany*

²*NA&P_{III/V} GmbH, Hans-Meerwein-Straße, 35032 Marburg, Germany*

³*Nonlinear Control Strategies, Inc., 7040 N Montecatina Drive, Tucson, Arizona 85704, USA*

(Received 3 December 2015; accepted 4 February 2016; published online 16 February 2016)

Semiconductor laser characteristics based on type-II band-aligned quantum well heterostructures for the emission at 1.2 μm are presented. Ten “W”-quantum wells consisting of GaAs/(GaIn)As/Ga(AsSb)/(GaIn)As/GaAs are arranged as resonant periodic gain in a vertical-external-cavity surface-emitting laser. Its structure is analyzed by X-ray diffraction, photoluminescence, and reflectance measurements. The laser’s power curves and spectra are investigated. Output powers at Watt level are achieved, with a maximum output power of 4 W. It is confirmed that laser operation only involves the type-II transition. A blue shift of the material gain is observed while the modal gain exhibits a red shift. © 2016 AIP Publishing LLC. [<http://dx.doi.org/10.1063/1.4942103>]

Many applications have a demand for lasers in the infrared regime. Prominent examples are telecommunication and optical data transfer where the wavelength of light sources has to be adapted to the available propagation media.¹ For instance, a minimum absorption in optical fibers is around 1.3 μm .² Other examples are frequency doubling for red emitters in digital projectors, where wavelengths above 1.2 μm are of particular interest, or medical applications.³ In the latter case, eye-safe emitters with wavelengths above 1.4 μm are desired where the corneal absorption can provide a natural protection of the retina.⁴

In the infrared, above 1.2 μm , conventional semiconductor lasers with gain media based on type-I quantum well heterostructures suffer from significant non-radiative Auger losses.⁵ In recent years, type-II band-aligned quantum wells have become a promising alternative. Especially, “W”-quantum well heterostructures have been considered which, despite the spatial separation of electrons and holes, still provide sufficient overlap between the electron and hole wave functions.^{6–9} In comparison to type-I systems, a type-II band alignment enables a more flexible band structure engineering in order to reduce intrinsic losses while the emission wavelength can be kept constant. Thus, such type-II lasers are promising candidates to surpass conventional type-I lasers with respect to wavelength versatility and performance in the infrared regime. To date, first lasers based on type-II quantum well heterostructures have been reported based on the InP, GaSb, and GaAs material systems with emission wavelengths even in the mid infrared.^{10–13} Particularly, at an emission wavelength of 1.2 μm , an edge emitter with a maximum output power of 50 mW at 20 °C was demonstrated.¹⁰

Recently, we have evaluated the potential of the GaAs/(GaIn)As/Ga(AsSb)/(GaIn)As/GaAs material system as gain medium for vertical-external-cavity surface-emitting lasers (VECSELs) with an emission wavelength of 1.2 μm .¹⁴

Photoluminescence (PL) spectra of such type-II multiple quantum well heterostructures (MQWHs) were measured and compared with the results from a fully microscopic theory. The involved excitonic transitions could be identified in an experiment–theory comparison for photomodulation reflectance spectroscopy measurements.¹⁵ Based on the good agreement between the experimental and theoretical results, also the absorption and gain properties were calculated using the semiconductor Bloch equations. Gain values as high as for type-I systems were predicted. Overall, it is expected that the previously investigated “W”-design will perform well as gain medium in optically pumped semiconductor lasers.

In this letter, we demonstrate a continuous wave pumped type-II semiconductor disk laser with an emission wavelength of 1.2 μm at room temperature. Therefore, we take on our previous approach and implement a GaAs/(Ga_{0.8}In_{0.2})As/Ga(As_{0.8}Sb_{0.2})/(Ga_{0.8}In_{0.2})As/GaAs 10× MQWH as resonant periodic gain structure. The sample growth is carried out by metalorganic vapor phase epitaxy (MOVPE) using a commercial horizontal AIXTRON AIX 200 Gas Foil Rotation (GFR) system.¹⁴ In preparation for the growth of the laser structure, a type-I (Ga_{0.8}In_{0.2})As/GaAs MQWH and a Ga(As_{0.8}Sb_{0.2})/GaAs MQWH are grown, in order to determine the individual growth conditions which are used for the growth of the type-II MQWH. The laser structure is grown bottom-up onto (001) GaAs substrate, starting with a (Ga_{0.52}In_{0.48})P capping layer and followed by the resonant periodic gain containing the “W”-quantum wells separated by Ga(AsP) strain compensating layers. The optical layer thicknesses of the capping layer and the barriers are matched to $\lambda/2$ with respect to the lasing wavelength. Finally, a distributed Bragg reflector (DBR) is grown, with 22 1/2 pairs of (Al_{0.1}Ga_{0.9})As/AlAs.

As in our previous work, the MQWHs are characterized using high resolution X-ray diffraction (HR-XRD). The determined In and Sb concentrations as well as the (GaIn)As and Ga(AsSb) layer thicknesses are summarized in Table I.

^{a)}Electronic mail: christoph.moeller@physik.uni-marburg.de

TABLE I. Measured In and Sb concentrations and layer thicknesses of the investigated MQWHs (i) (GaIn)As/GaAs, (ii) Ga(AsSb)/GaAs, and (iii) GaAs/(GaIn)As/Ga(AsSb)/(GaIn)As/GaAs.

	(i)	(ii)	(iii)
QW thickness (nm)	5.2	4.1	5.5/4.0/5.5
In concentration (%)	20.8	0	20.3/0/20.3
Sb concentration (%)	0	19.8	0/19.8/0

Furthermore, we record the PL spectra of all three structures. Regular PL measurements are performed with the (GaIn)As/GaAs and the Ga(AsSb)/GaAs MQWHs, where excitation and detection are carried out perpendicular to the surface of the sample. However, for VECSELS, it is more meaningful to record the edge PL, where the filtering by the Fabry–Pérot resonances from the microcavity, which is formed by the capping layer and the DBR, is avoided.¹⁶ Therefore, we excite through the ternary DBR using an 808 nm diode laser and detect the PL under an angle of 90°, i.e., only the PL emitted from the edge of the sample, with an optical spectrum analyzer (Yokagawa AQ6370B). The normalized spectra are presented in Fig. 1. It is observed that the characteristic PL of the type-I transitions according to recombinations inside an individual layer in the “W”-structure is suppressed. Overall, the HR-XRD and edge PL measurement of the VECSEL show that a MQWH very similar to the previously investigated structures was realized. Hence, the observed luminescence can be related to type-II transitions for which gain is expected.^{14,15}

One important requirement for VECSELS is to match the material gain peak wavelength and the microcavity resonance. For type-I setups, it is known that the red shift of the material gain is stronger than the red shift of the microcavity. Thus, following the definition of Hader *et al.*,¹⁷ a negative detuning is usually introduced for type-I VECSELS in order to achieve an efficient laser operation. This detuning can be used as design parameter to achieve a low threshold or high output power.

Due to the importance of the microcavity, the reflectivity of a processed laser chip is measured in order to evaluate the longitudinal confinement factor, i.e., the average light field intensity at the quantum wells. For the reflection measurement, a

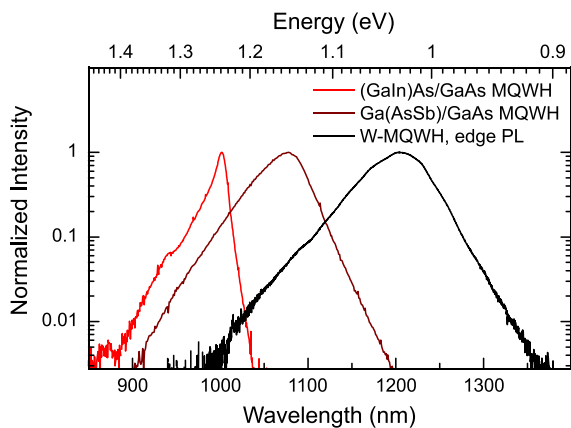


FIG. 1. Photoluminescence of the (GaIn)As/GaAs (red line) and Ga(AsSb)/GaAs (dark red line) $10 \times$ MQWH test structures as well as the edge PL of the laser sample with 10 GaAs/(GaIn)As/Ga(AsSb)/(GaIn)As/GaAs “W”-quantum wells arranged as resonant periodic gain (black line).

sample from an adjacent wafer position of the edge PL sample is flip-chip bonded onto a 350 μm thick chemical vapor deposition (CVD) diamond heat spreader via solid liquid interdiffusion bonding based on Au and In. Then, the substrate is removed by selective chemical wet etching onto the Ga(InP) capping layer. The processed VECSEL chip is mounted on a temperature controlled copper heat sink. To measure the reflectivity white light is focussed perpendicular to the processed chip and a beamsplitter is used to collect the reflected light in a spectrum analyzer.

The reflectivity measurement is shown as grey-shaded area in Fig. 2. An absorption dip within the DBR stop band is observed at 1168 nm. For the reflectivity simulation, the barrier and QW thicknesses are extracted from the HR-XRD results. The capping layer and the DBR layer thicknesses are varied in order to fit the experimental data by the transfer-matrix method.¹⁶ Consequently, the intensity distribution of the light field within the structure can be calculated, and the longitudinal confinement factor is determined. It is found that the drop of the measured reflectance at the short-wavelength side of the stop band is in agreement with the maximum of the longitudinal confinement factor. This also explains the deviation of the simulated reflectivity where the absorption of the QWs is not considered.

The comparison between the edge PL (cf. Fig. 1) and the reflectance as well as the simulation of the longitudinal confinement factor reveals that a large positive detuning of about 35 nm is present in this particular type-II VECSEL structure. This is in contrast to common type-I VECSELS where no laser operation should be achieved with such a detuning.¹⁷ However, for type-II quantum wells the exact carrier density and temperature dependent shift rates are not yet established. Still, it has been reported that a significant blue shift is obtained with increasing pump densities despite the simultaneous heating of the gain structure.^{10,18} These observations are also consistent with our recent investigations concerning the GaAs/(GaIn)As/Ga(AsSb)/(GaIn)As/GaAs material system.¹⁴

An outcoupling mirror with -100 mm radius of curvature is used to arrange a linear laser cavity with a length of 64 mm. The VECSEL is driven by an 808 nm diode pump laser (JenOptik JOLD-400-CAXF-6P2) under a 30° angle of incidence. A CCD camera was utilized to record the pump spot

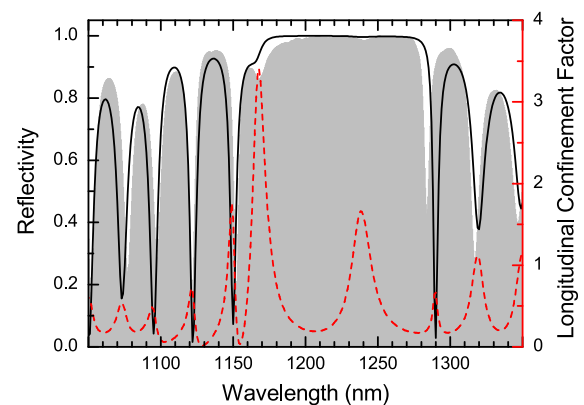


FIG. 2. Reflectivity measurement (grey-shaded area), reflectivity simulation (black solid line), and simulated longitudinal confinement factor (red dashed line) of the processed laser structure.

profile, and a super-Gaussian fit is applied in order to estimate the exact pump intensity. The complete procedure is described in more detail by Heinen *et al.*¹⁹ At full width at half maximum (FWHM), the elliptical pump spot is of the size $750\ \mu\text{m} \times 870\ \mu\text{m}$, which implies highly multi-transverse mode operation concerning the VECSEL. For comparison, the TEM_{00} mode size at the VECSEL chip for this cavity configuration is $270\ \mu\text{m}$ at FWHM. It is found that the pump spot exhibits a flat-top profile with a super-Gaussian order of $m = 3.00$. Hence, it is valid to estimate the pump intensity directly from the pump spot radius.¹⁹

Laser operation is achieved with output coupler transmissivities of 0.2%, 0.7%, 1.0%, and 1.5%. The best performance is observed with the 0.7% output coupler for which the laser power curves are recorded with different heat sink temperatures in 15°C steps between -15°C and 30°C (cf. Fig. 3). The net input power is denoted at the bottom x-axis, considering that measured 23.2% of the pump light is reflected. The net pump intensity is denoted at the top x-axis. At -15°C heat sink temperature, the maximum output power of 4 W is achieved, and the threshold pump intensity is $1.18\ \text{kW}/\text{cm}^2$. With increasing temperature, the threshold is continuously increasing to $1.43\ \text{kW}/\text{cm}^2$, $1.92\ \text{kW}/\text{cm}^2$, and $2.54\ \text{kW}/\text{cm}^2$ while maximum output powers are decreasing to 2.8 W, 1.6 W, and 0.6 W, for 0°C , 15°C , and 30°C , respectively.

In comparison to a type-I VECSEL in the same wavelength regime, the pump intensities at threshold are in the same order of magnitude. On the other hand, the slope efficiencies of less than 10% for the type-II structure are clearly smaller as in type-I systems with 31%–34% slope efficiency.^{20,21}

The optical spectrum analyzer is used to record the laser spectra while the power curve with 0°C heat sink temperature is recorded. The measurement is shown as false color plot in Fig. 4. The wavelength at lasing threshold is 1173 nm. A continuous red shift of the laser spectrum is observed although a blue shift of the material gain must be present due to the compensation of the large positive detuning. At the peak output power, a maximum wavelength of 1182 nm is observed. This result indicates that the maximum of the modal gain is dominated by the longitudinal confinement factor. If a linear shift of $0.12\ \text{nm}/\text{K}$ is assumed, which

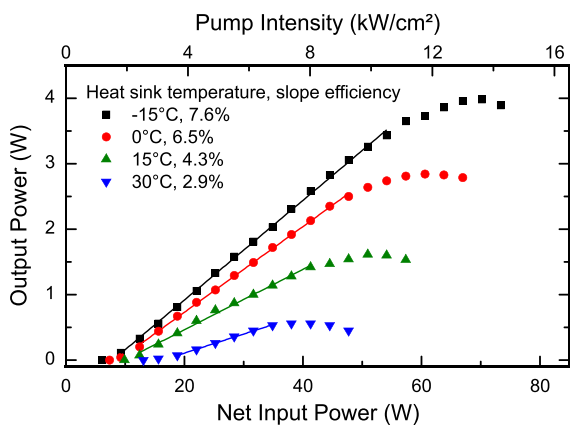


FIG. 3. Input/output characteristics for heat sink temperatures ranging from -15°C to 30°C .

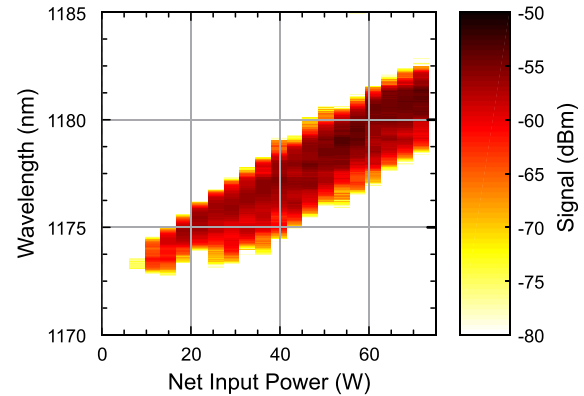


FIG. 4. Laser spectra corresponding to the power curve with 0°C heat sink temperature.

is a common value for the spectral shift of the reflectivity of such resonant periodic gain structures, temperatures of 60°C at threshold and 135°C at the maximum applied pump intensity are estimated. These values are similar to typical temperatures in type-I VECSELs.²²

In conclusion, we have demonstrated the feasibility of a VECSEL based on a type-II resonant periodic gain at $1.2\ \mu\text{m}$ emission wavelength. It emits up to 4 W at -15°C and 1.6 W at 15°C heat sink temperature with an emission wavelength between 1173 nm and 1182 nm. Measurements confirm lasing at the type-II transitions. The detuning is estimated by a comparison of the edge PL and reflectivity measurement. In accordance to previous reports, we have observed a significant blue shift of the material gain because the positive detuning of 35 nm between the low density PL peak wavelengths and the microcavity resonance is compensated. However, the red shift of the laser wavelength indicates that the modal gain is dominated by the microcavity resonance. The observed characteristic of decreasing thresholds and increasing slope efficiencies for reduced heat sink temperatures cannot only be an indicator for an increasing material gain but also for an improved overlap of material gain with the microcavity resonance. As for type-I systems, it is expected that the performance of type-II VECSELs is critically depending on the detuning. Therefore, an optimized design concerning the detuning of a type-II setup can potentially lead to a significant improvement of the laser performance. The characteristic blue shift of type-II structures with increasing carrier densities implies that the optimization of type-II VECSELs is completely different from the well established type-I VECSEL.

The presented results will facilitate the realization of more efficient lasers based on the GaAs/(GaIn)As/Ga(AsSb)/(GaIn)As/GaAs material system. In order to exploit the full potential, optimizations can be performed in interplay of experiment and theoretical quantum design,²³ but also with respect to optimized growth conditions. Furthermore, the design based on this material system has the potential for emission wavelengths up to $1.4\ \mu\text{m}$ and beyond.

The Marburg work was a project of the Sonderforschungsbereich 1083 funded by the Deutsche Forschungsgemeinschaft (DFG). The work at Nonlinear

Control Strategies, Inc. is supported via STTR Phase II, Contract No. FA9550-13-C-0009. The work from J. Hader and J. V. Moloney was also supported by the U.S. Air Force Office of Scientific Research (AFOSR), contract FA9550-14-1-0062.

- ¹E. Murphy, *Nat. Photonics* **4**, 287 (2010).
- ²G. P. Agrawal, *Fiber-Optic Communication Systems* (John Wiley & Sons, 2012), Vol. 222.
- ³S. Calvez, J. Hastie, M. Guina, O. Okhotnikov, and M. Dawson, *Laser Photonics Rev.* **3**, 407 (2009).
- ⁴J. A. Zuclich, D. J. Lund, and B. E. Stuck, *Health Phys.* **92**, 15 (2007).
- ⁵J. R. Meyer, C. L. Felix, W. W. Bewley, I. Vurgaftman, E. H. Aifer, L. J. Olafsen, J. R. Lindle, C. A. Hoffman, M.-J. Yang, B. R. Bennett, B. V. Shanabrook, H. Lee, C.-H. Lin, S. S. Pei, and R. H. Miles, *Appl. Phys. Lett.* **73**, 2857 (1998).
- ⁶J. R. Meyer, C. A. Hoffman, F. J. Bartoli, and L. R. Ram-Mohan, *Appl. Phys. Lett.* **67**, 757 (1995).
- ⁷N. Tansu and L. Mawst, *IEEE J. Quantum Electron.* **39**, 1205 (2003).
- ⁸J.-Y. Yeh, L. J. Mawst, A. A. Khandekar, T. F. Kuech, I. Vurgaftman, J. R. Meyer, and N. Tansu, *Appl. Phys. Lett.* **88**, 051115 (2006).
- ⁹J. Hader, J. V. Moloney, S. W. Koch, I. Vurgaftman, and J. R. Meyer, *Appl. Phys. Lett.* **94**, 061106 (2009).
- ¹⁰J. F. Klem, O. Blum, S. R. Kurtz, I. J. Fritz, and K. D. Choquette, *J. Vac. Sci. Technol., B* **18**, 1605 (2000).
- ¹¹R. Kaspi, A. Ongstad, G. C. Dente, J. Chavez, M. L. Tilton, and D. Gianardi, *Appl. Phys. Lett.* **81**, 406 (2002).
- ¹²C.-H. Chang, Z.-L. Li, H.-T. Lu, C.-H. Pan, C.-P. Lee, G. Lin, and S.-D. Lin, *IEEE Photonics Technol. Lett.* **27**, 225 (2015).
- ¹³S. Sprengel, A. Andrejew, F. Federer, G. K. Veerabathran, G. Boehm, and M.-C. Amann, *Appl. Phys. Lett.* **106**, 151102 (2015).
- ¹⁴C. Berger, C. Möller, P. Hens, C. Fuchs, W. Stolz, S. W. Koch, A. R. Perez, J. Hader, and J. V. Moloney, *AIP Adv.* **5**, 047105 (2015).
- ¹⁵S. Gies, C. Kruska, C. Berger, P. Hens, C. Fuchs, A. R. Perez, N. W. Rosemann, J. Veletas, S. Chatterjee, W. Stolz, S. W. Koch, J. Hader, J. V. Moloney, and W. Heimbrodt, *Appl. Phys. Lett.* **107**, 182104 (2015).
- ¹⁶A. Tropper and S. Hoogland, *Prog. Quantum Electron.* **30**, 1 (2006).
- ¹⁷J. Hader, G. Hardesty, G. Hardesty, M. J. Yarborough, Y. Kaneda, J. V. Moloney, B. Kunert, W. Stolz, and S. W. Koch, *IEEE J. Quantum Electron.* **46**, 810 (2010).
- ¹⁸W. W. Chow and H. C. Schneider, *Appl. Phys. Lett.* **78**, 4100 (2001).
- ¹⁹B. Heinen, C. Möller, K. Jandieri, B. Kunert, M. Koch, and W. Stolz, *IEEE J. Quantum Electron.* **51**, 1 (2015).
- ²⁰L. Fan, C. Hassenius, M. Fallahi, J. Hader, H. Li, J. V. Moloney, W. Stolz, S. W. Koch, J. T. Murray, and R. Bedford, *Appl. Phys. Lett.* **91**, 131114 (2007).
- ²¹S. Ranta, M. Tavast, T. Leinonen, N. V. Lieu, G. Fetzter, and M. Guina, *Electron. Lett.* **49**, 59 (2013).
- ²²B. Heinen, F. Zhang, M. Sparenberg, B. Kunert, M. Koch, and W. Stolz, *IEEE J. Quantum Electron.* **48**, 934 (2012).
- ²³J. V. Moloney, J. Hader, and S. W. Koch, *Laser Photonics Rev.* **1**, 24 (2007).

Paper V

C. Möller, **C. Berger**, C. Fuchs, A. Ruiz Perez, S. W. Koch, J. Hader,
J. V. Moloney, and W. Stolz

1.2 μm emitting VECSEL based on type-II aligned QWs

Proceedings SPIE **9734**, 97340H (2016)

DOI: 10.1117/12.2212438

1.2 μm emitting VECSEL based on type-II aligned QWs

C. Möller^{*a}, C. Berger^a, C. Fuchs^a, A. Ruiz Perez^b, S.W. Koch^a,
J. Hader^c, J.V. Moloney^c, W. Stolz^{a,b}

^aDepartment of Physics and Material Sciences Center, Philipps-Universität Marburg, Renthof 5,
D-35032 Marburg, Germany;

^bNAsP III/V GmbH, Am Knechtacker 19, D-35041 Marburg, Germany;

^cNonlinear Control Strategies Inc, 3542 N. Geronimo Ave., Tucson, AZ 85705, USA

ABSTRACT

Since the invention of VECSELS, their great spectral coverage has been demonstrated and emission wavelengths in the range from UV to almost MIR have been achieved. However, in the infrared regime the laser performance is affected by Auger losses which become significant at large quantum defects. In order to reduce the Auger losses and to develop more efficient devices in the IR, type-II aligned QWs have been suggested as alternative gain medium for semiconductor lasers.

We present the first room temperature VECSEL containing type-II aligned quantum wells arranged as resonant periodic gain. The quantum wells consist of (GaIn)As/Ga(AsSb)/(GaIn)As heterostructures. The structure was grown bottom-up on GaAs substrate and flip-chip bonded onto a diamond heat spreader. The device, pumped at 808 nm, emits >1 W of cw output power at an emission wavelength of 1.2 μm . A detailed study of the device is performed in order to investigate the potential of such novel type-II gain media for future applications. These investigations include the determination of the power and temperature dependent shift rates. The gain temperatures at laser threshold and at maximum output power are determined.

Keywords: Vertical-external-cavity surface-emitting laser, VECSEL, type-II quantum well, semiconductor disk laser

1. INTRODUCTION

On the basis of the GaAs material system a great spectral range from 675 nm to 1550 nm is covered with VECSELS [1], [2]. Applying highly efficient intra-cavity frequency conversion, this range can be even extended into the ultraviolet [1], [3] or into the submillimeter regime [4], respectively. However, the performance of GaAs based devices critically depends on the emission wavelength. At about 1 μm emission wavelength record output powers are achieved, even the mark of 100 W has been passed [5]. On the short wavelength side, the material gain decreases due to shallow quantum wells which may result in a poor quantum confinement and thermal escape of carriers. A good result is presented in [6] where 12 W of output power are generated at 920 nm. On the other hand, the realization of long wavelength devices comprises the growth of highly strained structures and, if an 808 nm pump is employed, large quantum defects. At 1180 nm the maximum output power exceeds 20 W [7], while hundreds of mW are achieved at 1550 nm [2]. In a nutshell, devices at the edge of the accessible spectrum are more sensitive against non-radiative loss mechanisms and constitute a challenge.

To decrease such inherent losses, mainly Auger losses, type-II quantum well structures for the use as gain medium in the infrared are investigated since the '90s [8], [9]. Type-II lasers have been demonstrated on the InP [10], [11], GaSb [12] and also the GaAs [13] material systems. In the latter case, a $(\text{Ga}_{1-x}\text{In}_x)\text{As}/\text{Ga}(\text{As}_{1-y}\text{Sb}_y)$ arrangement has been employed which has been suggested in previous investigations as a promising gain structure [8], [14], [15].

Recently, we have evaluated the potential of a $(\text{Ga}_{1-x}\text{In}_x)\text{As}/\text{Ga}(\text{As}_{1-y}\text{Sb}_y)/(\text{Ga}_{1-x}\text{In}_x)\text{As}$ arrangement, also referred to as "W" quantum well, as gain medium for a VECSEL with an emission wavelength of 1.2 μm [16]. To observe the desired wavelength, well thicknesses of 6.6/4.2/6.6 nm and compositions of $x=0.22$ and $y=0.17$ are suggested. The corresponding band alignment of this design including the first electron and the first two hole states are shown in Fig. 1.

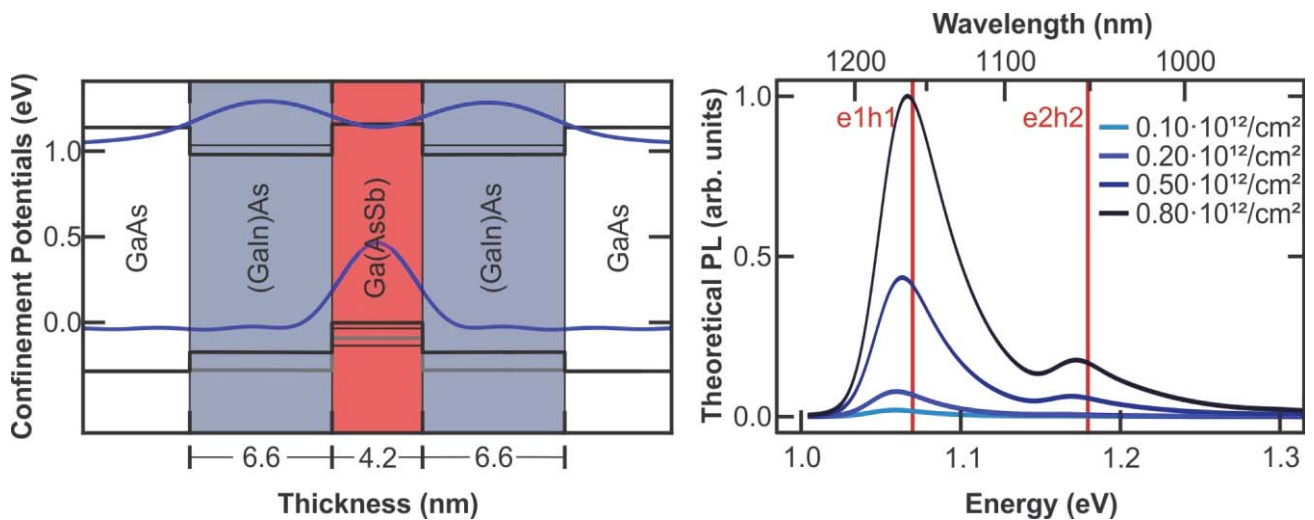


Figure 1. a) Band alignment of the $(\text{Ga}_{1-x}\text{In}_x)\text{As}/\text{Ga}(\text{As}_{1-y}\text{Sb}_y)/(\text{Ga}_{1-x}\text{In}_x)$ “W”-Structure with $x=0.22$ and $y=0.17$. The first electron state is shown as well as the two first hole states. The blue lines indicate the first electron and hole wave function. b) Calculated emission spectra of the structure in comparison with the energetic levels of the e1h1 and e2h2

The calculated photoluminescence spectra for a set of sheet carrier densities ($0.10 \times 10^{12}/\text{cm}^2$ to $0.8 \times 10^{12}/\text{cm}^2$) are shown in Fig. 1). Furthermore, the e1h1 and e2h2 transitions are indicated.

In our previous work, a $10 \times$ “W” multiple quantum well heterostructure (“W”-MQWH) based on this design was grown by metal organic vapor phase epitaxy (MOVPE). Photoluminescence (PL) spectra were measured and compared with a fully microscopic theory. The involved excitonic transitions, as indicated in Fig. 1, were identified by photomodulation reflectance spectroscopy measurements [17]. Based on the good agreement between the experimental and theoretical results, also the absorption and gain properties were calculated using the semiconductor Bloch equations and gain values as high as for type-I systems were predicted [16].

In this paper, a VECSEL is presented which comprises the previously investigated “W”-MQWH as a resonant periodic gain (RPG). The device is operated with heat sink temperatures between -10°C and 20°C . Power curves and laser spectra are shown. Furthermore, the thermal resistance is determined, which delivers insights into fundamental laser properties.

2. VECSEL PREPARATION AND SETUP

For the demonstration of the type-II VECSEL, we choose the approach of flip-chip bonding. Therefore, the VECSEL structure is grown bottom-up, starting with a half-wavelength $(\text{GaIn})\text{P}$ capping layer, followed by the RPG and terminating with a ternary $(\text{Al}_{0.1}\text{Ga}_{0.9})\text{As}/\text{AlAs}$ distributed Bragg reflector (DBR). The growth of the RPG is conducted similar to the growth of the previous MQWH structures [16], [17].

Special care is taken for the layer thickness of the $\text{Ga}(\text{AsP})$ pump absorbing and strain compensating barriers. In order to achieve a high modal gain, microcavity thickness and spatial quantum well spacing have to match the Fabry-Pérot resonance at the laser wavelength. For type-I VECSELs, threshold densities and temperatures can be estimated and the detuning can be designed accordingly. It is found that a negative detuning is required in order to achieve efficient laser operation [18]. However, in the case of the investigated type-II system, a blue shift of the material gain can be expected due to charge-separation and band-distortion [16], [19]. As a consequence, an opposite sign of the detuning should be required in case of a type-II VECSEL. But yet, threshold densities and gain temperatures are not known. As a first approach the structure is realized with a positive detuning of about 30 nm, i.e. the microcavity resonance is designed for 1170 nm at room temperature.

A sample is bonded onto a $350 \mu\text{m}$ thick diamond heat spreader using solid liquid inter-diffusion bonding based on gold and indium. The substrate is removed by chemical wet etching. Finally, the sample is mounted onto a thermo-electrically cooled copper heat sink.

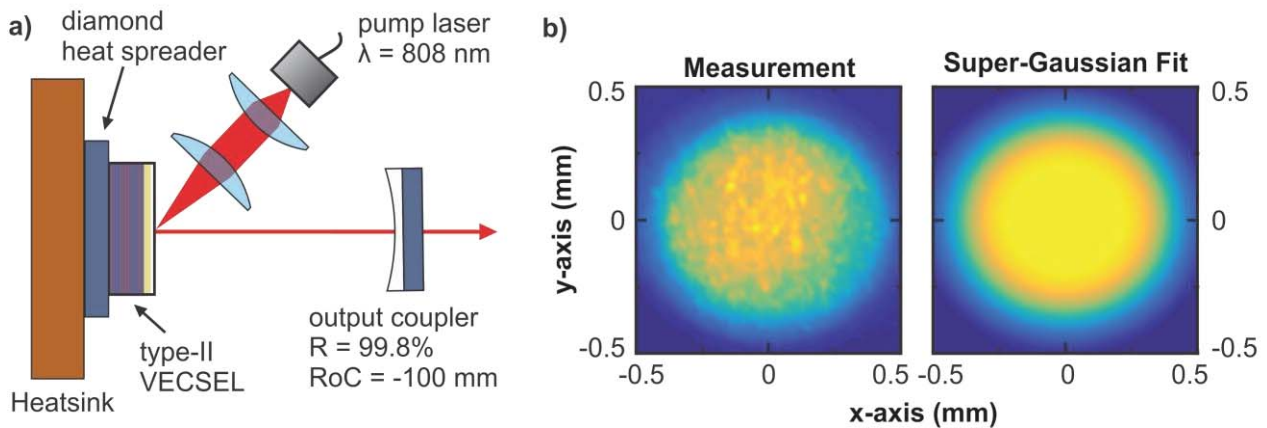


Figure 2. a) Scheme of the flip-chip bonded VECSEL in a linear cavity arrangement. The cavity length is 65 mm. b) The measured pump spot profile (left) and the super-Gaussian fit (right).

A scheme of the linear cavity which is arranged using an output coupler with 0.2% transmission and a radius of curvature of -100 mm is represented by Fig. 2a). An exact knowledge of the pump spot size enables an accurate determination of the pump intensity, which is a characteristic quantity particularly at the VECSEL threshold. Therefore, a pump spot size much larger in comparison with the fundamental transverse mode is used to determine the pump profile and spot size more accurately. The measurement of the pump spot profile as well as the corresponding super-Gaussian fit is shown in Fig. 2b). The measurement and fitting procedure is similar to [20]. Due to oblique pumping an elliptical pump spot is observed with full-width at half maxima of $800 \mu\text{m}$ and $730 \mu\text{m}$. The super-Gaussian factor is $m=2.6$ which corresponds to a flat-top like distribution.

3. EXPERIMENTAL RESULTS

Due to the large pump spot, the alignment of the external cavity is not critical and lasing is observed readily at room temperature. As a first investigation, power curves for different heat sink temperatures between -10°C and 20°C are measured while laser spectra are recorded simultaneously. The power curves are shown in Fig. 3a) with net input power

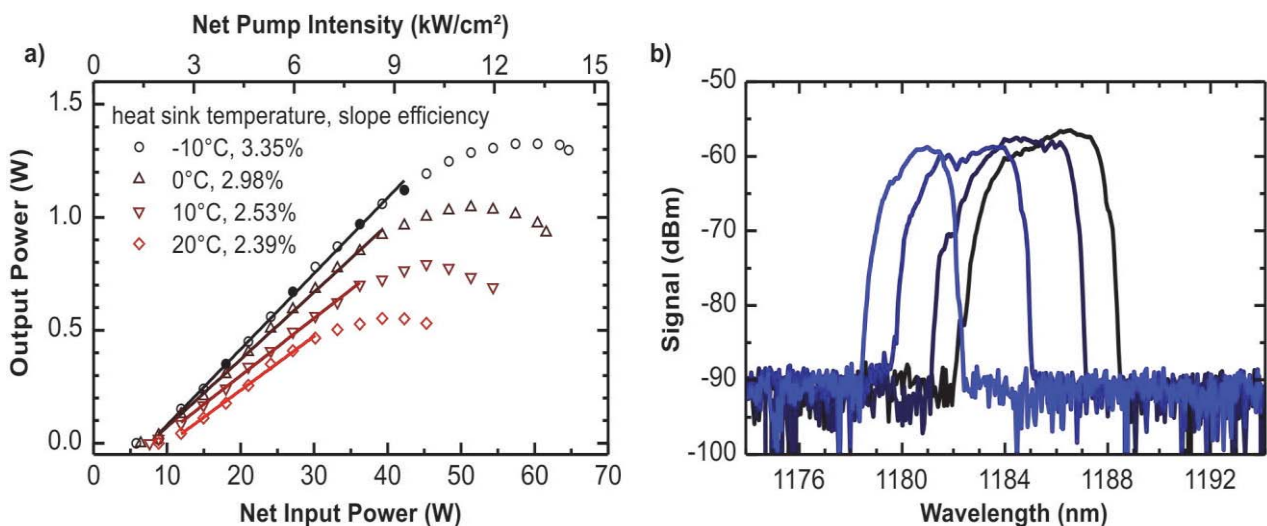
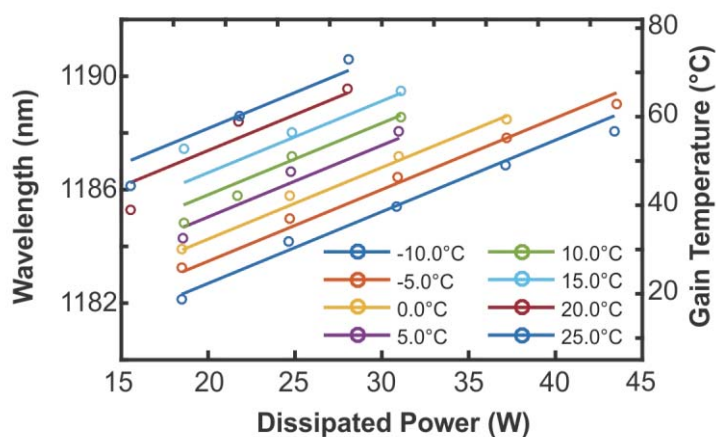


Figure 3. a) Power curves for heat sink temperatures of -10°C , 0°C , 10°C , and 20°C . b) Laser spectra at four different input powers and with a heat sink temperature of -10°C . The spectra (from left to right) correspond to the filled data points in a) (also from left to right).

at the bottom and pump intensity at the top x-axis. It is found that slope efficiencies are steadily increasing with decreasing heat sink temperature from 2.4% to 3.5%. Accordingly, the lowest threshold intensity (1.6 kW/cm²) and the highest output power, namely 1.3 W, are achieved at the lowest heat sink temperature of -10°C. The observed pump intensities at threshold are comparable to these of type-I devices [7].

Exemplary spectra from this power curve are shown in Fig. 3b), demonstrating laser emission around 1180 nm. To obtain a more detailed analysis of the spectral properties, heat sink temperatures T_{Hs} and dissipated powers P_d are varied systematically while the laser spectra are recorded. The measured data is shown as circles in Fig. 4. Each data point represents the maximum emission wavelength λ extracted from the spectrum at the long wavelength side and at a signal drop of 15 dBm. It is found that the laser emission wavelength can be well described by linear temperature ($\partial\lambda/\partial T$) and power dependent ($\partial\lambda/\partial P$) shift rates. This is illustrated by applying a linear regression to the measurement data. The procedure is identical to the thermal resistance (R_{th}) determination as described in [21]. The result is presented as lines in Fig. 4 and summarized in the table aside. The regression fits well for heat sink temperatures between -10°C and 5°C. For elevated temperatures considerable derivations occur only for the low dissipated losses. An explanation is that lasing is not established throughout the pumped region which results in an overestimation of the dissipated power with respect to the active region. For the applied heat removal design, and considering a pump spot radius of 380 μm , a regular thermal resistance of 1.62 K/W is observed [20]. Although a blue shift of the material gain is expected, the temperature and power dependent wavelength shifts are positive. However, it has to be considered that the microcavity exhibits a sharp resonance in comparison to the broad material gain of the type-II QWs [16]. As a consequence, the spectral shift appears to be dominated by the microcavity shift.



Linear regression [21]

$$\lambda = \frac{\partial\lambda}{\partial T} T_{Hs} + \frac{\partial\lambda}{\partial P} R_{th} P_d + \lambda_0$$

Results

Thermal resistance, R_{th}	1.62 K/W
Temp. wavelength shift, $\partial\lambda/\partial T$	0.16 nm/K
Power wavelength shift, $\partial\lambda/\partial P$	0.25 nm/W
Threshold wavelength, λ_0 (0°C heat sink temperature)	1179 nm

Figure 4. Illustration of the thermal resistance estimation based on the shift rate method [21]. The maximum emission wavelength (left y-axis) is plotted against the dissipated power (x-axis). The measurement data is denoted as circles whereas the result of the linear regression is shown as straight lines. The gain temperature is connected linearly to the emission wavelength (right y-axis). The table summarizes the results from the linear regression.

4. SUMMARY

A design for a type-II VECSEL with a $(\text{Ga}_{1-x}\text{In}_x)\text{As}/\text{Ga}(\text{As}_{1-y}\text{Sb}_y)/(\text{Ga}_{1-x}\text{In}_x)\text{As}$ QW arrangement for the emission at 1.2 μm was presented and implemented. The feasibility of the type-II VECSEL was demonstrated and first investigations were conducted including the measurement of the laser power curves. The proof-of-principle device generates considerable output powers of 1.3 W at -10°C heat sink temperature and 0.6 W at 20°C heat sink temperature, respectively. The emission wavelength is around 1185 nm. A thermal resistance measurement was performed which reveals the thermal and pump power dependencies. Threshold wavelengths and gain temperatures were measured which are important quantities with regard to an improvement of future type-II VECSELs in correspondence with the theory.

ACKNOWLEDGEMENTS

The Marburg work is a project of Sonderforschungsbereich 1083 funded by Deutsche Forschungsgemeinschaft (DFG). The work at Nonlinear Control Strategies Inc. is supported via STTR Phase II, Contract # FA9550-13-C-0009.

REFERENCES

- [1] J. E. Hastie, L. G. Morton, A. J. Kemp, M. D. Dawson, A. B. Krysa, and J. S. Roberts, "Tunable ultraviolet output from an intracavity frequency-doubled red vertical-external-cavity surface-emitting laser," *Appl. Phys. Lett.*, vol. 89, no. 6, p. 061114, 2006.
- [2] V.-M. Korpjarvi, E. L. Kantola, T. Leinonen, R. Isoaho, and M. Guina, "Monolithic GaInNAsSb/GaAs VECSEL Operating at 1550 nm," *IEEE J. Sel. Top. Quantum Electron.*, vol. 21, no. 6, pp. 480–484, 2015.
- [3] S. Calvez, J. E. Hastie, M. Guina, O. G. Okhotnikov, and M. D. Dawson, "Semiconductor disk lasers for the generation of visible and ultraviolet radiation," *Laser Photon. Rev.*, vol. 3, no. 5, pp. 407–434, 2009.
- [4] M. Scheller, J. M. Yarborough, J. V. Moloney, M. Fallahi, M. Koch, and S. W. Koch, "Room temperature continuous wave milliwatt terahertz source," *Opt. Express*, vol. 18, no. 26, pp. 27112–27117, 2010.
- [5] B. Heinen, T. L. Wang, M. Sparenberg, A. Weber, B. Kunert, J. Hader, S. W. Koch, J. V. Moloney, M. Koch, and W. Stolz, "106 W continuous wave output power from a vertical-external-cavity surface-emitting laser (VECSEL)," *Electron. Lett.*, vol. 48, no. 9, p. 516, 2012.
- [6] G. Bacher, H. Schweizer, J. Kovac, A. Forchel, H. Nickel, W. Schlapp, and R. Lösch, "Influence of barrier height on carrier dynamics in strained InGaAs/GaAs quantum wells," *Phys. Rev. B*, vol. 43, no. 11, p. 9312, 1991.
- [7] S. Ranta, M. Tavast, T. Leinonen, N. Van Lieu, G. Fetzter, and M. Guina, "1180 nm VECSEL with output power beyond 20 W," *Electron. Lett.*, vol. 49, no. 1, pp. 59–60, 2013.
- [8] M. Peter, R. Kiefer, F. Fuchs, N. Herres, K. Winkler, K.-H. Bachem, and J. Wagner, "Light-emitting diodes and laser diodes based on a GaInAs/GaAsSb type II superlattice on InP substrate," *Appl. Phys. Lett.*, vol. 74, no. 14, pp. 1951–1953, 1999.
- [9] R. H. Miles, D. H. Chow, Y.-H. Zhang, P. D. Brewer, and R. G. Wilson, "Midwave infrared stimulated emission from a GaInSb/InAs superlattice," *Appl. Phys. Lett.*, vol. 66, no. 15, p. 1921, 1995.
- [10] Chia-Hao Chang, Zong-Lin Li, Hong-Ting Lu, Chien-Hung Pan, Chien-Ping Lee, G. Lin, and Sheng-Di Lin, "Low-Threshold Short-Wavelength Infrared InGaAs/GaAsSb "W"-Type QW Laser on InP Substrate," *IEEE Photon. Technol. Lett.*, vol. 27, no. 3, pp. 225–228, 2015.
- [11] S. Sprengel, A. Andrejew, F. Federer, G. K. Veerabathran, G. Boehm, and M.-C. Amann, "Continuous wave vertical cavity surface emitting lasers at 2.5 μm with InP-based type-II quantum wells," *Appl. Phys. Lett.*, vol. 106, no. 15, p. 151102, 2015.
- [12] R. Kaspi, A. Ongstad, G. C. Dente, J. Chavez, M. L. Tilton, and D. Gianardi, "High power and high brightness from an optically pumped InAs/InGaSb type-II midinfrared laser with low confinement," *Appl. Phys. Lett.*, vol. 81, no. 3, p. 406, 2002.
- [13] J. F. Klem, O. Blum, S. R. Kurtz, I. J. Fritz, and K. D. Choquette, "GaAsSb/InGaAs type-II quantum wells for long-wavelength lasers on GaAs substrates," *J. Vac. Sci. Technol. B Microelectron. Nanometer Struct.*, vol. 18, no. 3, p. 1605, 2000.
- [14] J. R. Meyer, C. A. Hoffman, F. J. Bartoli, and L. R. Ram-Mohan, "Type-II quantum-well lasers for the mid-wavelength infrared," *Appl. Phys. Lett.*, vol. 67, no. 6, p. 757, 1995.
- [15] W. W. Chow and H. C. Schneider, "Charge-separation effects in 1.3 μm GaAsSb type-II quantum-well laser gain," *Appl. Phys. Lett.*, vol. 78, no. 26, p. 4100, 2001.
- [16] C. Berger, C. Möller, P. Hens, C. Fuchs, W. Stolz, S. W. Koch, A. Ruiz Perez, J. Hader, and J. V. Moloney, "Novel type-II material system for laser applications in the near-infrared regime," *AIP Adv.*, vol. 5, no. 4, p. 047105, Apr. 2015.
- [17] S. Gies, S. Kruska, C. Berger, P. Hens, C. Fuchs, A. Ruiz Perez, N. W. Rosemann, J. Veletas, S. Chatterjee, W. Stolz, S. W. Koch, J. Hader, J. V. Moloney, and W. Heimbrodt, "Excitonic transitions in highly efficient (GaIn)As/Ga(AsSb) type-II quantum-well structures," *Appl. Phys. Lett.*, vol. 107, no. 18, p. 182104, Nov. 2015.
- [18] J. Hader, G. Hardesty, G. Hardesty, M. J. Yarborough, Y. Kaneda, J. V. Moloney, B. Kunert, W. Stolz, and S. W. Koch, "Predictive Microscopic Modeling of VECSELS," *IEEE J. Quantum Electron.*, vol. 46, no. 5, pp. 810–817, 2010.
- [19] W. W. Chow, O. B. Spahn, H. C. Schneider, and J. F. Klem, "Contributions to the large blue emission shift in a GaAsSb type-II laser," *IEEE J. Quantum Electron.*, vol. 37, no. 9, pp. 1178–1182, 2001.
- [20] B. Heinen, C. Moller, K. Jandieri, B. Kunert, M. Koch, and W. Stolz, "The Thermal Resistance of High-Power Semiconductor Disk Lasers," *IEEE J. Quantum Electron.*, vol. 51, no. 5, pp. 1–9, 2015.
- [21] B. Heinen, F. Zhang, M. Sparenberg, B. Kunert, M. Koch, and W. Stolz, "On the Measurement of the Thermal Resistance of Vertical-External-Cavity Surface-Emitting Lasers (VECSELS)," *IEEE J. Quantum Electron.*, vol. 48, no. 7, pp. 934–940, 2012.

Paper VI

C. Fuchs, **C. Berger**, C. Möller, M. Weseloh, S. Reinhard, J. Hader,
J. V. Moloney, A. Beyer, K. Volz, S. W. Koch, and W. Stolz

*Electrical Injection Type-II (GaIn)As/Ga(AsSb)/(GaIn)As Single
“W”-Quantum Well Laser at 1.2 μm*

Electrical Injection Type-II (GaIn)As/Ga(AsSb)/(GaIn)As Single “W”-Quantum Well Laser at 1.2 μm

C. Fuchs,^{1, a)} C. Berger,¹ C. Möller,¹ M. Weseloh,¹ S. Reinhard,¹ J. Hader,^{2,3} J. V. Moloney,^{2,3} A. Beyer,¹ K. Volz,¹ S. W. Koch,¹ and W. Stolz¹

¹⁾Materials Sciences Center and Department of Physics, Philipps-Universität Marburg, Renthof 5, 35032 Marburg, Germany

²⁾Nonlinear Control Strategies Inc., 7040 N Montecatina Drive, Tucson, AZ 85704, USA

³⁾College of Optical Sciences, University of Arizona, Tucson, AZ 85721, USA

(Dated: 13 May 2016)

Highly efficient interface-dominated electrical injection lasers in the near-infrared regime based on the type-II band alignment in (GaIn)As/Ga(AsSb)/(GaIn)As single “W”-quantum wells are verified. The structure is designed by applying a fully microscopic theory, realized by employing metal organic vapor phase epitaxy, and characterized using electroluminescence measurements and broad-area laser studies. The characteristic blue shift of type-II material systems with increasing charge carrier density is observed and compared to theoretical investigations. The experimental data yields a shift of 93 meV/(kA/cm²). Low threshold current densities of 0.4 kA/cm², high differential efficiencies of 66%, optical output powers of 1.4 W per facet, and internal losses of only 1.9 cm⁻¹ are observed at a wavelength of 1.16 μm . No indication for type-I related transitions for current densities up to 4.5 kA/cm² is observed. A detailed atomic scale chemical analysis forms the basis for future improvements in laser performance.

The development of highly efficient semiconductor lasers in the near-infrared (NIR) wavelength regime is of great interest due to their application, e.g. in fiber-optic telecommunication systems^{1,2}. While present-day systems typically apply InP-based technology, the development of GaAs-based devices is still desirable because of the availability of the mature GaAs-based technology as well as an improved carrier confinement. Lasers in the 1.3 μm wavelength regime were demonstrated using (GaIn)(NAs)³ as well as Ga(AsSb)⁴ as active material. However, the performance of NIR lasers is, among other reasons, limited by Auger losses⁵.

As a result, type-II band alignments were suggested in order to suppress Auger losses⁵⁻⁷ and to enable a more flexible band structure engineering. The charge carrier recombination in such quantum mechanical systems occurs across an interface between two adjacent materials. An example for such a type-II band alignment is the (GaIn)As/Ga(AsSb) material system in which electrons are confined in a (GaIn)As quantum well (QW) and holes are confined in a Ga(AsSb) QW.

Type-II photoluminescence (PL) and electrical injection lasing from these structures was reported in the NIR regime on GaAs substrates^{8,9} as well as in the mid-infrared (MIR) regime on InP substrates^{10,11}. However, laser devices in the NIR regime exhibited a low output power of 140 mW per facet⁹ or laser emission from a type-I instead of a type-II transition¹². These results highlight the necessity of a careful device design using suitable microscopic models.

In addition to structures based on double QWs, an approach employing a “W”-type structure in which a

Ga(AsSb) QW is embedded in between two adjacent (GaIn)As QWs was proposed for laser applications in the NIR regime¹³. First broad-area laser devices with threshold current densities of $j_{\text{th}} = 0.37 \text{ kA/cm}^2$ as well as internal efficiencies of $\eta_i = 42\%$ and internal losses of $\alpha_i = 11 \text{ cm}^{-1}$ at 1.3 μm were realized using molecular beam epitaxy¹⁴.

Our recent experiments applying metal organic vapor phase epitaxy (MOVPE) have shown great promise due to a strong PL from these structures as well as a good agreement between experimental spectroscopic data and a fully microscopic theory¹⁵. Furthermore, the theoretical investigation predicted gain values which are comparable to type-I systems. Photomodulated reflectance (PR) spectroscopy was used to extensively characterize the quantum mechanical properties of these structures. The measurements supported the theoretical model and confirmed the predicted type-II transitions between the electron and the hole ground state (e1h1), the first excited electron and the first excited hole state (e2h2), and the electron ground state and the second excited hole state (e1h3) in “W”-QWs¹⁶. In order to prove the viability of this material system as active material for semiconductor lasers, an optically pumped vertical-external-cavity surface-emitting laser (VECSEL) was fabricated. The characterization of the VECSEL yielded a successful demonstration of lasing from the e1h1 type-II transition with a maximum continuous wave (cw) output power of 4 W¹⁷.

In this publication, highly efficient electrical injection (GaIn)As/Ga(AsSb)/(GaIn)As single “W”-QW (S-“W”-QW) lasers are designed based on a fully microscopic theory and realized using MOVPE. As interface characteristics are particularly important in these type-II structures, structural analysis by scanning transmission electron mi-

^{a)}Electronic mail: christian.fuchs@physik.uni-marburg.de

croscopy (STEM) is performed. The electroluminescence (EL) as well as the laser characteristics are evaluated in detail.

The growth process is carried out in an AIXTRON AIX 200 GFR (Gas Foil Rotation) reactor system using triethylgallium (TEGa), trimethylindium (TMIn), and trimethylaluminum (TMAI) as group-III, tertiarybutylarsine (TBAs) and triethylantimony (TESb) as group-V, and tetrabromomethane (CBr_4) and diethyltellurium (DETe) as dopant sources, respectively. The reactor pressure is set to 50 mbar and high-purity H_2 is used as carrier gas. The native oxide layer is removed from the n-GaAs (001) ($\pm 0.1^\circ$) substrate by applying a TBAs-stabilized bake-out procedure.

While the (GaIn)As/Ga(AsSb)/(GaIn)As S-“W”-QW active region is grown at a temperature of 550°C , the n-GaAs buffer, the n- and p-(AlGa)As claddings, the undoped GaAs separate confinement heterostructures (SCH), and the p^+ -GaAs cap are grown at a temperature of 625°C . The p-(AlGa)As layer is carbon-doped by employing a decreased V/III ratio instead of using CBr_4 as dopant source.

The $1.4\ \mu\text{m}$ ($\text{Al}_z\text{Ga}_{1-z}$)As ($z=0.4$) cladding layers together with the $0.2\ \mu\text{m}$ GaAs SCH layers serve as waveguide structure in order to confine the optical mode towards the active region. The active region itself consists of a 4 nm $\text{Ga}(\text{As}_{1-x}\text{Sb}_x)$ ($x=0.2$) and two 6 nm ($\text{Ga}_{1-y}\text{In}_y$)As ($y=0.2$) QWs. A highly doped p^+ -GaAs cap serves as contact layer in order to ensure small contact resistances. Gain guided devices are processed by thinning the sample to $150\ \mu\text{m}$, evaporating $100\ \mu\text{m}$ wide gold strips onto the p^+ -GaAs cap, and a large-area gold contact onto the n-GaAs substrate. Additionally, the remaining part of the p^+ -GaAs cap in between the top metal contacts is wet chemically etched off in order to prevent lateral current spreading. The resulting sample is cleaved to laser bars with cavity lengths between $800\ \mu\text{m}$ and $2070\ \mu\text{m}$. A schematic illustration of the resulting device structure can be found in the inset of Fig. 3.

An in-depth characterization is carried out using devices with varying cavity length. All experiments are performed using a pulsed excitation of 400 ns long pulses at a repetition rate of 10 kHz. A large-area germanium photodetector is used to measure the integral single-facet output power as a function of the current. Spectrally resolved EL measurements are carried out using a Yokogawa AQ6370B optical spectrum analyzer.

The detailed analysis of the active (GaIn)As/Ga(AsSb)/(GaIn)As “W”-QW heterostructure (“W”-QWH) is performed by atomic resolution STEM applying the high-angle annular dark field (HAADF) technique using a double-aberration-corrected JEOL 2200FS microscope.

The optical response of the “W”-QW active region is modelled using the semiconductor luminescence^{18,19} and Bloch^{19,20} equations. For the calculation of both the luminescence and material absorption, the single-particle band structure and wave functions are obtained from an

8×8 Luttinger $\mathbf{k} \cdot \mathbf{p}$ model^{21,22}. This treatment allows the determination of dipole transition and Coulomb matrix elements²³. Additionally, the microscopic Schrödinger–Poisson equation²⁴ is solved to take care of local charge inhomogeneities in the type-II “W”-QWH. Nevertheless, all charge carriers are assumed to be in thermal equilibrium and therefore, to be Fermi distributed in their respective bands. Higher order scattering terms are treated on the level of the second Born approximation^{22,23}.

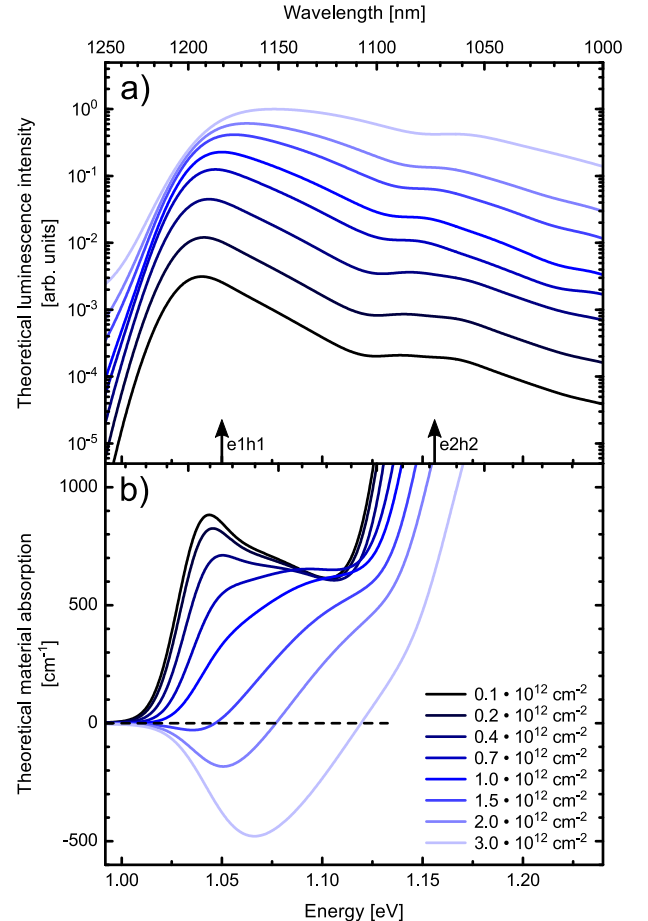


FIG. 1. a) Theoretically calculated luminescence intensity for different charge carrier densities ($0.1 \cdot 10^{12} \text{ cm}^{-2}$ - $3.0 \cdot 10^{12} \text{ cm}^{-2}$) in the active region at a temperature of 300 K. The single-particle transition energies of e1h1 and e2h2 are indicated as arrows for a charge carrier density of $0.1 \cdot 10^{12} \text{ cm}^{-2}$. b) Theoretically calculated material absorption for the same charge carrier densities in the active region and temperature.

The inhomogeneous broadening due to intrinsic statistical alloy fluctuations, layer thickness fluctuations, and interface roughness is taken into account by convolving the resulting spectra with a Gaussian²⁵. The only input parameters required for this theoretical approach are the nominal material parameters like thicknesses and concentrations in the specific QWs which can be extracted directly from high-resolution X-Ray diffraction (HR-XRD) measurements in combination with the

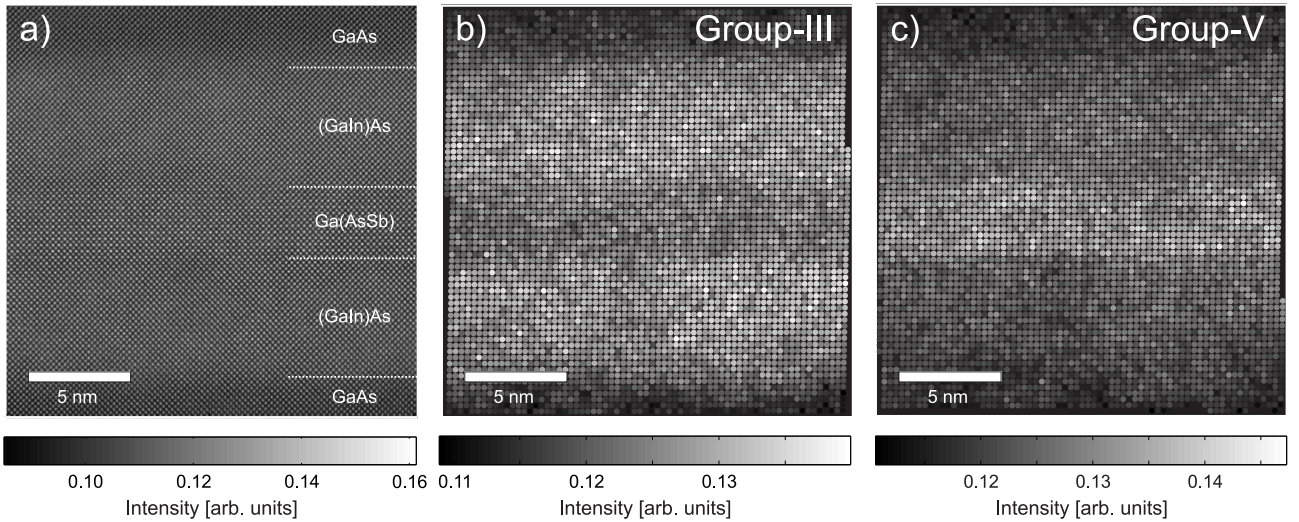


FIG. 2. a) Atomic resolution HAADF STEM image of the “W”-QWH. In order to increase the visibility of the individual layers, the intensity of the group-III and group-V sublattices are shown separately in b) and c), respectively.

atomic scale HAADF STEM analysis. A detailed description of this theoretical approach can be found in Ref. 15.

In comparison to earlier investigations of “W”-QWHs employing the (GaIn)As/Ga(AsSb)/(GaIn)As material system¹³, different compositions as well as a reduced hole QW thickness are chosen to optimize the wave function overlap. The theoretical analysis is carried out assuming layer thicknesses of 6 nm for the (GaIn)As and 4 nm for the Ga(AsSb) QWs and concentrations of 20% for In and Sb, respectively. The resulting theoretical luminescence intensity and material absorption are presented in Fig. 1 a) and b), respectively. Low excitation charge carrier density ($0.1 \cdot 10^{12} \text{ cm}^{-2}$) results in a luminescence peak at $1.19 \mu\text{m}$ while high excitation charge carrier density ($3.0 \cdot 10^{12} \text{ cm}^{-2}$) generates a gain peak at $1.16 \mu\text{m}$. The single-particle transition energies of e1h1 and e2h2 are indicated as arrows in Fig. 1 a) for a charge carrier density of $0.1 \cdot 10^{12} \text{ cm}^{-2}$.

In order to prove the successful realization of the “W”-QWH atomic resolution HAADF measurements were carried out as shown in Fig. 2 a). The MOVPE-growth direction is from bottom to top in this image. As the electron scattering is proportional to the atomic number of the scattering material, the HAADF intensity is sensitive to the chemical composition of the material. The visibility of the individual layers is increased by separating the intensity of the group-III and group-V sublattices as shown in Fig. 2 b) and c), respectively. In these maps, the intensity of each atomic column is derived by averaging the HAADF intensity in a circular region with a radius of 2 px ($\approx 0.04 \text{ nm}$) around its center. The slightly increased intensity in the Sb-containing region with respect to the GaAs barrier in Fig. 2 b) is most likely caused by “cross scattering” between the two sublattices²⁶ rather than In-diffusion into the Ga(AsSb) QW. The same behavior can be observed in the In-containing region in Fig. 2 c).

In the future, a further quantitative chemical analysis of the individual compositions in the “W”-QWH utilizing complementary contrast simulations²⁷ can allow for a precise determination of the actual hetero band structure for each monolayer.

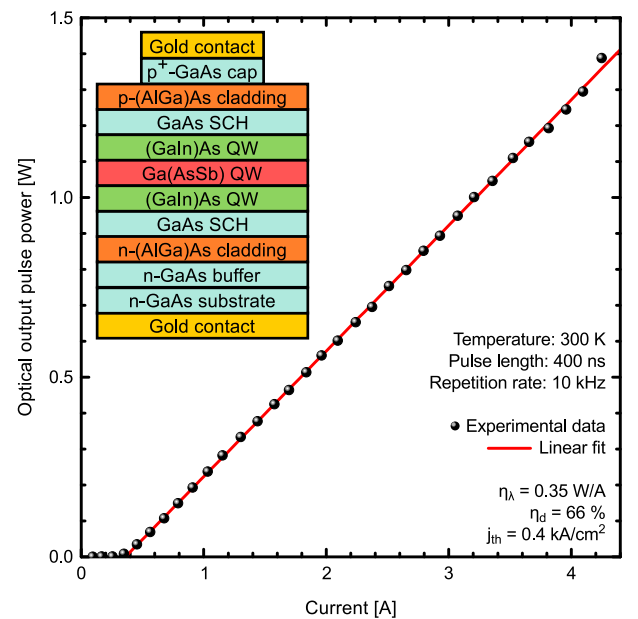


FIG. 3. Optical output pulse power per facet at room temperature of a $930 \mu\text{m}$ long (GaIn)As/Ga(AsSb)/(GaIn)As S-“W”-QW laser as function of the injection current. The inset schematically illustrates the device structure.

The optical pulse power measurements of a $930 \mu\text{m}$ long (GaIn)As/Ga(AsSb)/(GaIn)As S-“W”-QW laser reveal a distinct threshold behavior at a low threshold current density of $j_{\text{th}} = 0.4 \text{ kA/cm}^2$ at room temperature as shown in Fig. 3. Furthermore, an optical efficiency of

$\eta_{\lambda} = 0.35$ W/A per facet is observed resulting in a differential efficiency of $\eta_d = 66\%$, and a pump-limited maximum optical output power of $P_{\max} = 1.4$ W at a current of 4.2 A.

In order to prove that the laser emission is based on the e1h1 type-II transition spectrally resolved EL measurements are presented in Fig. 4). The considerable blue shift observed below laser threshold is in agreement with the theoretical results presented in Fig. 1 a) as well as those published in literature^{14,15}. An average blue shift of (93 ± 14) meV/(kA/cm²) is observed between 0.09 A (0.10 kA/cm²) and 0.35 A (0.38 kA/cm²) due to the charge carrier separation in type-II heterostructures^{13,15}.

Furthermore, the theoretical investigation predicts significant material gain above charge carrier densities of $1.5 \cdot 10^{12}$ cm⁻² as shown in Fig. 1 b). This is confirmed by the low threshold laser operation starting from a current of 0.39 A. No type-I transitions are observed for the entire current range in the LED or laser operation regime up to current densities of 4.5 kA/cm². A shoulder on the high energy side of the spectra occurs as shown in Fig. 4. This transition is several orders of magnitude weaker than the actual laser mode. The spectral position of this peak is in good agreement with the e2h2 type-II transition indicated in Fig 1 a).

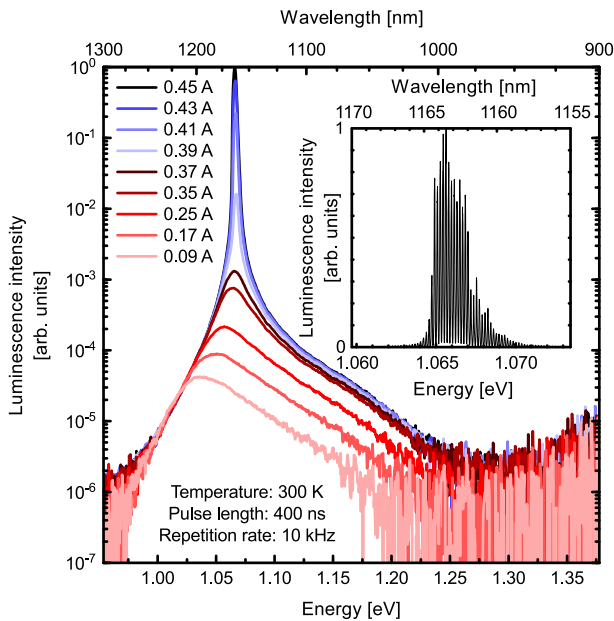


FIG. 4. Spectrally resolved electroluminescence measurements at room temperature of a 930 μm long (GaIn)As/Ga(AsSb)/(GaIn)As S-“W”-QW laser for different currents in the LED regime (0.09 A - 0.37 A, red) and directly above threshold (0.39 A - 0.45 A, blue). A high resolution measurement of the laser mode at 0.45 A is presented in the inset.

Laser operation is confirmed by measuring the high-resolution mode spectrum at 0.45 A which is shown in the inset of Fig. 4). The measurement reveals a laser mode at 1.164 μm and a mode spacing of 0.193 nm for

the chosen laser cavity length of 930 μm .

In addition, the internal losses α_i of these lasers are determined by analyzing the cavity length dependence of the differential efficiencies²⁸. Therefore, devices of different cavity lengths are characterized and the data is evaluated assuming an end-mirror reflectivity of $R = 0.3$. Multiple measurements of different laser devices are carried out for each cavity length and the results are averaged. The evaluation is performed using these average values and results in internal losses of only $\alpha_i = (1.9 \pm 0.5)$ cm⁻¹ and an internal efficiency of $\eta_i = (66 \pm 4)\%$.

In conclusion, the careful device design and optimization using a fully microscopic theory has resulted in highly efficient interface-dominated lasers in the 1.2 μm wavelength regime based on the type-II band alignment in (GaIn)As/Ga(AsSb)/(GaIn)As “W”-QWHs. An average blue shift of 93 meV/(kA/cm²) in the LED regime was observed which is in agreement with theoretical modelling. The MOVPE-grown S-“W”-QW edge-emitting lasers exhibited a high differential efficiency of 66%, a low threshold current density of 0.4 kA/cm², a pump-limited maximum optical output pulse power of 1.4 W as well as internal losses of only 1.9 cm⁻¹. No indication for type-I related transitions are observed in this optimized single “W”-QW material system in the studied operation regime up to 4.5 kA/cm². The nanoscale analysis of the local chemical compositions and the actual interface configuration form the basis for the future optimization of these type-II laser structures.

ACKNOWLEDGMENTS

The Marburg work is a project of Sonderforschungsbereich 1083 funded by Deutsche Forschungsgemeinschaft (DFG). The work at Nonlinear Control Strategies Inc. is supported by the Air Force Office of Scientific Research under the STTR Phase II, Grant # FA9550-16-C-0021. The work at the University of Arizona was supported by the U.S. Air Force Office of Scientific Research, Contract # FA9550-14-1-0062.

¹E. Murphy, Nat. Photon. **4**, 287 (2010).

²G. P. Agrawal, *Fiber-optic communication systems*, Vol. 222 (John Wiley & Sons, 2012).

³F. Höhnsdorf, J. Koch, S. Leu, W. Stolz, B. Borchert, and M. Druminski, Electron. Lett. **35**, 571 (1999).

⁴M. Yamada, T. Anan, K. Tokutome, A. Kamei, K. Nishi, and S. Sugou, IEEE Photon. Technol. Lett. **12**, 774 (2000).

⁵J. R. Meyer, C. L. Felix, W. W. Bewley, I. Vurgaftman, E. H. Aifer, L. J. Olafsen, J. R. Lindle, C. A. Hoffman, M. J. Yang, B. R. Bennett, B. V. Shanabrook, H. Lee, C. H. Lin, S. S. Pei, and R. H. Miles, Appl. Phys. Lett. **73**, 2857 (1998).

⁶G. G. Zegrya and A. D. Andreev, Appl. Phys. Lett. **67**, 2681 (1995).

⁷L. T. Heen and H. P. Hjalmarson, Phys. Scr. **T79**, 106 (1999).

⁸M. Peter, K. Winkler, M. Maier, N. Herres, J. Wagner, D. Fekete, K. H. Bachem, and D. Richards, Appl. Phys. Lett. **67**, 2639 (1995).

⁹J. F. Klem, O. Blum, S. R. Kurtz, I. J. Fritz, and K. D. Choquette, J. Vac. Sci. Technol., B **18**, 1605 (2000).

- ¹⁰C. Grasse, P. Wiecha, T. Gruendl, S. Sprengel, R. Meyer, and M. C. Amann, *Appl. Phys. Lett.* **101**, 221107 (2012).
- ¹¹S. Sprengel, C. Grasse, P. Wiecha, A. Andrejew, T. Gruendl, G. Boehm, R. Meyer, and M. C. Amann, *Appl. Phys. Lett.* **106**, 151102 (2015).
- ¹²B. N. Zvonkov, S. M. Nekorkin, O. V. Vikhrova, and N. V. Dikareva, *Semiconductors* **47**, 1219 (2013).
- ¹³W. W. Chow and H. C. Schneider, *Appl. Phys. Lett.* **78**, 4100 (2001).
- ¹⁴W. Chow, O. Blum Spahn, H. C. Schneider, and J. F. Klem, *IEEE J. Quantum Electron.* **37**, 1178 (2001).
- ¹⁵C. Berger, C. Möller, P. Hens, C. Fuchs, W. Stolz, S. W. Koch, A. Ruiz Perez, J. Hader, and J. V. Moloney, *AIP Adv.* **5**, 047105 (2015).
- ¹⁶S. Gies, C. Kruska, C. Berger, P. Hens, C. Fuchs, A. Ruiz Perez, N. W. Rosemann, J. Veletas, S. Chatterjee, W. Stolz, S. W. Koch, J. Hader, J. V. Moloney, and W. Heimbrod, *Appl. Phys. Lett.* **107**, 047105 (2015).
- ¹⁷C. Möller, C. Fuchs, C. Berger, A. Ruiz Perez, M. Koch, J. Hader, J. V. Moloney, S. W. Koch, and W. Stolz, *Appl. Phys. Lett.* **108**, 071102 (2016).
- ¹⁸M. Kira and S. W. Koch, *Prog. Quant. Electron.* **30**, 155 (2006).
- ¹⁹M. Kira and S. W. Koch, *Semiconductor Quantum Optics* (Cambridge University Press, 2012).
- ²⁰H. Haug and S. W. Koch, *Quantum Theory of the Optical and Electronic Properties of Semiconductors*, 5th ed. (World Scientific Publishing, 2009).
- ²¹J. Hader, N. Linder, and G. H. Döhler, *Phys. Rev. B* **55**, 6960 (1997).
- ²²W. W. Chow and S. W. Koch, *Semiconductor-Laser Fundamentals: Physics of the Gain Materials* (Springer, 1999).
- ²³J. Hader, S. W. Koch, and J. V. Moloney, *Solid-State Electron.* **47**, 513 (2003).
- ²⁴D. Ahn and S. L. Chuang, *J. Appl. Phys.* **64**, 6143 (1988).
- ²⁵J. Hader, J. V. Moloney, S. W. Koch, and W. W. Chow, *IEEE J. Sel. Topics Quantum Electron.* **9**, 688 (2003).
- ²⁶L. J. Allen, A. J. D'Alfonso, S. D. Findlay, J. M. LeBeau, N. R. Lugg, and S. Stemmer, *J. Phys.: Conf. Ser.* **241**, 012061 (2010).
- ²⁷A. Beyer, A. Stegmüller, J. O. Oelerich, K. Jandieri, K. Werner, G. Mette, W. Stolz, S. D. Baranovskii, R. Tonner, and K. Volz, *Chem. Mat.* (2016), 10.1021/acs.chemmater.5b04896.
- ²⁸L. A. Coldren, S. W. Corzine, and M. L. Masanovic, *Diode Lasers and Photonic Integrated Circuits*, 2nd ed. (John Wiley & Sons, 2012) Chap. 2.

Paper VII

C. Lammers, M. Stein, **C. Berger**, C. Möller, C. Fuchs,
A. Ruiz Perez, A. Rahimi–Iman, J. Hader, J. V. Moloney, W. Stolz,
S. W. Koch, and M. Koch

Gain spectroscopy of a type-II VECSEL chip

Gain spectroscopy of a type-II VECSEL chip

C. Lammers,^{1, a)} M. Stein,¹ C. Berger,¹ C. Möller,¹ C. Fuchs,¹ A. Ruiz Perez,² A. Rahimi-Iman,¹ J. Hader,³ J. V. Moloney,³ W. Stolz,¹ S. W. Koch,¹ and M. Koch¹

¹⁾Department of Physics and Material Sciences Center, Philipps-Universität Marburg, Renthof 5, 35032 Marburg, Germany

²⁾NAsP_{III/V} GmbH, Am Knechtacker 19, 35041 Marburg, Germany

³⁾College of Optical Sciences, University of Arizona, 1630 E. University Blvd., Tucson, AZ 85721, USA

(Dated: 16 March 2016)

In this work, gain dynamics of a novel VECSEL chip design based on type-II heterostructures is analyzed both theoretically as well as experimentally. For such a chip consisting of a GaAs/(GaIn)As/Ga(AsSb)/(GaIn)As/GaAs multi-quantum-well active region, optical transitions for laser operation take place across the interface of the heterostructure, with holes and electrons separately confined. In order to study the temporal evolution of gain in a type-II chip in comparison to conventional type-I structures, optical pump-probe spectroscopy is used. Our measurements in reflection geometry reveal a maximum reflectance of 1.008 at 1168 nm for a delay of 1.3 ns between pump and probe pulse. Starting at 0.6 ns after excitation, gain lasts for 1.5 ns. Here, the observed dynamics deviates from the earlier but shorter gain evolution in a comparable type-I structure. Gain spectra of the laser chip are predicted by a fully microscopic approach using the semiconductor Bloch equations, showing remarkable agreement with the obtained results.

Very recently, laser operation has been demonstrated in a type-II vertical-external-cavity surface-emitting-laser (VECSEL) structure¹, promising further wavelength flexibility in the infrared and reduced losses based on Auger processes.^{2,3} For such staggered-alignment gain structures, optical properties and carrier dynamics have been investigated with great interest.⁴⁻⁷ Lately, type-II semiconductor heterostructures with a “W”-type band alignment of the conduction band, separating spatially electron and hole confinement, were found to be a promising candidate for laser applications as reported in Refs. 8 and 9. Particularly, the combination of reduced intrinsic losses, a better access to emission wavelengths in the infrared regime circumventing limitations set by direct transition semiconductors, and room temperature operation make this material system attractive for applications, e.g. for optical data transmission.¹⁰

Especially surface emitters provide a suitable configuration for this kind of application and are in the focus of current research.¹¹ Up to date, both edge emitters as well as surface-emitting quantum-well lasers based on type-II material systems have been realized.^{12,13} To acquire a detailed understanding of carrier dynamics inside such a laser medium, time-resolved reflectivity measurements are of great concern. So far, gain measurements on semiconductor laser structures were mostly based on stationary methods. Techniques like the Hakki-Paoli and variable-stripe-length method are prominent examples in literature.¹⁴⁻¹⁷ Complementary, ultrafast pump-probe experiments have turned out to bring up a viable method to unravel the transfer and cooling dynamics, respectively, and has become the method of choice in order to investigate gain dynamics.¹⁸

In this work, we present a systematic experimental and theoretical investigation of reflectivity and gain properties of a type-II “W”-VECSEL. The sample studied in comparison to a conventional type-I chip is composed of a 10 x (GaIn)As/Ga(AsSb) “W”-MQWHs, which form the resonant-periodic-gain (RPG) medium. Theoretical calculations were performed over a wide range of carrier densities to provide detailed insight into the gain characteristics. These densities correspond to the situation at different temporal delays in the experiment. A fully microscopic theory enables us to do a thorough analysis of the sample’s reflection properties. Starting from the material composition obtained by high resolution X-ray diffraction (HR-XRD), we calculate the optical properties of this system. Afterwards, we used the obtained results to model the reflection spectra for the VECSEL chip. Thereby, modal gain is predicted for the VECSEL structure at a wavelength of about 1170 nm at 300 K. To retrieve spectral and dynamical gain characteristics experimentally, an optical-pump optical-probe setup in reflection geometry is used. For each measurement, the exhibited change of reflectivity ΔR was added to the reflectivity of the unexcited sample, which was measured within the same setup.

The VECSEL chip was grown bottom-up on exact GaAs (001) ($\pm 0.1^\circ$) substrate in a horizontal AIXTRON AIX 200 GFR (Gas Foil Rotation) metal organic vapor phase epitaxy (MOVPE) reactor system. It consists of a lattice matched (GaIn)P capping layer, the RPG with 10 MQWHs and a distributed Bragg reflector (DBR) consisting of 22 1/2 pairs of $(\text{Al}_{0.1}\text{Ga}_{0.9})\text{As}/\text{AlAs}$. Here, the MQWH consists of a “W”-shaped $(\text{Ga}_{1-y}\text{In}_y)\text{As}/\text{Ga}(\text{As}_{1-x}\text{Sb}_x)/(\text{Ga}_{1-y}\text{In}_y)\text{As}$ type-II band alignment, which forms the active region separated by GaAs/Ga(AsP)/GaAs barriers, as can be seen in the inset of Fig. 1 (b). In order to obtain a resonant structure, the optical layer thicknesses of the bar-

^{a)}Electronic mail: christian.lammers@physik.uni-marburg.de

riers as well as the (GaIn)P capping layer were matched to $\lambda/2$ with respect to the lasing wavelength. The layer thicknesses and compositions of the active region were determined by fitting a fully dynamical simulation to the high resolution X-ray diffraction (HR-XRD, (004)-reflection) pattern of the VECSEL chip. This analysis yields a $\text{Ga}(\text{As}_{1-x}\text{Sb}_x)$ ($x = 0.198$) and a $(\text{Ga}_{1-y}\text{In}_y)\text{As}$ ($y = 0.203$) layer thickness of 4.0 nm and 5.5 nm, respectively.

We utilize the semiconductor Bloch equations (SBE) to calculate the changes in absorption and refractive index induced by optical excitation of the sample.^{19–21} To achieve a sufficient level of accuracy in our calculations, we include all terms in the SBE up to the second Born level and take into account homogeneous broadening, i.e. intrinsic microscopic carrier scattering inside the semiconductors.^{22,23} Unavoidable and common growth inhomogeneities in such MQWH samples are modeled by an inhomogeneous broadening—a convolution of our theoretical spectra with a Gaussian distribution describing the variation of the bandgap energies.²⁴ Starting point for our calculations are the band structure and the corresponding wavefunctions. All these single-particle properties are accessed evaluating an 8×8 multi band $\mathbf{k} \cdot \mathbf{p}$ model.^{22,25} We assume all carriers to be in thermal equilibrium and therefore be Fermi distributed in their respective bands. Due to the type-II setup, local charge inhomogeneities can arise and we solve the Schrödinger–Poisson equation to obtain the changes to the confinement potential.²⁶ Based on the band structure and the single-particle wavefunctions we compute the dipole and Coulomb matrix elements.²³

Having modeled the absorption and refractive index changes induced by a certain carrier density, we can derive the overall optical properties of the VECSEL structure. Reflection properties of the sample are calculated using the transfer matrix method.^{21,27} A spectral filter function describes the spatial overlap of the quantum-well positions inside the RPG with the intensity maxima of the longitudinal light modes of the optical cavity.²⁸

In the following, we investigate the gain properties of our type-II chip structure. Figure 1 (a) presents numerical results for the material absorption at 300 K of the “W”-type MQWH. Here, we assumed an inhomogeneous broadening of 20 meV to account for growth impurities in our simulation. As the carrier density is increased from $0.1 \cdot 10^{12}/\text{cm}^2$ up to $3 \cdot 10^{12}/\text{cm}^2$ (bright to dark) the excitonic absorption peak vanishes and the absorption gets negative. This means that a spectrally-broad gain region is formed for this material composition in the RPG. Thereafter, we compute the modal gain for a carrier density of $3 \cdot 10^{12}/\text{cm}^2$, by multiplying the filter function (represented as dashed line in Fig. 2) with the gain of the full VECSEL structure. Thereby, the broad material gain shown in Fig. 1 (a) evolves into a narrow modal gain around 1170 nm, which is presented in Fig. 1 (b).

Next, we compare the simulated reflectivity to an experimental spectrum in Fig. 2. Here, the measured spec-

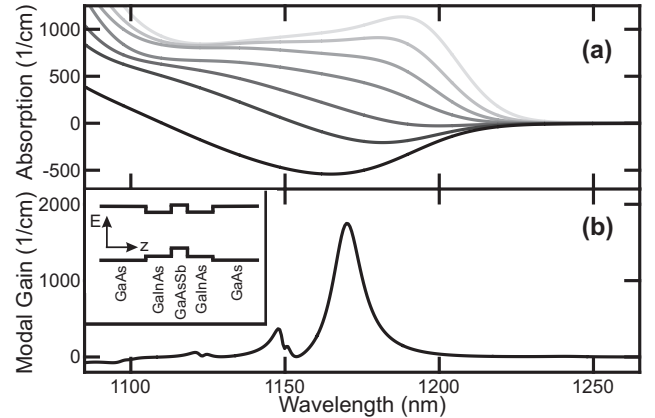


FIG. 1. Theoretical material absorption and modal gain. (a) Calculated material absorption for the active region of the type-II “W”-laser structure is presented for carrier densities ranging from $0.1 \cdot 10^{12}/\text{cm}^2$ up to $3 \cdot 10^{12}/\text{cm}^2$ (bright to dark). (b) A simulation of the modal gain for the full type-II VECSEL system is plotted for a carrier density of $3 \cdot 10^{12}/\text{cm}^2$. The temperature is set to 300 K for both calculations. An inhomogeneous broadening of 20 meV is used. The inset illustrates schematically the band alignment of the type-II heterostructure.

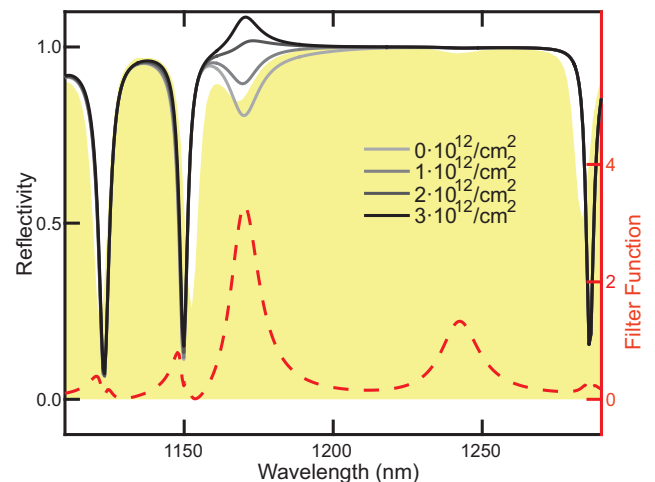


FIG. 2. Theoretical reflectivity (lines) of the type-II gain structure together with its calculated filter function (dashed line). Measured reflectance at room temperature for an unexcited chip is shown as shaded area in the background, while theoretical reflectivity spectra are presented for carrier densities between $0 \cdot 10^{12}/\text{cm}^2$ and $3 \cdot 10^{12}/\text{cm}^2$ (solid lines, bright to dark). Here, the system is considered at a temperature of 300 K with an inhomogeneous broadening of 20 meV.

trum plotted in the background of the diagram represents the system under unexcited conditions (shaded area). Thus, it can only be compared to the theoretical spectrum with vanishing carrier density ($0 \cdot 10^{12}/\text{cm}^2$). A direct comparison between experiment and theory shows a good qualitative agreement. Using our theory as a predictive tool, we increase the carrier density up

to $3 \cdot 10^{12}/\text{cm}^2$, which leads to a broad material gain. Thereby, we observe a gradual increase of the reflectivity at the absorption dip in the chip's stop band. By increasing the carrier density, we yield a vanishing absorption dip which evolves into a gain peak around 1171 nm. Looking at the filter function corresponding to the RPG and DBR (dashed line), we find the increase of the reflectivity being strongly correlated to the peaks of the filter function. As this configuration is spectrally not centered in the middle of the stop band, we observe two peaks, with the main peak exhibited around 1170 nm and a second one at 1240 nm. Most clearly, we see that the laser emission can only be expected at the maximum of the filter function, as there is no material gain at the second peak. This very narrow filtering of the spectrally-broad type-II gain from Fig. 1 (a) leads to a small region where the reflectivity reaches a level higher than 1. Overall, by applying our theory we are able to predict gain for this VECSEL setup at a wavelength of 1171 nm.

In the next part of our work, we will present gain measurements performed with the optical pump-probe technique. For the experimental studies, a 1 kHz, 5 mJ, 35 fs regenerative Ti:sapphire amplifier was used to acquire time-resolved differential reflectivity ΔR -spectra. The amplifier drives an optical parametric amplifier (OPA) to provide fs-pump pulses, and generates a fs-supercontinuum with which gain dynamics in the chip can be optically probed. Those differential reflectivity spectra were added to the reflectivity measurements of the unexcited sample in order to retrieve the time-resolved reflectivity of the excited sample. The reflectivity was acquired by probing the sample first and then replacing it by a silver mirror for a reference measurement. The pump spot diameter was determined to $75 \mu\text{m}$ using a knife-edge measurement. An InGaAs-CCD line cooled with liquid nitrogen was used as a detector in combination with a Czerny–Turner monochromator with a 80 Gr/mm diffraction grating as dispersive element. The excitation density of our pump pulse with a central wavelength of 1000 nm was set to $5.6 \cdot 10^{16}/\text{cm}^2$ in order to inject a sufficiently large amount of charge carriers. All experiments were carried out at room temperature.

The experimentally measured reflectivity of the unexcited VECSEL chip is governed by an interplay of material absorption with the filter function and features an expected dip at 1168 nm for the employed material and structure, as Fig. 2 and 3 indicate. However, by optical excitation of the sample with a short laser pulse, a bleaching of the absorption dip is induced, and consecutively within 1.3 ns a reflectivity $R > 1$ is obtained as a signature of gain. Thereafter, due to charge-carrier recombination on a timescale of several nanoseconds, the carrier density continuously decreases, which is traceable in time-dependent reflectivity spectra acquired at pump-probe delays of 2.1, 4 and 7 ns, respectively. The variable delay in this experiment allows one to monitor the evolution of charge carrier density, which provides a connection of experimental delay times and carrier densities

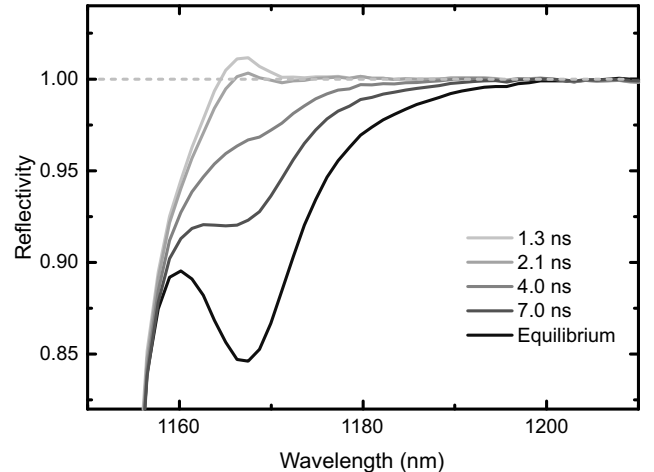


FIG. 3. Experimental reflectivity spectra of a type-II chip for pump-probe time delays ranging between 1.3 and 7.0 ns (solid lines, bright to dark). The maximum gain is reached at a delay of 1.3 ns with respect to excitation. The equilibrium situation corresponds to the reflectivity measured by the probe pulse without excitation.

used for theoretical modeling. One can presume that the thermal carrier distribution in the sample beyond a pump-probe delay of 1.3 ns approximately corresponds to the lattice temperature as assumed in the microscopic theory. Hence, a comparison between experimental and theoretical data is possible. Transient gain spectra extracted from the experiment (see Fig. 3) show a very good qualitative agreement with spectra arising from different carrier densities in the microscopic analysis (see Fig. 2). Nevertheless, there are some minor quantitative deviations. Firstly, in the experiment the absorption dip is located closer to the edge of the stop band in comparison to theoretical calculations. Accordingly, the spectral position of the maximum gain value was found at 1168 nm, which corresponds to the theoretically predicted maximum gain at 1171 nm. Secondly, the maximum gain value of 1.008 is lower than the value predicted by our calculations for a chosen high charge carrier density, which can be indeed overestimated. We assume that the reflectivity of the non-ideal DBR with finite number of mirror-pairs is lower at the edge of the stop band than its achievable maximum at the Bragg wavelength, as common for those structures. This circumstance limits the maximal gain value. However, the overall trend is in very good agreement. As a rule of thumb, a filter function centered in the middle of the stop band produces more gain.

The spectral width of the gain at a delay time of 1.3 ns amounts to 6 nm. This is a rather narrow gain spectrum compared to the rather broad gain spectra of the pure material gain (see also Ref.18), and is a direct result of the spectrally-narrow filter function of the cavity.

Figure 4 illustrates the chronological evolution of gain obtained from our measurement. For the type-II chip, gain starts at times around 600 ps, reaches a maximum

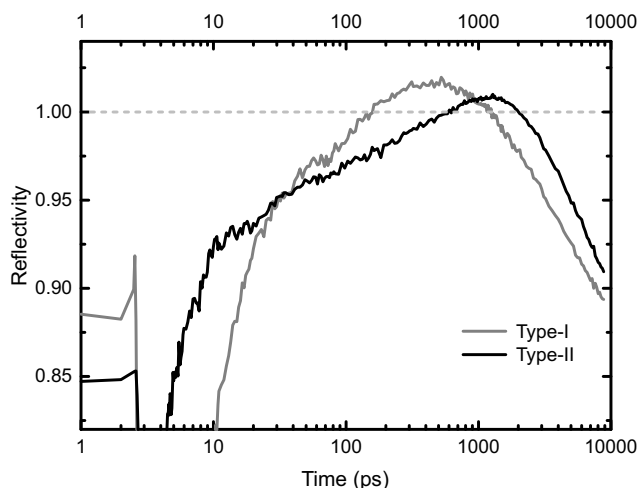


FIG. 4. Semilogarithmic plot showing the gain dynamics of the type-II “W”-VECSEL chip (black line) in comparison to a conventional type-I chip (grey line). For this plot, an offset of 2 ps was applied to the time axis in order to enable a logarithmic illustration.

at 1.3 ns and disappears 2.1 ns after excitation. In order to obtain these gain dynamics, we integrated transients from a spectral region of 1.2 nm around the peak value. For comparison, the same measurements were performed on a type-I VECSEL, exploiting spatially direct transitions. The respective chip, which emits at 1101 nm, features an RPG comprising 10 ($\text{Ga}_{0.71}\text{In}_{0.29}$)As QWs in between GaAs barriers. Again, the filter function lies at the edge of the stop band, providing a similar arrangement as for the type-II VECSEL chip. In the case of the type-I chip, gain appeared at 150 ps and lasted for 1.1 ns until a delay time of 1.25 ns. By fitting exponential functions to the decreasing reflectivity, we retrieve charge-carrier lifetimes for both VECSEL structures. These lifetimes amount to 3.3 ns and 7.3 ns for the type-I and type-II chip, respectively. Although the type-I structure produces a higher peak value of 1.016, the time span of gain provided by the material system lasts longer for the type-II structure, accumulating to 1.5 ns. As mentioned above, this can be seen as a direct effect of the spatial separation of charge carriers in type-II MQWHs, which exhibit a reduced recombination rate. Hence, high charge-carrier densities, which are a prerequisite for gain, are conserved for a longer period of time in comparison to a type-I heterostructure. It is reasonable to assume that a lower radiative recombination rate in a type-II structure can be a limiting factor with regard to the maximum amount of gain. The earlier beginning of measured optical gain in the type-I VECSEL structure is attributed to a faster cooling of the hot carrier distribution, which can be caused by a lot of parameters. For example, a lower number of excited charge carriers and a lower excess energy can cause this behavior. However, it could also be a hint towards an intrinsic difference in cooling dynamics

between type-I and type-II structures.

In conclusion, gain has been theoretically predicted for a novel gain-structure design employing type-II MQWH and the evolution of gain in such structures has been confirmed by time-resolving experiments. Furthermore, the gain dynamics of the type-II VECSEL chip have been compared with the performance of a type-I chip. For the type-II VECSEL, the time-dependent reflectivity obtained in an optical pump-probe measurement reaches a maximum of 1.008 at a wavelength of 1168 nm after 1.3 ns. The obtained gain spectrum is in very good agreement with the theoretically predicted one having its maximum at 1171 nm. Although a significantly higher gain value was obtained for the type-I VECSEL, reaching a maximum reflectivity of 1.016 delayed by 0.85 ns, the gain in the type-II chip lasted 0.4 ns longer in this experiment. We attribute the later onset of gain to slower carrier cooling dynamics in the type-II VECSEL chip. Moreover, the spatially separated confinement of electrons and holes in such type-II “W”-MQWH is understood to play a key role in gain dynamics, since it reduces the recombination rate. Owing to the fact that a type-II chip can be successfully employed in VECSELs and that the design allows for more wavelength flexibility compared to type-I structures, further efforts will be done in upcoming investigations in order to optimize the MQWH design with respect to gain and laser output. Thereby, type-II VECSELs may push available emission wavelengths further to the highly desired telecom wavelengths.

The authors from Marburg acknowledge financial support from the Deutsche Forschungsgemeinschaft via the Collaborative Research Center 1083 (DFG:SFB1083). The authors from Arizona are supported by the AFOSR grant FA9550-14-1-0062.

- ¹C. Möller, C. Fuchs, C. Berger, A. Ruiz Perez, M. Koch, J. Hader, J. V. Moloney, S. W. Koch, and W. Stolz, *Applied Physics Letters* **108**, 071102 (2016).
- ²W. W. Bewley, J. R. Lindle, C. S. Kim, M. Kim, C. L. Canedy, I. Vurgaftman, and J. R. Meyer, *Appl. Phys. Lett.* **93**, 041118 (2008).
- ³J. R. Meyer, C. L. Felix, W. W. Bewley, I. Vurgaftman, E. H. Aifer, L. J. Olafsen, J. R. Lindle, C. A. Hoffman, M. J. Yang, B. R. Bennett, B. V. Shanabrook, H. Lee, C. H. Lin, S. S. Pei, and R. H. Miles, *Appl. Phys. Lett.* **73**, 2857 (1998).
- ⁴K. Meissner, B. Fluegel, R. Binder, S. W. Koch, G. Khitrova, and N. Peygambarian, *Appl. Phys. Lett.* **59**, 259 (1991).
- ⁵R. Binder, I. Galbraith, and S. W. Koch, *Phys. Rev. B* **44**, 3031 (1991).
- ⁶I. Galbraith, P. Dawson, and C. T. Foxon, *Phys. Rev. B* **45**, 13499 (1992).
- ⁷I. H. Libon, S. Baumgärtner, M. Hempel, N. E. Hecker, J. Feldmann, M. Koch, and P. Dawson, *Appl. Phys. Lett.* **76**, 2821 (2000).
- ⁸C. Berger, C. Möller, P. Hens, C. Fuchs, W. Stolz, S. W. Koch, A. Ruiz Perez, J. Hader, and J. V. Moloney, *AIP Adv.* **5**, 047105 (2015).
- ⁹S. Gies, C. Kruska, C. Berger, P. Hens, C. Fuchs, A. Ruiz Perez, N. W. Rosemann, J. Veletas, S. Chatterjee, W. Stolz, S. W. Koch, J. Hader, J. V. Moloney, and W. Heimbrodt, *Appl. Phys. Lett.* **107**, 182104 (2015).

- ¹⁰E. Murphy, *Nat. Photonics* **4**, 287 (2010).
- ¹¹N. Schulz, J. M. Hopkins, M. Rattunde, D. Burns, and J. Wagner, *Laser Photon. Rev.* **2**, 160 (2008).
- ¹²J. F. Klem, O. Blum, S. R. Kurtz, I. J. Fritz, and K. D. Choquette, *Journal of Vacuum Science & Technology B* **18** (2000).
- ¹³I. Vurgaftman, W. W. Bewley, C. L. Canedy, C. S. Kim, M. Kim, J. R. Lindle, C. D. Merritt, J. Abell, and J. R. Meyer, *IEEE Journal of Selected Topics in Quantum Electronics* **17** (2011).
- ¹⁴B. W. Hakki, *J. of Appl. Phys.* **44**, 4113 (1973).
- ¹⁵L. Shterengas, R. Liang, G. Kipshidze, T. Hosoda, S. Suchalkin, and G. Belenky, *Appl. Phys. Lett.* **103**, 121108 (2013).
- ¹⁶K. L. Shaklee, R. E. Nahory, and R. F. Leheny, *JOL* **7**, 284 (1973).
- ¹⁷N. Kirstaedter, O. G. Schmidt, N. N. Ledentsov, D. Bimberg, V. M. Ustinov, A. Y. Egorov, A. E. Zhukov, M. V. Maximov, P. S. Kop'ev, and Z. I. Alferov, *Appl. Phys. Lett.* **69**, 1226 (1996).
- ¹⁸C. Lange, S. Chatterjee, C. Schlichenmaier, A. Thränhardt, S. W. Koch, W. W. Rühle, J. Hader, J. V. Moloney, G. Khitrova, and H. M. Gibbs, *Appl. Phys. Lett.* **90**, 251102 (2007).
- ¹⁹M. Lindberg and S. W. Koch, *Phys. Rev. B* **38**, 3342 (1988).
- ²⁰H. Haug and S. W. Koch, *Quantum Theory of the Optical and Electronic Properties of Semiconductors*, 5th ed. (World Scientific Publ., Singapore, 2009).
- ²¹M. Kira and S. W. Koch, *Semiconductor Quantum Optics* (Cambridge University Press, Cambridge, 2012).
- ²²W. W. Chow and S. W. Koch, *Semiconductor-Laser Fundamentals: Physics of the Gain Materials* (Springer, Berlin, Heidelberg, New York, 1999).
- ²³J. Hader, S. W. Koch, and J. V. Moloney, *Solid-State Electron.* **47**, 513 (2003).
- ²⁴J. Hader, J. V. Moloney, S. W. Koch, and W. W. Chow, *IEEE J. Select. Topics Quantum Electron.* **9**, 688 (2003).
- ²⁵J. Hader, N. Linder, and G. H. Döhler, *Phys. Rev. B* **55**, 6960 (1997).
- ²⁶D. Ahn and S. L. Chuang, *J. Appl. Phys.* **64**, 6143 (1988).
- ²⁷M. Born and E. Wolf, *Principles of Optics*, 7th ed., *Electromagnetic Theory of Propagation, Interference and Diffraction of Light* (Cambridge University Press, Cambridge, 1999).
- ²⁸M. Schafer, W. Hoyer, M. Kira, S. W. Koch, and J. V. Moloney, *J. Opt. Soc. Am. B* **25**, 187 (2008).

Wissenschaftlicher Werdegang

Name	Christian Berger
Geburtsdatum	28. November 1986
Geburtsort	Kassel
06/2006	Erlangung der Allgemeinen Hochschulreife an der Georg-Christoph-Lichtenberg Schule in Kassel-Oberzwehren
10/2006 bis 07/2009	Studium der Physik (Bachelorstudiengang) an der Philipps-Universität Marburg
03/2009 bis 07/2009	Bachelorarbeit zum Thema: "Model study of strong quantum-optical excitations" bei Prof. Dr. Mackillo Kira in der Arbeitsgruppe "Theoretische Halbleiterphysik"
04/2010 bis 09/2012	Studium der Physik (Masterstudiengang) an der Philipps-Universität Marburg
03/2012 bis 09/2012	Masterarbeit zum Thema: "Role of Dissipation in Entanglement" bei Prof. Dr. Mackillo Kira in der Arbeitsgruppe "Theoretische Halbleiterphysik"
seit 11/2012	wissenschaftlicher Mitarbeiter und Doktorand in der Arbeitsgruppe "Theoretische Halbleiterphysik" bei Prof. Dr. Stephan W. Koch an der Philipps-Universität Marburg

